Integrin nano-adhesions, the molecular clutch and actin dynamics in high speed T cell migration

Shannon, Michael James

Awarding institution:
King's College London

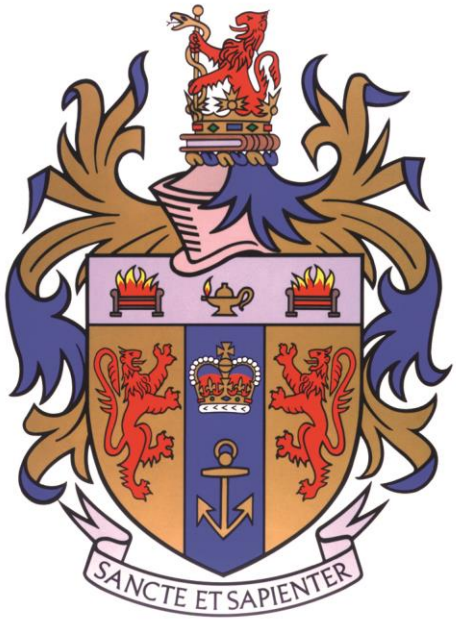

Integrin nano-adhesions, the molecular clutch and actin dynamics in high speed T cell migration

Michael James Shannon

Randall Division of Cell and Molecular Biophysics

King's College London

University of London

September 2017

Thesis presented for the degree of Doctor of Philosophy by Michael J. Shannon

Abstract

T cells navigate the body using constant actin flow, which transiently engages with a spatially and mechanically controlled ‘molecular clutch’ to produce torque and forward cell movement. The clutch is composed of affinity regulated integrin, actin linkers and phospho-regulators, modulated on the nanoscale as T cells move through blood vessels, tissues and lymph nodes. Cells with a point mutation in a gene linked to integrin signalling (PTPN22) exhibit increased adhesion and migration, and in humans the same mutation predisposes for seven different autoimmune diseases.

Here, super resolution localisation microscopy (SLM) in 2D and 3D is used to investigate nano-clustering behaviour in primary effector T cells, while live-TIRF microscopy is used to measure actin flow and engagement. Analysis tools that allow for precise interrogation of clustering in pointillist SLM data and flow/engagement in intensity based TIRF data were developed concomitantly.

Using these tools, it is apparent that integrin based “nano-adhesions” adopt regionally specific nanoclustering patterns upon cell migration, becoming smaller and denser in the focal zone/lamella as compared to the leading edge/lamellipodia. Nano-adhesion re-organisation is coupled to > 70% cortical actin engagement, with a degree of slippage where retrograde flow speed is always greater than cell speed.

T cell migration can be slowed by use of cations or actin inhibitors, or sped by dosing with chemokines or deleting PTPN22. Upon migration speed increase, integrin nano-adhesions become larger in the cell membrane and reduce their engagement with actin. PTPN22 deficient cells also display an increase in the nanoscale colocalization of LFA-1 with pY397 FAK and pY416 Src family kinases, which occur in adhesions smaller than nascent adhesions in non-leukocytes.

The local control of integrin LFA-1 nano-adhesions in migrating T cells is a new area of research that will improve our base framework for understanding immune cell migration, which may contribute to better understanding of migration defects that lead to autoimmune disease.

Acknowledgements

First of all I would like to thank my principal investigator Dylan Owen. He has allowed me the freedom to take this project in the direction I wanted, while keeping my feet on the ground. For this, and many hours in the public houses of London Bridge, some of them spent discussing science, I thank him wholeheartedly. Georgina Cornish has offered absolutely unwavering support and teaching on the biology side – for that and many other things, I thank her. I thank Andrew Cope for his candour and rigour, and for an appreciation of the bigger picture.

I must also thank all members of both groups – the Cope lab for their honest criticisms and help and the Owen lab, in particular George Ashdown. Thanks also to Juliette, and newer members of the lab, Ruby, Dave and Adam. Judith Pineau, the best Erasmus student a PhD student could ask for, gets a particular thank you for her curiosity, no nonsense attitude and ingenuity.

Thanks to all at Janelia farm – Satya Khoun, Teng-Leong Chew, Jesse Aaron – I will see you all again soon, I hope.

A huge thanks goes to all of the members of the Randall biophysics department: in no order Raquel, Rimple, Magali, Gaia, Richard, Dan, Tokuwa, Jake, Rosie and Sylvia in the early days; Fuad, Camille, Brooke, Justin and the rest of the Randall PhD and Postdoc community.

Thanks go to Anne Ridley and Maddy Parsons, for early consultations, lessons and friendly chats about science. Baljinder Mankoo, as well, for chats on science and wider life. The KBI program and everyone on it. David Giganti, a special mention to him, for many late nights in the lab discussing the elegant machinations of proteins in cells, and you know, everything else.

To all my effortlessly wonderful friends: Danielle, for teaching me the basics of treading lightly – still learning. Hazel, I am grateful for many days spent talking, riding around London and detailing our lives and thoughts together. Emma – I'm proud to know someone so intelligent, quick witted and candid. Charlie, I know I can always count on you. Many others have allowed me, surprised me, enlightened me, got me to think about the world differently – Karolina, Katie, Martha, Charlotte, C.H, Pyrrha, Tim, Adam, Tom MJ, Tom P and Alex and of course, Minnie.

My mum Catherine must be thanked, for her understanding and unquestioning support, plus her ability to make me see that problems are rarely as they first appear, and that all storms pass. My Dad, David, of course for his love and support. My brother Martin, for head clearing walks/runs through the woods of Gloucestershire.

My uncle Kevin, whose calm is instructive, and the rest of the Galkoons: Lai King, Hannah and Paul. George and Fran, for their stories, their advice and all else. Julia, Martin, Rosie and Mia up in Glasgow from the Shannon side, and Betsy and Bill – my fantastic grandparents. Long may we all forge ahead together, as there's so much to explore.

Acronyms and abbreviations

14-3-3	14-3-3 Serine/Threonine binding protein family
2ME	β-Mercaptoethanol
AF 647	Alexafluor 647
AIRE	Autoimmune regulatory element
APC	Antigen presenting cell
Arp2/3	Actin related protein 2/3
BSA	Bovine serum albumin
CBC	Coordinate based colocalization
CBL	Casitas B-lineage lymphoma
CCR4	C-C chemokine receptor 4
CCR7	C-C chemokine receptor 7
CCR8	C-C chemokine receptor 8
CXCR4	C-X-C chemokine receptor 4
CD28	Cluster of differentiation 28
CD3	Cluster of differentiation 3
CD4	Cluster of differentiation 4
CD8	Cluster of differentiation 8
CDC42	Cell division control protein 42 homolog
Cryo-EM	Cryogenic – electron microscopy
CSR	Complete spatial randomness
CXCL10	C-X-C motif chemokine 10
Cyto D	Cytochalasin D
DC	Dendritic cell
DMSO	Dimethylsulfoxide
EM	Electron microscopy
EM-CCD	Electro-magnetic charge coupled device
Ena/VASP	Ena/Vasodilator-stimulated phosphoprotein
Erk1/2	Extracellular signal related kinase 1/2

Fab	Fragment antigen binding fragment
FAK	Focal adhesion kinase
FAT	Focal adhesion targeting domain
FND	Fiducial nanodiamond
FOV	Field of view
FRET	Forster resonance energy transfer
Fyn	Proto-oncogene tyrosine-protein kinase Fyn
FZ	Focal zone
GA	Glutaraldehyde
GAP	GTPase activating protein
GEF	GTP exchange factor
GFP	Green fluorescent protein
GPCR	G-protein coupled receptor
Grb2	Growth-factor receptor bound protein 2
ICAM-1	Intercellular adhesion molecule -1
IgG	Immunoglobulin G
IL-2	Interleukin-2
IL-2R	Interleukin-2 receptor
iPALM	Interferometric-photoactivatable light microscopy
IS	Immune synapse
iSTORM	Interferometric stochastic optical reconstruction microscopy
laGFP	Lifeact-green fluorescent protein
LAT	Linker of activated T cells
Lck	Lymphocyte specific protein tyrosine kinase
LE	Leading edge
LFA-1	Lymphocyte function associated antigen 1
LN	Lymph node
Lyp	Lymphoid specific tyrosine phosphatase
mDia1/2	Diaphanous-related formin-1
MEF	Mouse embryonic fibroblasts
MFA	Multiemitter fitting analysis

MHC	Major histocompatibility complex
Mst1	Macrophage stimulating protein 1
MTOC	Microtubule organising centre
NHS	N-Hydroxysuccimide
NK	Natural killer
PBS	Phosphate buffered saline
PC	Pair correlation
PEP	Proline, Glutamic acid, serine, threonine (PEST) enriched phosphatase
PFA	Para-formaldehyde
PI3K	Phospho-inositol-3-kinase
pMHC	Peptide-Major Histocompatibility complex
PP2	Pyrazolopyrimidine 2
PSF	Point spread function
PTEN	Phosphatase and tensin homologue
PTPN11	Protein tyrosine phosphatase 11
PTPN22	Protein tyrosine phosphatase 22
PTP-PEST	Protein tyrosine phosphatase - PEST
PTPRC	Protein tyrosine phosphatase receptor type C
pY###	Phosphorylated tyrosine - ###
Pyk2/CAK	Proline-rich tyrosine kinase 2/cell adhesion kinase β
Rab11	Ras superfamily monomeric G-protein 11
Rab13	Ras superfamily monomeric G-protein 13
Rab5	Ras superfamily monomeric G-protein 5
Rac1	Ras-related C3 botulinum toxin substrate 1
RAP1	Ras-proximate-1
RAPL	Ras-proximate-1 ligand
RIAM	Rap1-GTP-interacting adapter molecule
ROI	Region of interest
RPMI	Roswell Park Memorial Institute medium
RT	Room temperature
sCMOS	Scientific Complementary metal–oxide–semiconductor

CXCL12	Stromal derived factor-1
SFK	Src family kinase
SH2	Src homology domain 2
SH3	Src homology domain 3
SIM	Structured illumination microscopy
siRNA	Short interfering ribonucleic acid
SLM	Single molecule localisation microscopy
SLP-76	Domain containing leukocyte protein of 76 kDa
SMLM	Single Molecule Localisation Microscopy
SPF conditions	Specific pathogen free conditions
Src	Proto-oncogene tyrosine-protein kinase Src (short for sarcoma)
STED	Stimulated Emission Depletion
STICS	Spatio-temporal image correlation spectroscopy
STORM	Stochastic optical reconstruction microscopy
TCM	T cell effector memory cell
TCR	T cell receptor
TEM	T cell central memory cell
Tfh	T follicular helper cell
Th1	T-helper cell type 1
Th17	T-helper cell type 17
Th2	T-helper cell type 2
TIRF	Total internal reflection fluorescence
TOI	Time of interest
TRA	Tissue resident antigen
Treg	T-regulatory cell
UBASH3A	Ubiquitin-associated and SH3 domain-containing protein A
V(D)J	Variable, diversity, joining
Vav1	Proto-oncogene vav 1
VLA4	Very late antigen 4
WASP	Wiskott Aldrich syndrome protein
WAVE	WASP-family verprolin-homologous protein

Zap70	Zeta chain associated protein kinase 70

Table of Contents

Chapter 1: Introduction

Preface

In the context of this thesis, the introduction will take us through the immune system as a whole, and the role of T cell migration from their inception as naïve T cells in the thymus through to effector $CD4^+$ and $CD8^+$ T cells, their polarised migration in tissues, lymph and along blood vessels. Known mechanisms for migration are explored at the level of biochemistry as well as using conventional fluorescence microscopy to study actin regulation and integrin signalling and clustering, before delineating the need for super resolution microscopy techniques to study adhesions in T cells on the nanoscale. Also presented is a more general overview of the importance of spatio-temporal molecular organisation, in particular molecular clustering, in the regulation of T cell migration and activation. Mechanisms of nano-adhesion regulation are posited in the context of several signalling pathways, with a focus on integrin adhesion clustering as a functional predictor of altered migration in the context of an autoimmune disease predisposing mutation in the phosphatase PTPN22.

1.1 Role of T cell migration in the immune system

T cells are necessarily amongst the most highly migratory cells of the body. The precisely orchestrated timing of targeted T lymphocyte migration is also called ‘homing’, and describes a voyage through peripheral tissues, lymphoid vessels and organs, and along vasculature, during which a process of differentiation occurs.

1.1.1 Naïve T cell migration and development

Antigen specific T cells are the mainstay of the adaptive immune system – they are powerful cells, which require tight regulation in order to support protective and aggressive immune responses, while preventing reaction to self tissue. To do this, immature thymocytes migrate from the bone marrow to the thymus gland, where they are committed to the T cell lineage

through notch signalling, inducing their development into naïve T cells[1,2]. In the thymus , T cell receptor (TCR) differentiation occurs, where a double negative (CD4/CD8 co-receptor negative) population located in the cortex undergo V(D)J recombination. Here, variable (V), joining (J), and diversity (D) genes segments rearrange to create a unique receptor composed of αβ or γδ subunits. Lymphocyte function associated antigen (LFA-1; CD11a/CD18; αLβ2) co-stimulation is important for deciding whether a T cell will express a TCR composed of αβ or γδ subunits[1]. T cells committed to one of these two lineages then move deeper into the thymic cortex, where they undergo positive and negative selection[1].

There are several protections in the thymus against the production of self-reactive T cells – a process called tolerisation. The structure of the TCR dictates its affinity for self-Major Histocompatibility Complex (MHC) – a kind of molecular plinth on which peptide antigens – from digested pathogens, are presented. There are two subtypes: MHC class one (MHC I) is presented by somatic non-immune cells, and MHC class two (MHC II) is presented by specialised antigen presenting cells (APCs) such as dendritic cells (DCs), macrophage and B cells. In the thymic medulla, thymocytes engage their TCRs with peptide-MHC expressed on

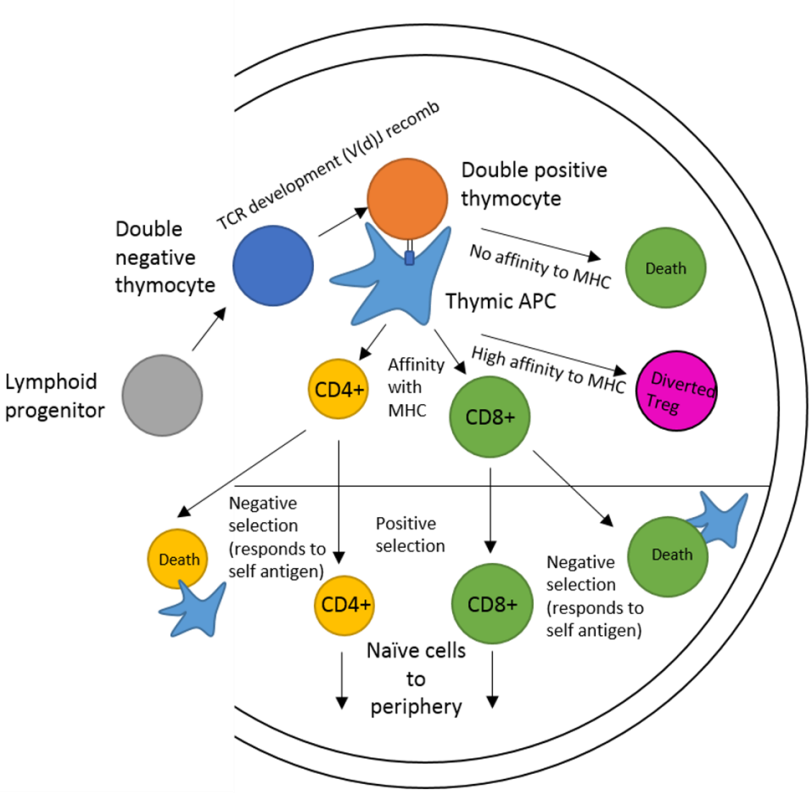

Figure 1-1: **Thymocytes develop into tolerised naïve T cells in the thymus.** Diagram showing the progression from bone marrow derived lymphoid progenitors, through TCR development and positive/negative selection in the cortex and medulla of the thymus gland to become single positive naïve T cells that exit into the periphery.

thymic APCs and thymic epithelial cells to test for reactivity. Where affinity is low for the MHC molecule itself, T cells are positively selected for further differentiation and become single positive for one or the other of CD4 or CD8. Where affinity is too high, they are deleted through clonal deletion, or are redirected to become T regulatory cells through clonal diversion[1]. Thymic APCs, which present self MHC to immature thymocytes, also express the AIRE protein (Autoimmune regulator) which induces the transcription of tissue restricted antigens (TRAs): antigens that are only expressed in the peripheral tissue. Thymocytes that react to such antigens, or to ubiquitous self-antigens also present in the thymus, are deleted by 'negative selection'[3,4] (Figure 1-1).

Self-tolerised naïve cells then exit the thymus gland and migrate to secondary lymphoid organs (spleen, tonsils, Peyer's patches, lymph nodes), where migratory dendritic cells present them with antigen that they have encountered, trapped, processed using ubiquitin ligases and presented using MHC ll. The draining lymph nodes are defined as secondary lymphoid organs where CD4 positive T cells generally encounter antigen, presented on MHC II on the surface of antigen presenting cells which have migrated there from distal tissues. CD8 positive T cells specifically bind to MHC I. The antigen presented on the MHC protein is called an octopeptide, and is the product of protesomal degredation of foreign (or self) proteins, whereupon an MHC carrying a specific octopeptide is called peptide-MHC (pMHC). Processing results in (billions) of possible octopeptides. As each T cell expresses TCRs specific for only one epitope, there are likely to be only 1 in 10 million $CD4^+$ and 1 in 100 million $CD8^+$ naïve T cells available for a given epitope.

Given this fact, the first predictor of the efficiency of an immune response is the ability of naïve T cells to effectively scan DCs in the lymph node. Estimates state that T cells are able to make contact ~ 500 different DC cells/hour[5,6], and that integrins – molecular hooks that bind to ligands presented on target cells - and actin, the flowing cytoskeleton - are highly involved in the scanning process. The speed of migration in the lymph node depends on the secretion of chemokines by APCs, fibroblasts and endothelial cells[7].

The second predictor of the strength of a response is clonal expansion: where a specific effector population explodes from a single cell of origin. A large population of initial effector T cells travels to the site of infection and tries to halt it: resolution of the initial infection is the goal of a new effector T cell. Effector T cells have effector cell abilities, and different homing objectives depending on their subtype. These cells circulate through vasculature, into and out of tissues to sites of infection and damage, where they interact with and activate leukocytes

such as basophils, mast cells and eosinophils (for example, in allergic responses mediated by Type 1 helper cells) and macrophages and neutrophils (in inflammatory responses mediated by type 2 helper cells – figure 1-2). At this stage, effector T cells that respond to self-antigen are deleted in a process known as 'peripheral tolerance'[8,9]. Other effectors travel back to the lymph nodes and activate B cells. Most of these cells die after the initial response, but some remain to become memory effector cells[10].

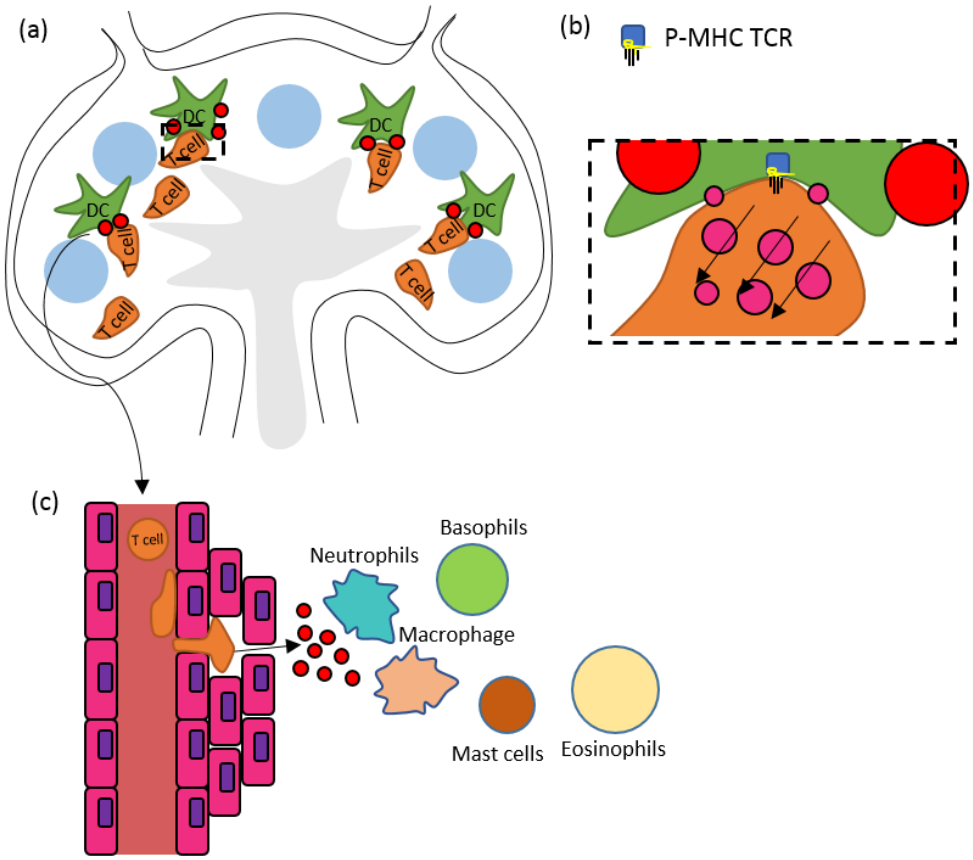

Figure 1-2: **T cells scan 500 dendritic cells per hour in the draining lymph node.** a) Naïve T cells enter the lymph node and interact with dendritic cells DCs. They migrate both randomly and in the direction of secreted chemokine (red circles). b) During this process, T cells co-opt actin retrograde flow (black arrows) and integrin engagement (pink circles) with ICAM-1 present in the lymph node and on DCs. MHC expressed on DC surface presents a unique octapeptide to the TCR. The affinity of this unique TCR to this unique octapeptide is measured by the T cell, which if properly co-stimulated differentiates into an effector T cell and undergoes clonal expansion. c) Effector T cells exit the lymph node and travel through vasculature to resolve the initial infection, activating other cells of the immune system.

1.1.2 Effector memory development

After resolution of the original infection, the contraction phase follows, where effector T cells that react too strongly and are in danger of damaging host tissue are deleted, and weak responders go into anergy – a refractive state in which T cells no longer respond or become activated. The remaining effector T cells persist in the absence of antigen and enter the memory phase: this population have functional migration changes, secrete interleukin-2 (IL-2) and other effector T cell specific cytokines[11,12], existing at 100 to 1000 times the population of naïve cells specific for a given antigen. Migration changes in the $CD8^+$ memory subset involve movement to many peripheral non-lymphoid tissues, where they can remain for long periods of time as resident defenders – also called tissue resident memory T cells (TRMs)[13,14]. Both $CD4^+$ and $CD8^+$ effector memory cells display a preference for certain tissues such as intestine[15] or skin[13] depending on the expression of certain cell surface markers.

Dissection of surface expressed receptors by flow cytometry has enabled the identification of several subsets which have different migration capacities: for example T helper cells, which are differentiated into at least 5 separate subtypes including T regulatory cells, Th1, Th2, Th17, follicular helper (Tfh). Indeed, specific effector T cell types can be further subdivided into those with particular migratory differences and capacities based on chemokine and adhesion receptors present on their surface. CCR7+ cells are now called central memory (TCMs) and CCR7- effector memory cells (TEMs), based on their functional migration phenotypes. TCMs preferentially recirculate in the blood, encountering antigen before returning to lymphoid organs – these cells do not display cytotoxic function; TEMs on the other hand migrate preferentially to nonlymphoid tissues and patrol the peripheral tissues[16]. Thus within the adaptive immune system, TEMs act as first responders to old threats, containing the invading pathogen quickly and specifically – provoking an immune response and communicating with antigen presenters. TCMs then shuttle to the lymph nodes and upon secondary challenge, stimulate B cells and generate new effector cells (figure 1-3).[16]

One of the functions of LFA-1 interaction with its cognate ligand intracellular adhesion molecule 1 (ICAM-1) is to induce a genetic program that results in late differentiation of T cells into certain types of effectors, namely Th1, Th17 and regulatory T cells[2]. Programmed cell fate, therefore, is an alternate function of LFA-1. Interaction between LFA-1 and ICAM-1 induces the Notch-mediated polarisation of effector T cells to a Th1 type profile[2,10]. Interestingly, in cells derived from mice completely deficient for LFA-1, the Treg population is unable to mediate suppression of the rest of the T cell population *in vitro*, and the mice

themselves showed a propensity for colitis and autoimmunity[17]. LFA-1 has also been implicated in maintaining normal levels of proliferation of CD4+ T cells after antigen stimulation[17,18]. Engagement of LFA-1 with ICAM-1 alone is enough to produce an IL-2/IL2R feedback response and T cell activation, with LFA-1 decreasing the required strength of the activatory signal, and a raised propensity to respond to low affinity antigens[10,17]. It is important therefore to consider LFA-1 in a wider context as a modulator of short to long term T cell responses as a population, which might occur holistically during the process of migration. Another way to look at it, might be to describe LFA-1/ICAM-1 as instrumental not just during migration, but also during the switch from migration to acting at an inflamed site. This phenomenon as whole can also be called the 'second touch' hypothesis, where subsequent to Ag mediated T cell activation at a site of infection, LFA-1/ICAM-1 fine tunes the response to ensure appropriate levels of activation[19].

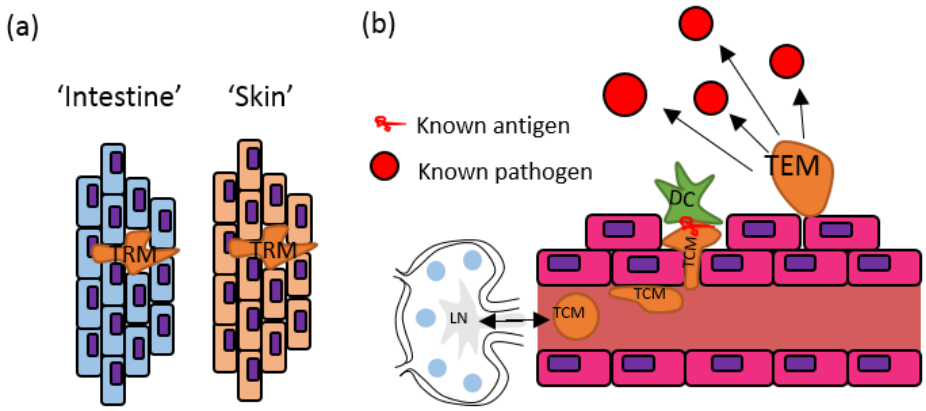

Figure 1-3: **Diagram delineating types of migratory memory T cells**. a) Tissue resident memory cells are targeted to different peripheral tissues depending on their cell surface receptors. b) T-central memory (TCMs) recirculate the blood, recognise previously encountered antigen and return to the lymph node and report on it, whereas T-effector memory cells deal with the threat directly in the periphery.

Recent work has therefore informed a holistic understanding of T cell differentiation in the context of migration, where migratory subsets differentiate further upon receipt of effector status. Effector T cells respond more easily, at lower antigen dose, without the requirement for such stringent co-stimulation than naïve cells. Their clonal re-expansion happens more readily. Whether effector T cells retain such abilities during long term memory is unknown [1], but that LFA-1 is required for co-stimulation of naïve but also effector memory cells is clear[1]. LFA-1 has therefore has many functions aside from migration, including genetic

reprogramming, all of which are tuned depending on the ligands present in the particular milieu of each individual T cell[20–22].

T cell migration capacity therefore is instrumental for naïve and effector T cells. Effector T cells home to peripheral tissues immediately after receiving antigenic stimulation, and are drawn to areas that contain pathogens by the actions of the innate immune system, which induces local inflammation and releases chemokine signals into the blood, targeting in particular CCR4, CCR8 and CXCR4 receptors. Indeed, the migration of antigen specific effector T cells to sites of new infection is very efficient[20].

Effector T cells of different subtypes respond to different chemokine signals, and traffic to different areas to maximise this efficiency as required. Certain effectors display tissue specificity to increase the probability of encounter with a pathogen of a certain kind – for example a gut pathogen compared to a skin pathogen[21], or those first encountered in the joints, lungs or central nervous system[22]. In order to achieve travel through all of these diverse environments, T cells must use a variety of different signalling molecules that work with the extracellular environment on a single cell level.

1.1.3 Effector T cell migration and LFA-1

The timeline of effector T cell migration involves their travel first of all from blood to tissue. In order to do this, weak tethers are expressed on the endothelium of blood vessels, namely the selectin family. T cells use these to adhere weakly, and begin a 'rolling' stage, prior to the binding of LFA-1 integrin to its ligand ICAM-1 and the induction of the 'crawling' stage. Importantly, adherence and crawling along blood vessels is greatly heightened during inflammation (whereas naïve cell ingress to lymph nodes is more constitutive, aided by addressins expressed on the surface of high endothelial venules). Shear flow from the pressure exerted in blood vessels plays a role in heightening the affinity and clustering of LFA-1 integrin (as well as VLA4, which mediates adhesion) and therefore its avidity in binding to ICAM-1, through what is known as a 'catch bond' [23] mechano-sensing mechanism (figure 1-4) – this is covered in more detail in section 1.2.3

LFA-1/ICAM-1 interactions are widespread, and mediate antigen specific and innate immune interactions, as well as adhesion, transendothelial migration and migration in tissues. While some leukocytes, are able to migrate unimpeded within the lymph node or through tissues of the interstitium or *in vitro* in a collagen gel without the use of the LFA-1/ICAM-1 clutch[24–26], T cells absolutely require it to migrate at optimal searching speeds of > 10 µm/min[15,24–30].

Intralymphatic T cell crawling and migration to distal lymph nodes depends on ICAM-1 and LFA-1[15] , and while traditionally LFA-1/ICAM-1 interactions are thought of as important in the moments preceding diapedesis, tight cooperation and many thousands of interactions are required for T cells to migrate through tissues and to recirculate during inflammation.

Return to the lymph nodes, as in the case of TCMs, involves T cell crawling migration through afferent lymphatic vessels (which have very low shear fluid flow), and into collection vessels/chambers (higher fluid flow) for transport into the draining lymph node[10]. It's a relatively understudied area, but recently was found to be heavily dependent on T cell crawling directed by LFA-1/ICAM-1 interactions, which are heightened during cell migration[15]. Such interactions are heightened by the presence of chemokines such as stromal derived chemokine (CXCL12, also known as SDF-1). *In vitro* T cells speed up their migration upon addition of CXCL12[22], and blockade of ICAM-1 *in vitro* or *in vivo* inhibits adhesion, crawling and transmigration alike.

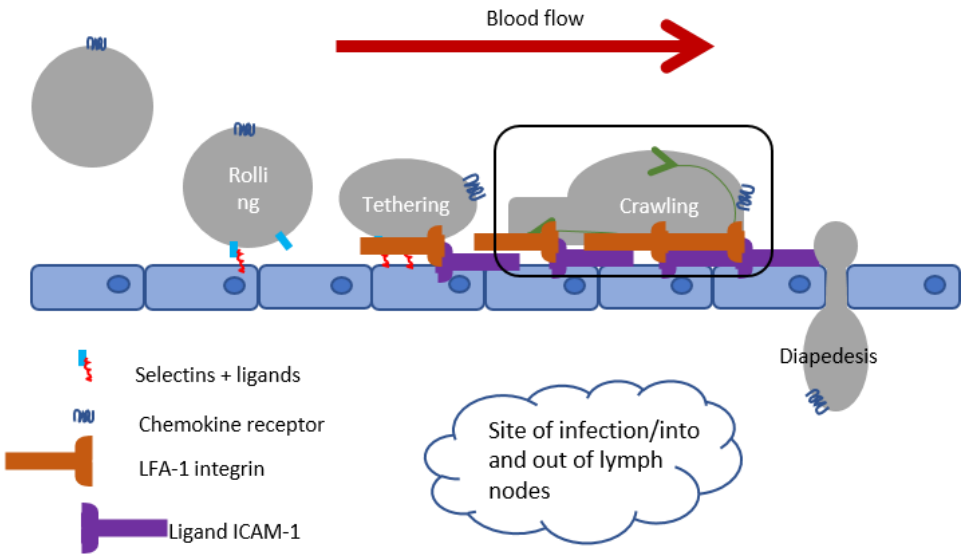

Figure 1-4: **Diagram showing T cell adherence to vessel walls.** T cells adhere weakly to the endothelium via selectins, before tethering more strongly using LFA-1 ICAM-1. The crawling step that precedes diapedesis using cooperative constant actin flow (green arrow) with integrin engagement in a clutch mechanism to elicit migration. The diapedesis phase also requires LFA-1 and actin.

Overall, LFA-1/ICAM-1 interaction is important at almost every turn for T cell migration in 2D and 3D. As T cells migrate, they adopt a polarised morphology which is common to all settings, 2D and 3D (section 1.2 and example figure 1-5). Their motility can be categorised as a

Brownian random walk, or a Lévy walk[31], depending on the presence of a chemokine gradient which induces more persistent migration or high concentrations of ICAM-1 or encounters with MHC expressing DCs, inducing slowdown or even stop signals.[32]

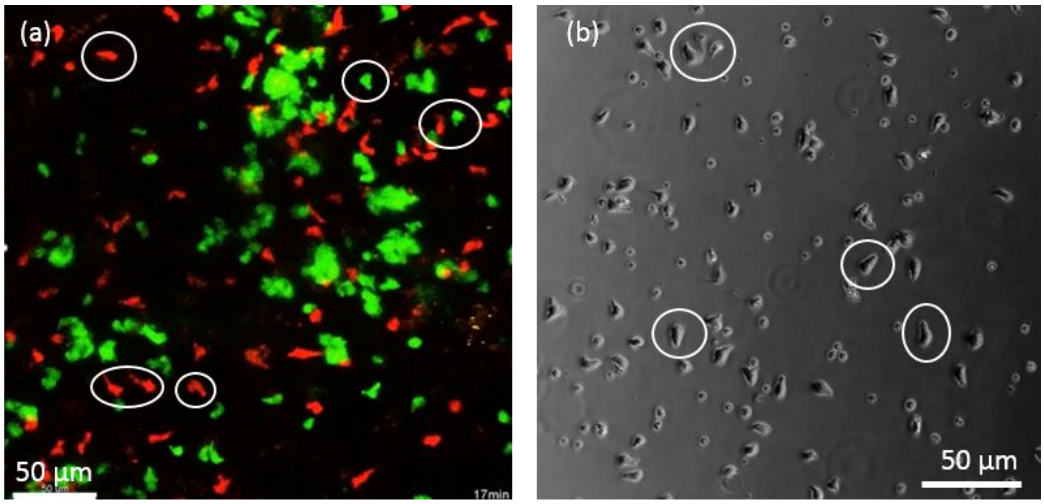

Figure 1-5: **Example data showing T cells migrating in vivo and in vitro.** a) Frame from a two-photon microscopy movie (adapted from Hor, J.L et al 2015) showing polarised migrating CD4+(red) and CD8+(green) T cells in the inguinal lymph node. b) example frame from my data: phase contrast movie of CD4/CD8 effector T cells migrating on glass coated with ICAM-1. Circles – example polarised cells.

T cells are described as having amoeboid motility, due to the shape of the cells during migration which resembles the amoeba *dictosteylium discoideum*, characterised by an actin rich lamellipodia/pseudopodia, membrane blebs, a large lamella and a trailing edge called the uropod[25]. Their speed is not constant, and during scanning, whether in the lymph node or peripheral tissues, actin plays a key role in creating the 'Lévy walk'[31] for maximal efficiency: a kind of 'stop and go' ponderous yet efficient ambulation, consisting of many small moves separated by longer trajectories. This type of movement likely increases the efficiency of T cells ability to correctly check for high affinity pMHC expressed on the APCs (MHC II) or virus infected cells (MHC I) they move over[20,31].

Only a fraction of T cells isolated from peripheral human blood migrate. It is these that also proliferate in culture and are studied, so studies are limited to the migrating population. Upon activation *in vivo*, the proportion of migrating cells vastly increases. T cell velocity is increased after addition of CXCL10 or CXCL12 chemokine, where the persistent stages of the Lévy walk pattern are enhanced[7,33,34]. T cell velocity has also been reported to increase while cells are scanning DCs in the lymph node, and in the paracortex of the LN, T cells move at almost

double the speed[5,6]. T cells stop completely upon recognition of foreign antigen and sufficient co-stimulation[32]. To do this, single cells co-opt actin, and adhesions which communicate force and with the outside environment of the cell and turn it into spatio-temporal chemical signals[35].

1.2 T cell migration: polarisation and the actin-integrin molecular clutch

In order to travel such huge distances each day, through the blood, tissues and lymphatics, T cells rely on the coordination of actin flow and integrin engagement[36].

To migrate, T cells **polarise** and adopt a particular tear drop shape that is in every sense related to the intrinsic properties of the actin network, as well as many signalling molecules which operate differently or preferentially in the front of the cell compared to the middle and back of the cell. A focus on integrin affinity states has led to the characterisation of the leading edge (LE) and focal zone (FZ). In the FZ, talin is more focused than in the LE, and characteristics bands of phospho Zap70 are present at the interface.[37]

1.2.1 Actin flow and actin regulators

In the lamellipodia (leading edge), actin forms a branching 'dendritic' network whereas in the focal zone, fibres are more elongated and stress fibre like. Whereas arp 2/3 directs polymerisation in the lamellipodia/leading edge, formins direct polymerisation in the cell middle. At the leading edge, the membrane is pushed forwards by the elastic energy released as nascent filaments unbend, having been in a constant state of polarised polymerisation (treadmilling) producing thermal energy to bend them in the first instance[38].

The pulling force of myosin 2, present exclusively in the lamella, provides the pulling force that drives retrograde flow, and results in the majority of force generation for persistent migration. This form of treadmilling is distinct from the type of treadmilling common to filopodia, in which actin bundles grow at the barbed ends and are disassembled at the pointed ends, while Ena/Vasp prevents branching allowing for continuous elongation of filaments. In the middle of cells, formin driven actin dynamics dominate, distinct from the type of dynamics present in the leading edge. Formins create elongated unbranched fibres by adding g-actin subunits at the barbed ends while ensuring the continued association of profilin, inhibiting

capping proteins and depolymerisation[39]. Although mostly thought of as effectors of Rho GTPases, mDia1 and 2 both mediate the assembly of stress fibres is multiple cell types.[39]

Actin regulators are also known to adopt a polarised localisation distribution. In particular, RhoG, CDC42 and Rac are known to direct actin dynamics in the lamellipodia of diverse cell types including T cells. These GTP regulated Rho GTPases signal predominantly to WAVE/WASP arp2/3 activators[40], which themselves bind the GEFs and GAPs that control Rho GTPase signalling forming a lamellipodial localised feedback loop likely to be highly spatially regulated[41]. Microtubule reorganisation is thought to be less important for migration in fast migrators such as T cells and neutrophils, due to the fact that the MTOC is not relocalised in front of the nucleus by CDC42 as in other cells[42].

As we have seen, T cells migrate with random directionality on an ICAM-1 coated plate in the absence of chemokine (figure 1-5). When chemokine is present in the way it is provided for these experiments, cells adopt a range of speeds. As T cells only require a 10 % difference in this gradient across the length of a single cell, CXCL12 addition, even without a distinct plate wide gradient causes cell speed increase[22]. T cells are able to respond to such small gradient of CXCL12 concentration due to the gradient potentiating power of PI3Ks, which are

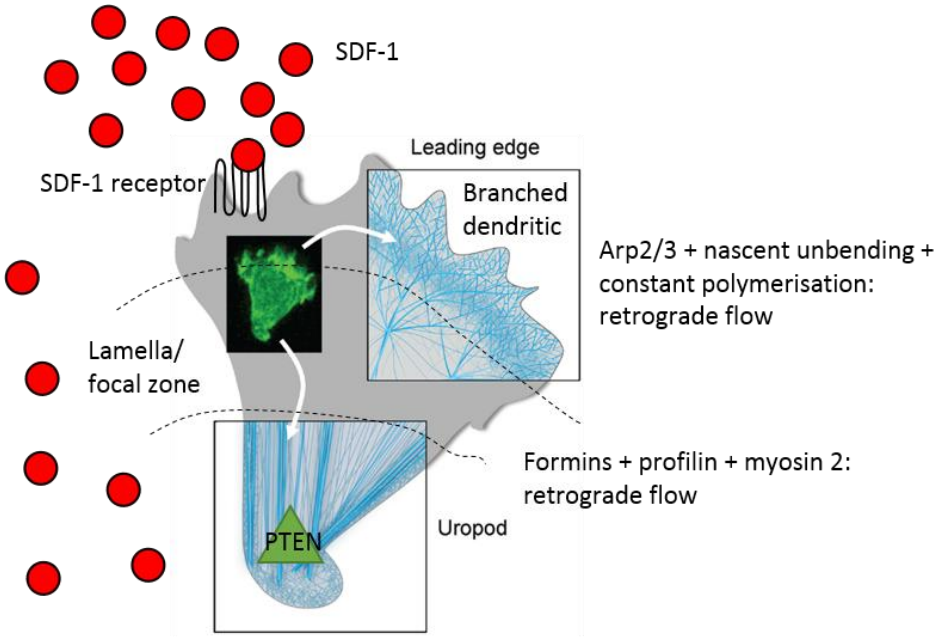

Figure 1-6: **Diagram showing two actin networks in T cells.** Leading edge actin is constantly polymerised under the control of Arp2/3, WAVE and WASP, producing a dense dendritic network. Nascent unbending pushes the membrane forward, while constant polymerisation ensures persistent treadmilling. Lamella actin is elongated and regulated by formins. CXCL12 presence aids migration through Rac signalling pathways forming transient gradients between the front and back of the cell. Adapted from Dupré.L 2015[100].

controlled by PTEN phosphatase. PTEN localises to the back of the cell in fast moving cell types such as Dictyostelium (figure 1-6)[25,43].

Actin flow generally represents actin that is not engaged with adhesions[44,45], and immobile actin in the external reference frame represents actin that is engaged indirectly to integrin LFA-1 (detailed in section 2.7.8). The cell moves over these immobile areas of f-actin, which are necessarily bound to integrin based adhesions. How much of the meshwork is stationary and bound in comparison to each contact point, and the size/affinity/composition of the integrin adhesion bound to a particular meshwork size is unknown. It is possible that in the future this question could be addressed through use of correlative super resolution microscopy of the actin cytoskeleton in conjunction with LFA-1, talin and vinculin as markers of tension, and phosphorylated Focal Adhesion Kinase (FAK) and phosphorylated Src family kinases (SFKs) as markers of activity (figure 1-7) which are covered in the next section.

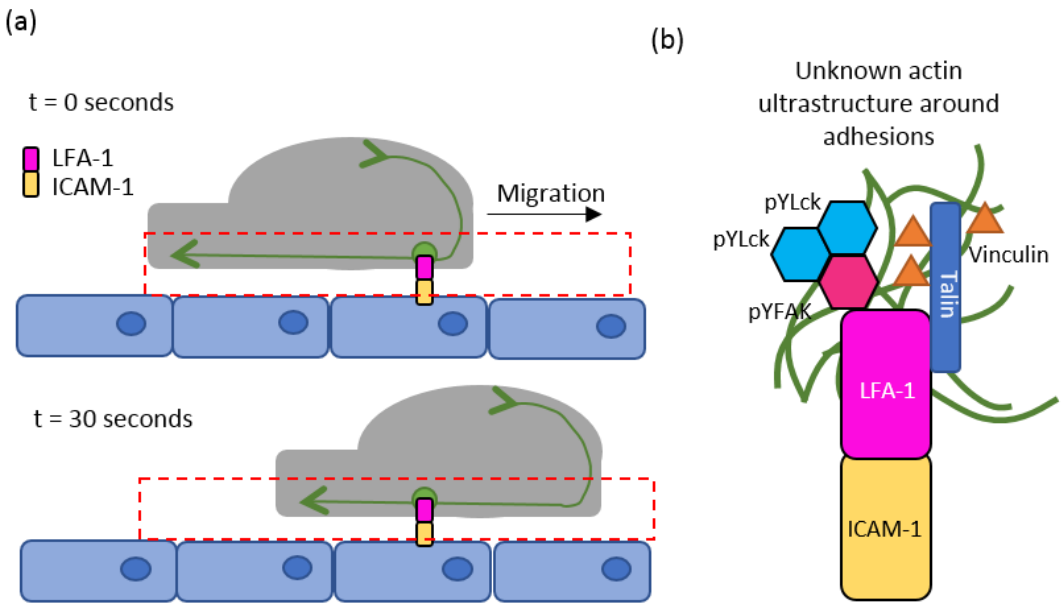

Figure 1-7: **Diagram showing immobile actin and adhesions in the external reference frame.** a) Cells (grey) use constant actin flow which transiently binds to adhesions based around LFA-1. The cell moves forwards due to translation of actin retrograde flow force through the adhesion to the substrate. Red dashed box = TIRF imaging zone. b) The basic structure of an integrin based adhesion contains LFA-1 bound to ICAM-1, linked to actin through talin and vinculin and regulated at an early stage by phosphorylated FAK and phosphorylated SFKs such as pY416 Lck. Actin ultrastructure when bound to adhesions is unknown.

1.2.2 Integrin signalling regulation

The integrin lymphocyte function-associated antigen-1 (LFA-1, αLβ2) participates in a wide range of adhesive interactions in T cells including antigen recognition, emigration from the vasculature, migration along vasculature, in between endothelial cells, through tissues and into and out of lymph nodes. [46,4727]. LFA-1 adopts both inside out and outside in signalling modalities. The former involves binding or activation of intermediates, inside the cell (emanating from for example the interaction between CXCL12 chemokine and the CXCR4 transmembrane GPCR) which causes conformational changes in LFA-1 itself, increasing or decreasing its affinity and spatial localisation. Spatial rearrangement of LFA-1 has been reported as a consequence of chemokine binding and RAPL signalling, where microclusters measured by diffraction limited microscopy gather differentially in the lamellipodia as compared to the lamella[48]. The latter involves direct binding of LFA-1 to its cognate ligand, ICAM-1, which induces conformational changes in the integrin itself. This mode of signalling can also be induced by the addition of cations such as Mg^{2+}, Ca^{2+} or Mn^{2+}, and conformation/affinity regulation has a direct consequence on the ability of integrins to transmit and translate force into cell migration[49]. This process is coupled to tension activation across the integrin and changes to the beta tail regions, where the high affinity form can bind both talin and kindlin [46,47,50–53].

Inside-out signalling involves the communication of an extracellular signal that affects integrin affinity or clustering through a different receptor to the integrin itself. In T cells, the best studied examples are the TCR and GPCR chemokine receptors like CXCR4. The general result of the inside out signal is to change either the conformation and therefore the affinity, or the clustering of integrin, both affecting its ability to interact with actin on inside of the cell, and cognate ligand (ICAM-1) in the extracellular environment[54].

Communication between the TCR and LFA-1 integrin during immune synapse formation is a good example of inside out signalling. TCR stimulation by pMHC results in an increase in affinity and clustering of LFA-1, increasing its binding to ICAM-1[54]. Key signalling intermediates involved in transducing TCR signals to LFA-1 include Vav1, which acts as a GEF to signal to Rho-GTPases such as Rac1, allowing LFA-1 to be released from actin and to reorganise to form part of the immune synapse[55]. Phosphorylation of Threonine 758 on the β2 chain of LFA-1 has also been shown to occur after TCR activation, resulting in binding of 14-3-3 proteins, Rac1 and CDC42 activation and consequent changes in LFA-1 clustering[56]. Similarly, activation of the CXCR4 chemokine receptor upon CXCL12 binding also results in this phosphorylation at T758,

again converging on the Rac-1 pathway by signalling through Tiam1 (a Rac-1 specific GEF) and representing the other best characterised example of 'inside-out' signalling, known to increase adhesion during T cell migration[56].

LFA-1 affinity regulation

LFA-1 has three distinct affinity conformations, classified as such due to their relative binding affinities for ICAM-1. These are: bent with a closed headpiece, extended with a closed headpiece, and extended with an open headpiece. During T cell circulation, LFA-1 is kept in an inactive state: the low affinity 'bent' forms (figure 1-8a) is inactive and doesn't signal[48]: it is thought that this conformational state is essential for T cell circulation in the lumen of the blood vessels, as it prevents adherence with other blood cells and ligands in the blood, as well as unwanted binding to endothelial walls[48]. Intermediate and high forms are extended, and change the conformation of the transmembrane tails (figure 1-8b and c) as well as the head group. In high affinity forms, the i-domain in the head group is available for catch-bond mediated binding of ICAM-1[57,58]. Catch bonding describes a bond that strengthens the more force is put across it[59–61]. Current understanding is that in T cell migration the force necessary is gained from actin flow, and the strength of the bond is increased upon application of shear flow such as in the blood during T cell crawling prior to diapedesis[53]. In neutrophils, the propagation of high affinity LFA-1 has been associated with a transition from rolling to complete arrest in the vasculature under shear flow[48].

Integrin LFA-1 is activated through inside-out signalling which involves crucially the binding of talin and kindlin, which themselves themselves maintain and promote the high affinity form[62,63]. Treatment of cells with Mn^{2+} ions (supplied in the form of $MnCl_2$) forces LFA-1 into its high affinity form by pushing open the alpha L and beta 2 subunits[64] through binding to the i-like domain.The affinity of LFA-1 within polarised T cells is non-homogenous. LFA-1 adopts a mixed population of LFA-1 affinities for optimal cell migration, with particular zones of migrating cells being delineated by affinity and colocalization with particular actin linkers. Intermediate affinity LFA-1 localises to the leading edge of migrating T cells, and binds actin in cooperation with α-actinin[65]. High affinity integrin is localised mainly to the focal zone/lamella region of cells, where it exists in tight collaboration with talin and vinculin, which binds to cryptic talin binding sites as talin is stretched under tension[34].

Most of the literature regarding LFA-1 affinity posits high affinity as the most 'active form'. It is true that high affinity LFA-1 experiences the most tension across its beta two subunit, and is actively maintained in such a conformation through this pulling force[53], but the addition of

Mn^{2+} results in increased cell adhesion to the point where cells stop moving, pointing towards the need for a mixed population of affinities. CXCL12 induced inside out signalling, which speeds up cell migration *in vitro*[22], has been shown to propagate the intermediate form of LFA-1 as well as the high affinity form, thus propagating this mixed population tuned for high speed migration(ref). CXCL12 chemokine can trigger transient switching intermediate/high affinity integrin in cells that are in solution with soluble ICAM-1: as the switch is not maintained, this points towards a tension requirement for maintenance of the high affinity form[66]. With these ideas held in mind, describing high affinity LFA-1 as the most 'active' form obfuscates and oversimplifies the discussion: what must also be taken into account is 1) the way LFA-1 transmits force derived from flowing actin, 2) the molecules that regulate the process and also 3) how both of these factors are regulated locally, spatio-temporally, on the nanoscale (figure 1-8).

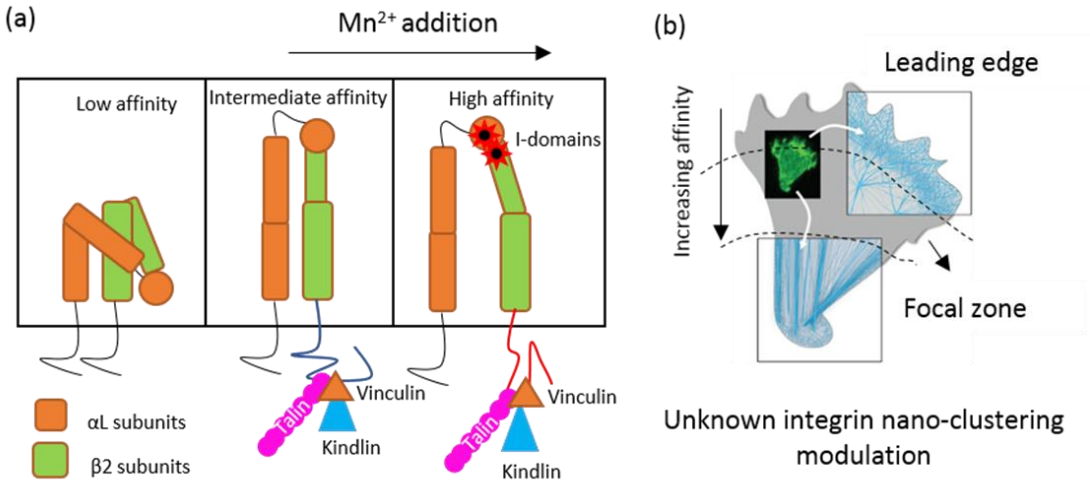

Figure 1-8: **Diagram showing 3 affinity forms of LFA-1 integrin, and where they are located in the cell.** A) LFA-1 is made of αL and β2 subunits. The bent form is inactive, the intermediate form has an altered cytoplasmic tail that binds talin, kindlin and vinculin. The high affinity form i-domains interact allowing stronger binding to ligand and further conformational change in the cytoplasmic tails. Manganese ions push affinity to the high form. b) Intermediate and high affinity integrin are mixed in the leading edge of polarised T cells but high affinity predominates further back in the cell. Integrin nanoscale organisation is unknown.

1.2.3 Focal adhesion kinase/Src family kinase regulation of tiny adhesions

In T cells, LFA-1 based adhesions most resemble 'nascent adhesions'[34]: described in non-leukocytes as < 200 nm sized small integrin based entities, newly formed and composed of

multiple molecules that mature into more complex, larger focal complexes and then focal adhesions. Based on the tiny size of integrin LFA-1 clusters in T cells and the fact that they do not mature into large adhesions[67], it is clear that a separate mechanism of maturation and organisation is present. This kind of organisation is likely integral to how T cells achieve such feats of distance during migration, and move through such a diverse set of environments. Studying T-cell like adhesions is useful for understanding this separate class of adhesions in T cells, which operate on smaller length scales yet share commonality in the types of proteins they use to operate.

Nascent adhesions, as the name suggests, are newly formed integrin based adhesions. They are formed in the lamellipodia in a single concerted step, recruiting several key proteins, amongst the first of which is phospho-397 FAK. Interestingly, nascent adhesions are FAK, Src kinase family (Lck and Fyn) and Erk1/2 rich – and inhibiting any one of those proteins results in adhesion maturation[68].

FAK and Src family kinases (SFKs) work together to strengthen signals emanating from LFA-1[69], where LFA-1 mediated activation is the strongest activating pathway of FAK[70] – a close relative of Pyk2 (protein tyrosine kinase 2, also known as cellular adhesion kinase (CAK)). pY397 FAK localises to nascent adhesions in other cell types and promotes smaller adhesions.

FAK has key tyrosine residues that can be phosphorylated to regulate its activity. Y397 is located in the linker region between the FERM and kinase domains, and is almost constitutively phosphorylated in T cells[69], suggested a spatio-temporal mechanism of regulation. LFA-1 activation triggers the spatial accumulation of FAK at the receptor, which precedes paxillin recruitment and binds in a complex containing kindlin and talin[69]. Active pY397 FAK recruits Src Family Kinases (SFKs) such as Lck and Fyn to adhesions, which bind via SH2 domains to this phospho residue[68,69,71]. pY397 FAK phosphorylates Lck at position Y416, and active Lck then phosphorylates the other tyrosine residues on FAK[72]. These include Y576 located in the kinase domain and known to increase FAK activity to its maximum, as well as Y925 located in the FAT domain thought to recruit Grb2, the adaptor protein[43]. In a situation where Lck activity is downregulated by the addition of PP2, phosphorylation of FAK is reduced[68].

Using this method, then pY397 FAK is recruited first to adhesions, which signals to SFKs as well as Erk1/2 and Zap70. The recruitment of SFKs and the strengthening of the adhesion follows, which themselves regulate the phosphorylation of FAK and are necessarily dependent on spatio-temporal regulation on a local level. This supports a growing body of evidence that

kinases like FAK are not simply 'binary switches', and that their location and frequency has functional effects within individual adhesions[73].

The spatio-temporal nature of FAK and SFKs include a sensitivity of FAK to mechanotransduction: fluctuations in force through adhesions are known to change the localisation of FAK[73]. In general, the application of force to focal adhesions results in adhesion maturation and an increase in size. Nascent adhesions have been shown to not require myosin 2 activity, and are therefore perhaps less dependent on force than larger adhesions. This could be relevant for fast T cell migration, where many tiny adhesions regulate transient interactions as opposed to forming strong long lasting anchor points[67]. Negative regulation of Pyk2 has been reported through PTP-PEST – a phosphatase in the same family as PTPN22. When PTP-PEST is removed, Pyk2 becomes hyper phosphorylated and signalling increases[74].

Actin dynamics also have a role in directing nascent adhesions and FAK, SFK localisation. Cytochalasin D treatment of non-leukocytes decreased the existence of vinculin containing nascent adhesions[35]. In these same cells, nascent adhesions disappear at the lamellipodial/lamella interface as dendritic actin passes by them[35]. This reliance on actin flow and the presence of vinculin suggests a force transducing role for such adhesions. Indeed, it is understood that talin recruitment follows pY397 FAK-pY416 Src, and focuses in the lamella, the focal zone of T cells, with concentrated high affinity integrin LFA-1[34]. Talin, along with vinculin is a key player in transducing force from actin through the adhesion to the substrate so that cells can move forward. No-one knows whether FAK precedes talin in nascent adhesions, but [75]FAK is one of the first proteins to be recruited to nascent adhesions.[75]

1.2.4 The molecular basis for force transduction in LFA-1 based adhesions

LFA-1 is a mechanosensitive unit in itself[53], but other molecules involved in many types of adhesions also play a key role in fulfilling a mechanosensitive function of adhesion complexes[45,76,77]. Due to the commonality of the proteins that T cell adhesions (despite differences in their size and density) and focal adhesions contain, including known force transducers, it is instructive to study large adhesions. Indeed, vinculin has been found to be present in nascent adhesions alongside pY397 FAK and pY416 Src[78], but it is in larger adhesions that force has been investigated to date[45,79].

In focal adhesions, alpha actinin, talin and vinculin make up the force transduction layer, by linking actin filaments directly to integrin[77,79]. FAK was also characterised in the 'core' layer of mature focal adhesions as a signalling molecule which is uncoupled from actin and instead

moves with the integrins to regulate the linkage to actin. Alpha actinin, talin, vinculin are coupled more often to individual areas of flowing actin (in mouse embryonic fibroblasts (MEFS)) than integrin itself, which was coupled more often to core proteins such as FAK[45,73]. This suggests that the integrin-actin linkage is highly regulated by the internal clutch, as well as by extracellular catch binding to ligand.

Talin precedes vinculin in adhesions, and promotes integrin clustering as well as a switch from low to intermediate/high affinity LFA-1. It's a multi-functional molecule, which has 11 vinculin binding sites, two actin binding sites and several sites for binding the integrin beta tail[80,81]. On binding to integrin, talin is stretched under tension transmitted from flowing actin through talin and integrin, which is anchored to its ligand ICAM-1 outside of the cell. This stretching reveals cryptic binding sites for vinculin, and therefore vinculin is a good marker for tension within adhesions. *In vitro,* required tension is 5 pN, and whether this can be modulated by clustering or association of various other clutch components is unknown.[82] Coupling of vinculin to talin can be thought of as a strengthening step, and is interesting because it doesn't necessarily necessitate the growth in size of an adhesion.

Vinculin is a mechanosensitive protein that promotes adhesion maturation and strengthening on the one hand, and rearranges actin on the other[45]. It is a functional delineator of the lamellipodia(leading edge) from the lamella(focal zone), which promotes the formation of many nascent adhesions in the leading edge of different cell types[45]. 14 different binding partners associated to FAs have been identified for vinculin, therefore it is likely to be highly spatio-temporally regulated. Indeed, super resolution iPALM work revealed that vinculin is spread throughout the z depth of large focal adhesions, and is oriented tail above head. Clare Waterman's lab reported that talin promotes vinculin activation, which then modulates retrograde actin dynamics and linkage to the actin[76]. As vinculin moves up in Z, in individual adhesions, this strengthens them[76]. Vinculin appears to precede pY397 FAK in nascent adhesions[78]. Whether this translates to T cell integrin based nanoadhesions is not known, but it is significant that vinculin is not related to the growth in size of nascent to focal adhesions[45]; indeed, FA growth does not appear to correlate with force, but depends on the speed of actin flow[45]. Further evidence of vinculins role in adhesion maturation lies in its competition for talin binding with RIAM (Rap1-GTP adaptor molecule), where RIAM-Talin modules are recruited to the membrane, and vinculin displaces RIAM at the talin N-terminal, suppressing adhesion turnover and promoting maintenance[81].

It is an open question therefore, about what it means for a T cell adhesion to be 'mature' as opposed to 'nascent', as on the nanoscale, T cell LFA-1 adhesions don't appear to get bigger in the lamella[67]: this warrants investigation into the functionality of integrin clustering in terms of cell migration.

1.2.5 Integrin recycling, FAK and SFKs

The transient stability during the kinetics of the formation of nascent adhesions (11.8 second on average) point to an idea that they are size limited: once they reach a certain size – around 200 nm^2, they are recycled.[78] It is unknown whether this is true in T cells, which must necessarily recycle their integrin constantly and at speed, and contain many integrin nanoclusters[67].

Recently active FAK was identified as having a key role in the recycling of integrins confined to the lamellipodia, where clathrin mediated endocytosis begins integrin transit through Rab5 and 11 endosomal compartments, while being maintained in an active, force bearing conformation by their association with FAK, Talin and PIPKIγi2 [83] (the latter transports talin to FAs in diverse cell types)[84]. It has been proposed due to this data that FAK and talin in endosomes are involved in a model of 'conformational memory' where they maintain integrin activity using tension, so that nascent adhesions can form quickly when integrin is re-added to the cell membrane[71,83]. In addition, Src kinase has been found in the same early endosomes in these non-leukocyte cells, which would be expected given its role in phosphorylating PIPKIγi2 in order to facilitate its function with talin[84]. Whether Lck or Fyn do this in T cells, and to what extent T cells localise FAK in vesicles above the height of the membrane is an open question.

In addition to the Rab 5 and 11 pathways, the Rab 13 pathway is implicated separately in the trafficking of integrin LFA-1 from the lamella/uropod to the front/leading edge cell membrane in T cells[85]. To do this RAPL binds to active Rap1, which forms a complex with Mst1. Mst1 binds directly to the cytoplasmic tail of the αL subunit in LFA-1, mediating it's uptake by Rab13 that recycles LFA-1 to the very tips of the leading edge. It is unknown whether these LFA-1 containing vesicles also contain talin and FAK, and this pathway is unaffected by modulation of the Rab 5/11 pathway[85,86]. The delineation of this Rab 13 dependent pathway and the Rab 5/11 pathways suggests that the content of the vesicles might be different depending on which pathway is being enacted. This would warrant further investigation by use of super resolution techniques to further investigate the composition and function of vesicular LFA-1 in migrating T cells.

Leading edge/focal zone based uptake of LFA-1 for recycling is thought to be coupled to adhesion disassembly in the uropod. Here, stretch activated calcium channels are opened. The increase in local calcium activate calcineurin and calpain, which cleave integrins[87]. The integrins, and associated molecules are then endocytosed: it is unknown whether vesicles emanating from the back of the cell, which originate from mature adhesions, are recycled in the same way as adhesions in the front/middle (figure 1-9.

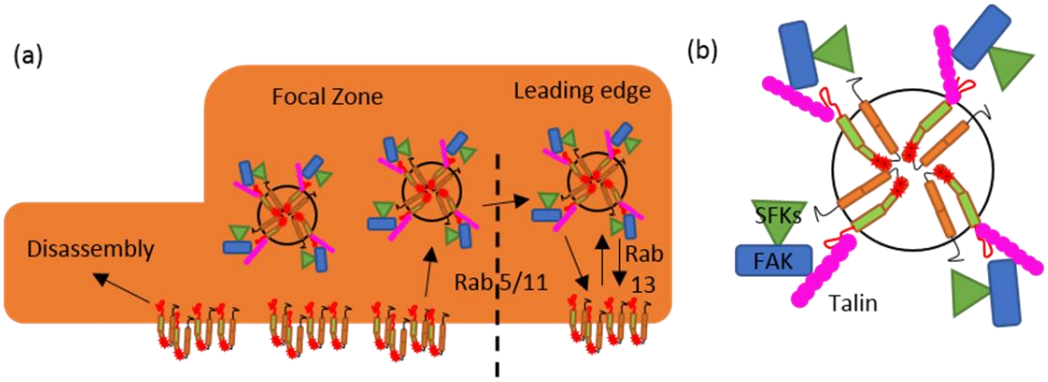

Figure 1-9: Diagram showing current model for LFA-1 recycling in migrating t cells. a) Integrin clusters are recycled from and to the membrane through Rab5/11 and Rab 13 dependent pathways. They are disassembled at the cell rear. B) LFA-1, talin FAK., SFK containing vesicles during Rab mediated recycling may be composed differently depending on which Rab pathway they are a part of.

1.2.6 PTPN22 modulates the clutch and predisposes for autoimmune conditions

PTPN22 is a modulator of integrin signalling downstream of integrin LFA-1. It is significant that PTPN22 acts to control LFA-1, and that when mutated, patients exhibit predisposition to autoimmune disease. Effector T-cells are essential for defence against pathogens, but can also drive autoimmunity. *PTPN22* encodes for a protein tyrosine phosphatase (PTP) that targets SRC and SYK family kinases, in which an amino acid substitution (R620W) has been found to predispose for multiple autoimmune diseases, including Rheumatoid arthritis, type 1 diabetes, vitiligo, Graves' disease and systemic lupus erythematosus[88–91].

Generally , PTKs are thought to amplify signalling, while PTPs control it and tune it, to communicate a specific spatio-temporal message that results in a local or global change in single cell behaviour[92]. The powerful and constitutive nature of PTK activity makes it important that PTP activity is maintained, especially in T cells, which go through changeable environments and have to respond in quite specific ways very quickly, while avoiding self-directed responses that might lead to autoimmunity.

There have been 57 PTPs identified in T cells, which have been linked to diverse roles including apoptosis, differentiation, proliferation, activation and migration. Certain PTPs have been linked to autoimmune conditions, and they include: PTPN2, PTPRC, PTPN11, UBASH3A, PTPRT and PTPN22[88,93]. The final example, PTPN22 is the most strong genetic predictor of autoimmune disease outside of MHC, as evidenced by gene wide association studies[91]. Mutation appears in patients at position 1858 in the coding region of the PTPN22 gene resulting in an arginine > tryptophan subsitition at position 620 – a region located in the SH3 binding polyproline domain of the protein[94]. In humans, the protein produced from the PTPN22 gene is called Lyp, while the mouse orthologue is called PEP.

As well as in T cell receptor signalling, PTPN22 has strong links to integrin signalling. Indeed most of the proteins mentioned above as being part of the TCR signalling pathway during APC conjugate formation and antigen recognition are also involved in the integrin signalling[67], so it should come as no surprise that PTPN22 is implicated in the control of T cell migration.

PTPN22 is most highly expressed in haematopoetic cells: highly migratory immune cells such as NK cells express the highest levels of PTPN22 followed by neutrophils, CD4+/CD8+ T cells, monocytes and dendritic cells[88]. The fact that expression levels seem to correlate to well with the need to dynamically migrate along blood vessels, through tissues and in between cells is indicative of an important role for PTPN22 in cell migration.

Diffraction limited fluorescence microscopy show that phosphorylated Lck, Zap70 and Vav1, three molecules intimately linked to integrin signalling, are colocalised with PTPN22 in the leading edge of migrating cells, but not in non-migrating cells[67].

Biochemistry revealed that PTPN22 acts to dephosphorylate these three proteins directly, and siRNA knockdown of PTPN22 resulted in upregulation of pLck, pZap70 and pVav1[67]. Erk1/2 is also hyper-phosphorylated in human PTPN22 knockdown, human PTPN22 R620W transfected, murine PTPN22 $^{-/-}$ and murine PTPN22 R620W knock-in T cells[67], a strong marker for sustained integrin signalling known to be present in nascent adhesions. Functionally, PTPN22 R620W substitution and PTPN22 knockout increased the migration velocity of murine T cells for cells migration on ICAM-1 coated dishes, a 2D *in vitro* system for studying cell migration (preliminary data: figure 1-10).

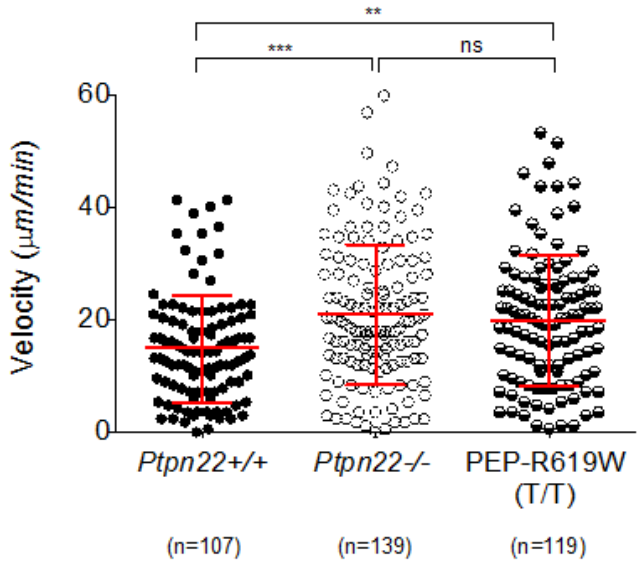

Figure 1-10: **PTPN22 -/- and PEP-R619W murine T-cells migrate faster than PTPN22 +/+.** Plot shows velocities (μm/min) of individually tracked (ImageJ manual tracking plugin) effector T-cells migrating on glass coated with 2μg/ml mrICAM-1.

The way PTPN22 functions at a molecular level is currently understood to be as part of a spatio-temporally regulated cooperative complex with Csk, which works together to deactivate Lck[94]. Csk (a kinase) and Lyp/PEP (PTPN22) form a complex through binding via the P1 polyproline domain of Lyp to an SH3 domain in Csk. It is significant that this domain is the one in which the R620W mutation occurs – thus it is this interaction that is thought to be abrogated in the T cells of patients with mutated PTPN22. It is thought that the Lyp/Csk complex is held at the membrane in active T cells by PAG (protein associated with GEMS)[92,95]. Here, Csk phosphorylates Lck at inhibitory tyrosine 505, inducing binding of pY505 with a self-SH2 domain, resulting in its inhibition. Concurrently, the activatory phospho-tyrosine pY394 Lck in the Lck kinase domain is de-phosphorylated by Lyp.

This overall deactivation of Lck, by phosphorylating an inhibitory tyrosine domain, and dephosphorylating an activatory one, has widespread consequences due to the amplification role of Lck in phosphorylating Zap70. Where PTPN22 is mutated or removed, uncontrolled Lck signalling downstream of integrin binding tends to be the result. Though there has been no direct evidence to date, it is possible that the phosphorylation of FAK, known to modulate the

strength, clustering and tenacity of integrin adhesions[68] is also affected by PTPN22, due to its direct relation within adhesions to the phosphorylation status of Lck.

The consequences of Lyp interactions lead to deeper signalling pathways which are also affected. As discussed, Lyp interacts directly with Lck, Zap70 and also Vav1. Vav1 is a RhoGEF which signals via the WASP/WAVE and WIP complexes to affect actin dynamics, and is known to be instrumental in the formation of polarised T cell modalities as well as the immune synapse during successful antigen recognition by the T cell receptor[41,96].

Indeed, integrin signalling is intimately linked to the T cell receptor signalling pathway: PTKs Lck and Zap70, Vav1, and the adaptors Grb2 and c-Cbl downstream of engagement of the T-cell receptor (TCR) and integrin lymphocyte function-associated antigen 1 (LFA-1) complexes[88], so it is likely that PTPN22 has an effect in both pathways. TCR signalling and integrin signalling overlap on many levels, and T cells must quickly switch between synapse mode and polarised migration mode many times and very quickly (figure 1-11).

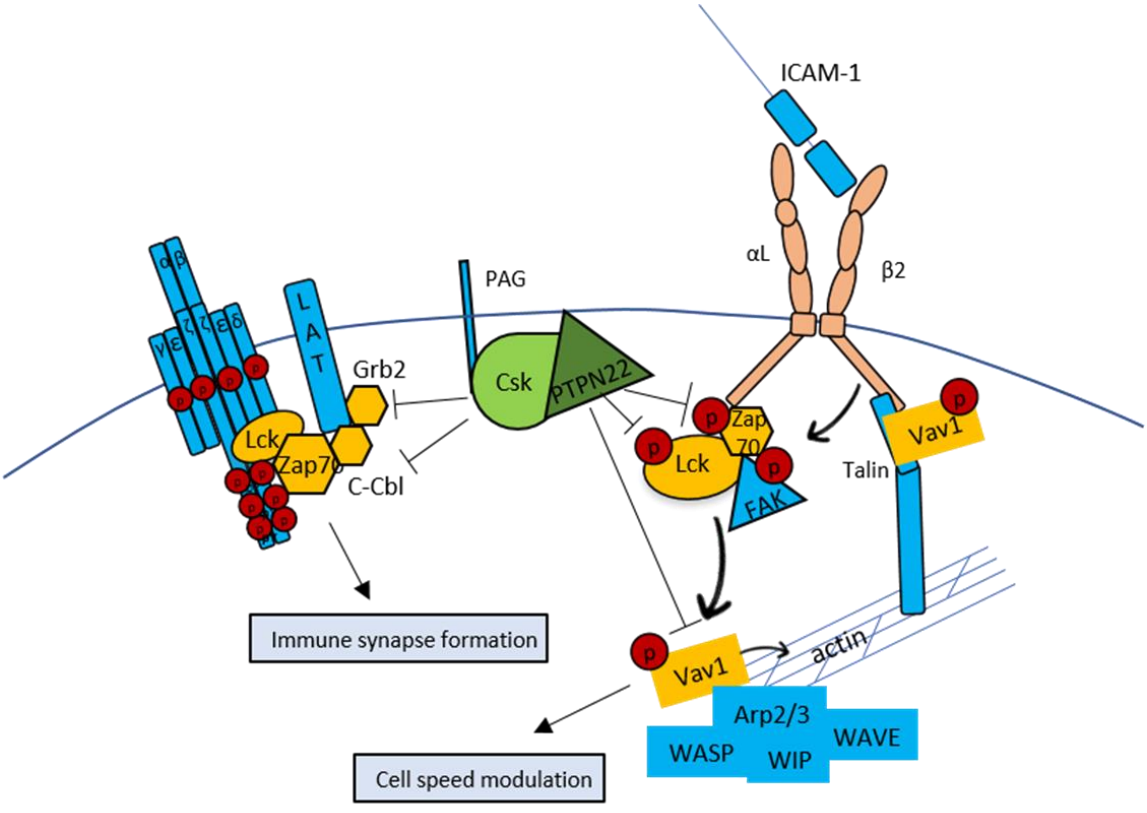

Figure 1-11**: Diagram showing known PTPN22 phosphatase signalling downstream of integrin LFA-1 and the TCR.** Direct interaction partners are coloured in yellow, indirectly affected proteins are coloured blue.

Recently, super resolution studies (dSTORM) have shown that PTPN22 is held in large clusters at the membrane in non-migrating T cells which appear to break apart or 'decluster' upon LFA-1:ICAM-1 engagement. PTPN22 re-localises to areas in the cell where LFA-1 is thought to undergo affinity maturation like the focal zone and leading edge, which is also clustered in these regions[34]. The mechanism by which PTPN22 increases the migration speed of cells, and its relationship to nanoclustering is unknown.

1.2.7 Summary of molecular system under investigation and what we hope to find out

Overall we have a system that, once LFA-1/ICAM-1 binding has occurred relies first on the association of talin which links to actin which exerts force[97]. Vinculin in then recruited to the adhesions which results in strengthening, and pY397 FAK is then recruited due to traction force and the action of myosin 2[98]. This reinforces adhesions and SFKs are recruited, which bind to pY397 on FAK, becoming phosphorylated at Py416 themselves. The recruitment of SFKs to FAK containing adhesions results in the further recruitment of FAK, which results in the recruitment of many different adhesion proteins, actin modulation and integrin clustering. PTPN22 is a phosphatase that acts downstream of LFA-1 upon activation of Lck – its mutation leads to a loss of function that results in uncontrolled integrin signalling, a functional increase in cell speed during migrating and in humans predisposes for autoimmune disease.

To probe this, the nanoscale structure of integrin adhesions in the membrane of migrating T cells will be studied. The literature points towards the existence of a molecular clutch organised on length scales previously uninvestigable by conventional means. How it links to actin on the nanoscale, whether nano-clustering has a functional effect in cells, and the effect of losing a key phosphatase involved with migration are unknowns. In order to investigate this, super resolution is required.

1.3 Super resolution microscopy to study integrin nano-adhesions

While most 'clustering' information about molecules in cells has actually been gleaned from biochemical assays to identify multimers in whole cell populations, the use of fluorescence microscopy has since provided ~ 300 nm resolution images that are able to discern microclusters of LFA-1 in T cells that form seconds after the addition of chemokine and addition of ICAM-1[33] . However, controversy has surrounded the nature of adhesions in T cells, as large focal adhesions are undetectable in these cells. Super resolution microscopy has since revealed that within those microclusters actually exist many nanoclusters, which exist mainly below the length scale of 'nascent adhesions' characterised in non-leukocytes[67]. The functionality of such nanoclusters are an untapped area of study out of the reach of conventional techniques, which is potentially fruitful for understanding T cell migration and its regulation on the nanoscale. To investigate the importance of nanoscale events in T cells, it is important to appreciate the work that has gone before.

1.3.1 Nanoclustering in T cells

The clustering of molecules in cells works spatio-temporally to gather signalling components required for a particular response[99]. Protein clusters in the membrane as well as within the cell, in vesicles for example, represent dynamic control platforms for molecules which must be made rapidly available to facilitate extremely dynamic T cell migration and immune synapse (IS) formation[19,100].

T cells operate a nanoscale reorganisation of clusters of molecules in the formation of the 'immune synapse' – the contact zone between an antigen specific T cell and an APC. The zonal organisation of such nano-clustered proteins in this synapse is sometimes called 'supramolecular' due to the formation of a bulls-eye like zones characterised by the presence of different subsets of signalling molecules[19,101–104]. The supramolecular precise and tunable organization of this synapse relies on the dynamic nano-clustering of proteins.

As well as LFA-1 integrin, several different T cell immune synapse formation molecules have been investigated by super resolution microscopy[67] and found to have functional consequences related to their clusters. Two examples are LAT (linker of activated T cells) and Lck[105].

Signalling events downstream of inside out and outside in integrin signalling are also regulated at the level of clustering and include Vav1[55] and SLP-76, crucial molecules involved in switch from polarised to centripetal actin flow in IS formation.

Cluster formation involves combinations of scaffold proteins, direct interactions, vesicular trapping or partitioning into lipid ordered domains, and more recently even cortical actin corralling[106] in which calpain is a mediating protease that frees LFA-1 to move laterally in the membrane[66]. Lipid order has been implicated in supporting the formation of signalling complexes of TCR[107] as well as LFA-1 heterodimers[108], which are both required for successful APC communication and synapse formation[109]. In the case of LFA-1 integrin, super resolution microscopy has allowed us to probe the dynamics of LFA-1 nanoclusters: for example by showing that LFA-1 preorganises in quiescent T cells and localises to ordered parts of the lipid membrane aided by by glycosylphosphatidylinositol anchored proteins[110,111]

It is clear that much of the regulation of such clusters happens below the diffraction limit of light, defined by Ernst Abbe in 1873. Abbe realised that achievable resolution through even the most perfect optical system is intrinsically limited by the diffraction of light, defined by its wavelength and the aperture of the instrument's optics. In practice, Abbe's diffraction limit states that optical microscopes cannot resolve two objects that are closer than $\lambda/2NA$, where λ is the wavelength of light and NA is the numerical aperture of the objective lens.

A lack of evidence for the functional relevance of such a ubiquitous phenomenon as clustering may be due to the limitations of the instruments, which have now been superceded by FRET techniques as well as super resolution microscopy[112]. The co-dependence of clustering phenomena on affinity regulation, mechanosensing, actin rearrangement and the involvement of multi-component complexes regulated differently in fast migrators like T cells have made it a difficult field to unpick, but super resolution microscopy combined with new analysis tools have the potential to uncover entire networks of nanoscale communication that direct migration.

1.3.2 Super resolution microscopy techniques

Coarse information about protein localisation can be extracted from conventional fluorescence microscopy images, but cannot be applied to the study of nanoscale molecular organisation. To circumvent the diffraction limit, a new family of super resolution fluorescence microscopy techniques have emerged, based on an ability to achieve resolution

beyond Abbe's diffraction limit of visible light, down to the range of 10s of nanometres for some techniques and 100 to 200 for others.

The choice of technique is suited to samples of different specifications. There are three main categories: structured illumination based techniques (including SIM)[113,114], point spread function (PSF) engineering (Stimulated Emission Depletion microscopy) and localisation microscopy (STORM and PALM) [115–117]. These approaches are presented in the following sections:

STED

Stimulated emission depletion (STED) relies on using an adapted confocal microscopy set-up, using a scanned focal point for illumination of the sample. To achieve super resolution, a toroidal (doughnut) shape depletion beam is used to surround the outside of the original illumination beam, with the effect that fluorophores within the doughnut are maintained in a depleted S_0 off state[118,119] (figure 1-12). The doughnut shaped depletion beam has a longer wavelength than the excitation light, and is scaled to the energy gap between the highest S_0 orbital and the lowest S_1 orbital. In practice this results in the illumination spot being shaped into a much narrower PSF, meaning only a few fluorophores at the centre of the spot are able to emit. The microscope requires extremely precise alignments as well as very strong illumination intensities generally unsuitable for live cells. In addition the sample must be raster scanned, limited the time resolution for live cell imaging. Data output is pixelated like conventional diffraction limited data, so is perhaps more useful for qualitative analysis of structures rather than quantitation of molecular clusters[120].

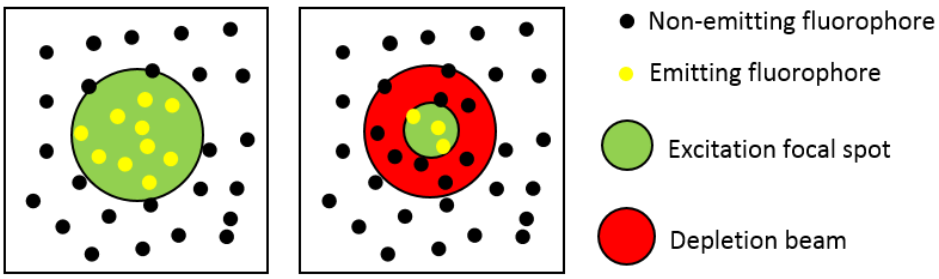

Figure 1-12: **STED methodology.** a) Illustration of a typical 200 nm wide illumination focal spot at the focal plane in confocal microscopy b) STED reshaped illumination beam, with doughnut shape stimulated depletion.

SIM

Structured illumination microscopy (SIM) relies on patterning the illumination light[121,122], typically using grating patterns and more recently a spatial light modulator (SLM)[114]. The purpose is to generate interference between the applied illumination pattern and the existent structures within the sample. Moiré fringes result from the superimposed patterns, which illustrate destructive and constructive interference (figure 1-13). The fringes themselves therefore contain information from both the known structured illumination pattern and the unknown sample structure, with a third piece of information being the fringes themselves. Measuring the low intensity fringe information (coarser than structures in the sample) and comparing it with the known illumination pattern allows derivation of high frequency sample information and subsequent reconstruction. During imaging, the grating or illumination pattern is shifted and rotated multiple times, to increase lateral resolution in all directions and build up a complete diffraction unlimited image. Its ability to be performed in widefield, and the use of a spatial light modulator allow for fast imaging, and the technique can be used with conventional fluorophores at low input laser power making it suitable for live cells. Ultimately, its resolution in the best case is limited to around 100 nm[121,122]. Nanoclusters in T cells are typically below this value in diameter, therefore a different approach was required here.

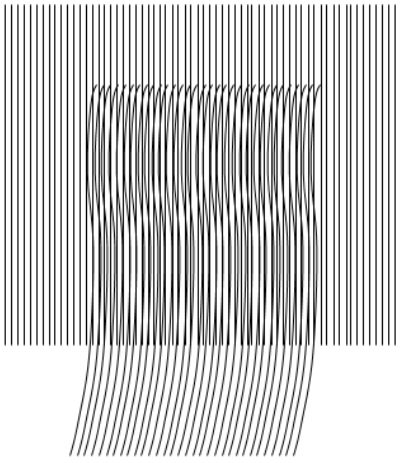

Figure 1-13: **Illustration of Moiré fringes being generated.** Two grating patterns are presented, one representing structures in the sample, and one representing a known structured illumination pattern.

STORM

Single molecule localisation techniques were introduced in 1989[123], and functionalised for use in biology in 2006[115,117,124]. They showed that spatially isolated fluorophores could be localised to a single centroid point using a gaussian estimation to discern the assumed position of the fluorescing molecule. The family of techniques under the umbrella of SMLM include photo-activated localisation microscopy (PALM), stochastic optical reconstruction microscopy (STORM) and related techniques, and achieve super resolution by temporally separating the emission of fluorophores. In a given field of view, only a sparse subset of the fluorophores are turned 'on' in each frame, so that their PSFs don't overlap, allowing precise estimation of their centroids. Multiple frames of different subsets of fluorophores can be localised to build up a reconstructed image. Resolution is assessed usually by dint of 'uncertainty'[125] and typically lies in the range 10 to 30 nm. The high resolution, added to the highly quantifiable point pattern nature of the output data makes this an ideal technique to use to study molecular clustering.

Although electron microscopy (EM) routinely achieves this level of resolution previously, it is limited to fixed samples, heavy metal staining artefacts often arise[126] and very specialized set-ups are required for vitrification in cryo-EM correlated to fluorescent microscopy[127,128]. SMLM combines the high specificity of antibodies or fluorescent constructs for proteins of interest with the resolution required to access rich information about the spatial localization of molecules.

Ratification of the technique has come in the form of results from fluorescence resonance energy transfer (FRET) experiments (which measure close interactions (< 10 nm) between proteins), that have since been replicated in super resolution studies affording similar resolution. In T-cells, (FRET) experiments have previously shown that Zap70, LAT, CBL and Vav1 all interact with TCR (reviewed in[36]). Since then, SMLM data has been gathered and the colocalization of such molecules measured: results have replicated what has been seen in FRET[36].

1.3.3 Stochastic optical reconstruction microscopy

In order to study protein clustering, fixed cells can be stained using an antibody and suitable emitter, typically alexa fluor 647. A high powered 640 nm laser is applied to the sample in total internal reflection fluorescence (TIRF)-mode, hitting the sample at ~ 63 degrees with respect to the coverslip. This induces an evanescent wave of excitation light at around 100 nm in depth. Fluorophores attached via antibodies to the protein of interest were excited in this region only, and the fluorescence emitted light travels back through the objective and through a filter cube. In this case the cube is an excitation bandpass filter that collects light in the range 670 nm to 790 nm and discards scattered light emanating from reflections with the coverslip. Distributions of photons from each emitter are detected as a point spread function (PSF) at the EMCCD detector (figure 1-14).

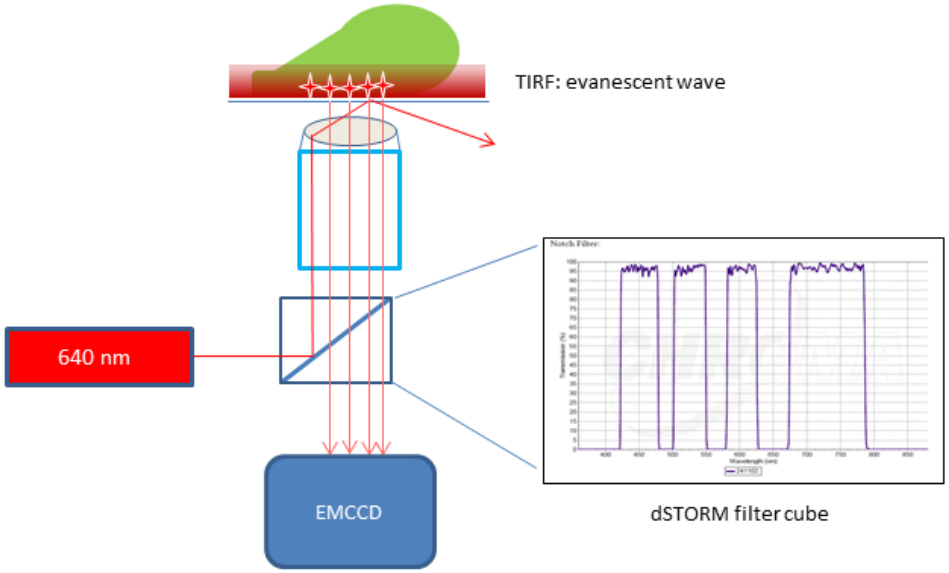

Figure 1-14: **Microscope set-up for STORM.** 640 nm laser is directed to the sample using a dichroic mirror, passing through the objective lens and reflecting off the glass coverslip, forming the TIRF evanescent wave in the sample. Emitted light passes through the objective lens and dichroic and is collected at the EMCCD detector.

STORM relies on exciting, detecting and localising populations of non-overlapping fluorophores to produce a coordinate map for each frame. Sequential frames of coordinates are then summed or reconstructed to give a final diffraction unlimited map of molecular positions[115]. To do this, the technique itself relies on the temporal separation of fluorophores

by exciting only a subset at a time using a high powered laser and the stochastic blinking capabilities of some fluorophores[129].

Within a population of fluorescent emitters, the method works by pushing some of the emitters into the 'dark' or 'triplet' state (figure 1-15) in the presence of a reducing buffer[115,118,130]. Electrons in a fluorophore absorb energy from the laser which pushes them to a higher energy level (S_0 to S_1). Vibrational relaxation releases heat energy to the surroundings as the electrons drop back to the lower S_1 state before dropping back to the S_0 state and releasing fluorescence. Occasionally, an electron in the S_1 state will be hit by a photon and can transfer to an intermediate triplet state T_1 (intersystem cross) (figure 1-15). High energy lasers and reducing buffers make this more likely in STORM and because this is random, a subset of electrons will be in this dark triplet state, and a subset will be releasing fluorescence by transferring from S_1 to S_0 ground state. The inclusion of glucose oxidase mitigates the photobleaching effects of free oxygen radicals produced as a by-product of fluorescence cycling[131].

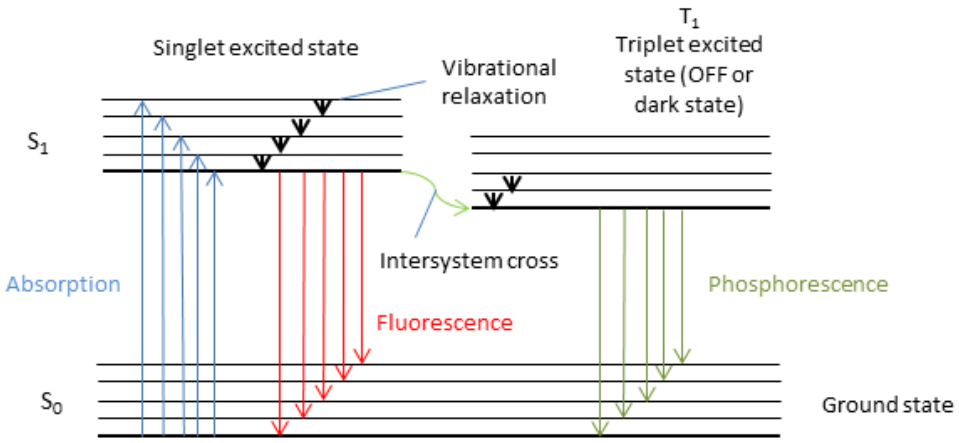

Figure 1-15: **Jablonski energy level diagram and its relation to STORM**

Emission signals from fluorophores are detected as gaussian point spread functions (PSF) on the camera (in x, y and z), with the most amount of photons at the centre and increasingly fewer photons detected near the edges. In x and y dimensions, this can be represented by a 3D gaussian fit of the signal (figure 1-16 middle panel). The central point of these gaussian fits can be found by linear profile, and plotted as a point (adapted from Zeiss microscopy U, online). Due to photo-blinking and a fast camera, individual non-overlapping PSFs can be imaged in sequential frames and localised. This is repeated thousands of times until enough

centres have been defined to build up a reconstructed coordinate map achieved through the temporal separation of fluorophores. Many localisation/reconstruction algorithms are available – thunderSTORM was used here[132].

Individual emitters can therefore be imaged, and the centre of each point spread function localised as a dot or coordinate (figure 1-16 a, b and c). Reconstruction of many frames, each with different subsets of localised emitters produces a pointillist map of molecular coordinates, each with a localisation precision of around 20 nm (figure 1-16d). Figure 1-17a shows a standard TIRF image of a cell showing diffraction limited LFA-1 microclusters – here the resolution is limited to ~ 300 nm (right pane is zoomed region of left pane in the leading edge of the cell. Figure 1-17b shows a localised pointillist STORM image of the same cell with a zoomed 2 μm^2 region to emphasise the pointillist nature of the data. Thompson's uncertainty

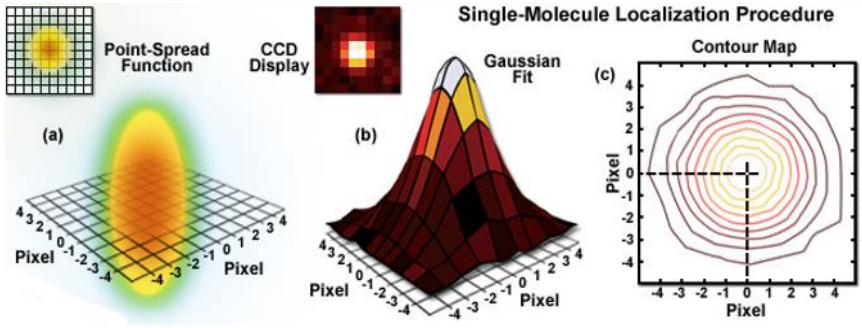

d)

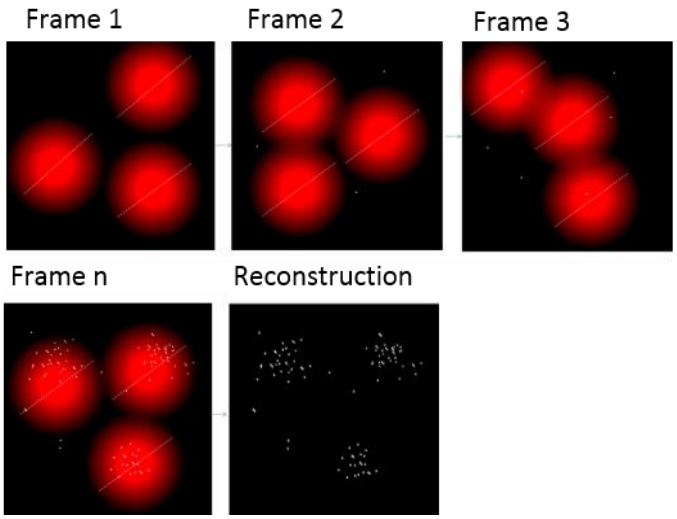

Figure 1-16: **Localisation procedure in STORM.** a) A 3D point spread function (large panel) is can be read out also as a 2D PSF (small panel). b) small panel shows what a single PSF looks like on the camera (CCD) display, where such PSFs can be fitted using a gaussian function (large panel). C) Using this gaussian function the centroid of the PSF can be defined as a single coordinate point and d) multiple frames with different subsets of the total population of fluorophores are localised separately and reconstructed after acquisition.

is one measure of resolution for this kind of data, which refers to the precision with which a given localisation has been carried out[125].

Thomson's uncertainty[125] depends on the collected number of photons, the PSF width (standard deviation of the PSF = s), the variance in local background noise (b), and the size of the camera pixels relative to the PSF (a). Localisation precision is therefore expressed as:

$$\sigma^2 = \frac{s^2 + a^2/12}{N} + \frac{4\sqrt{\pi}s^3b^2}{aN^2}$$

Here, and typically for data presented in this thesis, uncertainty ranges from 0 to 80 nm and peaks at around 10 nm (example in figure 1-17c).

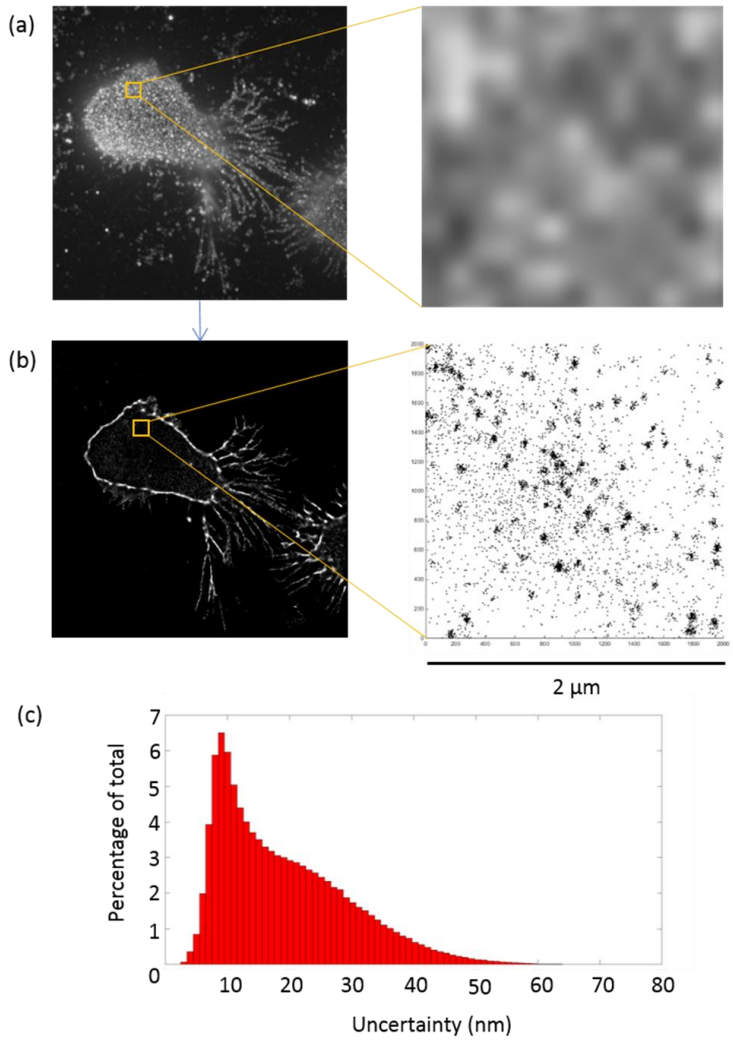

Figure 1-17: **STORM achieves super resolution pointillist images of cells with high precision.** a) TIRF image of LFA-1 integrin in a migrating T cell, with zoomed region. b) STORM reconstruction of LFA-1 integrin in the same cell, and representative coordinate map from zoomed region (right). c) uncertainty plot for all points in the reconstructed map.

1.3.4 3D SMLM: interferometric STORM

STORM and related SMLM techniques rely on TIRF optical sectioning to reduce background which would, in widefield mode for example, be detrimental to the precise localisation of individual fluorophores. 2D STORM imaging outputs a dataset consisting of a 2D projection of the ~100 nm TIRF imaging volume, ideal for imaging and quantifying membrane and membrane proximal clustering[115]. The penalty here is that SMLM has been limited such that 3D information is lost, limiting the ways you can interpret the data.

Recently, the umbrella of techniques have been extended to 3D, opening up a new region of potential nano-clustering based regulation further away from the membrane and as of yet untapped. Typically, a greater illumination depth is achieved in these techniques by using a highly-inclined and laminated optical sheet (HILO)[133], and a number of techniques based around exploiting the shape of the PSF have been implemented such as the use of astigmatic lenses[130], biplane imaging[130] and helical PSFs[130]. Here, a technique relying instead on interferometry is used to achieve 5 to 30 nm precision for molecules localised in z[134].

iPALM uses two objectives, one above and one below the sample, to collect photons emitted by a given fluorophore simultaneously down two separate optical paths. The photons are detected by two cameras, and the phase shift and therefore interference contrast is extracted, which contains information about the fluorophores position in Z[134]. Coverslips embedded with gold fiducials are used as a reference point, and x y positions of each fluorophore are derived in the same fashion as for 2D STORM. The output for iPALM data is similar to STORM data: a list of x y positions of fluorophores with associated uncertainties, this time with the addition of z dimension for each.

In this thesis, super resolution techniques used were 2D STORM and 3D iSTORM – denoting iPALM used with antibody labelling. Pointillist datasets were analysed using cluster analysis techniques developed in the lab, which are detailed as follows.

1.3.5 2D STORM cluster analysis

Analysis tools to quantify clustering in the case of conventional microscopy exist, and are based on measuring intensity distributions in images composed of pixels. SMLM outputs single molecule positions represented by coordinate based pointillist maps, hence new analysis tools have had to be developed to fully exploit this type of data. Several different frameworks exist, which provide different descriptors. A brief description of each is provided

here, with a justification for the use of model based Bayesian analysis for 2D and 3D SLM data presented in this thesis.

Ripley's K-function analysis

The theory behind this type of analysis comes from ecology and star mapping where the output is similarly coordinate based. The method used here is based on Ripley's K function[105,135–137], and works by drawing concentric circles of varying radii centred on each localisation(j) before counting the number of encircled neighbours: those inside are given a Kronecker delta value of 1, those outside the circle are given a value of 0. This value is normalised to the overall molecular density (A= area of ROI/ n=total localisations in ROI), linearised to scale with the radius and the equivalent function for a random distribution subtracted (figure 1-18).

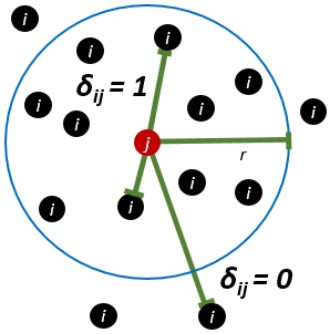

$$L(r)_j = \sqrt{\left(\frac{A}{n}\sum_{i=1}^{n}\delta_{ij}\right)/\pi}$$

$$\delta_{ij} = 1 \; if \; d_{ij} < r, else \; 0$$

Figure 1-18: **Linearised version of Ripley's K is used to define 'clusteredness' for each point.** a) diagram showing circle of radius r drawn around a given coordinate point j. b) linearised Ripley's K equation.

L(r) can be plotted against r to assess whether a given dataset is clustered, or composed of a mixture of clustered and un-clustered localisations. The peak of the curve gives an estimation of the length scale that the clustering occurs on, and curves can be compared between biological conditions to measure their impact on clustering per ROI as a whole. As the L(r) curve for a completely spatially random (CSR) distribution with no clustering will be equal to its radius, the two can be compared. This allows the estimation of the L(r) curve of a completely spatially random (CSR) distribution as, on average, will have L(r) equal to its radius, to which the ROI's curve can be compared. An easy way to assess clustering is to subtract r from L(r), and plot against r. Here, if the distribution is clustered, the curve will be above the x-axis. Below the x-axis means there is some abnormal dispersion, that is non random (Figure 1-19).

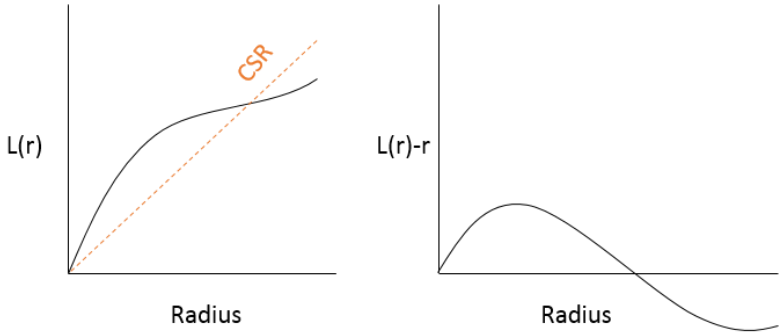

Figure 1-19: **Diagrams showing linearised L(r) for a given distribution compared to CSR, and an adaptation (right) that allows for clear comparison of cluster behaviours.**

This approach therefore gives a good indication of clustering as a whole, but lacks the ability to extract individual descriptors about clusters that might be important in terms of their nano-regulation for example: size, density and number. To address this, the approach can be expanded to use the Getis and Franklin variation to the K function[138], which applies an individual L(r) value to each localisation. This avoids averaging over the whole ROI, and clustering can be visualised by interpolating these values for each ROI. To then extract cluster metrics, these maps can be converted into binary maps by arbitrarily choosing a radius and threshold of points within such a radius for a cluster to be considered a cluster (figure 1-20).

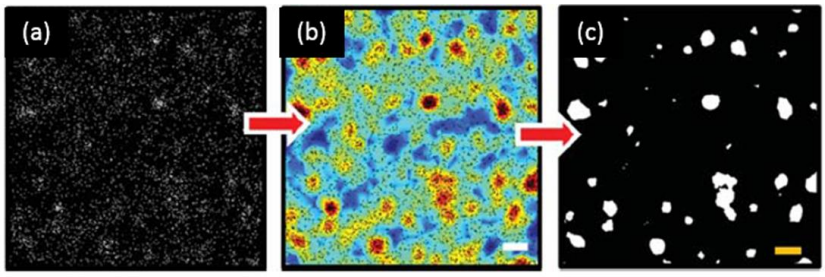

Figure 1-20: **Example cluster map, interpolation and binary map.** a) Pointillist map b) interpolated map based on Ripley's K values c) binarized map where clusters are defined over a given radius and threshold. Scale bar 200 nm. Adapted from Owen et al 2010.

This method of quantitation has been used to compare the distribution of LAT and Lck near the membrane of T cells undergoing activation via CD3 and CD28 molecules during the formation of the so called 'immune synapse'[105,137,139]. While this approach can provide comparative results and is computationally easy to carry out, it does not perform well with

sparse data with uneven background. As mentioned, the radius chosen to define a cluster as well as the number of points within such a radius for it to be defined a cluster is arbitrary and user defined. To solve this, a Bayesian algorithm was implemented to find the 'best value' for radius and threshold for each region of interest, based on comparisons to a model and the use of robust priors[140,141].

Bayesian cluster analysis

Bayesian statistics (description in [140,141]), as opposed to frequentist statistics relies on the use of a model, formed based on associated priors (probabilities), which provide additional information which is used to assess the measurements and provide a better estimate of the answer. The data is compared to the model and weighted based on those prior probabilities, and therefore the process can be likened to making an informed guess, mimicking human decision making principles.

Priors added to clustering data were assessed extensively in simulation and on real data in[141] and [140] . Briefly, they consisted of assumptions that each localisation has an independent probability of being a member of a cluster, that cluster shapes are roughly circular and gaussian. The algorithm is robust to flat top clusters or ellipses, and for all types of clusters seen for the data analysed in this thesis. Limitations of these priors lie in an inability to deal well with fibrous structures, but other algorithms are available to deal with these[142].

Next, clustering proposals were generated. For each point, an L(r) value is estimated, and points with L(r) above a threshold T are assigned to clusters, those below are assigned as monomers/background. By scanning both r and T over a large range, thousands of cluster proposals are generated and assigned a posterior probability based on how well it fits the model and priors. This 'best answer' is extracted and used for a given region to identify clusters with much less human input and no arbitrary decisions[140,141]. Figure 1-21 shows a pointillist map, and a heat map of posterior probabilities (scores) for each r and T. Example cluster maps below are taken from r and T values applied from different areas of the map, and highlight the problem of having a human carry out the analysis, who might choose any one of these solutions arbitrarily. In this case, the best answer is number 2 (figure 1-21). The "best" cluster proposal (i.e. defined by the highest probability score of the data given the model), is calculated for each ROI, where several ROIs are chosen per cell. This allows for diversity in the characteristics of clusters to be detected between ROIs. Cluster descriptors are then extracted from the best scored proposal: size, molecules per cluster, number of clusters, percentage molecules in clusters and total molecules (figure 1-21).

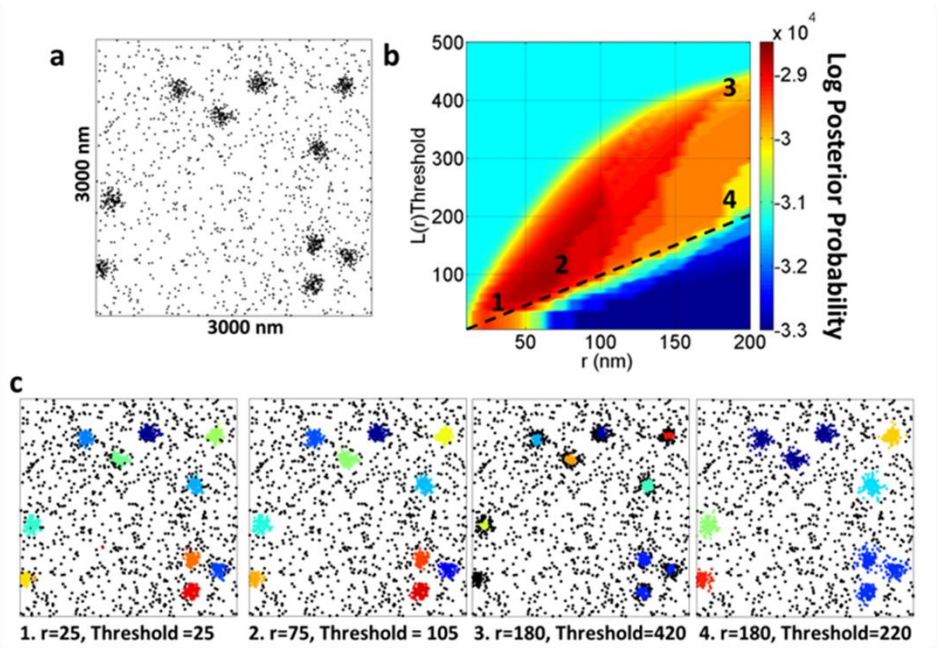

Figure 1-21: **Bayesian statistics to analyse clusters. a) example pointillist map, b)** 10000 proposals for the threshold and radius are generated. Plot is colour coded for posterior probability or 'score'. C) maps relate to radius and threshold settings from labelled areas of the heat plot. Adapted from Rubin-Delanchey et al.

Finally, as an extension to this, topographic prominence was implemented to apply clustering thresholds based on nearest neighbours as opposed to an arbitrary sea level[143]. This was shown to improve performance of the cluster analysis algorithm, rendering it less sensitive to interference of background points and neighbouring clusters by applying a TP value rather than an absolute value to each point.

1.3.6 3D iSTORM cluster analysis

Data generated using iPALM[134] provided a list of x, y and z coordinate with associated uncertainties. As such the workflow for cluster analysis of this data was similar to 2D: first priors and a model is set, cluster proposals with r and T are generated, and cluster descriptors are extracted after clusters have been discerned using the 'best answer'[144]. The method avoids user defined parameters, instead relying on well-defined Bayesian priors.

There are two main differences between 2D and 3D cluster analysis. The first is that a sphere is used instead of a circle to define L(r)3D for each point j.

$$L_{3D}(r)_j = \sqrt[3]{\frac{3V}{4n\pi}\sum_{i=1}^{n}\delta_{ij}}$$

Where V is the volume of the ROI, and the answer is normalised using the total localisation density within the ROI divided by V. The value is linearized by taking the cube root. The second is that edge effects are corrected using a 3D toroidal wrap as detailed in[144]. For practical analysis of data, the process is described in methods.

1.3.7 Colocalization analysis for 2D SMLM data

Multicolour SMLM can be achieved in several different ways, using either spectrally distinct fluorophores bound via antibodies to proteins of interest, fluorescent proteins, or multiplexed techniques like DNA PAINT[145] which relies on transient binding of DNA donor strands to target strands attached to antibodies, or madSTORM[146], which relies on sequential rounds of imaging followed by elution of antibodies for different molecular targets all conjugated to alexa-fluor 647. The advantages and disadvantages of these techniques are covered in section 3. All of these analysis techniques result in multiple channels of pointillist data for which, like for single colour SMLM, analysis tools have been developed concurrently.

Localisation microscopy derived pointillist data requires a different approach to dealing with colocalization as compared to intensity based pixel arrays derived from conventional microscopes as inherently, two points can't be in the same place. Therefore, efforts to quantitate such colocalization must be based on the proximity of points, the most simple method for which is called 'nearest neighbour'[147,148] – used frequently in ecology, geography

and astronomy. This method assigns a value to each point based on its proximity to each other point. To extend this to colocalization of two different species (of trees, stars or molecules), each localisation of species A is given a nearest neighbour value based on its proximity for localisations of species B[149]. The problem with this method is that it is a coarse quantitation, and gives only a general answer relating to how co-clustered the points in a given region appear to be.

An alternative is pair-correlation (PC)[150], which uses an autocorrelation function for the point pattern at different length scales. This provides a probability density around each point, for the probability of finding another point relative to random distribution (CSR). Clustered distributions display a value greater than 1, and unclustered distributions a value smaller than 1. To compare two channels with this method, again points from species A are considered with relation to point from species B.

Coordinate based colocalization (CBC) is another method, conceived by Malkusch et al[151]. This counts the number of localisations of species B around each localisation A within a given raidus r, and the same is done for self clustering (A localisations around each A point). This is normalised to the number of localisations within the largest observed distance and area for each species. The two distributions (A with B, and A with A) are compared and the Spearman rank correlation coefficient is derived for a measure of colocalization of the points in the point pattern. Thus, co-localisation is measured on a scale of −1 for anti-correlated to 0 for randomly distributed and 1 for correlated for each species separately. This method is useful for comparing between conditions but provides information about the colocalization of the point pattern as a whole, and nothing can be gleaned about the colocalization of molecules taking part in clusters, the most biologically interesting example.

The technique used for data in section 6 of this thesis is a modified form of that presented by Rossy et al[152]. This relies on Getis and Franklin's version of Ripley's K analysis, where the number of molecules within a specified radius of each molecule are counted and normalised to the total moelcules density to provide a linearised L(r) value as a measure of clusteredness. For colocalization, the level of cross-clustering L(r) cross is introduced, where points from population B are counted around each point A, and vice versa (thus this technique is an asymmetric method). L(r)cross can then be plotted against L(r) and the percentage of clusters co-localised with clusters as well as the free population of monomers can be extracted for each channel by applying thresholds to L(r) and L(r)cross.

The length scale employed, *r*, is arbitrary here, as this is a non-Bayesian technique. Asymmetric analysis is useful for data of this kind, as it can delineate a situation where all clusters of A are all associated with clusters of B, whereas some clusters of B are free of A[152]. Where clusters have high L(r) cross and high L(r), this signifies clusters colocalised with clusters. Taking the Pearson's coefficient between the two provides a single value as a measure of co-clusteredness. This is explored extensively in section 6.

1.3.8 Summary

The nanoscale dynamics of LFA-1 based adhesions are un-investigated in T cells, and have not been linked to function. Emphasis is put on the idea that an 'active' LFA-1 molecule should not be limited to statements about its 'affinity' – in fact this is a narrow view. Here, I explore the importance of nano-architecture in the regulation of LFA-1 itself, and the formation of complex adhesions which are too small to be resolved using conventional microscopy.

First, the linkage to the clutch is investigated in the context of actin flow.

Second, a full description of membrane and intracellular membrane proximal integrin LFA-1 nano-clustering is explored as a method of regulation during migration.

Third, the nanoscale 3D localisation of phospho 397 FAK, and the 2D colocalization of pY397 FAK and pY416 Src family kinases such as Lck are explored as proxy markers for integrin activity during cell migration.

The purpose of this project is to untangle these effects, with a series of carefully chosen inside out and outside in signalling modalities, and finally with a genetic knockout of a phosphatase intimately linked with both T cell migration and autoimmune disease.

Chapter 2: Methods

2.1 Murine T cell culture

All tissue culture was performed using aseptic techniques in Class 2 biological safety cabinets.

2.1.1 Transgenic mice

Ptpn22 deficient mice were generated and genotyped for use in experiments as described[153]. The generation of PEP-R619W knockin mice was as described[154]. The lines were re-derived into the Biological Services Unit at King's College London and bred on a C57BL/6 (Harlan) background for a minimum of 10 generations in SPF conditions, in compliance with Home Office regulations and local ethically approved guidelines.

2.1.2 Primary murine T cell culture

8 week old mice were culled, lymph nodes and spleens harvested and sieved through 70 µm strainers (BD Biosciences, 352350) in warm RPMI-1640 to achieve a single cell suspension. Cells were centrifuged at 300 x g for 5 minutes at RT and the cell pellet re-suspended in complete medium (RPMI-Glutamax, 10% FBS; Penicillin, Streptomycin, Sodium Pyruvate, 20 mM Hepes, 20 µM 2ME). Cells were stimulated at a density of 3 million per ml with the addition of 1 µg/ml of Concanavalin A (Sigma L7647) for 2 days. After this time, activated cells were isolated and dead cells excluded by layering on a Ficoll gradient; cells were centrifuged for 10 minutes without a brake at 1800 rpm. Layered T cells were re-suspended at 2 million

per ml in complete medium and 20 ng/ml recombinant IL-2 (proleukin) added for expansion for 5 days.

2.1.3 Cell sorting based on GFP expression

Lifeact GFP positive cells derived from transgenic C57/B6 mice were a gift from Karen Liu (King's College London), characterised in[155,156]. These cells were sorted using a FACS Aria II flow cytometer. 50 million cells were resuspended in buffer containing 1 % BSA in PBS and 1 million intermediate to high expressing lifeact GFP positive T cells were separated into 20 % serum culture medium. These were then centrifuged at 300 x g for 5 minutes at RT and the cell pellet re-suspended in complete medium (RPMI-Glutamax, 10% FBS; Penicillin, Streptomycin, Sodium Pyruvate, 20 mM Hepes, 20 µM 2ME), before being grown as above. Analysis of data was performed using BD FACS Canto software.

2.1.3 Cryopreservation

Primary cell suspensions were cryopreserved at 50^6 cells/vial in FBS containing 10 % DMSO and stored in liquid nitrogen. Cryovials were thawed at 37℃ and cell suspensions washed in prewarmed complete media and re-suspended in complete medium at 3 x 10^6 cells per ml stimulated with ConA and grown in 20 ng/ml IL-2 (as stated above).

2.1.4 Modulation of T cell migration

Various chemicals and proteins were used to modulate T cell migration. All of the following were added directly to the 'migration media' and mixed with the cells before they were plated. Cells were incubated in this state for 10 minutes before imaging. Stromal Derived Factor 1 (CXCL12) chemokine (Peprotech 250-20A-10) was used at a concentration of 150 ng/ml, Manganese Chloride ($MnCl_2$) (Sigma M1787) was used at a concentration of 5 µM and Cytochalasin D (Sigma C2618) was used primarily at a concentration of 0.5 µM.

2.2 Time lapse phase contrast microscopy: imaging and analysis

2.2.1 Cell migration assay

Cells were used for microscopy on day 5 to 9 post-stimulation with Concanavalin A. Glass slides of #1.5H thickness (Ibidi 80827) were coated with 2 µg/ml murine recombinant ICAM-1 (R&D systems 796-IC-050) for 1.5 hours at 37℃ . Cells in culture were centrifuged at 350 x g and re-suspended in warm equilibrated serum free migration medium (RPMI-Glutamax,

Pen/Strep, Sodium Pyruvate, 30mM Hepes, 20 µM 2ME) to a density of 1 x 10^6 cells per ml. 200 000 cells were added to each 200 µl well and the imaging dish placed at 37 degrees celcius in the incubator to settle onto the glass for five minutes before live imaging or fixation for single molecule detection.

2.2.2 Phase contrast time lapse microscopy

Imaging was performed using a Nikon Eclipse TI-e microscope. Cells plated on glass coated with ICAM-1 were transferred to a prewarmed Nikon Eclipse TI-E 37°C microscope chamber, supplied with 5 % CO_2. A 10 x objective was used for imaging for a 15 minute period, with 50 ms exposure time and 25 seconds between frames.

2.2.3 Automatic tracking to quantify T cell migration

Image files were imported in the nd2 format with attached metadata to the ICY interface. Pixel size and time between frames was detected from the metadata and a modular protocol was followed, resulting in reliable automated cell tracking data, which could then be exported to Graphpad prism or matlab for statistical analysis. See results chapter 4 for a description of the full protocol.

2.3 Fixation and labelling for super resolution microscopy

Hand in hand with our ability to discern nanoscale structures came a realisation that chemical fixation with PFA alone resulted in aberrations, epitope destruction and inconsistency that can't be detected by diffraction limited microscopy. In addition, multi-labelling of proteins and false clustering can become apparent through the use of primary/secondary antibody labelling approaches or the use of Fab fragments. Several fixation and labelling methods were trialled by observation of cell morphology and by quantitation of membrane protein clustering (see results section 4): the following details the method used for all subsequent experiments in chapter 6.

2.3.1 Fixation protocol for nanoscale structure discernment

Migrating T cells were fixed with a classic pH shifted fixation protocol using 3% PFA + 0.1 % glutaraldehyde in kPIPES 80 mM, $MgCl_2$ 2mM, EGTA 0.5 mM and 2mM sucrose at pH6.8 for 10 min followed by 3%-PFA + 0.1 % glutaraldehyde in Borax 100 mM for 10 min.

2.3.2 Direct primary antibody labelling by (N-Hydroxysuccinimide (NHS) esterification)

BSA had to be removed from the unlabelled antibody stock to avoid unwanted fluorophore binding to serum proteins.

If BSA was present in the unlabelled antibody stock, this was first removed with a BSA removal solution (Abcam 173231: proprietary formulation most likely based on polyethylene glycol exclusion) in a 5:4 ratio (100 µl of antibody per 80 µl of BSA removal solution). The mix was centrifuged at 13 000 x g for 5 minutes, the supernatant removed and the pellet resuspended in Sodium Bicarbonate (Sigma 144-55-8) 0.1 M pH 8.3 'reaction buffer'.

If BSA was not present in the unlabelled antibody stock the antibody in solution was transferred into reaction buffer using a 5 ml Zeba column with a 7 KDa molecular weight cut off (Thermo-Fisher 89892). Zeba column was placed into a 15 ml falcon tube and centrifuged once at 1000 x g for 2 minutes to elute the original solution, then loaded with 1 ml of Sodium Bicarbonate 0.1 M pH 8.3 and centrifuged again at 1000 x g for 2 minutes 3 times, with fresh Sodium Bicarbonate added each time. The antibody solution was then added to the centre of the column, which was placed in a fresh 15 ml falcon tube before being centrifuged once more for 2 minutes at 1000 x g.

After either of the above two steps, the antibody eluent is now in a 'reaction buffer' containing 0.1 M Sodium Bicarbonate at pH 8.3. The appropriate amount of NHS ester dye, either Alexa Fluor 647 (Thermo Fisher A20106) or CY3b (GE life sciences PA63100) was added in a molar ratio of 1:3 (antibody:dye) and the mixture was left to incubate at room temperature for 1.5 hours, with gentle agitation applied every 15 minutes. After 1.5 hours, a second Zeba column was equilibrated this time with PBS: first the carrier solution was eluted, and then three rounds of 1 ml PBS were loaded into the column and passed through by centrifugation at 1000 x g for 2 minutes each time.

Finally, the conjugated antibody:dye mix was added to the centre of the equilibrated column which was centrifuged at 1000 x g for 2 minutes to trap free dye in the column and elute only the conjugated antibody. A coloured solution at this end stage was an indicator that the conjugation and separation had occurred successfully. For storage, BSA was then re-added at 0.1 % to this conjugated antibody solution.

2.3.4 Combined fixation and labelling protocol

Migrating T cells were fixed using 3% PFA + 0.1 % glutaraldehyde in kPIPES 80 mM, $MgCl_2$ 2mM, EGTA 0.5 mM and 2mM sucrose at pH6.8 for 10 min followed by 3%-PFA + 0.1 % glutaraldehyde in Borax 100 mM for 10 min.

For antibody staining, the following steps were carried out on fixed cells, each separated with three PBS washes. Cells were quenched for auto-fluorescence with $NaBH_4$ for 15 minutes, L-Lysine 0.1 M for 15 minutes, blocked with 10 % normal goat serum (Thermo Fisher 50062Z) for 30 minutes then stained with primary directly conjugated antibody in 0.1 % BSA for 1.5 h at RT.

Antibodies used for staining were anti-mouse CD11a (LFA-1) 2D7 clone (Biolegend, UK), Phospho-FAK (Tyr397) Antibody (31H5L17), ABfinity Rabbit Monoclonal (Thermo Fisher) and Phospho-Src Family (Tyr416) (D49G4) Rabbit mAb #6943BF (Cell signalling technology).

2.4 Stochastic Optical Reconstruction Microscopy (STORM)

2.4.1 Imaging buffer

Fixed and stained cells were placed in an oxygen scavenging buffer comprised of three parts which were stored separately. **Part A** was comprised of 4 mM Tris (2-carboxyethyl) phosphine hydrochloride (Sigma 51805-45-9), 50 % glycerol (Sigma 56-81-5), 25 mM KCl (Sigma 7447-40-7), 20 mM Tris HCl (Sigma 1185-53-1), 20 µg/ml Catalase (Sigma 9001-5-2) and 1 mg/ml Glucose Oxidase (Sigma G2133) all at pH 7.5, made up to a total volume of 5 ml and stored in aliquots of 50 µl at – 20 ℃. **Part B** contained 100 mg/ml glucose and 10 % glycerol and in practice was made to a total volume of 40 ml and stored in aliquots of 400 µl volume at – 20 ℃. **Part C** contained 1 M Cysteamine-HCl, and in practice was made up directly prior to imaging to 1 ml volume.

For imaging, an aliquot of each of Part A and Part B was thawed and added to 100 µl of freshly made Part C, supplemented with 450 µl PBS to a total volume of 1 ml. This mixture was added to each imaging well and made to fill up the well, preventing excess oxygen from entering the system.

2.4.2 dSTORM imaging

dSTORM imaging was performed on a Nikon N-STORM microscope using a Nikon Plan Apo 100 x NA oil immersion TIRF objective. Cells were imaged under TIRF illumination with a 15 mW

633 nm laser with the 405 nm laser set to maintain photo-blinking and transition to the triplet state by gradually increasing its power from 0.1 to 1 mW. Laser powers were determined using a power meter over the top of the objective. Emitted fluorescence was collected at wavelengths between 640 and 790 nm, EM gain 300on an Andor iXon EM-CCD camera at RT. Acquisition time was for ~2.5 minutes: 10 000 frames were collected at 10 ms exposure time per frame and pixel size on this microscopes camera was 160 nm.

2.4.3 Localisation to produce coordinate maps

Molecular coordinates were calculated using ThunderSTORM localisation software[132], with settings applied to match the microscope and camera ie: 160 nm pixel size, 5.32 photoelectrons per A/D count, base level (noise) 99.73 and EM gain 300. Uncertainty values for each localised emitter were calculated using Thompson's method[125]. Due to the density of the clustered proteins, it was important to optimise the localisation for emitters in regions of high density. To this end thunderSTORM was run with multi-emitter fitting analysis (MFA)[157] enabled and set to attempt fitting of up to 3 overlapping fluorophores. Several post processing steps were included after initial localisation with MFA.

First, 'remove duplicates' was used and set to 'uncertainty'. Then the image was drift corrected by cross correlation. Third, 'merging' was applied to address multi-blinking and was set to 30 ms for at ¾ the pixel size – in this case 100 nm. Post processed pointillist maps were exported with x values, y values and uncertainty values for each coordinate, so as to be compatible for the cluster analysis algorithm used in the lab.

2.4.4 Bayesian cluster analysis of STORM data

Around ten 2 μm^2 regions were chosen for analysis using imageJ plugin 'MTrackJ'[158] to specify the centre of each ROI within the leading edge or mid cell region of each pointillist STORM image of a migrating cell. Regions were then cropped out and computationally analysed for clusters using a Bayesian algorithm[141] combined with topographic prominence[143] for which the protocol is described here[140]. A unique radius and cluster threshold was scored against a model and chosen for each region of interest: Radius proposals ranged from 0 to 200 in 10 nm increments and threshold proposals ranged from 0 to 275 in increments of 5. Bayesian priors set on the data were that each localisation has a 50 % probability of being clustered, that clusters background points are distributed evenly over each ROI, that clusters are independent of each other and that points within a cluster are independent and identically distributed. After cluster identification, descriptors were extracted and split into five metrics

described on a per region basis: 1) Total molecules per region, 2) number of clusters, 3) percentage of molecules in clusters, 4) radius of clusters and 5) number of molecules per cluster.

2.5 3D Interferometric STORM (iSTORM) imaging and analysis

iSTORM (iPALM system in STORM mode) was performed at the Advanced Imaging Centre at Janelia farm, VA under the supervision of Jesse Aaron, Satya Khuon and Teng-Leong Chew. The technique allows us to derive 3D coordinate maps of the bottom 600 nm of the cell, with 15 nm isotropic resolution. The technique uses both interferometry and astigmatism to discern z positions, and conventional 2D PSF localisation for x , y coordinates. These methods were used in sections 5.4 and 6.1.

2.5.1 Sample preparation for iSTORM

Custom gold nanorod embedded fiducials were coated with ICAM-1 as per section 2.2. Cells were added to the dish and were fixed and stained as per section 2.3.4. dSTORM buffer (described in 2.4) was added to the sample, and a second coverslip was placed on top and secured with epoxy resin. The coverslip 'sandwich' was then sealed at the edges with Vaseline passed through a needle. This sample was then transferred to the microscope.

2.5.2 iSTORM imaging

Sample was roughly focused in x and y based on the position of a gold nanorod fiducial in a field of view containing no cells. Z alignment, focusing, and positioning of the detector was all altered to maximise the amount of constructive/destructive interference at the detector. Upon moving the stage and moving to a new cell, the focusing and alignment step was repeated, before imaging at high 633 nm laser power with bursts of 405 nm light for 30,000 30 ms frames.

2.5.3 iSTORM data analysis

X, Y and Z coordinate maps were derived from iSTORM datasets using Peakselector localisation software developed by Harald Hess (supplied by H. Hess and G. Stengel at the Howard Hughes Medical Institute, Janelia Farm Research Campus). Data was filtered to produce accurate pointillist maps with average 15 nm isotropic uncertainty values per localisation. 3D cluster analysis was then performed as described here.

2.6 Single cell correlative live tracking + multicolour dSTORM by multiplexed madSTORM

Cells were first tracked during migration using the 'large image' function in Nikon elements software and the 100 x objective lens. Cells were fixed, and their positions were recorded, and then multiplexed antibody madSTORM[146] technique was used (discussed in introduction) to achieve multicolour imaging. Using the same fluorophore bound to antibodies for different targets avoids problems related to crosstalk between channels, as well as chromatic aberration. Extensive photobleaching is avoided through use of the elution buffer, and antibodies are removed, so that there is no build of steric interference for looking at multiple close together target. Fiducial nanodiamonds (a gift from Keir Neumann at the NIH, Bethesda) were used in the technique to allow accurate registration of each channel.

2.6.1 Phase contrast tracking with 100 x lens and tiling

Cells were added to ICAM-1 coated plates, and placed into the incubator for 10 minutes. These were then transferred to the microscope stage, under 100 x magnification. The 'large image' function was used (Nikon Elements software) to image a 6 x 6 tiled region with 15% overlap of 36 fields of view, in timelapse, over a period of 10 minutes. Cells were then fixed on the stage using the fixation protocol described in 2.3.4, and their individual positions recorded using the Nikon Elements software. Slide was then removed from the stage for subsequent steps.

First, there is the cell tracking step including registration of cell positions, followed by staining for the first target, which is then imaged by dSTORM in the same cells as were tracked in the first step. The antibody is then eluted using a buffer, and the sample stained for the second target before being refound and imaged in dSTORM. This process is repeated for several targets, and then the separate images are aligned using fiducials.

2.6.2 Nanodiamond fiducials for registration

80 to 100 nm fiducial nanodiamonds (a gift from Keir Neumann at the NIH) were diluted 1 in 100 from an arbitrary stock solution. The working solution was vortexed for 1 minute, centrifuged for 30 seconds at 3900 x g, and the supernatant sonicated for a 1 minute. 500 µl of this solution was added to the dish of fixed cells, and left for 30 minutes at RT.

2.6.3 madSTORM multiplexed imaging

Optimised staining protocol for target A was performed as described (2.3.4) for target A, imaging dish was returned to the microscope in roughly the same position as for the cell tracking step. and STORM imaging was performed as described (2.5). In between, sample is removed from the microscope and madSTORM elution buffer is applied as described[146]. The second target is then stained for and imaged, and the data exported as ND2 files which are localised individually using ThunderSTORM with the same settings described in 2.4.3.

2.6.4 Alignment of multiplexed STORM images

Images were aligned based on the positions of 3 or more well-localised fiducial nanodiamonds present in each field of view, using a custom Matlab script courtesy of Pedro Almada from the Henriques group at UCL. Individual fiducials are picked by drawing an ROI, and are localised in the script based on a gaussian approximation of their PSF in the first frame of the acquisition. The position of the ROI is moved as necessary for each fiducial in each acquisition channel, centroids for each are acquired, and an average x y linear transform is applied to each point in the localised images.

2.6.4 Analysis of 3 colour STORM images

3 colour pointillist maps were analysed channel per channel with Bayesian cluster analysis software (2.4.4), and colocalization was analysed using Rossey's method as described[152].

2.7 Live T cell timelapse -TIRF microscopy and analysis

2.7.1 Tests for transgenic versus transfected lifeact GFP T cells

Primary mouse T cells are fragile *ex vivo* and transfecting them with lifeact GFP by electroporation – an effective live cell compatible f-actin label in many cell lines – was foreseen to be difficult in primary cells. A useful alternative were cells isolated from life-act GFP positive transgenic mice (C57BL/6). These cells ubiquitously expressed lifeact GFP and did not require transfection. To test whether such cells were more useful for migration studies, their cell speeds were compared to transfected cells and untreated cells by imaging untreated, laGFP transgenic and laGFP transfected (electroporation) cells using phase contrast, and tracking them using automated tracking software (icy). Transfected cells had

reduced cell speeds and displacements around half that of both transgenic cells and untreated cells, therefore transgenic laGFP positive mouse cells were used for future experiments to measure actin flow (Figure 2-1).

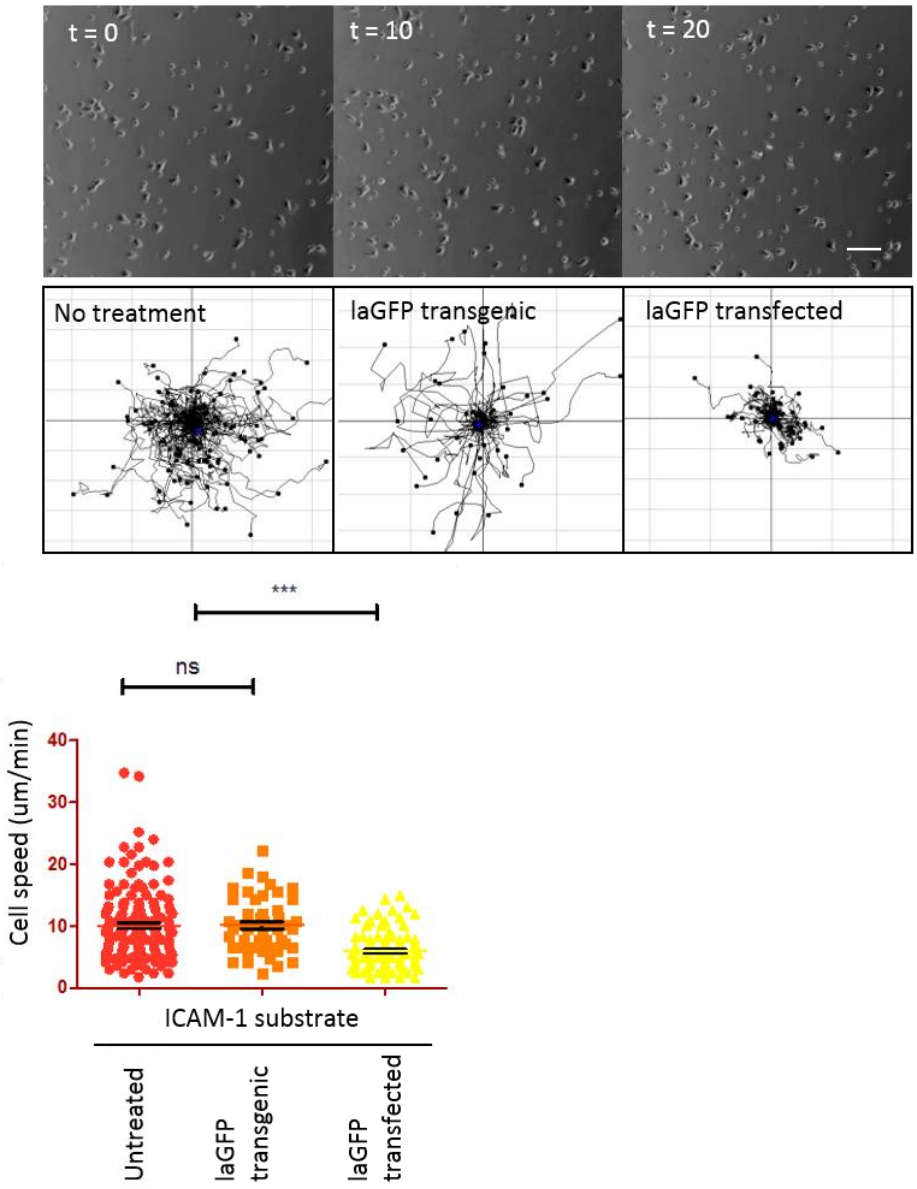

Figure 2-1: **Phase contrast microscopy and cell tracking of untreated mouse T cells, mouse T cells transfected with laGFP ex vivo, and transgenic T cells from lifeact GFP positive mice.** a) phase contrast timecourse example frames b) spider diagrams showing displacement and c) cell speeds in the three conditions. Scale bar 30 µm.

A range of laser powers were also explored, as preliminary data showed that primary mouse T cells would stop migrating entirely when exposed to high laser power. TIRF microscopy uses

an exponentially decaying evanescent wave to illuminate a portion of the sample only, and so in this respect is already less damaging to cells. In addition, laser light is spread across the sample, which causes less damage than a high powered, concentrated beam or whole sample illumination as in confocal microscopy. Laser illumination had to be tightly controlled here, to ensure cell migration was not subdued, while maintaining a high enough emission signal for subsequent image analysis.

2.7.1 Migration assay for lifeact GFP positive transgenic T cells

Life-act GFP positive transgenic mouse T-cells (C57BL/6) were used for microscopy on day 5 to 9 post-stimulation with Concanavalin A. Glass slides of #1.5H thickness (Ibidi 80827) were coated with 2 µg/ml murine recombinant ICAM-1 (R&D systems 796-IC-050) for 1.5 hours at 37℃ . Cells in culture were centrifuged at 350 x g and re-suspended in warm equilibrated migration medium without serum (RPMI-Glutamax, Pen/Strep, Sodium Pyruvate, 30mM Hepes, 20 µM 2ME) to a density of 1 x 10^6 cells per ml. 200 000 cells were applied to each 200 µl well and the imaging dish placed at 37℃ in the incubator for five minutes before being transferred to the microscope chamber and placed onto a Nikon Apo TIRF 60 x NA 1.49 oil immersion lens on a Nikon Ti inverted microscope.

2.7.2 Imaging

The actin in lifeact GFP positive live migrating T cells was imaged in TIRF mode on a Nikon Ti inverted microscope, using a Nikon Apo TIRF 60 x NA 1.49 oil immersion lens. A large field of view was possible through use of an Andor Neo sCMOS camera (Andor, Belfast, UK) with a pixel size of 110 nm. Cells were imaged for 1 minute periods using the 488 nm laser at low power and 1 second exposure, at 37 °C. Fluorescence emission was collected back through the objective, scattered laser light separated using a dichroic and fluorescence emission captured in the range 470 to 900 nm (Brightline 488 nm dichroic beamsplitter, Semrock).

2.7.3 Analysis of actin flow and engagement

ND2 files from the microscope were opened using Fiji (ImageJ) and criteria were used to select cells for analysis. Cells chosen were single cells, unopposed in their migration by neighbours, they migrated in a straight line, and were present in the field of view for at least 20 frames (20 seconds). Cropped files were then exported as .tif files for further processing. Our analysis windows or 'Time of Interest' (TOI) for actin flow and engagement in all succeeding analysis were 5 frames i.e. 5 seconds.

2.7.4 Thresholding the images to create an accurate cell mask

Prior to further analysis, images were thresholded to remove background. From the original image, Otsu thresholding is used, followed by an opening function is used to delete all objects of less than 4 pixels, removing most of the noise outside of the cell. To avoid fragmentation of darker areas of the cell, dilation with a 4 pixel disk is used as a structuring element. To stay as close as possible to the cell outline, erosion with a 4 pixel disk is then used, to compensate for the dilation. Finally, objects that are smaller than 50 pixel are filtered out. Finally, an optional manual step involves removing any remaining objects that might link the cell mask to the border of the field of view.

2.7.5 Extracting immobile actin information

In the external reference frame of the cell, immobile actin represents actin that is engaged with the molecular clutch (figure 2-5). To calculate this proportion, the zero component of the temporal Fourier transform was taken (over our accepted analysis window of 5 seconds). The output is the percentage of actin immobile over this time period per pixel. For a 'per cell' measurement a threshold amount of 50 % was applied to each pixel for it to be counted as immobile. The percentage of immobile pixels was then calculated and normalised to cell area.

2.7.6 Switching the reference frame to derive cell speed and analyse fast actin flow

Since effector T cells effectively move at speeds ranging from 5 µm/min to 40 µm/min, and the analysis region for flowing actin must be kept constant and within the moving cell over the time course, we chose to change the reference frame to that of the moving cell, rather than the microscope. To do this, we adapted a stationary cell program[159], that allows the repositioning of the cell of interest to the same position and with the same inclination as the first frame. To do this, the centroid of the cell is brought to the centre of the image, the inclination is adapted to correlate best with the preceding frame, and finally the centroid is re-adapted. As an output of this, the program was adapted to give the cell speed averaged over each TOI directly from this transform. An example TIRF image series is shown in figure 2-2, where the cell has been stationarised and therefore appears centrally in the field of view (figure 2-2, bottom row of panels).

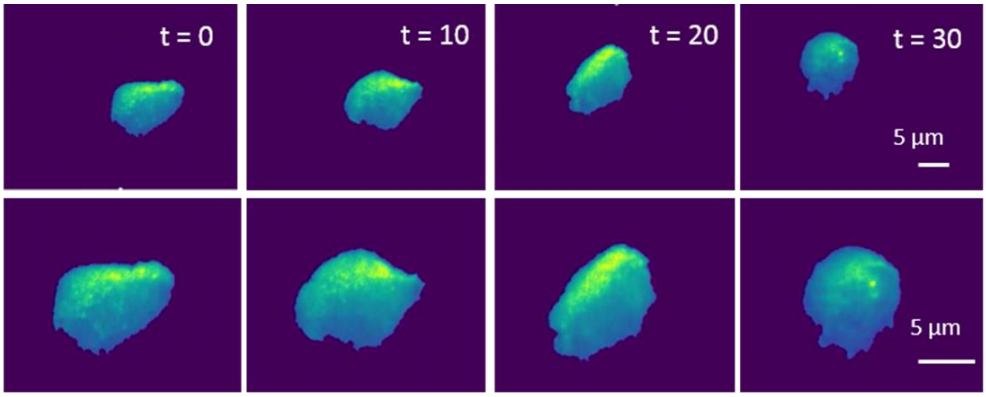

Figure 2-2: Cells were centralised in the field of view to change the reference frame from external to internal. Top row: Example 'cleaned' frames from TIRF movies. Bottom row: Example frames after cell was computationally moved back to a central position in the field of view in each frame, changing the reference frame and allowing further analysis of actin flow.

2.7.7 Actin flow measurement in the internal reference frame: Spatio-Temporal Image Spectroscopy (STICS)

STICS is described[160] and consists of the calculation of the temporal and spatial correlation lags between fluorescence images in automatically assigned analysis subregions, after removal of the immobile fraction by filtering the zero-frequency time components in Fourier space. Switching to the internal reference frame allowed us to image actin in fast moving cells, but also meant that actin retrograde flow speeds were all a combination of cell speed + actin flow speed, and so moved greater distances. In order to encompass all measurable actin flow, but maintain the greatest number of vectors possible, a range of analytical subregion sizes were tested (figure 2-3). At the level of 64 pixels, flow speeds were no longer increasing, indicating that almost all fast vectors were being successfully detected. The analytical subregion size was therefore set to 64 pixels, tiled across the ROI with an overlap of 16 pixels (figure 2-3).

The output is a matrix describing the mean velocity and directionality of vectors in a given analysis grid region over a given time period given as a number of frames or TOI. In addition to this, the TOI is shifted for each new analysis so that there is overlap between each. TOI shift was set to 5 frames (5 seconds) with a 2 frame overlap. The script was adapted to remove the

immobile fraction over each TOI separately, to improve signal to noise which changes drastically over the course of a 1 minute movie.

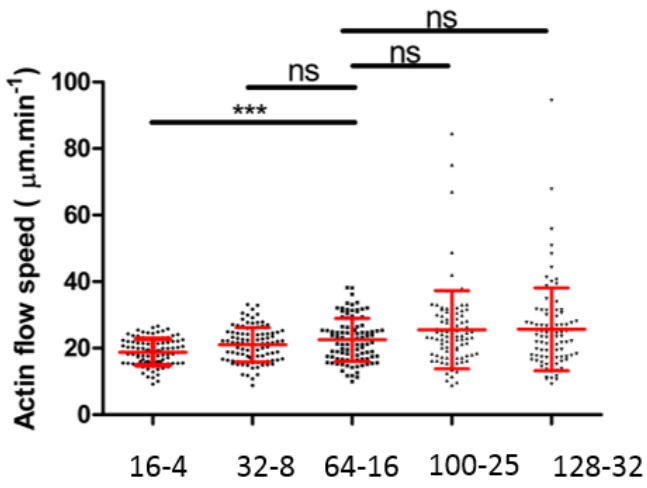

Figure 2-3: **STICS subregion size test to discern size at which the fastest flow speeds are detected.** Plot showing actin flow speed at different subregion sizes. ***p<0.0001

2.7.8 Actin flow as a function of distance from the cell front

After optimising the analysis protocol in these ways and changing to the internal reference frame, it was also possible to derive actin flow as a function of distance from the front of the cell. To do this, a line vector was drawn across the approximate leading edge (figure 2-4, bottom left panel), and each vector calculated as an absolute distance from this line, before being converted to a percentage of total length of the ROI (pink, bottom panel). An example plot for a single cell of actin flow as a function of distance from the cell front shows retrograde actin (red) at a constant speed level throughout the cell, whereas anterograde actin is confined to the cell front (figure 2-4).

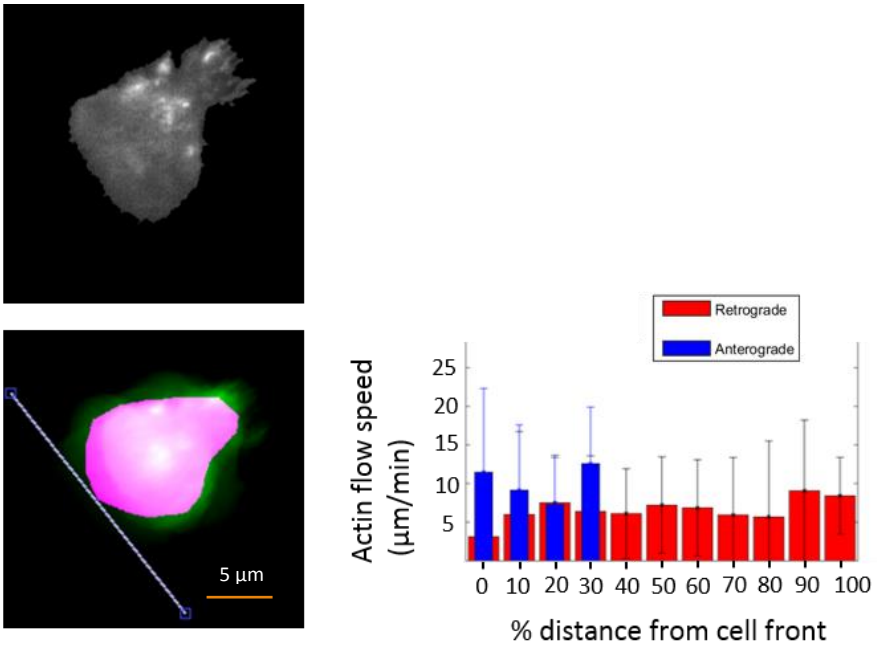

Figure 2-4: **Retrograde/anterograde actin flow or % immobile actin can be measured as a function of distance from cell front.** A tangent is drawn on a projection of all of the frames of a TIRF movie (a). b) Plot showing retrograde (red) and anterograde (blue) actin flow as a function of distance from the front of the cell. Scale bar 5 µm (orange).

2.7.8 Explanation of internal/external reference frames and actin analysis workflow

In this internal reference frame, retrograde actin flow reflects the speed of the cell plus that of the actin flow. The adhesions themselves move backwards in the internal reference frame, and therefore so does the actin that is attached to them (right panels, figure 2-5). Therefore immobile actin in the internal reference frame is measured as flowing at exactly the same speed as the cell itself, whereas flowing actin exceeds the cell speed value. In the external reference frame, the cell moves over the adhesions (figure 2-5, left panels), and so engaged actin really is immobile and engaged with adhesions. A flow diagram for actin flow and engagement analysis is provided below (figure 2-6).

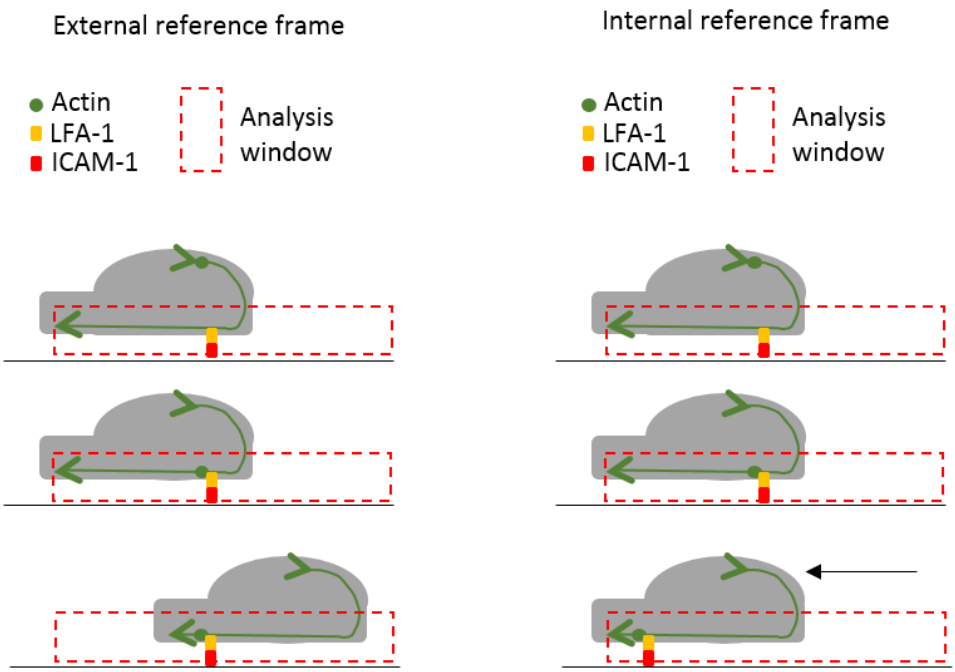

Figure 2-5: Actin immobility is a proxy measure for actin engagement. Engaged actin is measured as stationary in the external reference frame, because the cell itself moves over the f-actin engaged with the adhesion. In step 1, actin is polymerised at the front of the cell and is pulled backwards 2) an adhesion links the flowing f-actin to the substrate and 3) the cell translates the actin flow into forward movement. Switch to the internal reference frame (panels on the right), however, and the engaged adhesion has moved backwards in the cell the same distance that the cell moved forwards (black arrow).

2.8 Statistics

Unless otherwise state, data are presented as median with IQR from at least three replicates of single experiments. For multiple comparisons between conditions, one-way analysis of variance (ANOVA) and Kruskal Wallis post testing was used. All statistical analyses were performed with Graphpad Prism software.

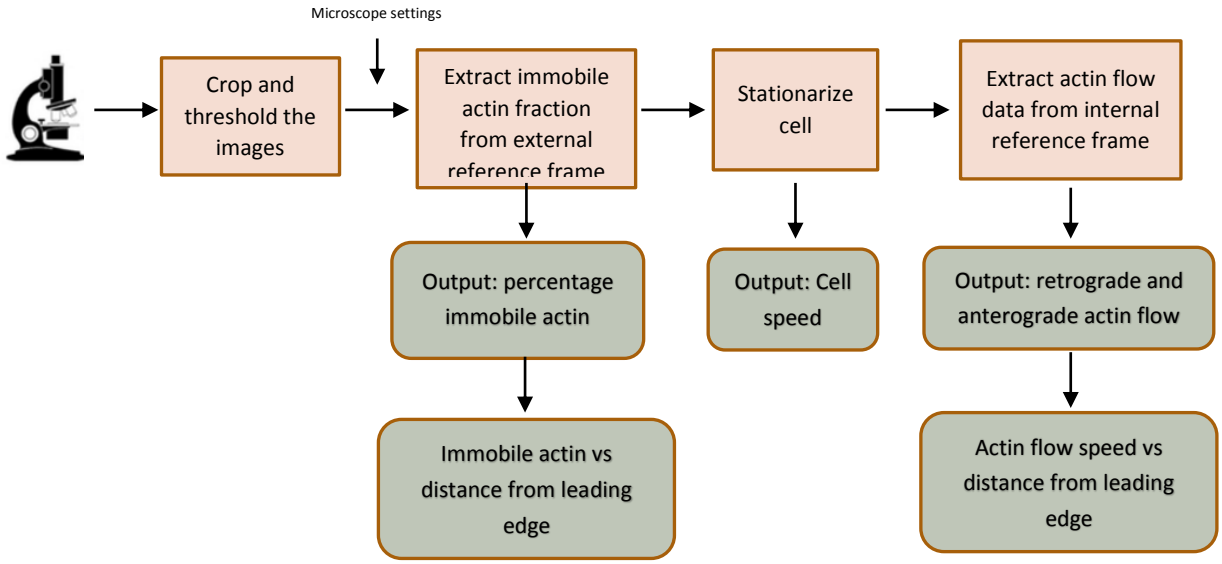

Figure 2-6: **STICS analysis flow diagram showing output summary and metrics taken from actin vector fields.**

Chapter 3: Imaging optimisation

3.1 Preface

Super resolution microscopy is subject to artefacts that are present but not visible in conventional diffraction limited microscopy. High resolution, and super resolution microscopy have benefitted from the development of commercial microscopes, simple experimental protocols and easy to use software. Uptake and usage is becoming widespread, and soon such techniques will rightly be viewed as tools used by non-experts. It is of prime importance therefore that new users be aware of potential artefacts that become visible in fluorescent images of such high resolution. Improper chemical fixation, labelling strategies, 'imaging buffer' composition, or a lack of consideration for microscope settings/image processing after acquisition can all contribute to a false image and are explored here.

3.2 Introduction to fixation for super resolution

The importance of cell fixation is often overlooked in fluorescence microscopy unless super resolution is the goal, where artefacts become clear. Typically, scientists undertaking diffraction limited microscopy can afford to use paraformaldehyde (PFA) (structure shown in figure 3-1) in a simple buffer like PBS, or in solution with distilled water. This maintains the tertiary structure of a portion of the fixed proteins, and is therefore adequate if the broad

cellular location, or colocalization of two protein species is the goal[161,162]. However, the use of PFA alone creates a number of known artefacts.

The first is that by running an electrophoretic gel stained with Comassie blue of the soluble fraction from a 3% PFA fixed cell suspension, around 50% of the cellular material runs the full length of the gel, indicating that it has remained non-crosslinked[163]. More recent work, comparing well tested electron microscopy fixation techniques, for which ultrastructure has been a much longer term concern, shows that PFA fixation transiently makes holes in the membrane and washes away many of the membrane proteins before they can be crosslinked[164].

In order to address this problem, glutaraldehyde (GA) (structure in figure 3-1) can be used, which undergoes the same crosslinking Mannich reaction with amine groups that formaldehyde does, but at a faster rate, thus preventing protein loss through the membrane[161,162]. It has been reported that a combination of PFA and a very low concentration of glutaraldehyde prevents loss of membrane proteins, as measured by light and electron microscopy of endosomes in inner hair cells[165].

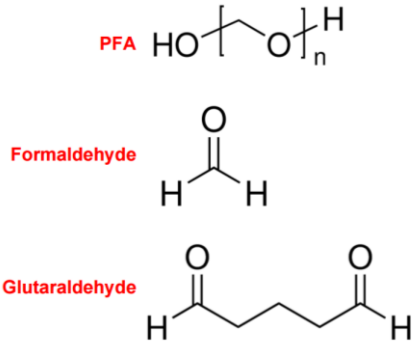

Figure 3-1: **Chemical structures of related aldehydes used for chemical cell fixation**. Paraformaldehyde (PFA) becomes formaldehyde when exposed to water. Glutaraldehyde, is a faster fixative. Adapted from image from Sigma Aldrich website.

On the other hand, glutaraldehyde fixation can lead to the introduction of free aldehyde groups that are known to change the tertiary structure of proteins such that previously available antibody epitopes are made unavailable[164] (schematic in figure 2). The concentration of GA is highly predictive of this phenomenon, so must be carefully tuned to provide a net benefit[164]. In addition, free aldehyde groups emit a high level of auto-fluorescence, a problem as super resolution images rely much like conventional fluorescence images on a high signal to

noise ratio. It is important that prior to staining this signal is reduced using a suitable chemical fluorescence quencher (such as Sodium Borohydride).

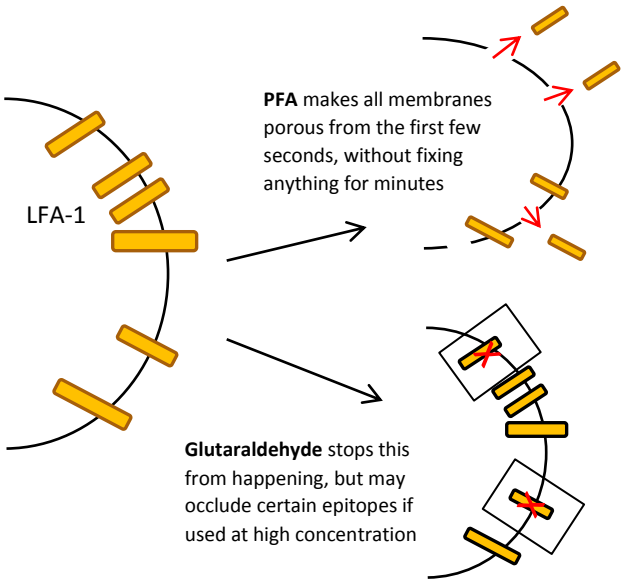

Figure 3-2: **Membrane molecules like LFA-1 may be lost from the membrane through use of PFA alone.** Glutaraldehyde prevents this loss through faster fixation but can result in epitope masking. Yellow rectangles = LFA-1 integrin. Red crosses = epitope masking.

Even with the addition of GA to the PFA mix, Mannich fixation isn't fast or strong enough to prevent osmotic imbalance and consequent swelling from sudden exposure to low sugar or salt content solution. Glucose can be used to ensure that the outside/inside of the cell remain isotonic, but in certain cell types glucose transporter proteins can allow passage of the glucose, causing shrinkage. Sucrose is a useful alternative for mammalian cells, which do not have sucrose transporter proteins, and so cannot exchange the sugar with the outside environment. This prevents water loss or gain, and was predicted to be especially important in primary T cells, possibly due to thin and cholesterol poor membrane areas such as the leading edge, which may be more susceptible to swelling due to osmotic stress. [166].

Finally, the composition of the buffer must also be taken into consideration for maintaining proper ultrastructure. This has traditionally been tested by imaging the actin cytoskeleton, where breaks in the fibres due to epitope loss, or deformations in fibres due to warping are easily identifiable under the super resolution microscope and the fibres can be compared against established electron microscopy images[167]. A buffer for the preservation of the cytoskeleton was used here, as a starting point from which to optimise for membrane integrin proteins. The buffer relies on Magnesium Chloride and EGTA to stabilise actin filaments, and is

characterised here[168–171]. To ascertain whether tonicity of the buffer and the addition of glutaraldehyde make a difference to super resolution imaging of LFA-1 integrin in primary mouse T cells, various combinations were trialled in order to test for known artefacts related to fixation[163,172,173].

3.2.1 Fixation buffer optimisation to produce reliable super resolution images

Isotonicity is an important factor when imaging live cells, but is often overlooked during fixation. To test whether cells were sensitive to sugar tonicity during fixation, migrating T cells were treated with a fixative consisting of 'cytoskeletal buffer' with and without sucrose and imaged throughout the process of fixation (brightfield). Cells migrated across the ICAM-1 coated glass slide and stopped the instant the fixative was added. Figure 3-3 (top panels) shows a frame from a timelapse movie before fixation (left) and after fixation (right) in the absence of sucrose: the white line shows the size of the cell in the left pane and the red line shows how much the cell has swollen (representative image n = 100 cells). Cells fixed in the presence of sucrose (figure 3-3 bottom panels) maintained their size compared to their live migrating counterparts.

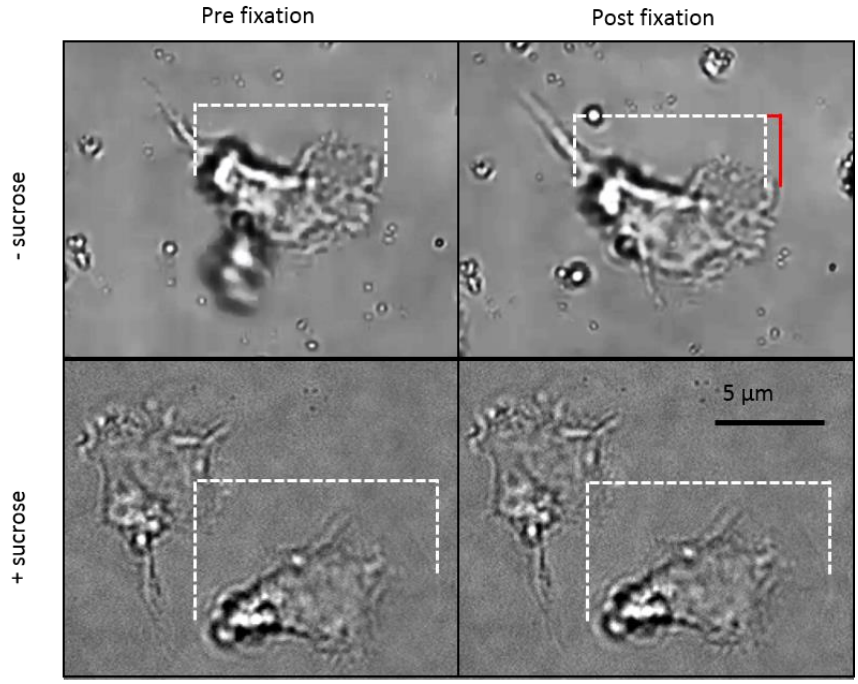

Figure 3-3: **Cells imaged using 100 x brightfield microscopy pre and post fixation, with or without sucrose.** Top panels show a cell fixed without sucrose before fixation (left) and after fixation (right), where the red line shows an increase in cell size. Bottom panels show cells fixed with sucrose present. White dashed line shows no change in size.

To address the question of whether the addition of 0.1 % glutaraldehyde (concentration recommended by the Kusumi lab[173]) better retained molecules in the membrane, cells were fixed with and without the addition of the GA and analysed by STORM and cluster analysis (detailed in methods). Cells were fixed with 'cytoskeletal buffer' containing 3 % PFA or 3 % PFA plus 0.1 % GA and left unpermeablised: fixed cells were stained for LFA-1 with a primary conjugated antibody and imaged by dSTORM and cluster analysis carried out. Representative LFA-1 coordinate maps (n = 12 cells) are shown in figure 3-4a, and example cluster maps are shown in figure 3-4b. Quantitation by extraction of cluster metrics from the maps in xb (n = 43 regions) show that more molecules are present in total (figure 3-4c) and within individual clusters (figure 3-4d) in the membrane of cells fixed in the presence of GA 0.1 %.

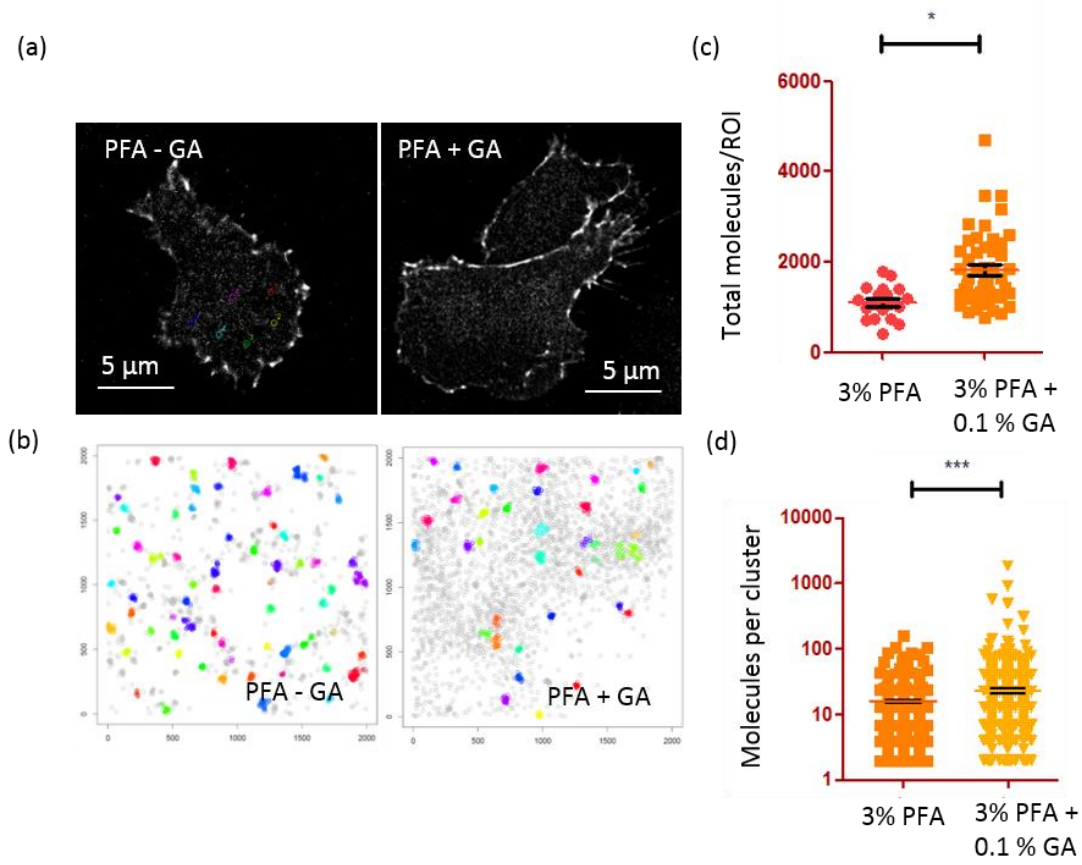

Figure 3-4: **Effects of glutaraldehyde inclusion during cell fixation.** A) Pointillist maps of cells fixed with PFA alone (left) or PFA + 0.1 % GA. b) example regions with clusters identified in arbitrary colours. c) plots showing total molecules per region and d) the number of molecules per cluster. n = 12 cells and 62 regions of interest. *P < 0.01 , ***P < 0.0001.

With these results, the final fixation buffer mix for subsequent experiments made use of this cytoskeletal buffer mix, with glucose supplanted for sucrose, and a low percentage of

glutaraldehyde (0.1 %) added to PFA (3 %). A fixation strategy similar to this was demonstrated to be the most successful in ensuring the proper immobilisation of molecules in the cell membrane[173].

3.3 Antibody based labelling for super resolution

The use of fluorescently tagged antibodies is widespread in fluorescence microscopy, and allows biologists to specifically label a single target of interest and measure its localisation within a cell. Usually, the primary antibody is unlabelled and a secondary antibody conjugated to many fluorophores is used to enhance the fluorescence signal as much as possible. This is because in conventional microscopy, ultrastructure and nano-clustering are hidden behind the diffraction limit, so broader answers are acceptable. For super resolution, the effects of using a large secondary antibody loaded with fluorophore must be considered (figure 3-5).

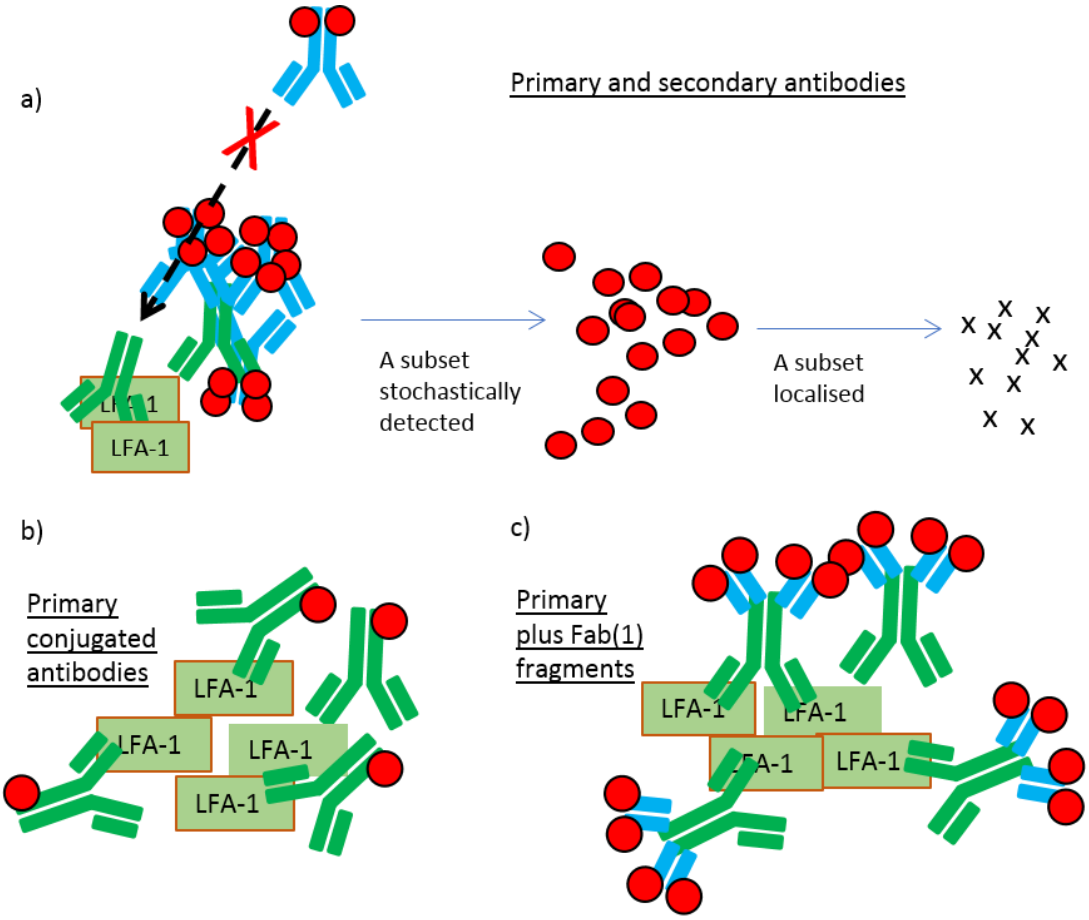

Figure 3-5: **Schematic showing different antibody labelling techniques.** (a) diagram showing secondary antibodies (blue) with attached fluorophores (red) and subsequent localised coordinates (crosses). b) primary antibodies directly conjugated to fluorophores and c) Fab(1) fragments (blue) with fluorophores bound to primary antibodies.

First of all, the size of the antibody relative to the molecule of interest must be taken into account. IgG antibodies have an average size of around 10 to 15 nm in length. Thus with a

primary plus secondary labelling protocol, the detected fluorescent signal will necessarily be 20 to 30 nm from the target of interest. While TIRF STORM images are achieved in two dimensions, antibodies arrange themselves in 3 dimensions, and on both sides of a group of target molecules[174] (figure 3-5a). This is problematic for structures as well as clusters of molecules, which may then appear as large clusters that are 60 nm away from the target.[175] It is proposed that to some extent, Fab fragments and nanobodies solve this 'linkage error'[176] due to their small size – however they can engender a different problem.

Multiple binding of secondary antibodies (or Fab fragments) to primary antibodies are usually a desired outcome of their manufacture, and work to boost the fluorescent signal emanating from a tagged molecule. In addition, secondary antibodies come ready loaded with many fluorophores, again, increasing the fluorescence output. For super resolution, though, this is a problem, as a huge number of molecules can be detected, forming a false cluster, for even a single target molecule of interest. To add to this problem, the number of secondary antibodies that will bind a single primary antibody is highly variable, and once bound, multiple secondary antibodies will occlude surrounding epitopes, leading to overall an unrealistic (albeit aesthetically pleasing) super resolved image (figure 3-5c).

The use of secondary antibodies directed to primaries (figure 3-5a) introduces variability into the number of molecules and size of clusters due to multiple binding and multiple fluorophores. The use of Fab fragments targeted to primary antibodies solves the size occlusion and linkage error issues, but still multiple bindings and multiple fluorophores add to the variability which increases cluster heterogeneity and reduces replicability (figure 3-5c). Primary conjugated antibodies (figure 3-5b) each bind to individual target epitopes, and the number of fluorophores can be manually tuned by altering molar concentrations during antibody:fluorophore conjugation for a more representative answer, therefore these are desirable for our purposes.

To test whether the antibody labelling method used changed the number of detected molecules, three separate labelling strategies were applied to fixed T cells. Cells were fixed during migration on ICAM-1 coated glass using cytoskeletal buffer supplemented with sucrose, 3 % PFA and 0.1 % GA as described above and in methods. The three labelling strategies were:

1) a directly conjugated alexa fluor 647 primary antibody to LFA-1 (conjugation described in methods)

2) an unlabelled primary antibody to LFA-1 (the same clone) followed by a secondary antibody conjugated to alexa fluor 647.

3) an unlabelled primary antibody to LFA-1 (the same clone) followed by a Fab fragment conjugated to alexa fluor 647.

dSTORM was carried out on the cells, and 2 μm^2 ROIs were taken for analysis. The first measure, the total number of molecules, was a measure of how many emitters, related to the number of LFA-1 molecules, was detected per ROI. LFA-1 appears the least abundant where the directly labelled 1^0 antibody is used, more abundant where a 2^0 antibody is bound to this primary, and much more abundant where a Fab fragment is used, possibly due to a lack of steric hindrance and resultant multiple bindings of several Fabs to individual primary antibodies (Figure 3-6).

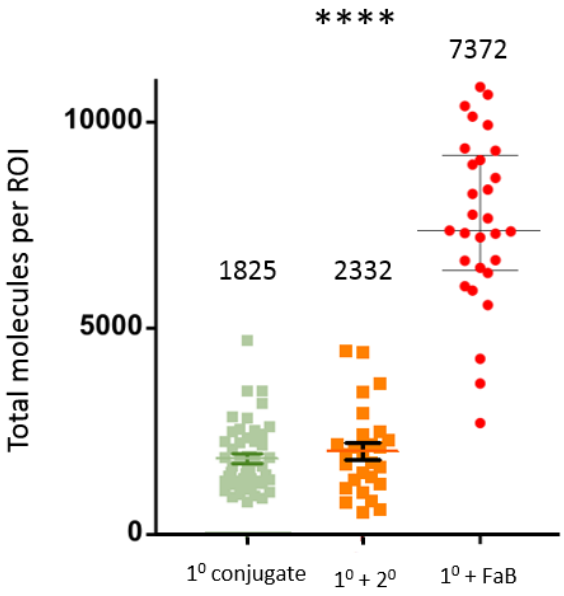

Figure 3-6: **Total detected molecules are amplified by use of a secondary antibody or a Fab fragment.**

As the Fab fragment was giving extremely high molecule counts, which were much higher than published values for LFA-1 abundance using similar super resolution microscopy techniques in human T cells, thereforetheir use was discontinued during further experiments.

Next, cluster analysis was undertaken (see methods) on the ROIs in the two remaining conditions and the radius of clusters and the number of molecules per cluster was measured. The labelled primary conjugate gave larger clusters (figure 3-7a), which also contained less

molecules than when the unlabelled primary and labelled secondary were used together (figure 3-7b).The most likely reason for this effect is steric hindrance, where secondary antibodies are occluded from binding sites on separate primary antibodies, and are therefore unable to reach their targets.

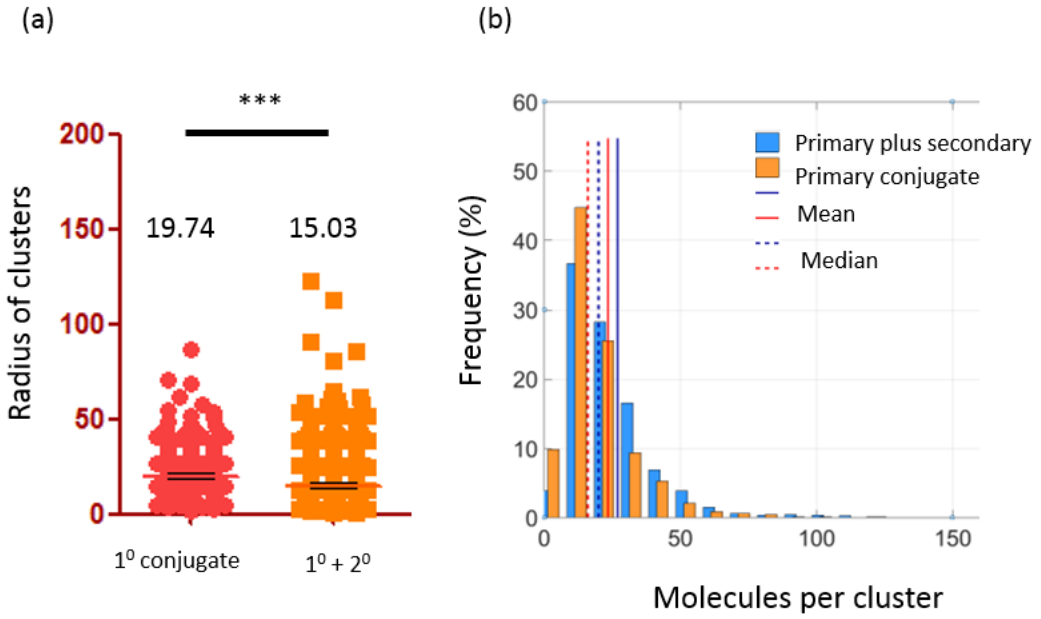

Figure 3-7: **Comparison of the size of clusters and number of molecules per cluster when using labelled primary antibodies versus primaries and labelled secondaries.** A) plot of the radius of clusters and b) the molecules per cluster in each method.

3.3.1 Discussion of fixation and labelling for super resolution

A plethora of fixation methods are readily used to study cells in different contexts. Now that light microscopy is able to reach TEM like resolution levels, it is natural that many of the lessons learnt there for preserving fine structural detail must be replicated here.

To this end, a recipe for 'cytoskeletal buffer' was the starting point, characterised using super resolution of actin by Xiaowei Zhuang[130]. It is clear from these experiments that the fixative is not fast enough to stop the loss of fluid from cells, therefore maintaining iso-tonicity through the addition of sucrose to the buffer is necessary.

Using analysis of cluster characteristics, certain metrics on the effect of adding a low concentration of glutaraldehyde were tested. The use of PFA alone results in the loss of molecules from the non-clustered population, but also from the clustered population – therefore glutaraldehyde at this low concentration is essential.

The size of the probe – so called linkage error – is a concern for single molecule work, as is the occlusion of antibodies from the target of interest; both contributing to an erroneous or simply false clustering map. In line with this work, use of a directly conjugated antibody resulted in lower molecule counts per region taken from STORM maps of migrating T cells. This fits with the theory that the combined effect of multiple secondary polyclonal antibody (Pab)/Fab bindings plus a high degree of fluorescent labelled per probe mean that the signal from even a single target molecule will be artificially enhanced. The interquartile range in the graphs , is also much larger using secondaries or Fabs, indicating high experimental variability due to this effect. As most of the subsequent work relies on comparing relative clustering between conditions it is important to keep variability low.

Finally, directly conjugated primary antibody staining was compared to the use of secondary probes in terms of two other metrics. These were the size (radius) of clusters, which decreased with secondaries, and the number of molecules per cluster, which decreased as well. Together, use of secondary antibodies made smaller, less dense clusters. This could reflect the occlusion of target molecules by neighbouring secondary antibodies[177], forming smaller clusters as there is nothing else for secondary antibodies to bind to. The conclusion here is to use primary conjugated antibodies, after fixing with 3 % PFA + 0.1 % GA in 'cytoskeletal buffer' with glucose switched for sucrose.

3.4 Image acquisition and software optimisation for localisation and cluster analysis

Super resolution images are representations of nanoscale molecular distributions. To ensure that reconstructions do not fall prey to artefacts associated with the reconstruction process (where spatially separate fluorescent emitter point spread functions (PSFs) are localised in individual frames to produce coordinate maps, which are then summed together to produce a diffraction unlimited map), several aspects must be taken into consideration. These include dealing with overlapping point spread functions: in a case where there are two fluorophores which emit and their PSFs overlap in the same frame, the software scan struggle to localise both emitters. Overlapping PSFS are more probable to exist in clusters where molecules are closer together, therefore control for this phenomenon is essential to prevent bias against detected clustered molecules.

Secondly acquired and localised maps must be carefully post processed to ensure faithful representations of molecular populations. The uncertainty, a measure of localisation precision based on photon output and size and shape of the PSF, must be taken in to account when calculating clustering[140,141]. Drift correction must also be taken into account, and is especially important for nanoscopy in general. Merging is a useful post processing step to minimise the effects of multi-blinking fluorophores – a problem inherent to STORM which means that emitters might be localised more than once. Finally, due to the sheer number of calculations required for localisation and cluster analysis algorithms in datasets consisting of thousands of molecules in hundreds of cells, computer processing power was taken into consideration and tested here to inform the design of the experiments.

3.4.1 Overlapping PSFs

Preliminary data acquired using dSTORM imaging of fluorescently labelled LFA-1 in migrating T-cells was very dense and appeared to be highly clustered by eye (Figure 3-8). Raw data collected from the STORM microscope consists of thousands of emitters in thousands of frames which must all be localised with sub-diffraction precision to produce a molecular coordinate map. Hence, optimising the localisation for emitters in regions of high density was essential.

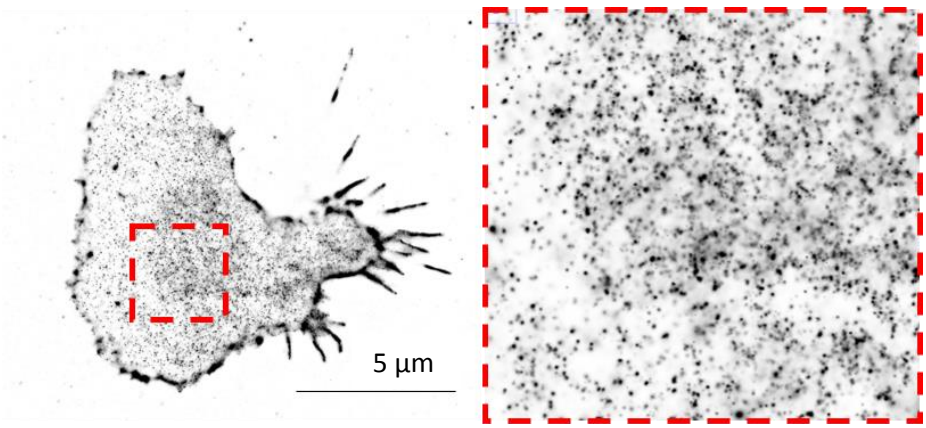

Figure 3-8: **LFA-1 distribution in an example migrating cell, imaged by dSTORM.** Left panel shows whole cell, right panel a zoomed region. Molecular coordinates are displayed as gaussian representations of their 'uncertainty' values.

To correctly identify molecules in very densely labelled areas of the image, slightly overlapping point spread functions are assessed using 'multiple-emitter fitting'[157]. MFA selects overlapped point spread functions in individual frames and fits them against a model of first one, two, then three possible fluorophores to find which one fits best to the data (figure 3-9). This answer is then applied, so as to avoid negative bias against densely clustered molecules. Multiple-emitter fitting (MFA) produces points that are far closer together than would otherwise be possible in dense samples after optimisation of laser powers and buffer compositions for blinking that is as sparse as possible.

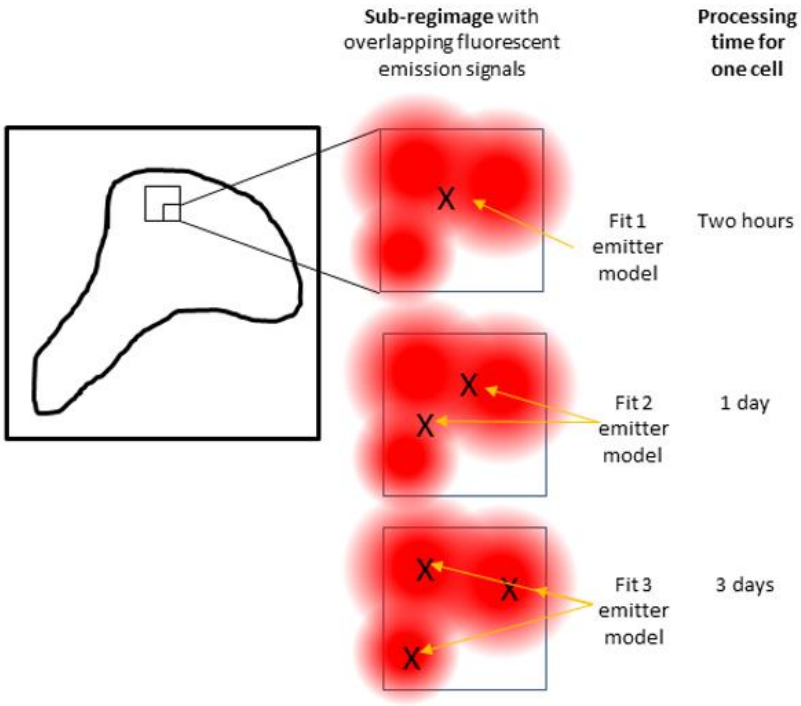

Figure 3-9: **Multi-emitter fitting schematic.** Panels show overlapping fluorophores in a subregion of interest. 1,2 and 3 localisations are tested. Processing times are listed on the right.

To test the ability of proprietary (Nikon elements) software and user developed software (thunderSTORM), the latter with MFA enabled, to localise densely clustered molecules, we ran the same raw dataset through both programs. thunderSTORM with MFA [132,157] enabled picked up large dense clusters of LFA-1 that Nikon software was unable to detect. ThunderSTORM with MFA enabled has the ability to localise molecules within dense clusters, which the Nikon software simply discounts. As a result, thunderSTORM was used for all future localisation (**Figure 3-10**).

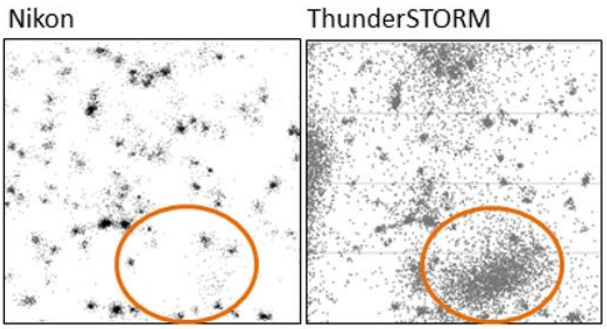

Figure 3-10: **thunderSTORM localisation with MFA identifies large dense clusters invisible to Nikon localisation.** Orange circles show populations of molecules detected in thunderSTORM (right panel) which were missed in Nikon (left panels).

3.4.2 Post processing: uncertainty, drift correction and merging

Post processing options were also important to optimise for these datasets. Firstly, molecules in the reconstructed image have *uncertainty values* – a measure of how well the localisation algorithm has been able to define the centre of a given point spread function (PSF), based on photon output, and camera/background noise[125]. An upper limit is often applied to this value to negate molecules that are badly localised and this value is often cited as a vague determinant of image resolution. A side effect of MFA is that some of the localised molecules may still be badly localised (have high uncertainty) – for spread PSFs the algorithm can localise the same fluorescent emitter twice, in slightly different locations, resulting in the potential for false clusters. False pairs of molecules like these are corrected for by using the 'remove duplicate molecules' function in thunderSTORM: localised points with overlapping uncertainty values are removed.

An important consideration for nanoscopy images is accurate drift correction, which can be carried out using fiducial markers or by cross correlation. Fiducial markers produce generally more precise drift correlation than cross correlation, especially in the case of 'averaged fiducial correction'[115] which correct the image in each frame and accounts for stage wobble as well as drift in a single direction. Precise titration is required, as the signal from a fiducial bead can occlude analysable parts of the image, and typically must be selected manually by the user post acquisition. Fiducials are therefore more compatible with longer acquisitions, but require more sample preparation/processing steps. Cross correlation is faster in terms of human effort, and over short acquisition times produces good overall drift correction; mostly this was used here, as acquisitions were limited to 10 000 frames.

This can be followed by a 'merging' step, which corrects for variable duty cycles of fluorophores like alexafluor 647: multiple blinking cycles are an inherent property of blinking fluorophores used in dSTORM[129]. Two phenomena arising from this quality that can confound the analysis and result in false clusters are long on times, where an emitter remains on for several frames as well as multi-blinking, where an emitter blinks several times: both result in each PSF being localised as a different molecule. Merging corrects for this to some extent by merging the signal (resulting in only one localisation) over a user supplied number of frames . This is optimised for this data in the results below by plotting the total number of localisations against the number of frames a fluorophore has to appear in for it to be merged into one localisation – where the asymptotes of this graph meet was the chosen value (30 ms for AF647 **figure 3-11**).

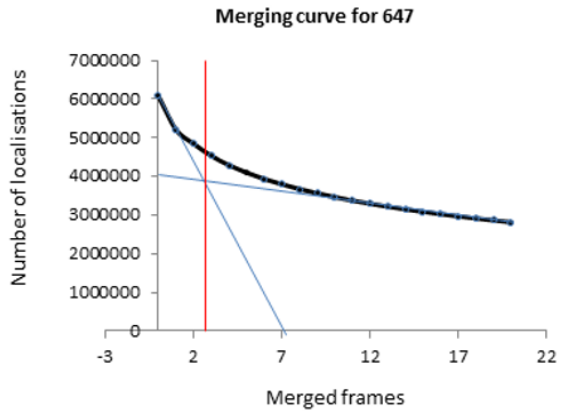

Figure 3-11: **Determining the optimal number of frames to merge during post processing.** The total number of localisations in a representative image was plotted against the merge time in frames. The intersection of the left and right asymptotes of the curve represents average optimum merge time: 3 frames (30 ms).

3.4.3 Tuning required acquisition length for optimal speed of analysis

After optimising the software parameters, we revisited the data acquisition itself to further optimise the efficiency of the experiments. Super resolution images can consist of anything from 20 to 20 million frames of data. We wanted to find out a reasonable number of frames for a reconstruction that would allow us to extract precise and replicable cluster metrics (methods), while balancing the need for shorter computational analysis times for the high n-numbers required for work based in heterogeneous primary mouse T cells.

One way to speed analysis is to reduce the number of acquisition frames. Here migrating cells were fixed and stained with LFA-1 and cluster analysis carried out (methods). Comparing a 10 000 frames acquisition with a 20 000 frame acquisition, more molecules were detected in the 20 000 frame acquisition (figure 3-12a), but there was only a very tiny difference in the radius of clusters (n = 10 cells p = 0.04 figure 3-12b) based on measuring thousands of clusters.

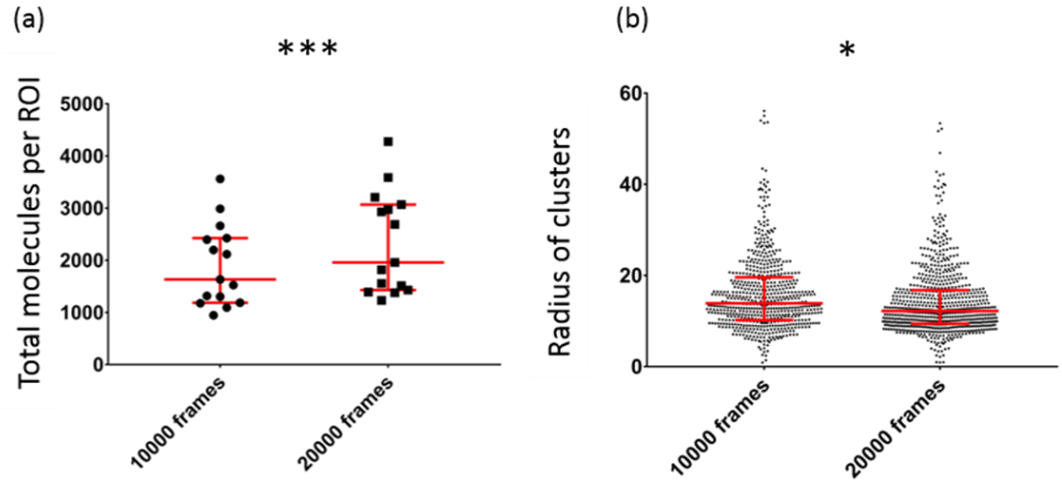

Figure 3-12: **Total molecules per ROI and radius of clusters measured in images acquired over 10000 or 20000 frames.** a) the total molecules per cluster and b) the cluster radius.

The total number of detected molecules in STORM imaging is prone to variability between samples[172]. To test the robustness of the other clustering metrics to more drastic changes in the total number of molecules, an increasing threshold on uncertainty was applied during post processing to a dataset of n = 11 cells, which had the effect of decreasing the number of detected molecules available for analysis (figure 3-13a). Cluster analysis was carried out to measure the effect of fewer molecules on cluster metrics, with the total molecules treated as an independent variable (as this was done during post processing on a single dataset to benefit from internal consistency). Results showed that even at drastically lower molecule counts, only the percentage of clustered molecules was affected (figure 3-13b). All other metrics – the number of clusters, the radius of clusters and the molecules per cluster -remain the statistically the same even when there are far fewer molecules available for analysis (figure 3-13 c to e).

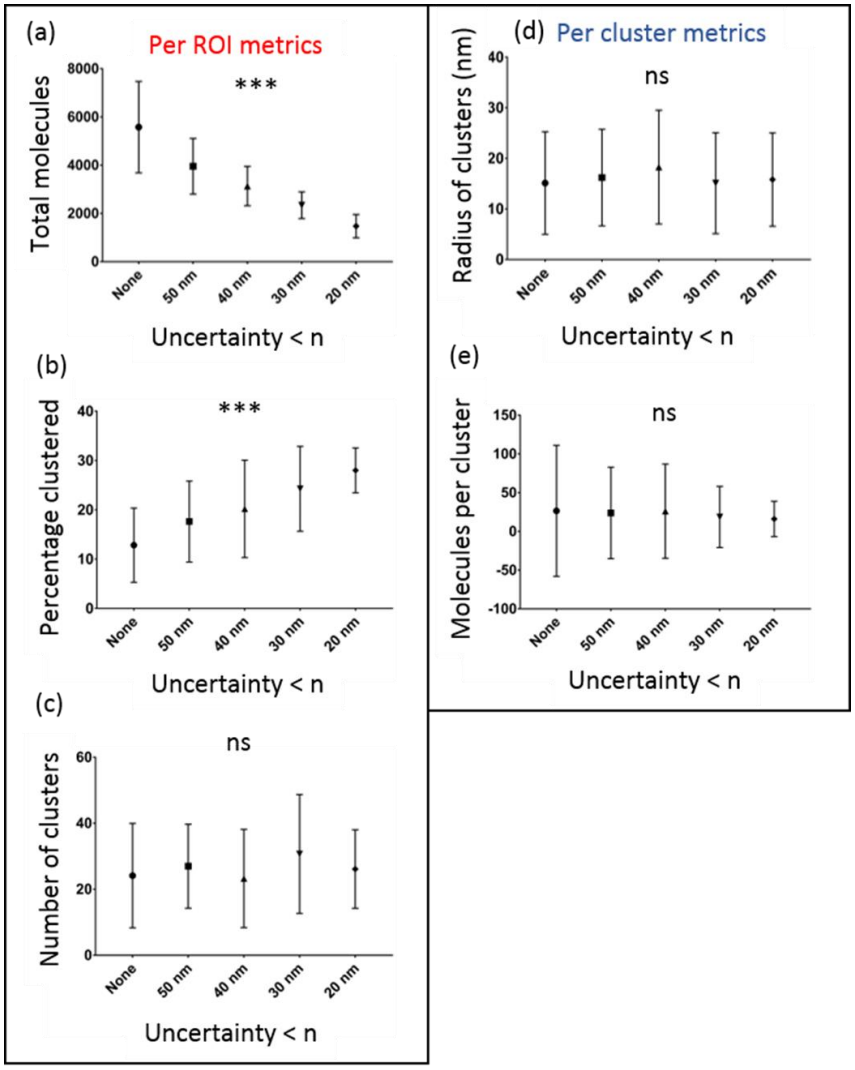

Figure 3-13: **Total molecules per ROI reduced with an uncertainty filter did not affect the radius, molecules per clusters or number of clusters detected.** Left: per ROI metrics: a) the total molecules, b) % clustered and c) number of clusters plotted against uncertainty thresholds (measured in nm). Right: individual cluster metrics d) the radius of clusters and e) number of molecules per cluster.

Processing was optimised in this way to ensure that the localisations were as precise as possible, and analysis could be done in the shortest time possible, while suffering no appreciable loss of information with relation to analysed clusters. Optimised pointillist maps were exported with x values, y values and uncertainty values for each coordinate, so as to be compatible for the cluster analysis algorithm used in the lab. 2 μm^2 regions were then selected based on a central coordinate point. The process undertaken to optimise this process is outline in figure 3-14.

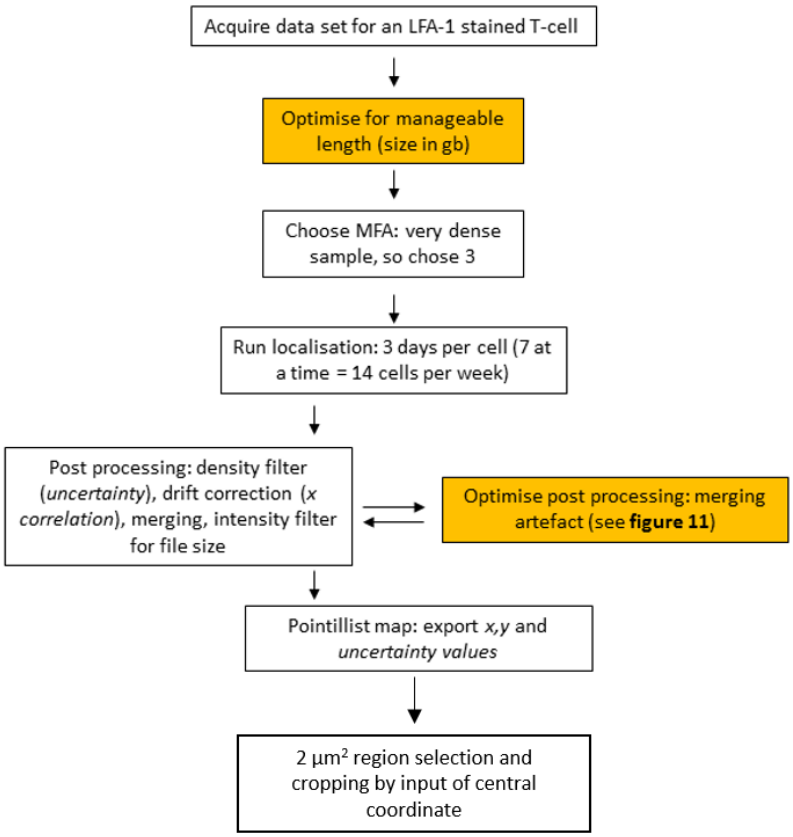

Figure 3-14: **ThunderSTORM workflow diagram.** Two things were optimised for this data, the size of the file (10000 frames) and the number of frames to merge in post processing should there be temporally overlapping fluorophores (orange boxes).

3.4.4 Tuning cluster analysis for optimal performance/processing time

A model based Bayesian statistical approach[140,141] combined with topographic prominence[143] was used to analyse clusters. The algorithm has been demonstrated to work in many different datasets, but where large n numbers are concerned requires a large amount of processing power. Thus, the number of proposals explored for the radius and threshold of clusters were cropped, in order to maximise the speed of the analysis while maintaining the accuracy.

While the Bayesian cluster analysis papers are published[140,141] and examples of its efficacy are available in simulation as well as with experimental data there, it was useful to test the ability of the code to deal with heterogeneous data within these specific data sets. To this end, regions with small clusters of LFA-1 were compared with regions of large clusters of LFA-1. Bayesian cluster analysis allows us to extract less subjective information on clustering which is optimised for each region: for example a region in where there are nanoclusters, as opposed to a region of mainly microclusters. Figure 3-15**a)** shows a pointillist map with small nanoclusters picked up due to the algorithm setting a small radius as the 'best value'. In figure 3-15b**)**larger 'microclusters' are picked up due to a larger 'best answer' for the radius being chosen by the algorithm to account for these large entities. This figure also shows the ability of the Bayesian cluster analysis algorithm to identify clusters in the presence of heterogenous background (figure 3-15b).

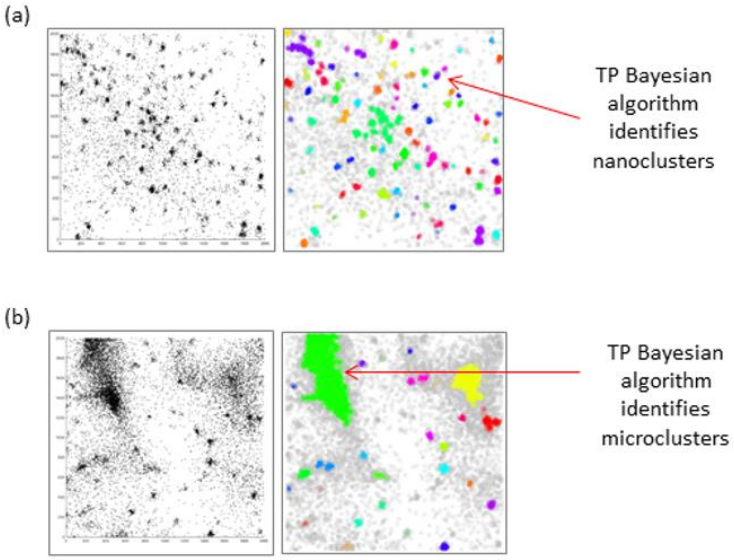

Figure 3-15: **Bayesian cluster analysis carried out on a region of interest containing small clusters versus large clusters.** A) Shows a 2 μm^2 coordinate map (left) and the same map with small clusters identified. b) coordinate map with large clusters identified.

The technique required a lot of processing power and multiple threads to be run in parallel:analysis of all possibilities for best radius and threshold would have taken ~ 1000 hours (41.6 days) for 300 regions after prior localisation of coordinate maps (n = 300 regions proposed size of datasets for biological analysis from 6 mice). The analysis was therefore optimised for greater speed with the same accuracy by cutting the minimum and maximum proposals for radius and L(r) threshold – the major bottleneck in terms of processing speed.(**Figure 3-16**). Figure 3-16a) shows an example threshold map adapted from[141] showing a full radius and threshold scan. Black lines show upper limits for the detected 'best answer' in this data. Figure 3-16b) shows example cluster maps in which the step size for radius or threshold were increased from 5 to 10: the clusters identified are the same. Figure 3-16c) shows a table indicating that changes to the step size setting (blue) didn't change the cluster metrics (grey) or the ideal answers (yellow) derived for a single region of interest. As a result of these tests, a threshold limit of 10 to 270 and a step size of 10 for both radius and threshold was used for future analysis, reducing analysis time to under 1 week per dataset.

a)

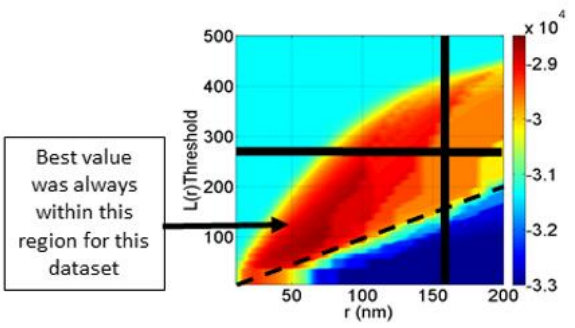

b)

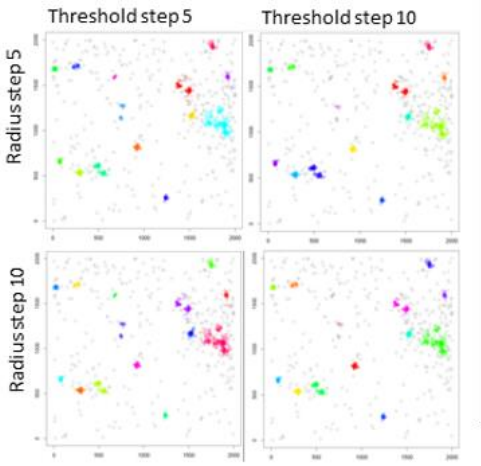

c)

Step size radius	Step size threshold	Range radius	Range threshold	Number of clusters	Percentage in clusters	Mol per cluster	Mean radius	Ideal radius	Ideal threshold
5	5	10 to 160	10 to 270	14	58	33	26	50	90
10	10	11 to 160	11 to 270	13	54	34	23	50	95
5	10	12 to 160	12 to 270	13	54	34	23	50	95
10	5	13 to 160	13 to 270	14	58	33	26	50	90

Figure 3-16: **Optimising the Bayesian analysis routine for maximum computing speed.** Proposals for radius and threshold could be reduced while not affecting the results a) Heat map adapted from (Delanchey et al. 2015) – black lines show the limits for this data. B) Cluster maps showing that increasing the scanned step size from 5 to 10 results in no change to the identified clusters. C) Table showing changes to the step size (blue), results from analysed cluster metrics (grey) and the best answer derived from the cluster analysis for a single example map.

Finally, a basic workflow for cluster analysis of SMLM datasets is added to aid the process in conjunction with the published protocols paper (figure 3-17).[140]

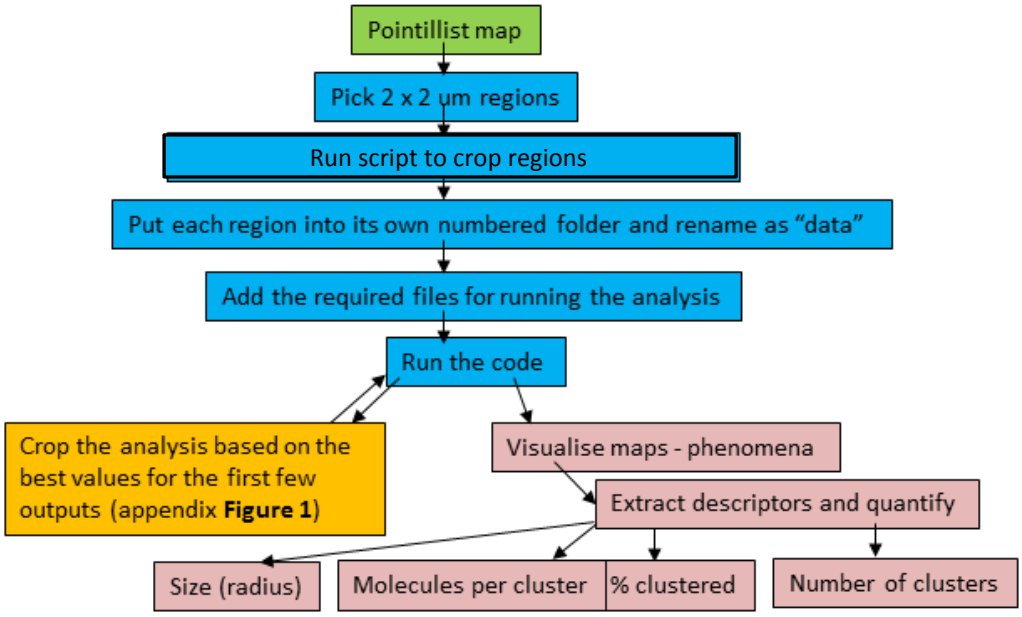

Figure 3-17: **Bayesian cluster analysis workflow.** The orange box shows another speed optimising step, which was undertaken based on the max and minimum clusters in a subset of the data.

3.4.5 Discussion for STORM image acquisition and analysis section

Artefacts due to image processing errors can be a problem in super resolution microscopy. Here, some are discounted due to the goal of searching for relative answers that differ between conditions, rather than absolutes such as real target molecule counts. At the current point in time, due to the nature of antibody labelling and the stochasticity of blinking, such absolute quantitation is not possible. Instead, by controlling for potential artefacts in the image reconstruction process, nanoscale characteristics can be accurately reproduced between experiments, and therefore can be compared between conditions.

thunderSTORM is available freely as an imageJ plugin, and worked well for our analysis. Enabling multi-emitter fitting allowed us to detect more molecules, most of which were participating in dense clusters. It is important to point out that those molecules in clusters are more likely to be overlapped by other fluorophores than molecules outside of clusters. Therefore with MFA disabled, you select against detecting molecular clustering and lose information.

Several post processing modules were used in the thunderSTORM module, the most important of which was 'merging'. This controls for fluorophores with long 'on' times and for alexafluor 647 in the conditions at KCL's Nikon centre, the optimum value was set at 30 ms. Those fluorophore on for longer than this time period were merged into a single molecule to avoid the creation of false localisations that might contribute to forming clusters.

Finally, time and computational power saving measures were explored. By decreasing the number of frames acquired, and by ascertaining that the number of localised emitters in a given image doesn't appreciably change the answers from the cluster analysis, we felt confident to cut the number of acquired frames to 10 000. Similarly, the cluster analysis proposals were cut to a range applicable to my dataset. Using these changes, the speed of analysis was improved to around 1 cell per day. In addition, many cells could be run through thunderSTORM in batch, and in parallel, making the analysis feasible in the long term and providing a full set with repeats in 3 mice per week.

3.5 Multicolour STORM imaging optimisation

Previously, multi-colour nSTORM has been used with dye pairs to look at microtubules/clathrin[178] and directly conjugated transferrin[179]. While useful in these specific applications, this technique has proved difficult to set up for diverse targets of interest. dSTORM is more versatile and has also been used for two colour analysis[180,181].

The first section (3.5.1) describes the investigation of many fluorophores to assess desirable STORM characteristics, and the second section (3.5.2) describes a multiplexed technique using sequential rounds of alexa fluor 647 localised to different targets was used[146]. Multi colour STORM is a new field thus thorough exploration of possible false readouts was needed to ratify the technique for multi-channel cluster analysis.

3.5.1 Assessment of alternative dyes

Successful two colour dSTORM depends on using fluorophores with good photoblinking characteristics[129,178]. To test this in our system, T cells were stained with a mouse primary anti-pan Lck antibody and detected with anti-mouse secondary antibodies conjugated to different fluorophores to identify fluorophores with similar blinking properties to AF647 in conventional STORM buffers (**Table 1**). At this point, secondary antibodies were used due to their low cost for testing, and our focus only on the characteristics of the fluorophores during these experiments. Only alexa fluor 568 (AF568) and Cy3b performed well enough in terms of clear, localisable blinking to be taken forward for further testing (table 1).

When cluster maps of single stained T-cells were compared side by side however, staining patterns looked quite different (figure 3-19). Many more nanoclusters were visible in alexa-fluor 647 based images (figure 3-19a, left panel) than in either AF568 (middle panel) or Cy3b

based images (right panel) The molecules that were localised had similar uncertainty profiles (< 20 nm (**Figure 3-19c**).

Fluorophore	Peak excitation	Peak Emission	Buffer composition	Blinking
Cy2	492	510	GLOX + MEA pH 5	No
Cy2	492	510	GLOX + MEA pH 7	No
Cy2	492	510	GLOX + MEA pH 10	No
Cy2	492	510	GLOX + β mercaptoethanol pH 5	No
AF 488	493	519	GLOX + MEA pH 5	No
AF 488	493	519	GLOX + MEA pH 7	No
AF 488	493	519	GLOX + MEA pH 10	No
AF 488	493	519	GLOX + β mercaptoethanol pH 5	No
Atto 488	501	523	GLOX + MEA pH 7	No
Atto 488	501	523	GLOX + MEA pH 10	No
AF 568	578	603	GLOX + MEA pH 5	+
AF 568	578	603	GLOX + MEA pH 7	++
AF 555	555	565	GLOX + MEA pH 5	+
AF 555	555	565	GLOX + MEA pH 7	+
Cy3b	559	570	GLOX + MEA pH 5	++
Cy3b	559	570	GLOX + MEA pH 7	+++
AF 647	651	667	GLOX + MEA pH 7	+++++

Figure 3-18: **Assessment of alternate fluorophores for use in two colour STORM.** Cells were stained with antibodies conjugated with the fluorophores in this table at high concentration. Bad blinking + good blinking +++++.

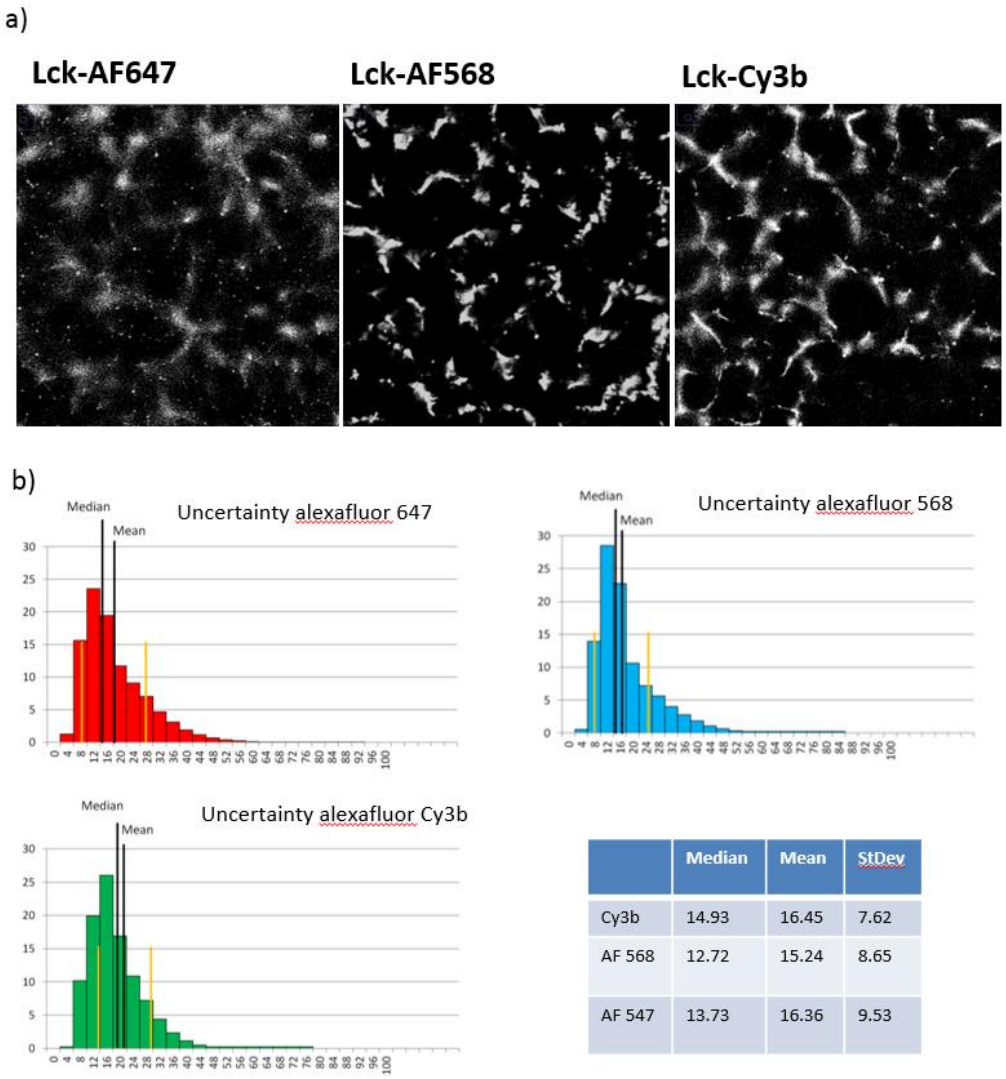

	Median	Mean	StDev
Cy3b	14.93	16.45	7.62
AF 568	12.72	15.24	8.65
AF 547	13.73	16.36	9.53

Figure 3-19: **Pointilliist STORM maps of Lck labelled with three different fluorophores A)**The staining pattern of Lck stained with alexafluor 568 and Cy3b were compared with the best fluorophore for STORM: alexafluor 647. **B) Uncertainty is the same for Lck tagged with af 647, Cy3b or af 568.** Each localisation has a precision level or "uncertainty" based chiefly on the number of photons emitted. Uncertainty values for the three fluorophores tested here for two colour STORM were very similar.

In order to assess fluorescent crosstalk, an assay was designed to measure aberrant fluorescent signal detected in the wrong channel. Crosstalk is especially a problem in STORM because high laser power is needed for fluorophore blinking, therefore even the tails of the emission spectra present a problem. To analyse percentage crosstalk, T-cells were stained separately with rabbit anti-Lck/anti-rabbit Cy3b or rabbit anti-LFA-1/anti rabbit AF647 and the signal collected in both channels (figure 3-20). Without the addition of a photon threshold, AF647 was emitting into the Cy3b channel at a high level (figure 3-20b), and the AF647 had some crosstalk from Cy3b (figure 3-20c). To try to improve this false background detection photon filters were used in postprocessing: increasing levels of this filter were applied to the

data and plotted against 'percentage error' for 647 crosstalk into cy3b channel and vice versa. 'Percentage error' was calculated where percentage error = number of aberrant localisations/total number of correct + aberrant localisations. Figure 3-20e shows that the 647 bleedthrough into the cy3b channel (blue diamonds) was high and was unaffected by increasing detected photon thresholds. The orange dots show Cy3b bleedthrough into the 647 channel which was lower and also unaffected by photon thresholds. Due to this problem, and the sub-optimal quality of Cy3b images of Lck (figure 3-20a) compared to af 647 labelled images of Lck (figure 3-20d), the use of dual labelled samples using different spectrally distinct fluorescent dyes on our system was discarded. As a result, multiplexed imaging using the same fluorophore for each separate target was explored as a completely separate alternative.

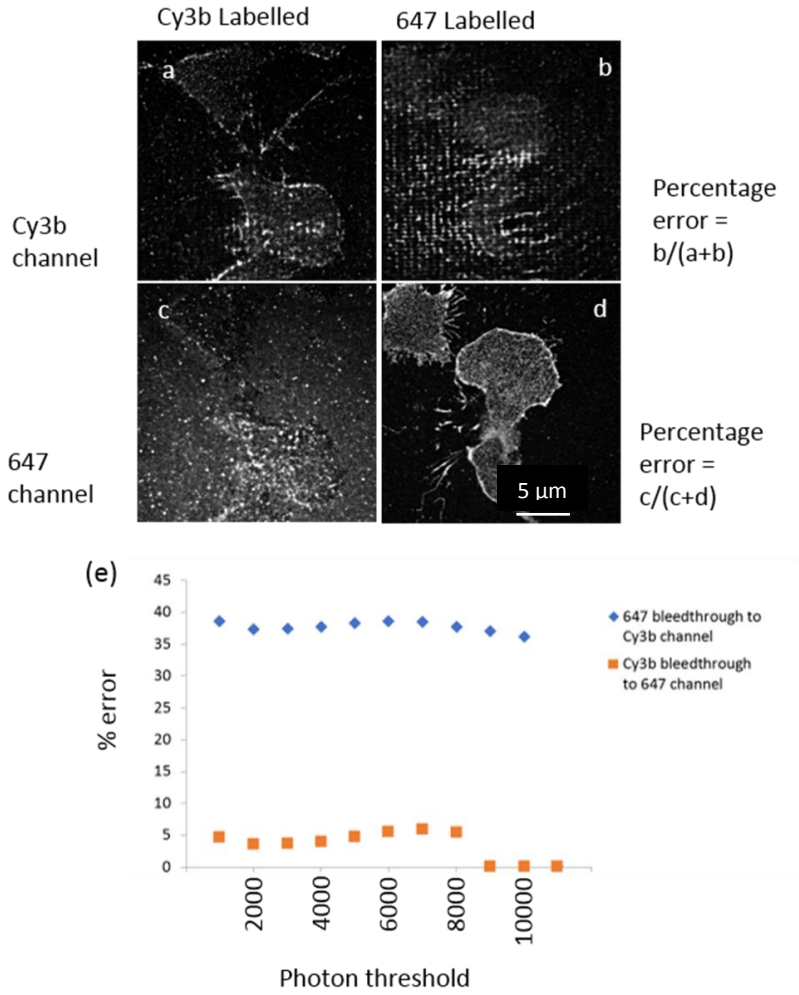

Figure 3-20: Crosstalk analysis of Lck labelled with Cy3b of alexafluor 647 a) and d) are representative images of cells labelled with cy3b or 647 and imaged in the correct channels. c and d) are labelled with cy3b and 647 but imaged using the 647 and 568 nm laser respectively. e) Percentage error for 647 detected in the cy3b channel (blue) and cy3b detected in the 647 channel (orange) plotted against increasing photon thresholds.

3.5.2 Correlative migration and Multicolour STORM imaging using the same dye

Using our Nikon dSTORM system at King's College London with the dyes currently available, use of spectrally distinct dyes to image separate molecules in super resolution was discounted. Instead, a multiplexed sequential antibody staining/elution based approach was taken to achieve multi-colour super resolution imaging, the main advantage of which is an immunity to crosstalk and chromatic aberration (madSTORM[146]).

This was coupled to a new way to achieve correlative live imaging of single cells in a wide field of view using a tiled 6 x 6 array of 36 fields of view at 100 x magnification using the STORM microscope (figure 3-21a). Each array took 30 seconds to capture, which was fast enough to capture T cell migration speeds up to the moment of fixation, the sample remaining on the stage throughout. An example tracked cell is shown in figure 3-21b, where at t = 60 seconds, the cell was fixed by addition of optimised fixation buffer (methods) to the dish in the microscope. After fixation, cells were removed from the microscope chamber for sequential rounds of staining and madSTORM antibody elution. Imaging cells during migration up to the point of fixation and then recording their positions meant that cells could be relocated, and clustering data derived from madSTORM imaging correlated directly to speed characteristics of single cells in the moment before fixation. Therefore this technique provides the possibility for more direct correlations between the functionality of adhesion nanoclustering on cell migration speed.

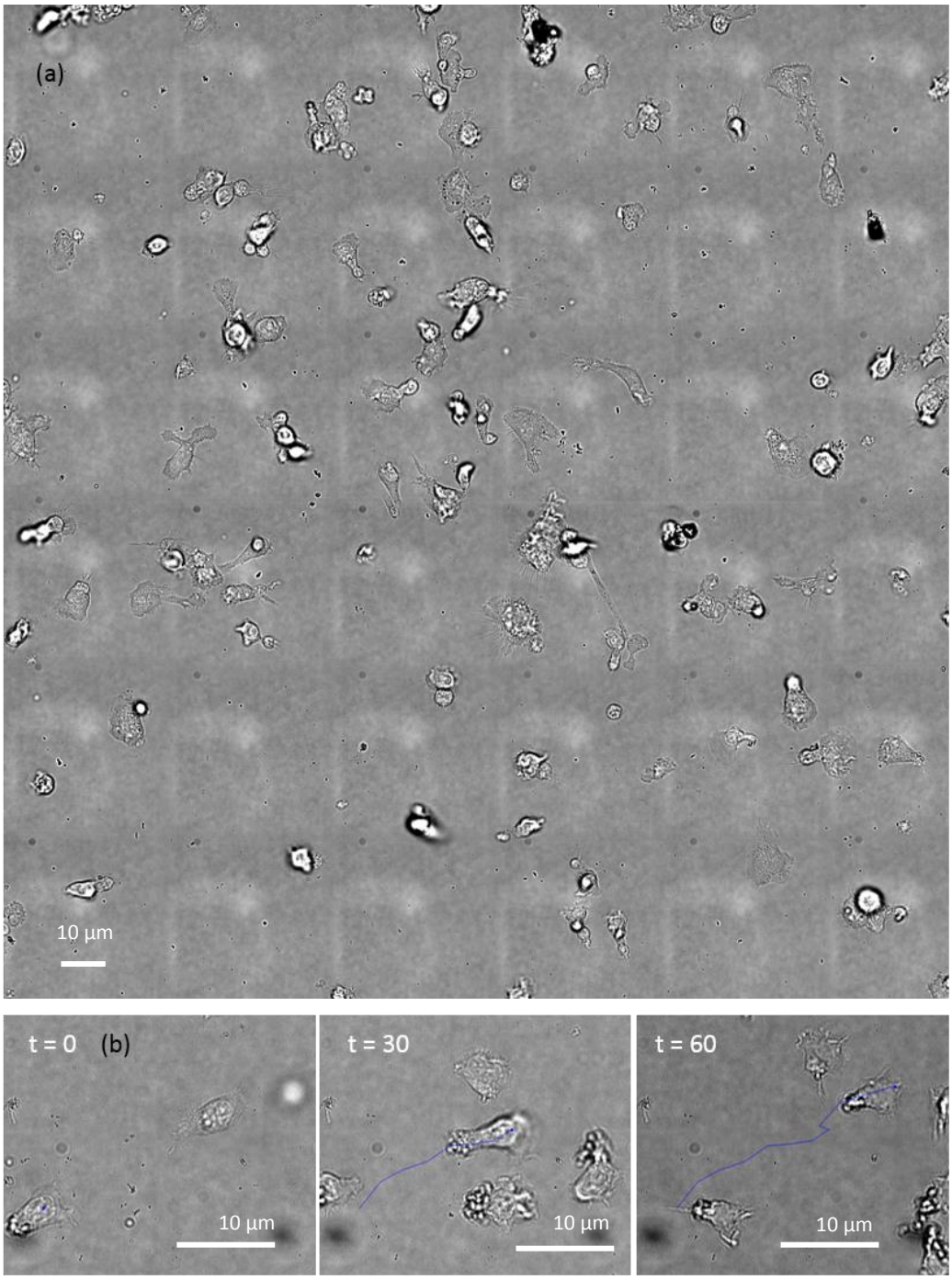

Figure 3-21: **Cell tracking for madSTORM. a**) example frame from 6 x 6 stitched image. b) Example zoomed image of a migrating T cell, manually tracked using imageJ manual tracker software (blue line). T (seconds).

The multiplexing consisted of sequential rounds of antibody staining, imaging and elution for each target of interest. The elution method required use of a buffer called madSTORM which is detailed here[146] and in methods. In this manner, 3 separate channels of super resolution data could be built up, free of crosstalk due to antibodies being physically removed before the

next round of imaging, and free of chromatic aberration on account of using the same fluorophore (alexafluor 647). The microscope set up was the same as for single colour microscopy, with the added proviso that it was important that the stage itself was not moved/altered during imaging. Separate super resolution images were then aligned based on the centroid points of super stable nano-diamond fiducials (FNDs), which are present in all image channels and are immune to wash off, for later analysis.

To optimise this system, the first focus was to establish that the antibodies after each round of imaging were being successfully washed away. This was done by imaging the same cells after treatment with the buffer, to make sure that no antibody signal remained. Figure 3-22 shows an example cell that has been tracked during migration, fixed on the stage and sequentially stained with three different antibodies (detailed in methods). Reconstructed super resolution images were then aligned based on FND positions and super resolved images prepared for later analysis (see results chapter 6). An example cell is shown with three separate TIRF images, then three separate localised images of three targets of interest discussed later, namely: LFA-1, phoshpho-tyrosine 397 FAK and phoshpho-tyrosine 416 Src. In each case, a TIRF image in (figure 3-22a) and a localised super resolution image in (3-22b) is shown, followed by the same cell imaged after madSTORM eluent has been added to remove the antibodies.

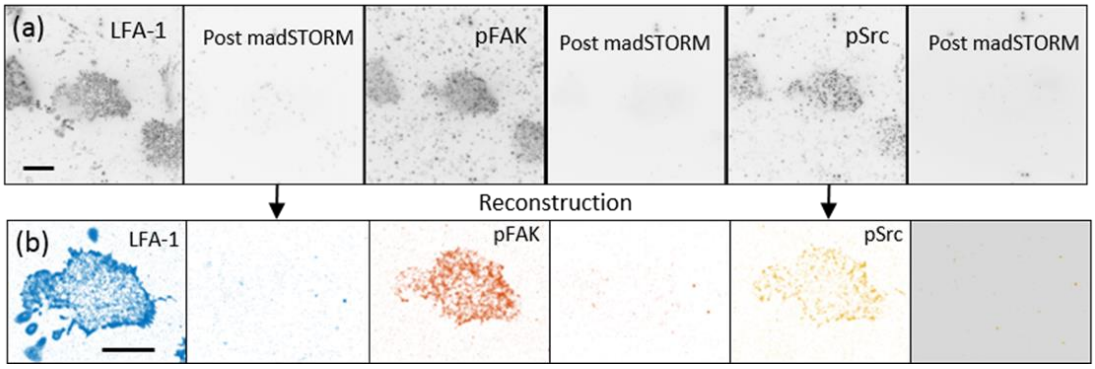

Figure 3-22: Correlative multiplexed imaging protocol using madSTORM. a) Example TIRF images of each target: LFA-1, pY397 FAK, py416Src, followed by TIRF images of the same field of view after madSTORM elution step. b) shows reconstructed pointillist images of the same fields of view. Scale bar 5 µm.

Finally, images were aligned using the fiducial nanodiamonds. The channels were aligned using a custom FIJI plugin. Briefly, a set of nanodiamonds is manually identified that is common to all channels in a given position. The lateral shift between channels is calculated for each corresponding pair of nanodiamonds and all the shifts are averaged into a per-channel value. Finally, the localizations on each channel's ThunderSTORM table were adjusted for the

measured shift. An example merged image of the whole cell, tracked in figure 3-21, is shown in figure 3-23. In the zoomed region (right panel), differential colocalization of clusters of the three separate molecules is clear.

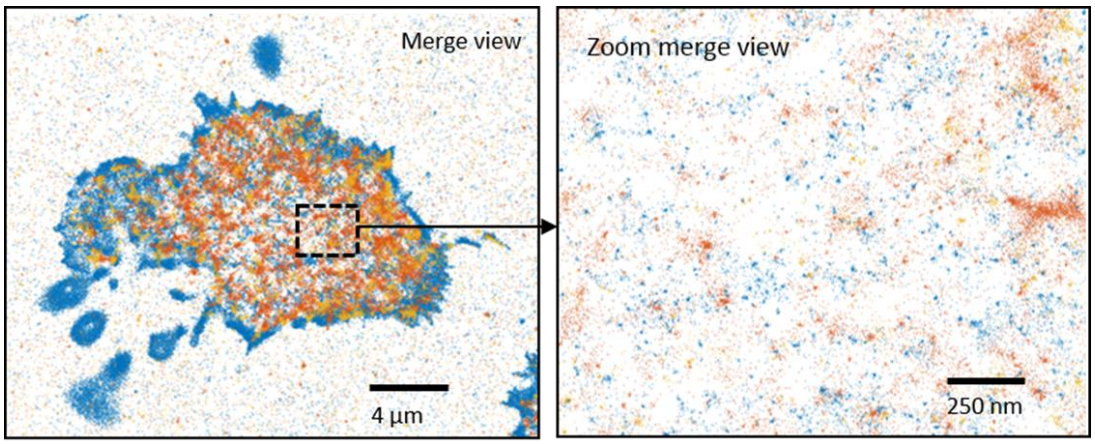

Figure 3-23: **Correlative multiplexed imaging using madSTORM.** Aligned merged view of all three channels: alexa fluor 647 labelled : LFA-1 (blue), pY397 FAK (orange) and py416Src (yellow), with a zoomed ROI on the right hand side.

3.6 Summary of optimised methods

The aim of these studies were to first collate known procedures for dealing with super resolution imaging data, and then to modify and ratify them for use in migrating T cells.

Here I have set out both general rules that hold true for my data, as well as optimisation steps that should be undertaken before carrying out any super resolution experiment. Fixation and labelling worked best in our system using cytoskeletal buffer complete with sucrose, 3 % PFA and 0.1 % GA. Proper use of the most advanced current localisation software allowed us to optimise our image acquisition and processing to streamline computation time, and balance this with highly reproducible pointillist images for further analysis. Bayesian cluster analysis provides a reduced amount of human decision making, and was optimised for use on this data. A comparison of multicolour imaging techniques is provided, and multiplexed single cell correlative imaging optimised for use in further experiments.

Chapter 4: Actin dynamics

4.1 Introduction: Actin flow, adhesions and cell speed

The importance of actin flow and engagement as the engine that drives cell migration has been investigated in many migrating cell types, including slower moving fibroblasts, and faster moving dendritic cells, neutrophils and T cells [24,34,38,40,79,166,182–186]. The leading edge/front of the cells is made up of a thin extended network of 70° branched actin fibres that form a dense mesh. F-actin is polymerised at the cell front, and is pulled backwards through the cell; this happens constantly, as a product/consequence of cell polarisation[168]. At the same time, the actin is pulled over adhesion complexes: in most mammalian cells these are large, multi-component 'focal adhesions' at varying spatio-temporal stages of existence. In T-cells, the same components form much smaller adhesions, which contain many of the same components as commonly referred to 'focal adhesions' in fibroblasts[76,80,187,188]. Transient engagement of the actin with these adhesions is part of a mechanism that translates force from flowing actin through the cell to the substrate, and is called the molecular clutch[79,182,183,185,189–191].

It is known that not all of the f-actin is cells is engaged with adhesions. To allow for migration dynamics, two or more networks of f-actin work concurrently in a 'slipping and gripping'[38,44] mechanism to facilitate movement by linking highly regulated flowing actin to the substrate outside of the cell via thousands of tiny integrin based adhesions[35,75,81,192–194]. The nature of this mechanism is what dictates cell speed: what isn't known is how this works in migrating T cells, which move in a diffusive and sub-diffusive manner, and so necessarily have a highly dynamic mode of migration. Here I measured the flow speed and engagement level of F-actin in activated, polarised migrating T cells moving in response to integrin LFA-1 binding ligand ICAM-1.

To alter cell speed while maintaining cell polarisation and overall migration, cells were treated with chemokines, chemical inhibitors and ionic compounds targeting specific biochemical pathways related to integrin and actin. A wide range of signalling pathways were chosen to be targeted, in order to potentially disentangle differential effects on the actin network and the molecular clutch. Specifically, T cell velocity was altered by: addition of chemokine CXCL12 or cation manganese (Mn2+), inhibition of actin polymerisation and de-repression of Src and Syk family kinase activity. I correlated stationary and moving F-actin speeds with the overall velocity of the whole cell. Conditions predicted to decrease cell speed were as follows:

1. Cytochalasin D is an actin polymerisation inhibitor. When added to cells, it prevents G-actin from being polymerised into f-actin, preventing efficient pushing forward of the leading edge and reducing the number of fibres available for retrograde flow. Again this was predicted to decrease cell speed[195,196].
2. Manganese Chloride dissociates to release the divalent cation Mn^{2+} in solution, which binds to the integrin LFA-1 beta 2 chain by displacing Ca^{2+} ions at the I-domain. This changes the conformation of LFA-1 to a high affinity binding state, resulting in increased binding to ICAM-1, and much higher cell adhesion to the substrate[197].
3. Increasing the concentration of ICAM-1 on the plate from a standard concentration of 2 µg/ml to 100 µg/ml, was predicted to saturate available LFA-1 binding points, and increase adhesion [198–200] which in these experiments was expected to slow migration speed.

To define the opposite situation, in terms of actin engagement and actin flow, cells were exposed to conditions that were predicted to increase cell speed during migration:

1. CXCL12 chemokine binds to a GPCR called CXCR4, and therefore works indirectly on integrin through an outside-in signalling pathway[33,34,201–207]. By inducing GPCR signalling, CXCL12 activates Pyk2/FAK which is linked to the early formation of focal adhesions[208]. It also induces signalling through PLCγ1 which causes calcium release, and the activation of the RAP1 and RIAM pathways to induce faster cell migration.

2. PTPN22 is a phosphatase that acts downstream of integrin to control its signalling[93], by dephosphorylating Lck[67] (detailed in introduction). Removal of the phosphatase was predicted to affect migration dynamics by taking away this control switch[67]. Here, $PTPN22^{-/-}$ mouse T cells were isolated and proliferated in the same way as the $PTPN22^{+/+}$ cells used for all other conditions, and were imaged with no further treatment.

4.2 Modulation of T cell migration velocity

It was important in to ensure that this was a study of the effects of the treatments on cell migration, and not simply a study of the aberrant effects of complete actin polymerisation shut down (in the case of cytochalasin D), affinity overload (in the case of Manganese) or ICAM-1 saturation (at raised ICAM-1 concentrations). All of these treatments (apart from PTPN22 knockout) were therefore subject to titration gradients to ensure that the majority of cells on a population level (within a field of view on a microscope slide) were 1) affected by the treatment and 2) remained polarised and migrating, albeit with altered migration speed. T cell migration assays were carried out by plating effector T cells on ICAM-1 coated dishes and imaging them using phase constrast microscopy at 10 x magnification velocity was measured using automated tracking in icy (for details see M&M). The following data shows the tracked speeds of migrating T cells in the presence of different concentrations of Cytochalasin D, $MnCl_2$, ICAM-1 and CXCL12.

Figure 4-1 shows example frames from 10 x phase contrast movies in which cells were plated on a microscope slide pre-coated with ICAM-1 at 2 µg/ml and treated with different concentrations of Cytochalasin D. Cells appear round and polarised, and remained migratory for the length of the movie (15 minutes).

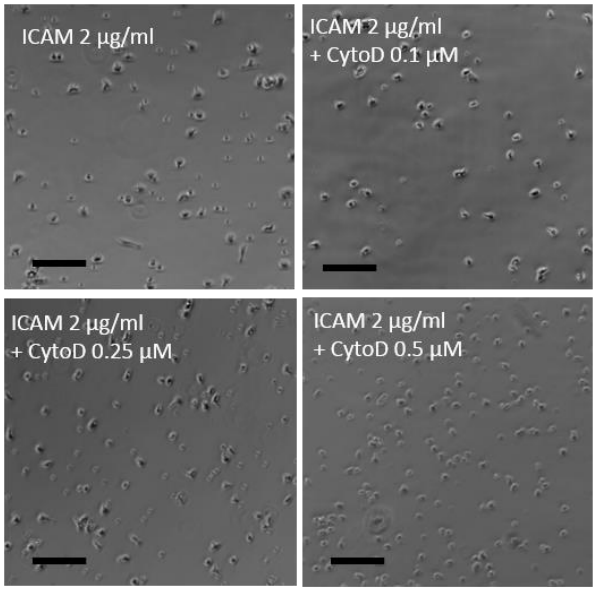

Figure 4-1: **10 x phase contrast movie frames showing cells migrating on ICAM-1 coated coverslips treated with Cytochalasin D.** Untreated (top left) cells migrating on 2 µg/ml ICAM-1 surface were compared with cells treated with 0.1, 0.25 and 0.5 µM Cytochalasin D. Scale bar 40 µm.

Figure 4-2 shows the automatically tracked cell speeds (Icy) derived from these movies, where 0.5 µM Cytochalasin D was sufficient to reduce T cell velocity while maintaining cell polarisation and migration. A maximum concentration of 0.5uM CytoD was chosen in this case because higher levels were toxic to T cells indicated by ruffled membrane, cell rounding and detachment from ICAM-1 coated plates. Untreated cells migrating on ICAM-1 moved at a median speed of 9.6 µm/min, while cells treated with 0.1 µM Cytochalasin D were significantly slower. Raised concentrations of Cytochalasin D caused even greater cell speed slow down.

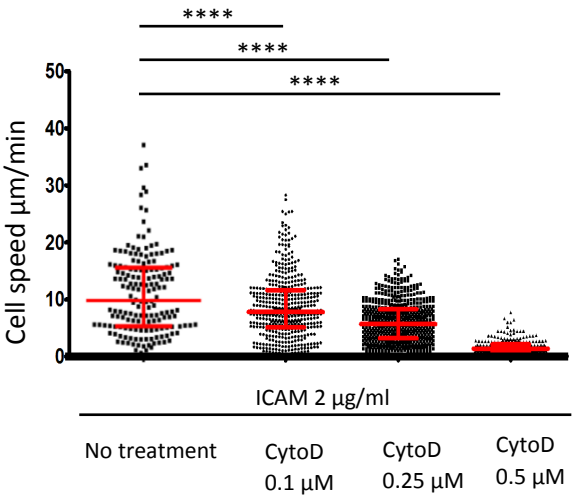

Figure 4-2: Cytochalasin D titration in migrating cells plated on ICAM-1 coated coverslips. Plots show cell speed at different concentrations of Cytochalasin D. n = 300 cells per condition. ****P < 0.0001.

Figure 4-3 shows that cells dosed with high concentrations of Mn^{2+} also remained polarised and migratory – no major morphology changes occurred. Above this concentration (5 µM), Manganese ions would come out of solution and forms large aggregates visible at 10 x magnification making them unsuitable for imaging and quantitation.

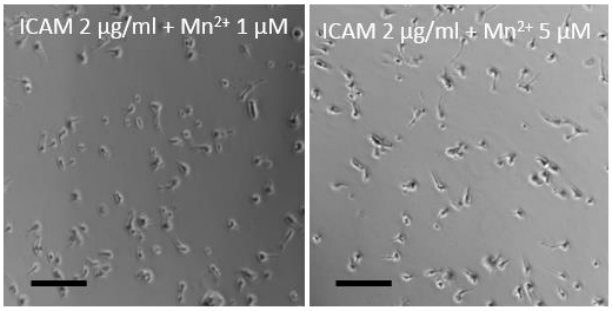

Figure 4-3: **10 x phase contrast movie frames showing cells migrating on ICAM-1 coated coverslips treated with $MnCl_2$.** Cells were imaged migrating on 2 µg/ml ICAM-1 after treatment with 1 or 5 µM of Mn^{2+} ions in solution. Scale bar 40 µm.

Figure 4-4 shows the automatically tracked cell speeds (Icy) derived from these cells treated with Manganese. Both concentrations of Manganese reduced the speed of cells to ~ 2 µm/min, significantly lower than cells migrating on ICAM-1 that were left untreated (figure 4-2).

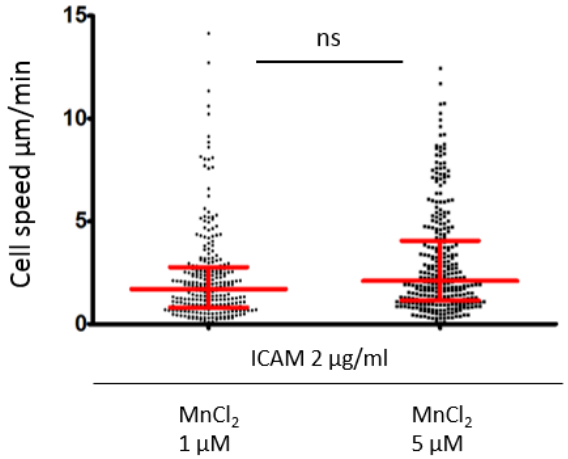

Figure 4-4: **Manganese ion titration in migrating cells plated on ICAM-1 coated coverslips.** Plots show cell speed at different concentrations of Mn^{2+}. n = 300 cells per condition. ****p < 0.0001.

Figure 4-5 shows phase contrast frames of cells migrating on two increased concentrations of ICAM-1: 10 µg/ml and 100 µg/ml, both reported to increased the density of ICAM-1 on the coverslip. Cells maintained their polarised shape and migrated throughout the movie.

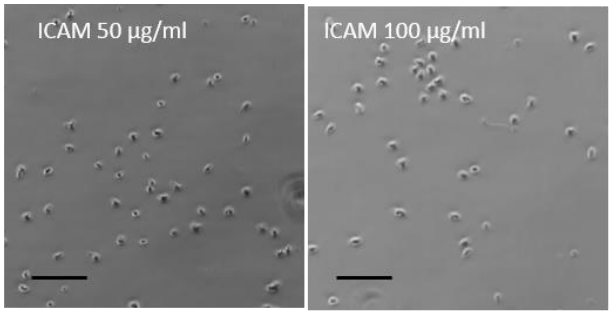

Figure 4-5: **10 x phase contrast movie frames showing cells migrating on different concentrations of ICAM-1 on the coverslip.** Migrating cells on a 50 µg/ml or 100 µg/ml ICAM-1 surface. Scale bar 40 µm.

Figure 4-6 shows the cell speeds for cells migrating on high concentrations of ICAM-1. Both 10 µg and 100 µg of ICAM-1 resulted in cells migrating at reduced speeds compared to untreated cells (figure 4-2). 100 µg/ml ICAM-1 caused the cells to migrate significantly slower that 10 µg/ml.

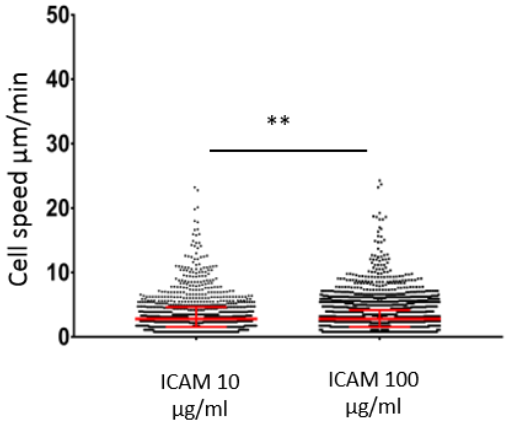

Figure 4-6: **Increased ICAM-1 concentration on coverslips.** Plots show cell speed at different concentrations of ICAM-1. n = 300 cells per condition. **** p< 0.0001.

Figure 4-7 shows cells dosed with CXCL12 chemokine at 150 ng/ml and 50 ng/ml. Concentrations of CXCL12 were chosen in a range shown to increase chemotactic migration, and were tested here in our experimental system, free of a concentration gradient[201] . Example phase contrast frames showed that CXCL12 treated cells remained polarised and migrating.(*n = 300 cells per condition. ****p < 0.0001*)

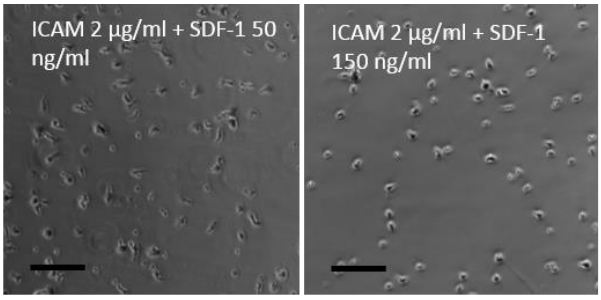

Figure 4-7: **10 x phase contrast movie frames showing cells migrating on ICAM-1 coated coverslips treated with CXCL12 chemokine.** Cells were imaged migrating on 2 µg/ml ICAM after treatment with 1 or 5 µM of Mn^{2+} ions in solution. Scale bar 40 µm.

Figure 4-8 shows cell speeds derived from automatically tracked CXCL12 treated cells. Cells treated with 50 ng/ml had significantly increased speeds as compared to untreated cells (figure 4-2). Cells treated with 150 ng/ml CXCL12 had almost double this cell speed.

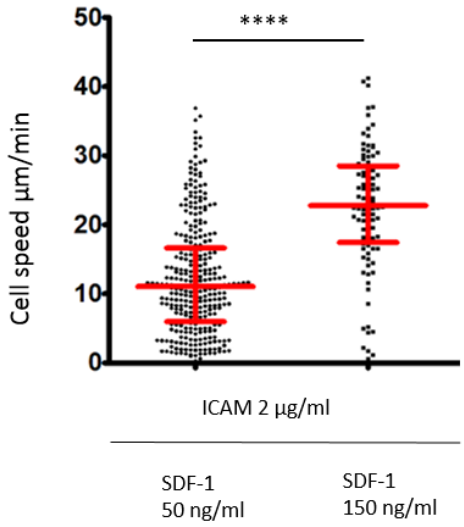

Figure 4-8: **CXCL12 titration in migrating cells plated on ICAM-1 coated coverslips.** Plots show cell speed at different concentrations of CXCL12. n = 300 cells per condition. ****p < 0.0001.

Having ascertained concentrations of the substances detailed in this section that would produce extreme cell migration phenotypes, while still allowing cells to migrate, we next wanted to apply these conditions to cells with labelled f-actin, in order to investigate their effects on dynamic actin flow, as well as actin engagement.

4.3 Retrograde and anterograde actin flow correlate with cell migration speed

In order to measure cell speed and actin flow in migrating T cells, lifeact GFP transgenic T cells were isolated from the spleen and lymph nodes of mice. At day 6 to 9 post activation, lifeact GFP positive effector T cells were plated onto an ICAM-1 coated dish and exposed to the treatments described above.Their cell speeds and actin flow dynamics were extracted and analysed using modified STICS software described in methods, to discern whether actin flow and engagement was affected differently in different pathways. Figure 4-9 shows 3 example frames from a 1 minute TIRF timelapse, in which the cell has been translated to the internal reference frame, and then analysed by STICS. Figure 4-9b) shows example vector maps for different time points in the image sequence. Actin retrograde flow was separated from anterograde flow (see methods) for all subsequent analysis.

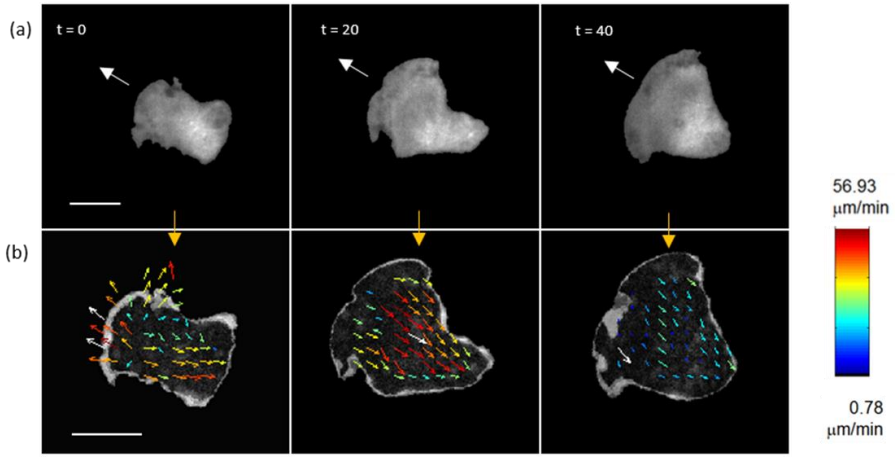

Figure 4-9: **STICS analysis of f-actin flow.** a) Stills from TIRF movies of migrating lifeact GFP T cells after translation to the internal reference frame: cells are centred in the field of view. White arrow = direction of migration. B) STICS vector map stills (coloured by speed). Representative image from n = 4 mice = 200 cells per condition. Scale bar 5 µm.

Figure 4-10 compares whole T cell speed and retrograde actin flow velocity extracted from the internal reference frame of migrating T cells (n = 200 cells from 4 separate mice - described in more detail in methods). T cells migrating on ICAM-1 (2 µg/ml) alone (first bar, figure 4-10) had an average cell speed of 13.19 µm/min (blue), with retrograde flowing actin moving faster at 18.95 µm/min (orange) (figure 4-10), n = 200 cells per condition from 4 separate mice. P< 0.00001.

The conditions predicted to slow down cell migration successfully did so, through three separate mechanisms. Compared to cells migrating on ICAM-1 alone, cells treated with Cytochalasin D at 0.5 µM, a fungal compound that inhibits actin polymerisation, and cells treated with Manganese Chloride at 5 µM, which increases integrin affinity, both slowed down to around a third of the speed of migration (figure 4-10). A high concentration of ICAM-1 added to the plate (100 µg/ml) provided an intermediate case, where cell speed was both reduced to levels just above those of the Cytochalasin and Mn^{2+} treated cells.

In all three of the conditions, retrograde actin flow was decreased concomitantly with cell speed (figure 4-10). Notably, actin flow speed always remained much higher than cell speed: the percentage values above the bars in figure 4-10 show that in slowed down cells (treated with Cytochalasin, Manganese, or a high dose of ICAM-1) there was still an average actin speed of around 14 to 18 µm/min that was 192 %, 239 %, and 91% higher than the cell speed (3 to 7 µm/min) respectively. The conditions predicted to speed up cell migration also successfully did so. Adding CXCL12 (150 ng/ml) to cells, or using mouse cells deficient for PTPN22 led to faster cell migration, which was also coupled to faster actin retrograde flow (figure 4-10, right hand bars) . The percentage difference between the speed of actin and the speed of the cell was much reduced in comparison to untreated cells and slow cells: here the percentage increase from cell speed to actin speed was only 36 and 27 % respectively.

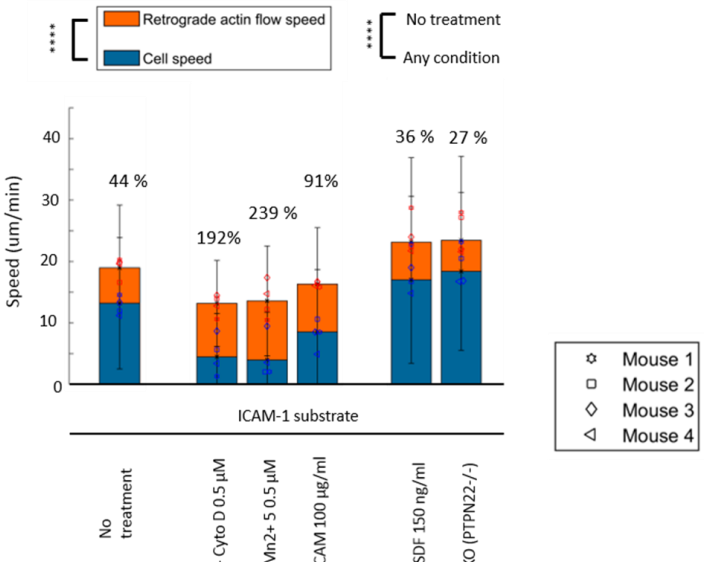

Figure 4-10: **Retrograde actin flow from STICS analysis of cells with chemically modulated cell speeds. P**lot showing median cells speeds (blue bars and blue symbols for each mouse) and actin speeds (orange bars and orange symbols for each mouse) for each condition. Percentage values = percent increase actin/cell speed. n = 4 mice, 50 cells per mouse, 200 cells per condition. ****P<0.00005

Anterograde flow speeds (figure 4-11) followed the same trends as the retrograde flow. Cell slow down conditions - Cytochalasin D and Mn^{2+} treatments - resulted in slower anterograde flow speeds ($p<0.0001$). High plate bound ICAM-1 concentration resulted in an intermediate set of flow speeds, matching an intermediate cell speed, whereas conditions in which cells sped up – CXCL12 addition or PTPN22 deletion – caused a speed increase in the anterograde actin flow network ($p<0.0001$).

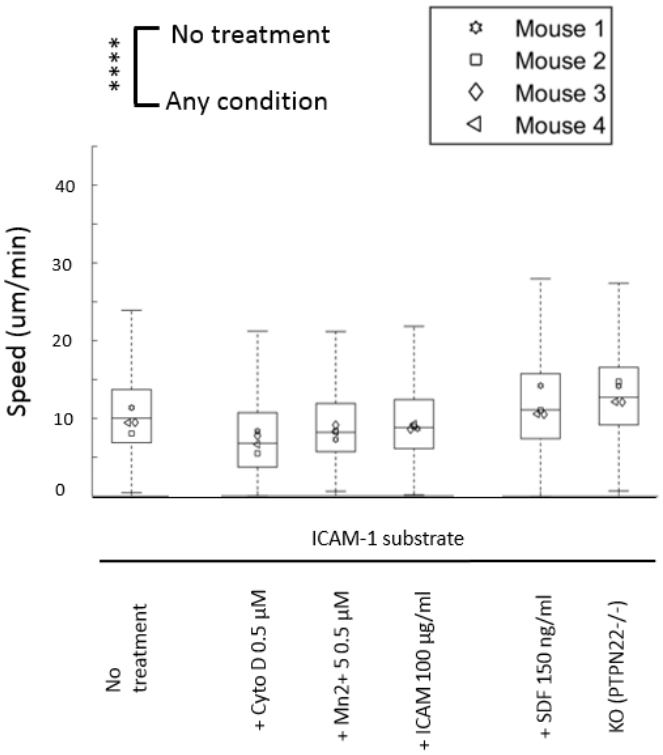

Figure 4-11: **Anterograde flow from STICS analysis of cells with chemically modulated cell speeds.** Plot showing anterograde actin flow speeds for each condition. n = 4 mice, 50 cells per mouse, 200 cells per condition. ****P<0.00005

4.3.1 Actin flows at a similar speed in all membrane proximal regions

By drawing a flat line at the front of the cell and calculating the distance each flow vector is from this line (top right hand panel where the constant region of interest is shown in pink, figure 4-12), the actin flow speed could be calculated as a function of distance from the leading edge/front of the migrating cell (detailed in methods and in section 4.3). Graphs in figure 4-12 are derived from one experiment (n = 20 cells per condition) and are representative of four separate experiments. Error bars represent interquartile ranges and

bars are median speed values of vectors within a given distance bin (0 to 10 %, 10 to 20 % etc).

Here, anterograde flow was localised to the cell front only: not exceeding 30 % distance into the cell in most conditions (blue bars, figure 4-12). The proportion of anterograde vectors did not change to a large extent between conditions (a,b an c in figure 4-12), indicating that all cells, no matter their migration speed, have a proportion of anterograde flow that is detected using this system at the cell front.

This is coupled to actin retrograde flow that appears to be at the same level of speed, with some fluctuations, throughout the cell (red bars, figure 4-12). There is no apparent change in this distribution for actin retrograde flow throughout the cell in any of the slow down

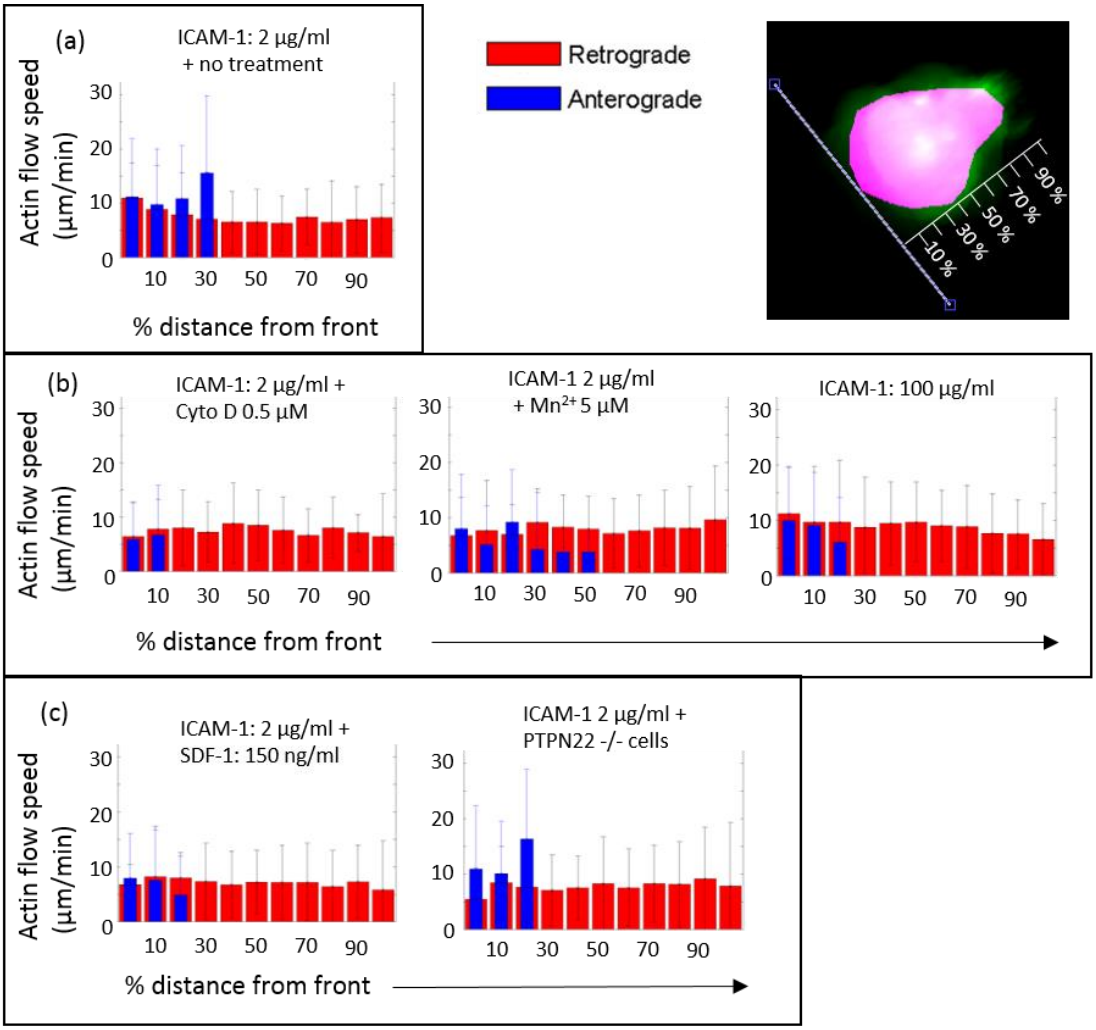

Figure 4-12: **Anterograde and retrograde actin flow plotted as a function of distance from the cell front maintain their flow speeds.** A through c) retrograde actin speed (red) and anterograde actin speed are plotted against distance from a line drawn at the front of the cell (shown in panel – top right), in cells migrating on ICAM-1 left untreated (a), treated with slow down conditions Cytochalasin D 0.5 µM, Mn^{2+} 5 µM, or high [ICAM] 100 µg/ml (b) or treated with CXCL12 150 ng/ml or in cells deficient for PTPN22 (c).

conditions (cells treated with 0.5 µM CytoD, 5 µM Mn^{2+} or 100 µg/ml plate bound ICAM-1) or the speed up conditions (150 ng/ml CXCL12, or cells deficient for PTPN22 migrating on ICAM-1).

4.4 Actin engagement increases as cell speed decreases

In order to extract a measure of how much actin was engaged to adhesions, the immobile fraction was measured in the external reference frame. In this reference frame, actin attached to adhesions appears stationary as T cells move over stationary adhesions to translate retrograde actin flow into forward cell movement. The amount of immobile actin is therefore a proxy measure for actin engagement with adhesions. As this measurement was carried out on the same cell data (n = 4 mice, 200 cells per condition) as analysed in figure 4-10, but the analysis is done in a completely separate way (as described below) results can be treated as complementary to the actin flow data provided by using STICS. To extract the number of pixels that contained immobilised actin, actin in cells was imaged in TIRF and a temporal Fourier transform was taken of the fluorescence image series in the original external reference frame (figure 4-13a). Figure 4-13a shows the same example cell as in figure 4-9, in the external reference frame and therefore moving forwards in the field of view.

By measuring the percentage of the pixels in the image that contained immobile actin (criteria: > 50 % of pixel intensity immobile over the period of the 5 second analysis window), cells migrating on ICAM-1 (2 µg/ml) displayed around 70 % of their pixels to contain immobile F-actin (Figure 4-13b). Slower cells, such as those treated with Cytochalasin D or Manganese (and to an intermediate extent, the high ICAM-1 100 µg/ml condition) had significantly increased percentages of pixels displaying immobile actin (figure 3b) $p<0.00001$. Cells migrating faster, such as those treated with CXCL12 or those cells deficient for PTPN22 had significantly lower percentages of pixels containing immobile actin (figure 4-13b) $p<0.0001$.

Figure 4-13c shows that in all conditions, and within single cells, the fraction of pixels in which actin was immobile in the external reference frame was inversely correlated to cell speed (r values for correlation shown in table, figure 4-13c) $p < 0.0001$. The slow cells (treated with Cytochalasin, Mn^{2+} or high ICAM-1) displayed a much weaker inverse correlation to immobile/engaged actin than fast migrating cells (CXCL12 treated or PTPN22 deficient), as detailed in the table containing spearman's r values between the percentage of pixels containing immobile actin and the cell speed

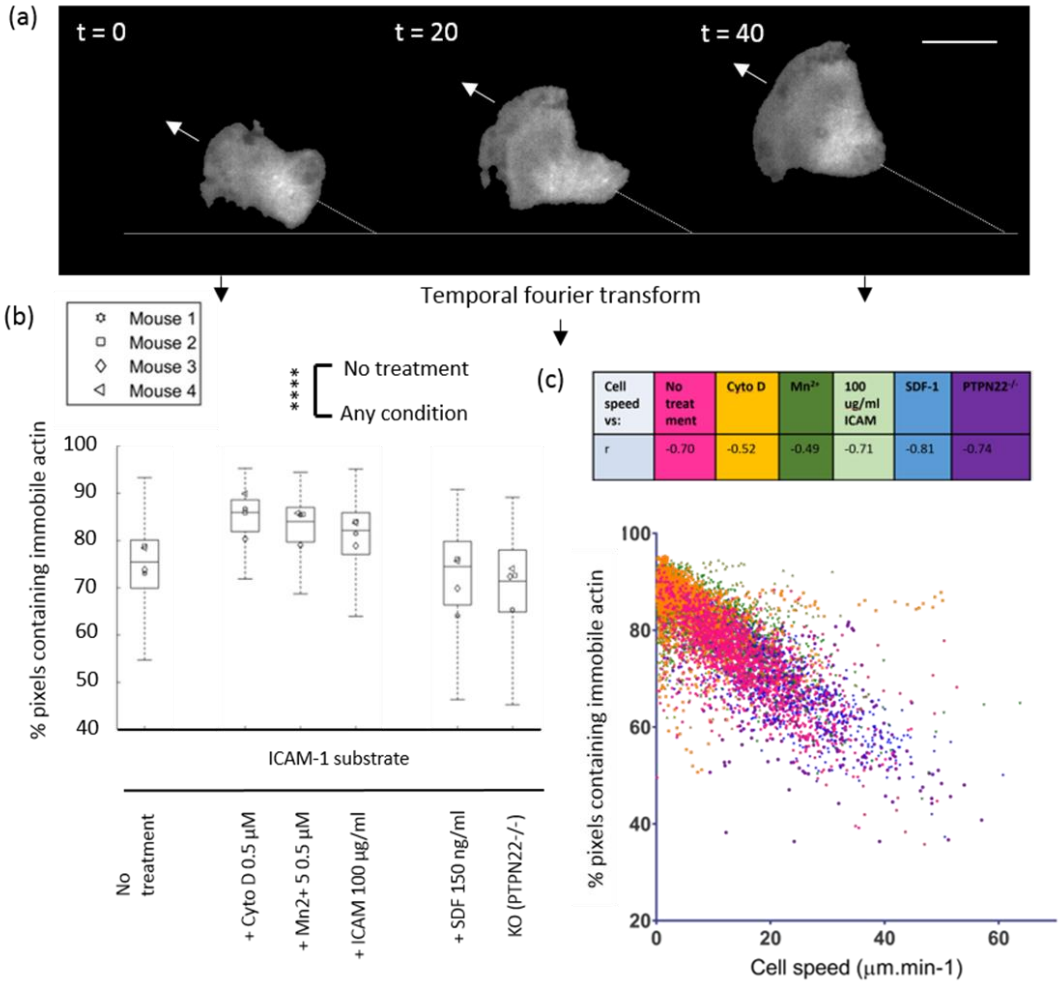

Figure 4-13: **Percentage of pixels containing immobile actin is inversely correlated to cell speed.** a) Still from a TIRF movie (external reference frame) of laGFP in a migrating T cell. White arrow = direction of migration. Dashed white line shows displacement in the external reference frame. b) plot of percentage of total pixels containing > 50 % immobile actin for each condition. c) plot of percentage pixels containing immobile actin versus individual cell speeds. Individual conditions are colour coded in the table, their spearman's r values listed.

4.5 Discussion of actin flow and engagement

Migrating T cells use constantly polymerising actin and nascent fibre unbending to push the membrane forward at the cell front[38], and myosin II to pull the fibrous structure backwards through the cell[44,183,192,195]. Adhesion to immobilised ICAM-1 through integrin LFA-1 links to the retrograde flowing network and generates torque moving the cell forward. The aim of this section was to quantify the relationship between migrating T cell velocity, generated via LFA-1 adhesion to ligand ICAM-1, and the intracellular flowing actin network.

Overall I concluded that; 1) T cell speed can be modulated through inside-out and outside-in integrin signalling and inhibiting actin polymerisation; 2) the rate of anterograde and retrograde actin flow correlate with T cell speed; 3) the proportion of immobile and engaged actin is inversely proportional to T cell speed; 4) the fastest moving T cells are more efficient at translating moving actin into T cell velocity.

It was important in to ensure that this was a study of the effects of the treatments on cell migration, and not simply a study of the aberrant effects of complete actin polymerisation shut down (in the case of cytochalasin D), affinity overload (in the case of Manganese) or ICAM-1 saturation (at raised ICAM-1 concentrations). All of these treatments (apart from PTPN22 knockout) were therefore subject to titration gradients to ensure that the majority of cells on a population level (within a field of view on a microscope slide) were 1) affected by the treatment and 2) remained polarised and migrating, albeit with altered migration speed.

By filtering vectors based on their angle relative to the direction of the migrating cell (see methods), I was able to separate and measure anterograde versus retrograde flowing actin. Anterograde flow represents forward flowing actin close enough to the coverslip to be detected in the TIRF excitation zone of 100 to 150 nm. In figure 4-12, where actin flow speeds are plotted as a function of distance into the cell, we see that anterograde flow and retrograde flow are by no means mutually exclusive at the front of the cell, and in fact make up a mixed network, as reported in other migrating cell types[35,169]. In addition, we see in my data that almost all of the anterograde flow is present in the front of the cell, the so called arp2/3 rich ‘leading edge’, and not in the formin driven middle ‘focal zone’. Data presented here provides extra delineation between the lamellipodia and the focal zone/lamella, due to the existence of anterograde actin flow exclusively in the lamellipodia and not in the lamella.

This type of flow also scales with cell speed, similarly to the retrograde actin flow, suggesting that what this it represents is newly polymerised f-actin that is pushing the cell membrane

forwards (figure 4-14). This is indicative of a continuous engine of actin flow in migrating T cells, composed of anterograde polymerised actin and retrograde pulled actin which scale together to dictate possible cell speed. Data presented in this section show that anterograde flow is as related to cell speed as retrograde flow. One possible explanation for a mixed population of antero/retrograde actin in the leading edge could be that polymerising/unbending actin is pushing the cell forward at a slightly raised z height as compared to actin that is treadmilling backwards underneath it (figure 4-14). Alternatively, or cooperatively, rearrangement of the arp2/3 based branching network in the leading edge may serve not only to push the cell membrane forwards, but also to rearrange adhesion proteins in the membrane through corralling[209], or to recruit complexes or to aid in recycling[210] – it could be this portion of actin that is manifesting as anterograde in my data. To address whether anterograde flowing actin is moving on a different plane in the cell to retrograde cortical actin would require a z stack with no more than 1 second time intervals between frames, with high enough resolution for further analysis of the slices using a STICS like software compatible for 3D: an example of such a system would be the 'lattice light sheet'[211] available at the time of writing at Janelia farm research centre.

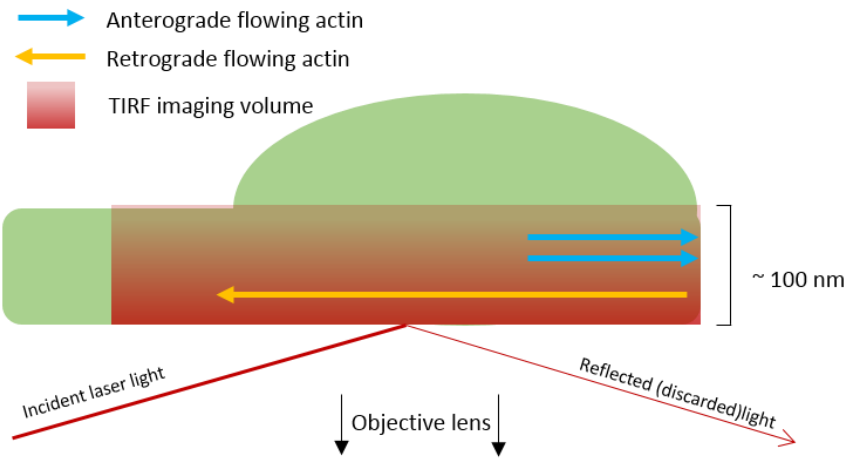

Figure 4-14: **Newly polymerised actin pushes the cell membrane forwards, while cortical actin is pulled backwards through the cell.** Both forms of actin are captured in the 100 nm TIRF imaging volume.

Modulation of inside-out/outside-in signalling

I was able to quantitate changes in the actin flow and proportion of adhesions formed under conditions known to slow T cell velocity; 1. by blocking F-actin polymerisation, 2. increasing integrin affinity and 3. Increasing ICAM-1 ligand density on the plate. In these cases, data

presented in this section showed that these cells moved slower, actin retrograde and anterograde flow was slower but immobile, engaged actin was increased.

Effects on cell speed were predicted and manifested as expected: Cytochalasin D is a fungal compound that caps barbed ends slowing actin polymerisation. Actin polymerisation is required to generate bent fibres that can push the membrane forwards in the lamellipodia, and to elongate straight fibres in the lamella which are pulled backwards by Myosin 2, therefore reducing the speed of retrograde and anterograde flow, as seen here. Engagement of actin with adhesions was increased, which suggests that the longer dwell time induced by slowing down actin flow increased the time spent bound to each adhesion.

Manganese ions bind to the I domain of the LFA-1 dimer, inducing a high affinity form of the molecule. Manganese ion binding results in not only the induction but also the maintainence of high affinity integrin, which may increase the lifetime of otherwise dynamic attachment and de-attachment of LFA-1 to ICAM-1 within adhesions – one possible reason for the speed decrease and increased actin engagement seen here. In addition, these effects could be compounded by the homogenisation of an optimised system of mixed affinity integrin. It is known that integrin affinity is zonal – more is available in the focal zone than the leading edge of T migrating cells[34], and that high affinity integrin signals differently and may develop into a mature adhesion with the association of other proteins. If affinity induced adhesion maturation happens cell wide due to the addition of Manganese ions, and is no longer zonal, this could result in the slowdown of actin flow cell velocity and increased engagement seen here.

The two cases could be compared to adding snow tires to a car (high affinity integrin) versus slowing down the engine by changing to a lower gear. In the first case the car (the cell) moves slower because of increased friction/contact with the road and the engine necessarily slows down (the actin flow), and in the second case the car slows down because the engine is directly slowed down, itself inducing longer dwell times of the tires at any one fixed point on the road.

Increasing the density of ligand ICAM-1 was expected to more fully saturate membrane LFA-1 binding points and potentiate its avidity, increasing adhesion. Data presented here exhibited an intermediate (significant) reduction of T cell velocity and actin flow speed. This suggests that cells require a greater impetus than simply high ligand density to stop during crawling type migration (as a precursor to diapedesis for example). Under these conditions, actin

engagement increased (again – to an intermediate level), which would be expected with more adhesions available due to a greater density of ICAM-1 on the plate: [33]

In all 3 cases (Cytochalasin D treatment, Manganese treatment and increasing ligand concentration on the plate) actin flow decreased but remained at a level ~ 3 x cell speed, suggesting that there is a large proportion of unengaged flowing actin. This could represent a lower limit of actin flow speed, and that the engine continues to run even where there aren't dynamically signalling active adhesions to bind to. This lower limit suggest that that it is the complexity of the linkage: the status of the regulatory kinases[37,43,93] and structural proteins associated with the adhesion[72,197,212,213], that dictates the tenacity of the clutch and therefore the cell speed. How closely the regulation of nano-clusters in T cells matches the regulation of nascent adhesions in non-leukocytes[78] is an open question.

I was also able to quantitate changes in the actin flow and proportion of immobile adhesions formed under conditions of fast T cell migration facilitated by 1. adding chemokine CXCL12 or 2. deleting the SRC and SYK family phosphatase PTPN22. In both cases, cell speed was increased, actin retrograde and anterograde flow was increased and actin engagement measured by its immobility in the external reference frame was decreased.

CXCL12 signalling is a known regulator of integrin clustering, integrin affinity and actin flow. Binding to the CXCR4 receptor releases its Gi and Gs proteins, activating multiple signalling pathways including those related to integrin LFA-1 driven migration, driven by Ras/Zap70 complex formation which upregulated Erk1/2 activation[7]. Erk is known to be associated with focal adhesions and nascent adhesions in many cell types as well as the motor phase of lamellipodial advance[214–217]. CXCL12a signalling leads to activation of key proteins involved with coordinating actin flow and engagement to integrin such as WASP, Cas, Nck, and FAK[218]. Addition of soluble CXCL12 is thought to induce transient microgradients across cells, which have been shown to only require a 10 % difference in concentration across the cell for these pathways to be activated[22]. Data presented in sections 4.2.2 and 4.2.3 can therefore be put into context, where the end result of CXCL12 signalling is an increase in cell speed caused by strong but transient attachment to adhesions (reduced actin engagement), coupled to a cooperative increase in the speed of the actin engine (both anterograde and retrograde flow).

PTPN22 is a cytoplasmic phosphatase known to negatively regulate SRC and SYK family kinases. In migrating T cells it has been shown to negatively regulate previously identified targets Lck and Zap70, common to the CXCL12 described above. Activated human T cells expressing a 'loss of function' mutant form of PTPN22 and murine activated Ptpn22$^{-/-}$ T cells

have increased adhesion under conditions of 0.5dyn.min shear flow and have elevated levels of actively phosphorylated ERK1/2 after migration over immobilised ICAM-1[67]. In the absence of PTPN22, phospho-394 Lck is increased[67] which is known to phosphorylate FAK within adhesions[68]. This added to the fact that PTPN22 deficient cells have reduced phospho-Vav1, a RhoGEF known to signal via the WASP/WIP complex[88] to regulate actin suggests a possible explanation for the results seen here, where actin engagement is decreased suggesting more transient binding to small adhesions regulated by Lck and FAK, and actin flow is increased due to increased signalling via phospho-Vav1 to the WASP/WIP/WAVE complexes[88], resulting in faster cell migration.

In all conditions, engaged actin was inversely correlated to cell speed. The correlation was more strongly negative in fast cells as opposed to slow cells, suggesting a decoupling in these cells of engagement translating to cell speed. When actin speed was analysed as a function of distance from the leading edge, the absence of large changes in the speed of the retrograde flowing actin in the leading edge compared to the focal zone suggests that it is the composition of the adhesions themselves, that changes the way actin interacts with adhesions within different zones and thus the speed of the cell. That the trends involving actin flow and engagement investigated here were the same between slow down, and speed up conditions, and that within conditions faster cells displayed less immobile actin as described above, suggests a common regulatory mechanism for slow down or speed up signals, which might exist within the adhesions themselves.

Data presented in this section provides evidence that actin flow is increased, but actin engagement with adhesions is decreased to facilitate cell speed increases in migrating T cells. It is known T cell migration dynamics are dependent on the density of adhesive ligands on the substrate, the microclustering of LFA-1 adhesion receptors on the cells[43,219], and the affinity of the receptors for the adhesive ligands[220–223], but due to the small size of T cell adhesions, study of their spatial arrangement has been limited until recently. To this end, we employed super resolution microscopy to study the effects on migration speed of integrin clustering in itself, and the link this has to actin engagement and flow.

Chapter 5: LFA-1 nano-adhesions

5.1 Preface

In the previous section, experiments revealed that actin engagement is inversely correlated with cell migration speed, and actin flow is positively correlated with cell migration speed, in single cells as well as across conditions in which cells migrate slower or faster. In this section, the link was investigated between actin flow and engagement and integrin based adhesions in migrating T cells – specifically, whether their nano-spatial arrangement in the membrane and in the membrane proximal zone is functionally important for T cell migration. Then, phosphorylated intermediates were used as proxies for integrin activity, to give more of an insight into the regulation of integrin nano-adhesions, that result in a particular cell migration phenotype. Due to the nanoscale nature of the molecular clutch, its ability to cluster in the membrane, and the many signalling molecules it has in common with focal adhesions, super resolution microscopy to localise single molecules was required, coupled with novel quantitation techniques to objectively discern clusters.

Specifically, we aimed to use the same battery of conditions that slow down or speed up migrating T cells, to find out whether they have an effect on LFA-1 surface integrin organisation.

Integrin nanoclusters are known to cluster in the membrane, and upon cell polarisation and migration, are known to adopt a regional affinity set up where higher affinity integrin is located in the focal zone[224]. Our first aim was to discern whether integrin membrane nanoclustering was also distinct in different regions of the cell.

5.2 Population level cell migration speed modulation

dSTORM microscopy relies on labelling a fixed sample with antibodies. Typically, dSTORM datasets here consisted of ~ 40 cells derived from millions of T cells isolated from 3 separate mice, and cells were chosen based on a qualitative assessment of a 'polarised' morphology, a phenotype known to be associated with cell migration. It was therefore necessary that close to 100 % of cells in a particular sample under a particular set of experimental conditions were migrating at the time of analysis, and not simply polarised but non-migrating. In order to address this problem, cell samples cultured under different speed modulating conditions were split into two: one set of the same cells were subject to phase contrast microscopy at 10 x magnification for cell tracking, while the other set were fixed and analysed by dSTORM microscopy. Multiple large fields of view meant that around 1000 cells were imaged migrating for each condition.

In order to ensure that all cells were tracked in the field of view, and to make the analysis of such large numbers of cells feasible, we adapted a cell tracking program using the modular programming algorithm and active contours in Icy[225]. Various thresholds and filters were applied to the raw phase contrast movies in order to achieve a binary image composed of cell masks (detailed in methods and section 3.4).

The binarised cell images were then analysed using the 'active contours' module which maintains an outline around each cell[225]. The maintained outline means that where two cell outlines meet, during a cell-cell collision for example, they are not allowed to merge into one cell, remaining separate at all times. Boxes are coloured arbitrarily, and denote migrating cells undergoing tracking. Crucially, the program also begins a new track each time there is a collision: this avoids measuring the effects of artificial slow downs due to cell collisions, allowing correlation of this work with the actin flow measurements, in which only single, non colliding cells were analysed.

To ensure that only migrating T cells were being tracked, object size filters were applied to cut out fast moving debris derived from any remaining dead cells to the data. Using a 20 pixel size filter, which is supplied as an area of a polygon composed of 20 square pixels each of length 0.88 µm, corresponding to a 15.488 μm^2 maximum area, debris was filtered out and all migrating cells tracked. This initial size was chosen due to the average size of a polarised migrating T cell, which is at least 8 µm in length and 3 µm in breadth = 30 µm^2[225]. Example

images where dead cell debris (blue arrow) is clearly removed through use of this filter are shown in figure 5-1.

In order to verify that the automatic tracking was working correctly, the same field of view was tracked manually and automatically. Manual tracking was carried out using an existing

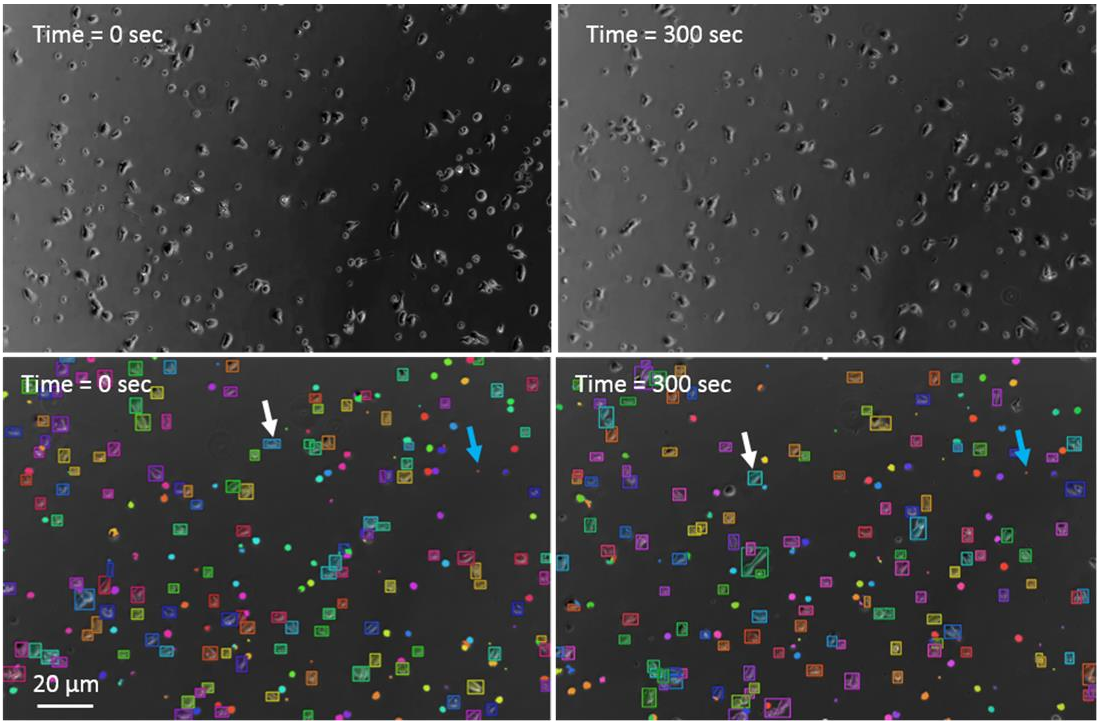

Figure 5-1: **Phase contrast movies and automatic tracking stills.** Boxes denote cells undergoing tracking,. The white arrow denotes a cell that has been tracked, and the blue arrow a piece of debris that has been ignored.

imageJ plugin (https://imagej.nih.gov/ij/plugins/track/Manual%20Tracking%20plugin.pdf), which works through use of a computer mouse to identify the centre of each cell in each frame of the phase contrast timelapse movie (figure 5-2a, left hand panel and spider diagram corresponds to manually tracked cells and right hand side to automatically tracked cells). Spider diagrams, where each cell track is centred to a single point of origin, show visually that displacement of the cells was similar (figure 5-2b). The quantitation of cell speeds confirms that the average cell speed from automatic tracking matches the average cell speed for manually tracked cells. Many more tracks (n = ~ 500 per FOV) are detected by the automatic tracking program, due to a new track being started each time there is a cell cell collision (figure 5-2). Automatic tracking was faster and less prone to human error, therefore this method was taken forward for further experiments and analysis of cell speeds under a battery of 'slow down' and 'speed up' modulations.

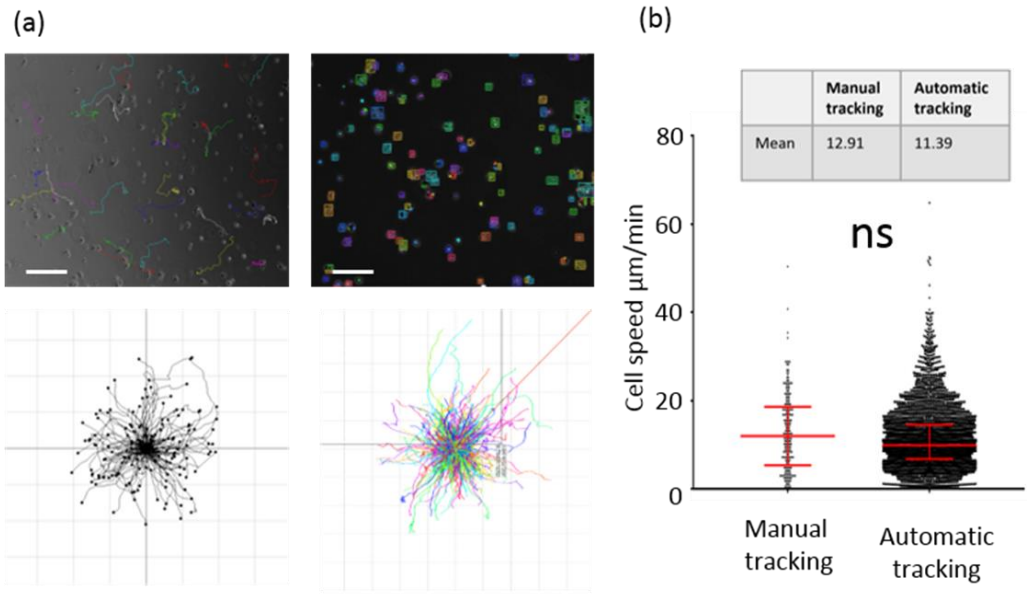

Figure 5-2: **Automatic tracking compared to manual tracking for cell speed.** a) example timelapse movies of manually tracked cells and corresponding spider diagram where tracks are centred on a single point of origin (left) and the same for automatically tracked cells (right). b) plot showing cell speeds for manual tracking and automatic tracking. Scale bar 50 µm.

~1000 cells were imaged and analysed under each condition. Representative final frames from a series of fields of view are shown for each condition in figure 5-3a. Spider maps of displacements centred on a single point of origin show clearly that cells treated with either Cytochalasin D at 0.5 µM or Mn^{2+} ions at 5 µM were reduced. High ICAM-1 (100 µg/ml) conditions appear to be indistinguishable in terms of displacement compared to the 2 µg/ml condition. In contrast, where CXCL12 is added to cells at 150 ng/ml, or when cells deficient in PTPN22 are evaluated, cells move noticably further (figure 5-3b). Cell speed quantification confirms that the batches of cells used for the dSTORM experiments in the next section were indeed affected by the treatments in the expected manner. Untreated cells migrating on ICAM-1 migrated at a median speed of 10.13 µm/min, whereas Cytochalasin D (0.5 µM)and Manganese (5 µM) caused an extreme slow down of cells (6.67 µm/min and 7 µm/min respectively), high ICAM-1 concentration (100 µg/ml) an intermediate slow down (8.92 µm/min), and CXCL12 addition (150 ng/nml) or PTPN22 knockout caused a statistically significant speed up (11 µm/min and 11.06 µm/min respectively (figure 5-3c).

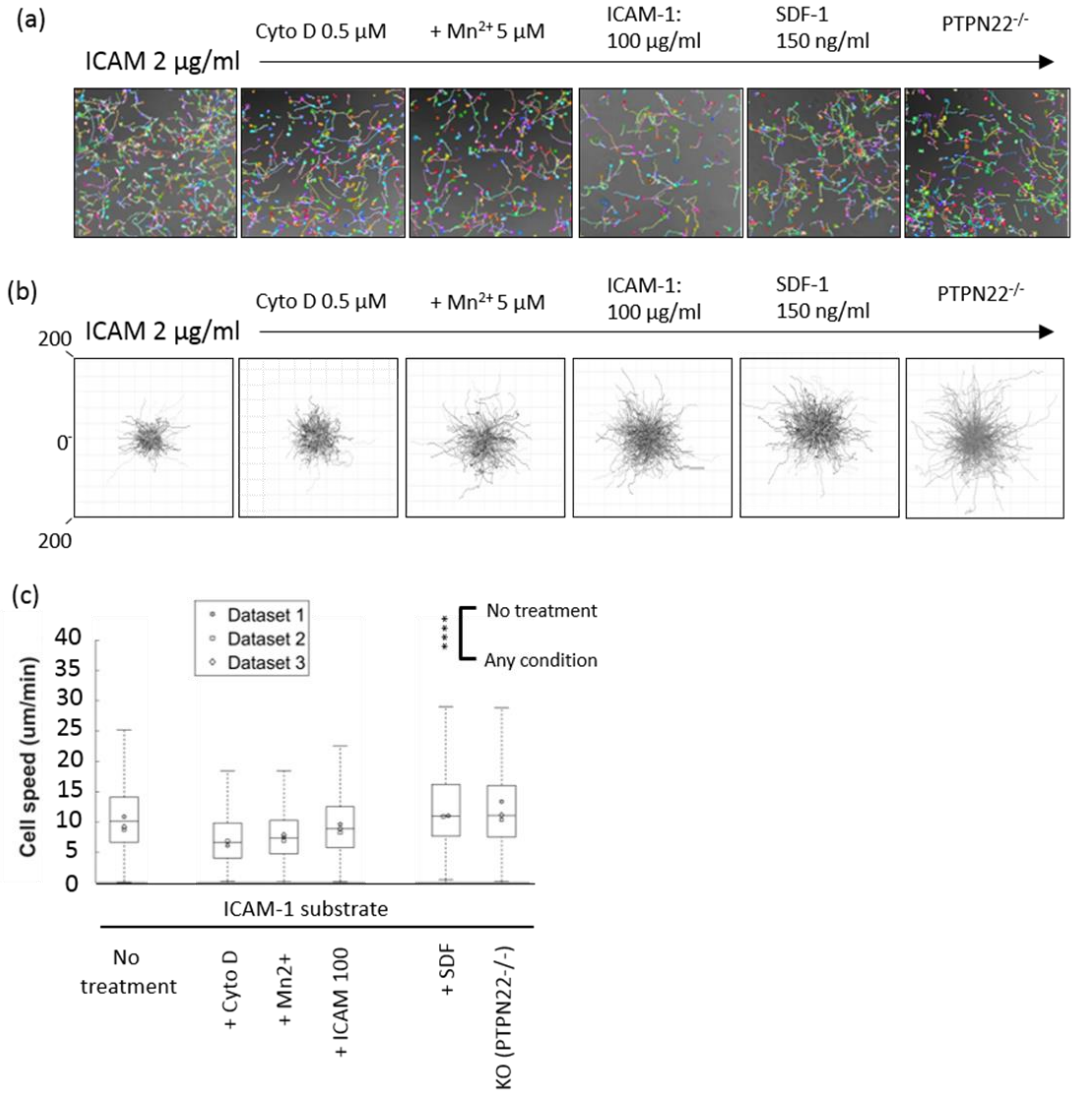

Figure 5-3: **Cell speeds derived from automatic tracking for migrating cells using in STORM experiments.** a) example tracked cells for each condition. b) example spider diagrams for each condition. c) box plot showing median cell speed under each condition with interquartile range. n = ~500 cells per condition from 3 mice. *** P<0.00001.

Having received one of the treatments described, sample tubes containing cells were split in two, where half the population were imaged by phase contrast microscopy and tracked to give the results above, and the other half were fixed and stained to be imaged by STORM microscopy. This correlative approach ensured that in the following experiments, cells imaged by STORM had been affected by the treatments consistently and on a population level, so that integrin clustering as a consequence of these conditions could be reliably investigated.

5.3 Membrane LFA-1 integrin clustering

The advent of super resolution localisation microscopy has allowed us to interrogate programs of nanoclustering behaviour that were previously hidden behind the diffraction limit of light. Previous work identified functionally relevant microclusters in T cells [212], but also pointed to the fact that each diffraction limited 300 to 500 nm microcluster could in fact contain thousands of molecules. To interrogate this, localisation microscopy (STORM)[115] affording sub 20 nm resolution (measured by Thompson's uncertainty[125]) was coupled to new cluster quantitation techniques that reduces human decision making. After identification of clusters, metrics were extracted on individual cluster size and density, as well as three parameters normalised to 2 μm^2 regions: the number of clusters, the total number of molecules, and the percentage of molecules participating in clusters.

In common with other fluorescent microscopy techniques, STORM requires the targeting of molecules of interest using fluorescent probes bound to antibodies. In order to ensure correct targeting, and reduce artefacts related to antibody size and number of fluorophores, directly conjugated antibodies were used (detailed in section 3.3). Two monoclonal antibody clones reported to target the native state extracellular domain of LFA-1 were tested here for their ability to target crosslinked LFA-1 presented after cell fixation. Antibodies were tested in non-permeablised cells which were imaged by dSTORM microscopy (figure 5-4). The 2D7 rat derived anti-LFA-1 monoclonal antibody provided a strong signal, whereas the M17/4 clone provided almost no signal. A non targeting 'isotype control' from the same species showed almost zero signal in this highly sensitive microscopy technique (dSTORM), indicating that there was almost no non-specific staining using this clone (figure 5-4).

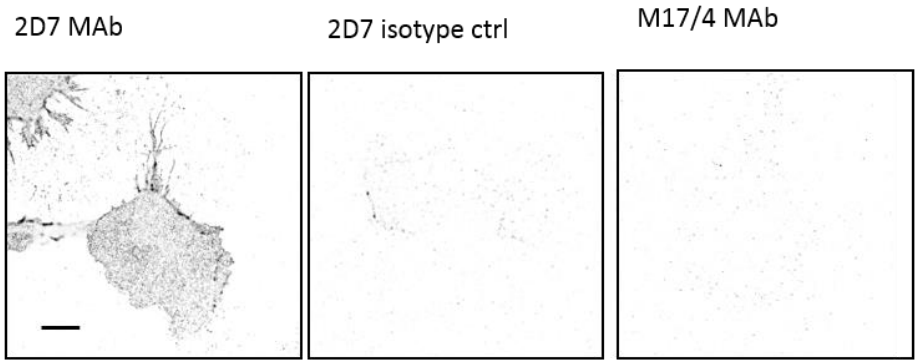

Figure 5-4: **The 2D7 antibody clone against LFA-1 showed widespread staining, the non-targeting isotype control showed no specific staining and M17/4 anti LFA-1 clone showed no specific staining**. N = 10 cells per condition. Scale bar 5 μm.

It was important for these studies, based on investigating the link between ICAM-1 engaged LFA-1, that initially only membrane LFA-1 was targeted, and not intracellular LFA-1. This is because while TIRF is ostensibly a 2D technique, actually a small 3D volume is imaged.. In this case, we wanted to study the nanoclustering of ICAM-1 engaged integrin in the cell membrane that may be contributing to forward cell migration (as has been carried out in human T cells)[67], therefore we wanted to limit the physical penetration of the LFA-1 targeting antibody. To probe this, cells were fixed using an optimised protocol (detailed in section 3.3) that limits the loss of membrane molecules, and cells permeablised with triton were compared with cells left unpermeablised prior to staining. Samples were stained for LFA-1 and imaged by confocal microscopy. Reconstructed z stacks through the volume of a representative cell preparation are shown in figure 5-5, in unpermeablised cells, staining was limited to the cell membrane (Figure 5-5a n = 20). In permeablised cells, LFA-1 staining is clearly seen throughout the cell (figure 5-5b n = 16).

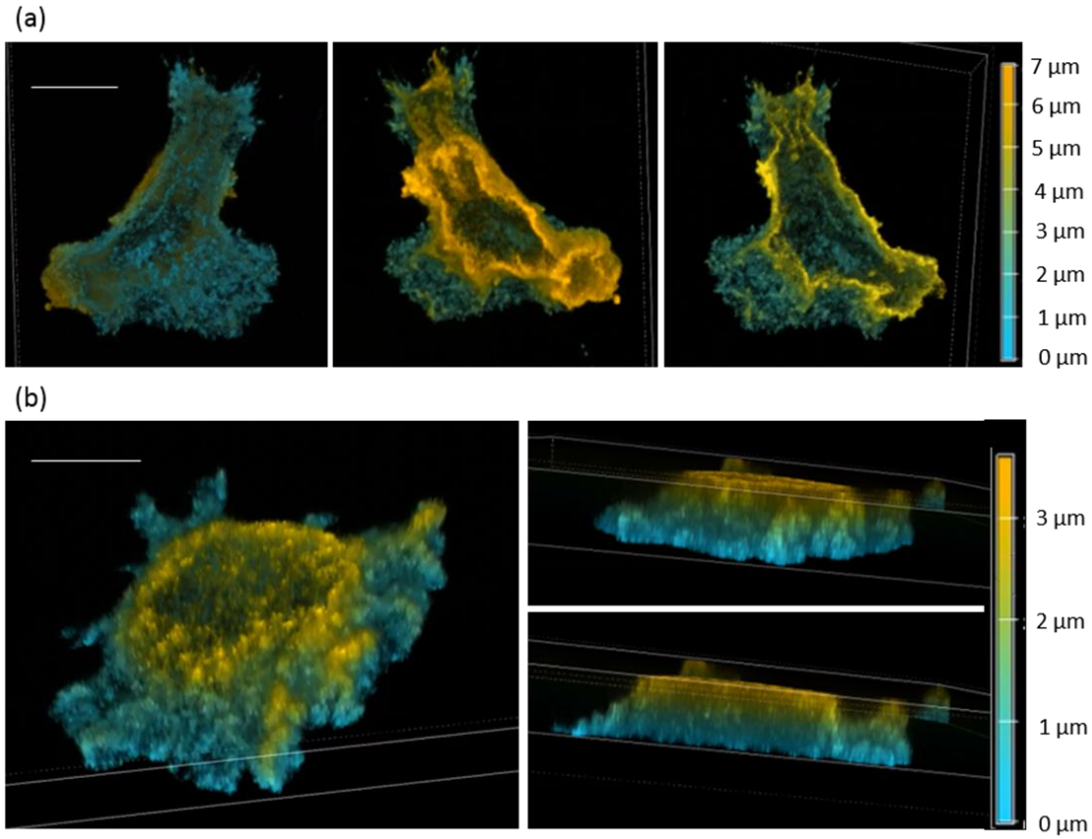

Figure 5-5: **Confocal 3D z stacks of non-permeablised and permeablised cells stained for LFA-1**. a) non-permeablised cells stained for LFA-1 – z dimension is pseudo-coloured as per colour bar. b) permeablised cells stained for LFA-1 and accompanying colour bar. Scale bar 5 µm.

After verification that the anti-LFA-1 antibody was targeting solely membrane LFA-1, cells were exposed to the battery of inside out and outside in signalling conditions characterised in

section 5.1 which speed up or slow down T cell migration. Each panel in figure 5-6 shows a representative pointillist localisation map of a single cell, containing 1000s of coordinates describing membrane LFA-1 positions. Below each cell image are example cluster maps from either leading edge or focal zone of the T cell membrane. Stationary cells simply plated on an uncoated glass coverslip appear round (figure 5-6a top left panel) and were compared with migrating cells plated on ICAM-1 at 2 μg/ml which are polarised and can be divided up into 'leading edge' and 'focal zone' (figure 5-6a top right panel) – regions that are distinct in terms of integrin affinity[34,65,224] and actin network composition and dynamics (Chapter 5). Cells plated on this immobilised ICAM-1 surface were exposed to either Cyto D 0.5 μM, Mn^{2+} 5 μM or a high concentration of ICAM-1 (100 μg/ml) to slow them down – cell speeds for these samples were shown in figure 5-6b. CXCL12 at 150 ng/ml was added, or PTPN22 removed (germline knockout) to speed cell migration (figure 5-6c). Fixed and LFA-1 stained cells imaged by dSTORM were analysed using a Bayesian cluster analysis algorithm (detailed in chapter 2) to reduce human decision making when identifying clusters[140,141]. Visualising the cluster maps, which show individual clusters differentiated using arbitrary colours, it is clear that T cells adopt a distribution of tiny nanoclusters, which are on a length scale that is < 100 nm and therefore smaller than nascent adhesions in other cell types (coloured panels in figure 5-6). Metrics were then extracted from these nanoclusters and are quantified in the next section.

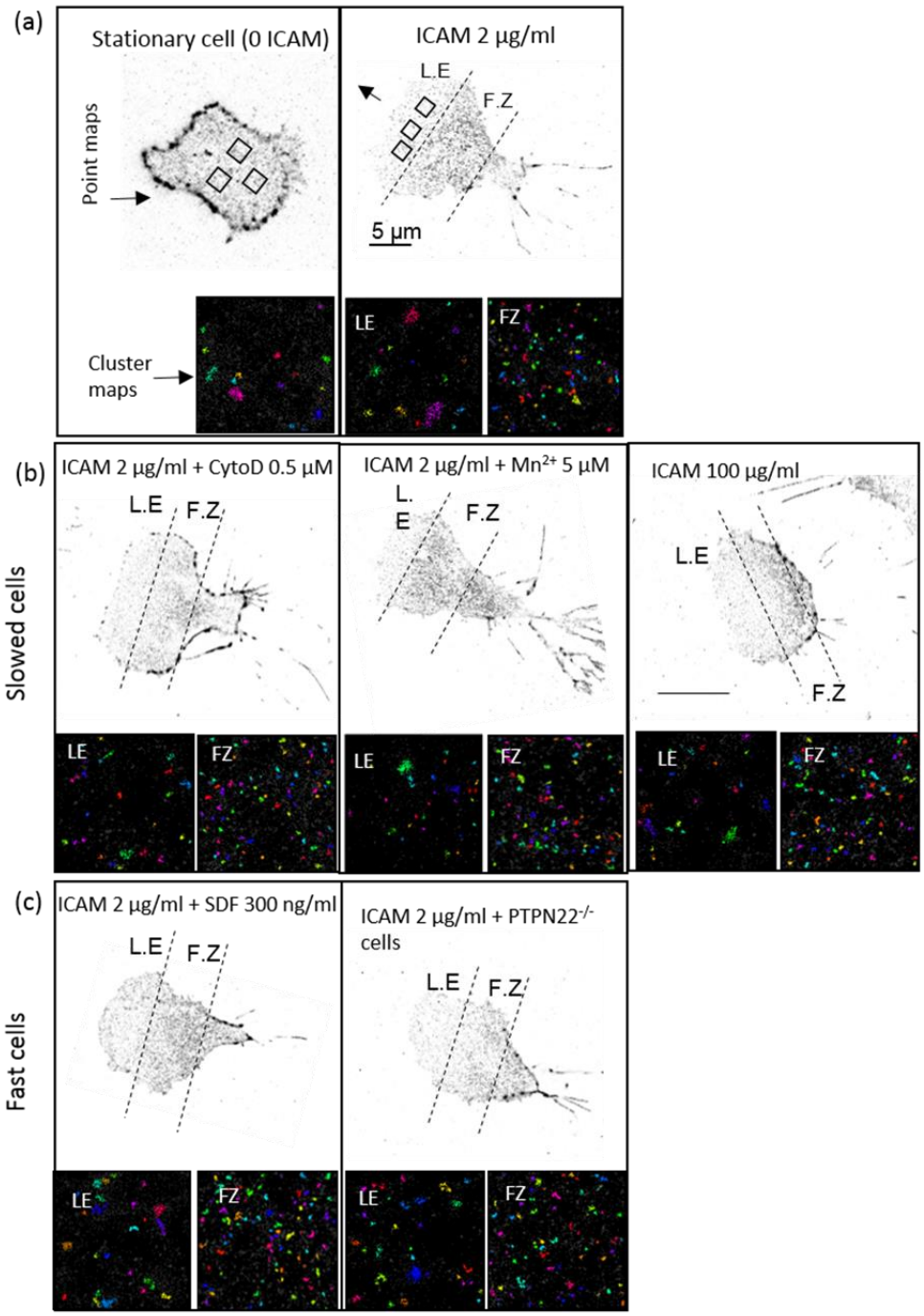

Figure 5-6: **Super resolution STORM images of membrane LFA-1 integrin in migrating effector T cells.** Each panel shows a single representative pointillist map of the integrin molecules detected by STORM, and cluster maps (black background) derived from Bayesian cluster analysis of 2 μm^2 regions selected from the leading edge and focal zone of polarised T cells. a) stationary cells (0 ICAM-1) (left) and migrating (2 µg/ml ICAM-1) with no treatment (right) are followed by conditions that slow cell migration (b) cytochalasin D 0.5 µM, Mn^{2+} 5 µM, high ICAM 100 µg/ml and conditions that speed cell migration (c) CXCL12 150 ng/ml and the use of PTPN22-/- cells.

5.3.1 Regionally distinct LFA-1 nanoclustering in migrating T cells changes to induce high speed migration

Cluster analysis of the leading edge and focal zone of migrating T cells was carried out and metrics were extracted on total molecules, percentage molecules in clusters and number of clusters. The transition from stationary cells (clear bars) to migrating cells (orange and blue bars) resulted in a redistribution of integrin nano-clusters, such that there were more molecules, a higher percentage of them were involved in clusters (a 2 fold increase, figure 5-7a) and there were more clusters (2.5 fold increase figure 5-7c).

Upon migration, while the total number of available LFA-1 molecules remained the same (figure 5-7a), the percentage of clustered molecules per region (figure 5-7b) and the number of clusters per region (figure 5-7c) were significantly increased.

The focal zone always has more clusters - at least twice as many - (figure 5-7c) and more molecules (figure 5-7a) as compared to the leading edge. The percentage of molecules in clusters is always reduced by ~ 15 % in the focal zone as compared to the leading edge, meaning there is more non-clustered LFA-1 in this region (figure 5-7b). These FZ/LE phenomena are constant across conditions, in all migrating cells.

Migrating cells displayed a high degree of regional discrimination in the clustering characteristics of LFA-1 in the focal zone as compared to the leading edge: clear from visualising representative cluster maps in figure 5-6 and in the quantitative analysis in figures 5-7 and 5-8. In the focal zone in all conditions where cells were migrating (blue bars in figure 5-7), there were more LFA-1 molecules (figure 5-7a) and more clusters within regions, meaning clusters were more closely spaced than in the leading edge (orange bars). While there were always more LFA-1 molecules in the focal zone, a large proportion of these were not participating in clusters: there was always a smaller percentage (~15 % reduction) clustered in the focal zone as compared to the leading edge. Therefore the focal zone (compared to the leading edge) has significantly more total LFA-1, a lower percentage clustered, and more clusters per ROI.

In comparing between conditions which slowed down the cells versus those that sped up the cells, the focal zone and leading edge maintained their regional differentiation. In ‘slow down’ conditions: Cytochalasin D or Manganese addition, or a high level of plate bound ICAM-1, there was no change in the total number of membrane LFA-1 molecules (figure 5-7a) or the number of clusters per region (figure 5-7c). The percentage of molecules in clusters (figure 5-

7b) described a slight but significant decrease in cell 'slow down conditions' (CytoD, Mn and ICAM-1 100 µg/ml).

In fast moving cells, there was a change in the percentage clustered in CXCL12 treated fast migrating cells, and a slight decrease in PTPN22 deficient cells as compared to untreated cells. In both CXCL12 treated and PTPN22 deficient cells, the differentiation in the percentage of clusters between the leading edge and focal zone was no longer present: the percentage clustered was the same in both regions.

Where cells had increased migration speed, as in CXCL12 treated cells or cells derived from PTPN22 deficient mice, the total number of molecules (bars on the RHS of figure 5-7a) and the

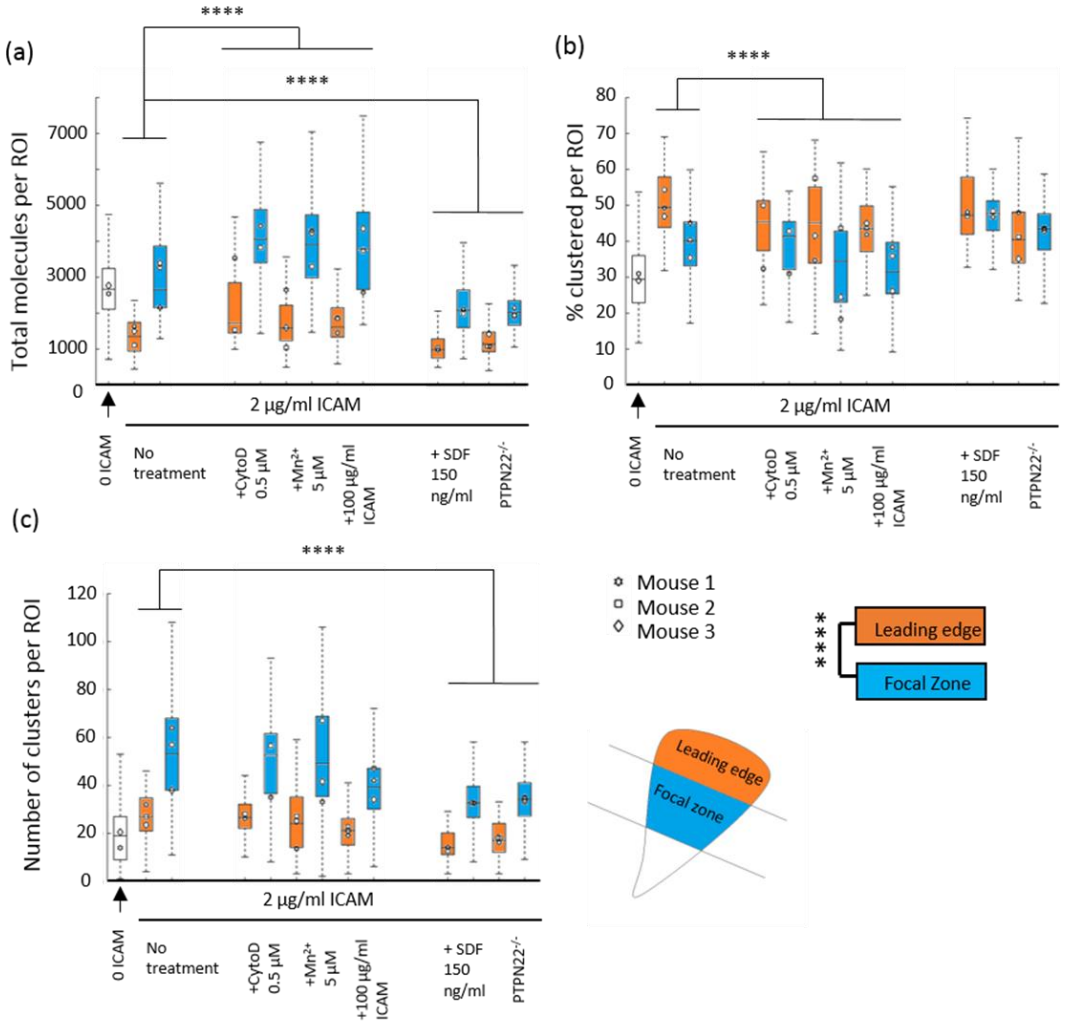

Figure 5-7: **Integrin membrane nano-clustering quantified in T cells treated with slow down or speed up signals.** In each plot, metrics extracted for stationary cells have clear bars, and migrating cells are split up into leading edge (orange bars) and focal zone (blue bars). From left to right, conditions proceed: 0 ICAM-1, then 2 µg/ml ICAM-1 on the coverslip with added Cytochalasin D, Mn^{2+} or high ICAM (100 µg/ml), then 2 µg/ml ICAM-1 with CXCL12 at 150 ng/ml or using cells deficient for PTPN22. Metrics extracted consist of a) total molecules per region, b) percent clustered per region, and c) number of clusters per region. (n = 350 ROIs and 40 cells per condition from 3 separate mice). ****p<0.00001

number of clusters (bars RHS figure 5-7b) were significantly decreased. The total molecules decreased by an average of 25 % percent (figure 5-7a), and the number of clusters decreased in fast cells by an average of 37 % in the leading edge and 35 % in the focal zone (figure 5-7c). The changes therefore occurred cell wide, and the cells maintained their leading edge/focal zone differentiation.

5.3.2 Individual clusters have different sizes and densities in the focal zone as compared to the leading edge

In conjunction with 'per ROI' metrics described above, clusters could also be discriminated based on their individual characteristics: namely their size (as measured by their radius) and their molecular content (the number of molecules per cluster). Taken together, any decrease in size with a maintained or increased number of molecules necessarily can be taken as an increase in cluster density. Figure 5-8 shows the quantitation for this.

Between stationary and migrating cells, a regional discrimination is very clear: clusters are smaller (average 14 % significant decrease) and contain more molecules (average 6 % significant increase)if they are located in the focal zone part of the cell membrane as compared to the leading edge (n = 350 ROIs and 40 cells per condition from 3 separate mice). This is maintained across all migrating conditions, whether the cells are moving faster or not (figure 5-8).

In slow cells, very discrete changes in the molecular density and size of clusters are present in both zones as compared to migrating cells. These are changeable across individual conditions, for example with Cytochalasin D addition, there is an increase in the number of molecules per cluster. This doesn't occur in Manganese treated cells but is replicated in cells migrating on a high concentration (100 µg/ml) of ICAM-1.

In fast cells (treated with CXCL12 or deficient for PTPN22), clusters become 25 % larger (figure 5-8a), with 23 % increase in molecular content (figure 5-8b) (n = 350 ROIs and 40 cells per condition from 3 separate mice). These are large percentage changes, but are extremely small on the nanoscale, equating to only a few nanometres and 5 to 10 molecules per cluster.

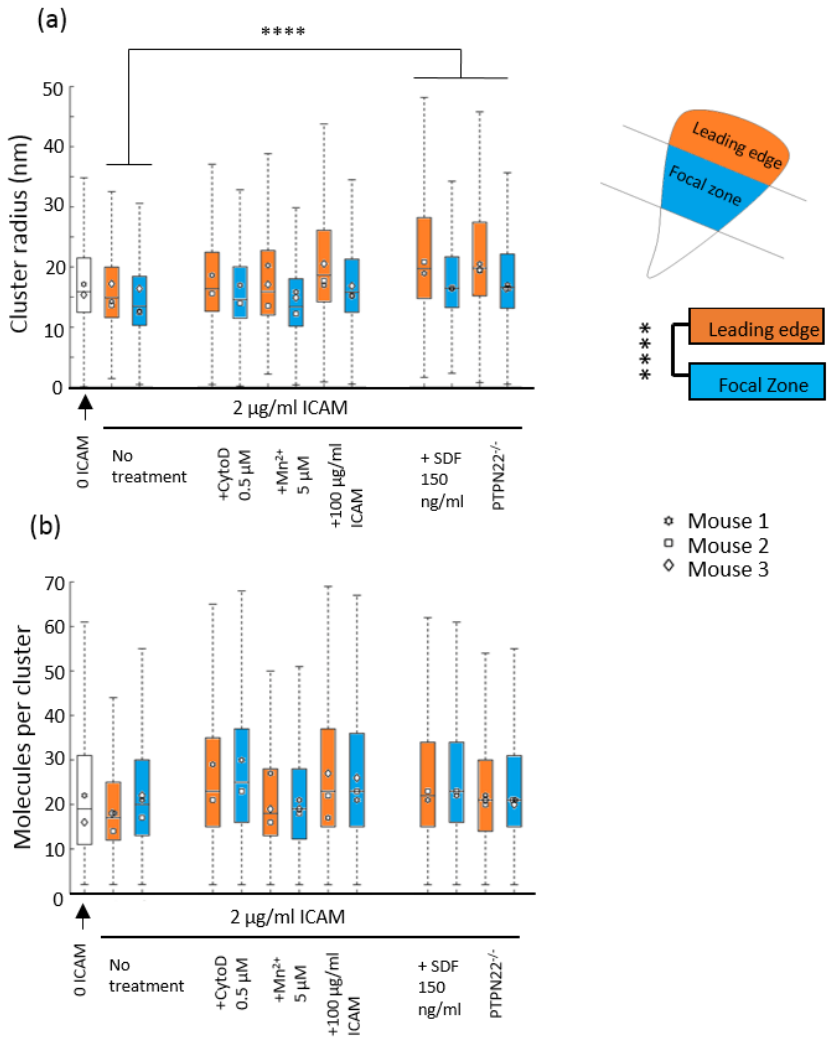

Figure 5-8: **Individual integrin membrane nano-clusters adopt a regionally discriminate size and density to achieve cell migration.** In each plot, metrics extracted for stationary cells have clear bars, and migrating cells are split up into leading edge (orange bars) and focal zone (blue bars). From left to right, conditions proceed: 0 ICAM-1, then 2 µg/ml ICAM-1 on the coverslip with added Cytochalasin D, Mn^{2+} or high ICAM-1 (100 µg/ml), then 2 µg/ml ICAM-1 with CXCL12 at 150 ng/ml or using cells deficient for PTPN22. Metrics extracted consist of a) cluster size measured as radius and b) molecules per cluster. (n = 350 ROIs and 40 cells per condition from 3 separate mice). ****p<0.00001

5.3.3 Discussion for 2D membrane integrin nanoclustering

The aim of these experiments was to assess first the existence, then the nanoscale characteristics of LFA-1 membrane nanoclusters present in migrating T cells when cells change their speed of migration. There were three main novel findings:

1. Nano-adhesions adopt different sizes, densities and closeness to one another

2. Smaller, denser LFA-1 nano-adhesions group together in the focal zone, whereas larger adhesions adopt a sparse distribution in the leading edge

3. Nano-adhesions become larger in faster moving CXCL12 treated and PTPN22 negative cells

Specifically here, an antibody targeting the extracellular domain was used to selectively label LFA-1 in the membrane of unpermeablised fixed cells (figure 5-5). This was important in the first instance because it is membrane LFA-1 that forms the basis of adhesions, by binding to ICAM-1 present in the extracellular environment. It should be noted that antibody labelling itself works on probabilities – steric hindrance[176,226]and binding affinities mean that only a subset of the target molecules will be bound. In addition to that, dSTORM is by definition a stochastic detection technique – only a random subset of the available fluorophores within the population of bound antibodies will emit enough photons to be localised successfully when the image is reconstructed[115]. What was made certain here, by use of multiple experimental repeats, was that the clustering metrics extracted were constant (replicable) within the same experimental condition. In order to assess a more complete picture of molecular clustering, many new techniques are in development, including smaller probes[177,227], live cell compatible super resolution multi-blinking probes[228–233], and many different kinds of quantitative algorithms[234,235]. Here, using primary antibody labelling, extracted metrics allow us to give relative answers that can be compared between regions of the cell, as well as between conditions in which cells move at different speeds on a population level. The metrics used here afforded us the required information to make clear conclusions regarding the total molecules, the percentage of clustered molecules, and the number of clusters: three interconnected parameters. In addition, conclusions are brought regarding the individual clusters: their radius and molecular content, when taken together, these measures can be considered one of density.

We find that there is clear LFA-1 nanocluster delineation between the focal zone and the leading edge – two regions of the migrating T cell that are already known to be distinct based on the selective affinity status of LFA-1[34,65,224], as well as in terms of the directionality of cortical actin flow as described in section 4 In all conditions regardless of cell speed, describing the focal zone in comparison to the leading edge, it had:

- almost double the amount of LFA-1 molecules

- A decreased fraction incorporated into clusters

- More clusters, that were more closely packed together (a twofold increase per area).

Taken together, this means that there is a greater population of free LFA-1 monomers in the membrane and more clustering in the focal zone as compared to the leading edge (shown in model, Figure 5-7).

Individually, cluster size and molecular content was assessed and also found to be regionally distinct across all measured conditions. Clusters were smaller and contained more molecules in the focal zone region compared to the leading edge. Nascent adhesions in other, less motile cell types are known to build their molecular content to develop into focal complexes/adhesions[35,75,81,192–194,236,237], whereas here adhesions become smaller and denser Most of this work has been done using diffraction limited microscopy: with super resolution, it is possible to see relative changes in size and molecular density, and it is using this that we see a novel set-up – T cells appear to concentrate their many tiny nano-adhesions on two length scales – larger nanoclusters get smaller and denser individually, as well as groups of clusters becoming more closely packed together (figure 5-9).

Cell speed increase elicits nanocluster modulation

Cells treated with CXCL12, or deficient for the PTPN22 gene, which codes for a phosphatase that would usually act as a negative regulator of integrin, migrate faster (Figure 5-2). Here for the first time we observe nanocluster modulations in membrane LFA-1: fewer molecules and fewer clusters, which are themselves larger, that correlate to cell speed increases in this system (shown in model, Figure 5-9). These two integrin signalling pathways act in different ways: CXCL12 binds to the CXCR4 GPCR[203] while PTPN22 would usually dephosphorylate Lck downstream of integrin activation[67,93]. Convergence of the CXCL12 pathway and the PTPN22 deficient pathway suggests downstream linkage between the two which results in changes in the spatial organisation of membrane LFA-1. Indeed, both conditions are known to result in an increase in pErk increased signalling and phosphorylation of the Src and Syk family kinases as well as FAK[67,204,206]. Experiments addressing the nanoscale colocalization of molecules common to the CXCL12 and PTPN22 pathways are described later in section 6.

While regional (LE/FZ) changes are clear, the radius and molecular content of clusters between slow down and speed up signals is less clearly defined using these measures and techniques. Interquartile ranges are large, describing great heterogeneity in the data, which consists of 1000s upon 1000s of clusters. Such vast heterogeneity present in these two

parameters are indicative of more regulation at work, and that the size characteristics of certain clusters on either edge of this distribution might be functionally important.

Here we are limited to looking at the median values, and more experiments are needed to assess the functional impact and possible significance of certain size and density classes of nanoclusters and their colocalization with other adhesion components: in other words, what it means to be a small, dense cluster, and why this affects cell migration. Secondly to assess whether the small but consistent (across three mice) increase in cluster size in the case of fast migrating cells is functionally relevant, a directly correlative approach is required, where clustering is measured in single cells of known speed.

One such approach is shown in section 6, where we adopt a new method – a correlative approach where clustering of multiple molecules of interest can be measured in single cells, whose speeds before the moment of fixation are known. In these experiments, a multiplexed staining approach allows for super resolution of pYFAK and pY416 Src (targeting Lck and Fyn in the case of T cells), which are used as proxy measures for different stages of integrin cluster activation. The characteristics of marked 'active' clusters are assessed.

In addition to the role of LFA-1 in the cell membrane, the membrane proximal intracellular population is also likely to be functionally important for cell speed during migration. A T cell moving at 10 µm/min that is around 10 µm in length necessarily forms new adhesions that go through their lifespan in a maximum of 1 minute. Therefore the role of integrin recycling, and the characteristics of the membrane proximal population are likely to be significant for cell migration. To begin this investigation, we wanted to find out whether LFA-1 integrin 1) formed nanoscale arrangements intracellularly, as well as in the cell membrane, 2) was similarly regionally distinct in any said arrangements between the leading edge and focal zone and 3) whether such arrangements are functionally important in any of the conditions that change cell speed.

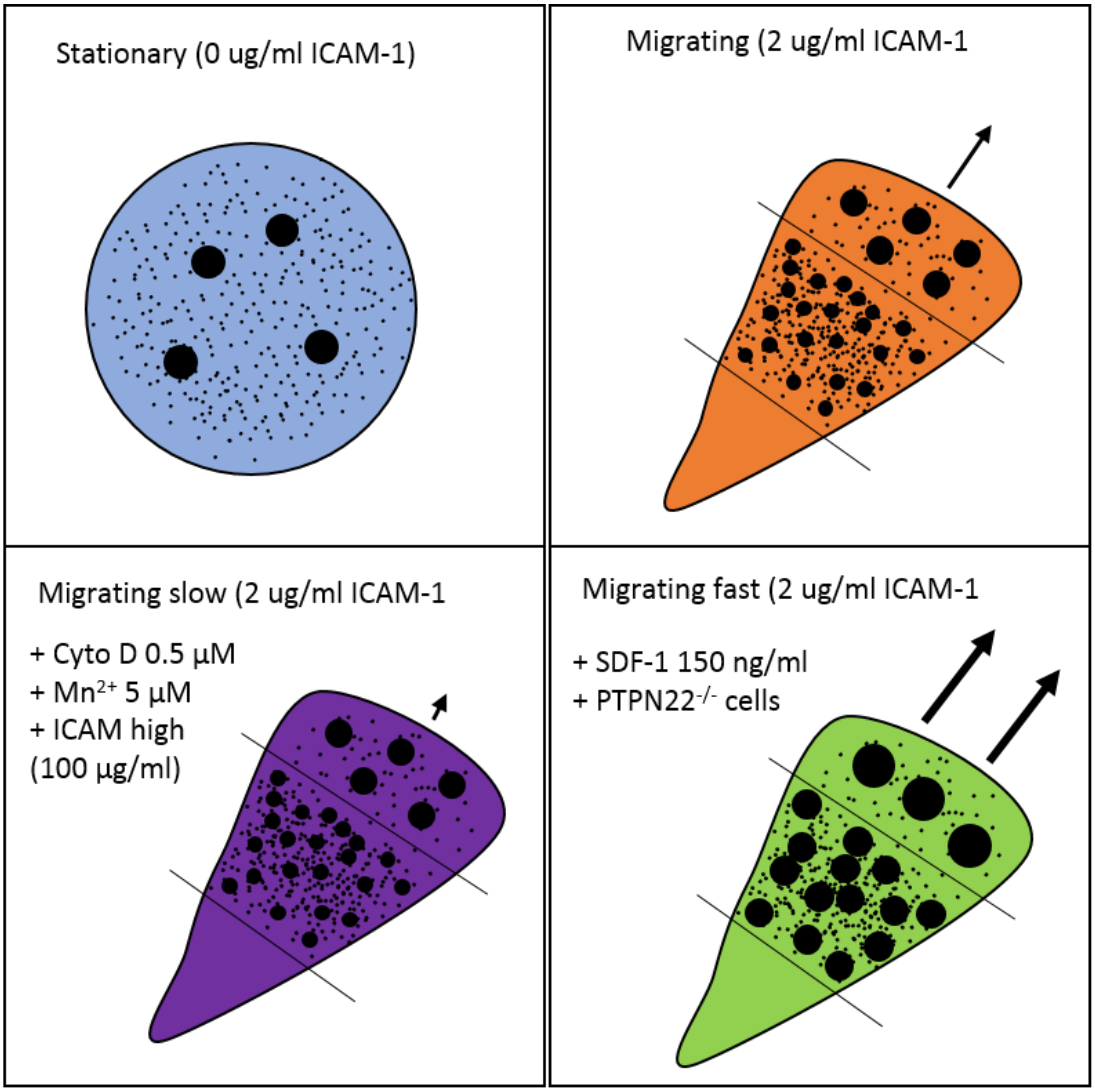

Figure 5-9: **Membrane LFA-1 nanoadhesions concentrate in the focal zone, and get larger cell wide upon cell speed increase (CXCL12 treated or PTPN22 deficient cells.** T cells concentrate their clusters on two length scales in the focal zone, both individually clusters get smaller and denser, and as a group clusters gather closer together. Cell speed up increases the size of clusters whereas slow down has little effect.

5.4 Intracellular LFA-1 integrin clustering

While the transmembrane population of integrin LFA-1 is of direct importance in terms of its clustering and association with ICAM-1, the intracellular population also remains un-investigated at the length scales afforded by super resolution microscopy. Necessarily, integrin LFA-1 clusters are harvested from the membrane at the end of their lifetime – when the cell has moved over/past the adhesion[210,238]. The recycling of integrin LFA-1 to and from the cell membrane is well characterised biochemically[239], but again, the nanoscale characteristics of intracellular LFA-1 integrin, and whether these are also modulated during cell migration speed changes have been hidden behind the diffraction limit of light, and are now available using new microscopy techniques and novel quantitation techniques.

To address this question, interferometric STORM (iSTORM)was used, which allows for isotropic minimum resolution of 30 nm in x y and z to a depth of 420 nm from the coverslip[134]. By imaging at this depth, we hoped to be able to investigate a population of integrin LFA-1 which is being actively recycled: fixed and therefore frozen at a moment in time, to determine whether the characteristics of this portion are implicated in cell migration velocity. Here, 3D iSTORM allows investigation of the intracellular and membrane LFA-1 pools together, which can then be compared to the 2D results for membrane LFA-1 alone. The process of imaging the cells, localising the images and analysing them using a new 3D compatible version of the cluster analysis algorithm are shown in figure 5-11. Using 2 µm x 2 µm x 420 nm ROIs, cluster parameters per ROI were extracted, which were then plotted as a function of z with the height of the coverslip taken as 0 nm. Again, these regions were taken from either the focal zone or the leading edge, and the cells exposed to the same battery of slow down and speed up signals. Migrating mouse T cells were plated onto gold nanorod embedded ICAM-1 coated glass coverslips and subject to slow down or speed up signals. To ensure the efficacy of the slow down and speed up signals on a population of cells, treated or untreated cells from the same vial were split into two: half of the volume were plated onto microscope dishes and imaged migrating by phase contrast microscopy before being tracked using automated tracking software, while the other half were plated onto iSTORM coverslips and fixed during migration. Mn^{2+} and Cytochalasin D slowed down cells successfully, and CXCL12 treatment or PTPN22 knockout caused cells to speed up (figure 5-10).

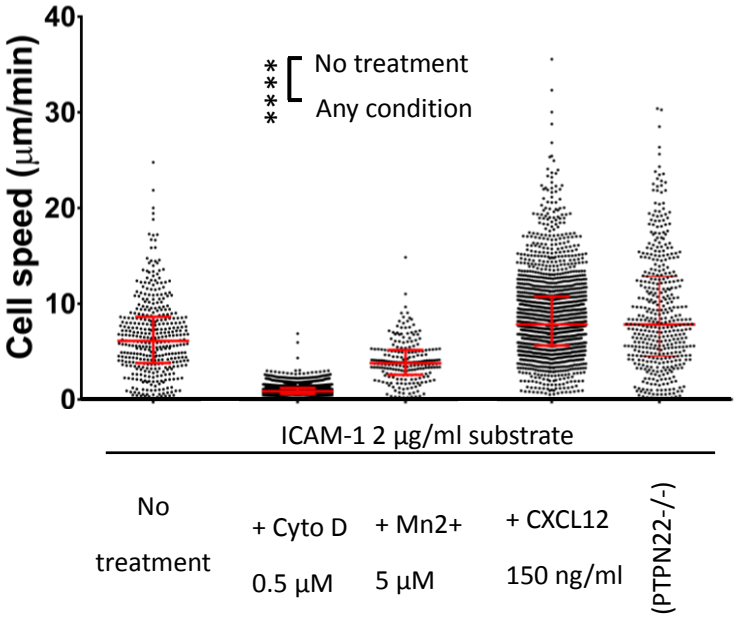

Figure 5-10: **Population level cell speeds of cells used for iSTORM.** Cell tracking was performed on the same samples used for iSTORM microscopy to confirm that the 3D cluster data correlate to conditions that change cell speed. Cells migrating on ICAM-1 coated coverslips were treated with a battery of slow down or speed up conditions.

Cells were then stained for LFA-1 and imaged using iSTORM (methods), which provides a 3D coordinate map of molecular positions at 30 nm isotropic resolution over a depth of ~ 420 nm. Figure 5-11a shows LFA-1 in an example whole cell imaged by iSTORM where molecules are displayed as Gaussian estimates of their uncertainty in x and y, with the z direction colour coded (colour bar in 5-11a). In the magnified cut outs (right hand panels in figure 5-11a), different populations of clusters at different heights are clearly visible. This is especially clear on the side view panel (figure 5-11a, bottom right), where a blue population of molecules exists above the green and yellow membrane proximal population. To analyse this 3D coordinate data, we used a 3D version of the Bayesian cluster analysis algorithm which takes full account of the uncertainty in assigning clusters. Once 3D clusters had been assigned in the 420 nm imaging volume (Figure 5-11b), metrics could be extracted and compared between conditions.

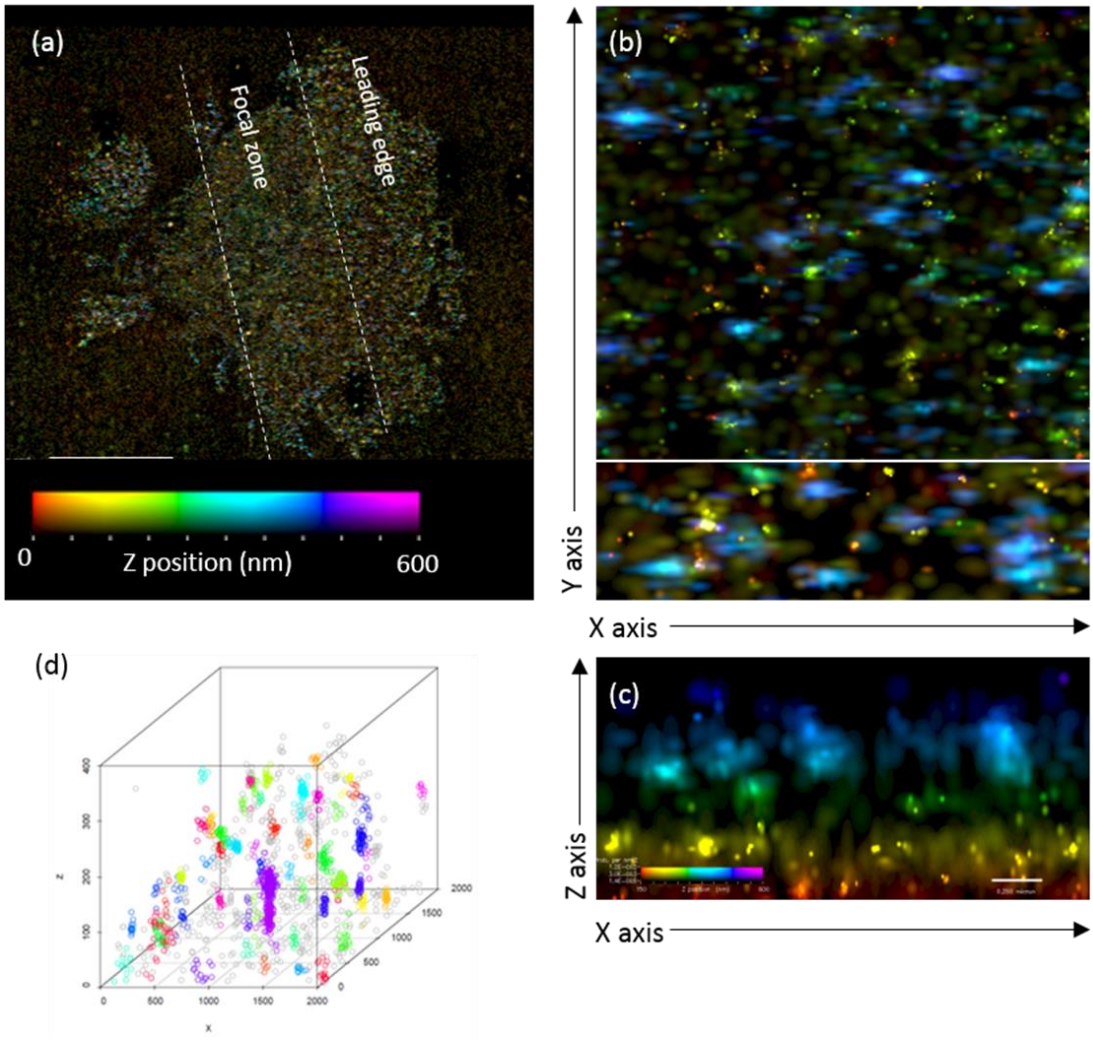

Figure 5-11: **Representative image of LFA-1 imaged in a migrating T cell by iPALM and analysed using a 3D version of the Bayesian cluster analysis algorithm.** A) shows a whole cell. B) shows magnified sections of this cell, where clusters of LFA-1 are pseudocoloured as per the z position scale bar in a). C) shows a side view of the cutaway in b. d) shows an example cluster map derived from 3D Bayesian cluster analysis. Scale bar 5 µm.

5.4.1 3D LFA-1 clustering irrespective of the z dimension

In order to interrogate whether nanoclustering changes were specific to membrane LFA-1, or whether they happen in the intracellular zone above the height of the membrane, metrics for clusters per 2000 x 2000 x 420 nm region were analysed in cells stationary (0 ICAM-1 on the plate) or migrating (2 µg/ml ICAM-1 surface) at different speeds, treated with slow down: Cytochalasin D at 0.5 µM, Mn^{2+} 5 µM or speed up: CXCL12 150 ng/ml or PTPN22 knockout signals. Cluster metrics were plotted irrespective of the z height, such that the following represent overall answers for LFA-1 clustering across the entire 420 nm depth.

In the transition from stationary to migrating, where the cells are exposed to an ICAM-1 coated glass coverslip surface, the total number of molecules per volume region is significantly increased (first three bars figure 5-12a) n = 3 mice, 20 cells, ****p<0.00001. This is coupled to a significant decrease in the percentage clustered (figure 5-12b), and no change in the number of clusters (figure 5-12c). Across conditions and speed changes, the leading edge and focal zone don't display significant changes in any condition (figure 5-12a, b and c), unlike for membrane 2D LFA-1 clustering data (section 5.3).

In migrating cells, across the slow down and speed up conditions, the total molecules per cluster remains largely the same between migrating cells moving at normal speed, and in slowed cells treated with Mn^{2+} ions or Cytochalasin D (Figure 5-12a). The exception is in the leading edge of Mn^{2+} treated migrating cells, which contain significantly fewer LFA-1 molecules than their untreated counterparts (figure 5-12a, middle bars). Fast cells treated with CXCL12 have the same level of total LFA-1 in the intracellular population as untreated cells. Fast cells deficient for PTPN22 have a significantly reduced level of intracellular LFA-1, (figure 5-12a bars on the far right of the plot).

The percentage clustered decreases slightly upon cell migration - comparing stationary cells (grey bar) with migrating cells across the leading edge (orange) and focal zone (blue) (figure 5-12b). Only PTPN22 deficient cells display a significant intracellular decrease in the percentage molecules taking part in clusters. CytoD, Mn and CXCL12 treated cells showed no change from untreated cells in the percentage clustered over the whole imaging volume.

The number of intracellular LFA-1 clusters doesn't change in the transition from stationary to migrating. Treatment with Cytochalasin D causes an increase in the number of clusters in the leading edge and focal zone, as does CXCL12 treatment. PTPN22 deficiency causes a decrease in the number of clusters, which is more clear in the leading edge.

There is no change in the number of clusters (18 to 20) per region in stationary cells as compared to migrating cells (first 3 bars, figure 5-12c). CXCL12 treatment increases the number of clusters specifically in the leading edge of the 3D imaging volume, and PTPN22 significantly and decreases the number of clusters cell wide (final two bars, figure 5-12c).

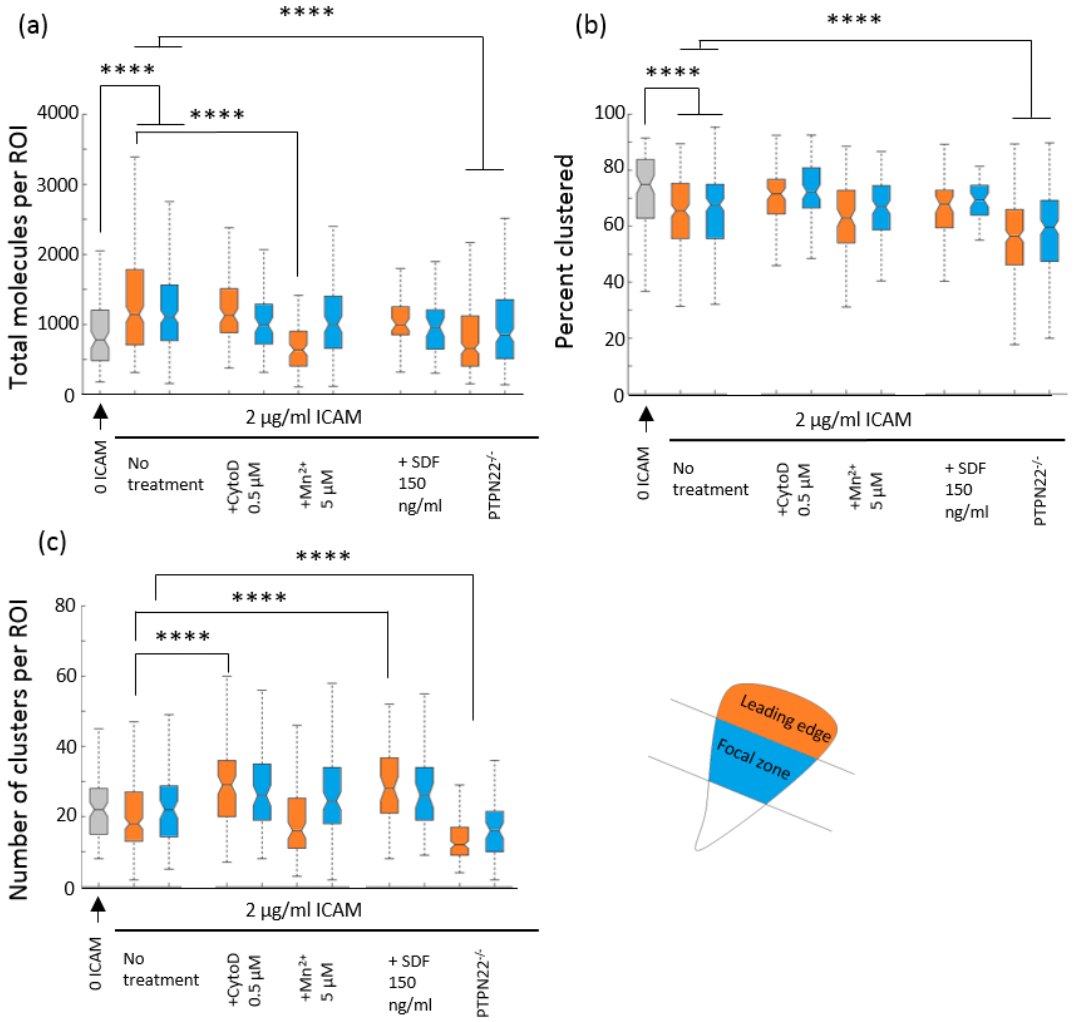

Figure 5-12: **Overall 3D nanoclustering of LFA-1 in stationary versus migrating T cell, treated under a battery of conditions that change migration speed.** Cluster parameters per ROI were extracted from the 3D imaging volume and plotted irrespective of their z positions: the total molecules (a), the percentage of those molecules in clusters (b) and the number of clusters (c). N = 20 cells from 3 mice 200 + ROIs per condition. ****p< 0.0001

Individual cluster characteristics: size and density

Individual cluster characteristics for LFA-1 nanoclusters in this 420 nm volume were also extracted. Upon cell migration, comparing grey bars representing stationary cells with orange and blue bars for migrating cells, the size of intracellular LFA-1 clusters increases significantly in both regions (figure 5-13a). In all slow down conditions (middle bars – Cytochalasin D and Mn^{2+} treatments), there is a significant decrease in the size of clusters when compared to untreated migrating cells. In fast migrating cells treated with CXCL12 there is no change as compared to untreated cells, but in cells deficient for PTPN22, there is an increase in the size of clusters (figure 5-13a n = 20 cells from 3 mice. ****p<0.00001).

The number of molecules per cluster is constant across speed changes, and even between stationary and migrating cells. The exception to this is in PTPN22 deficient cells, which have an increased number of molecules per cluster. Combined with size data, these cells therefore have larger clusters which also increase their molecular content in the intracellular compartment, across the leading edge and focal zone (figure 5-13b).

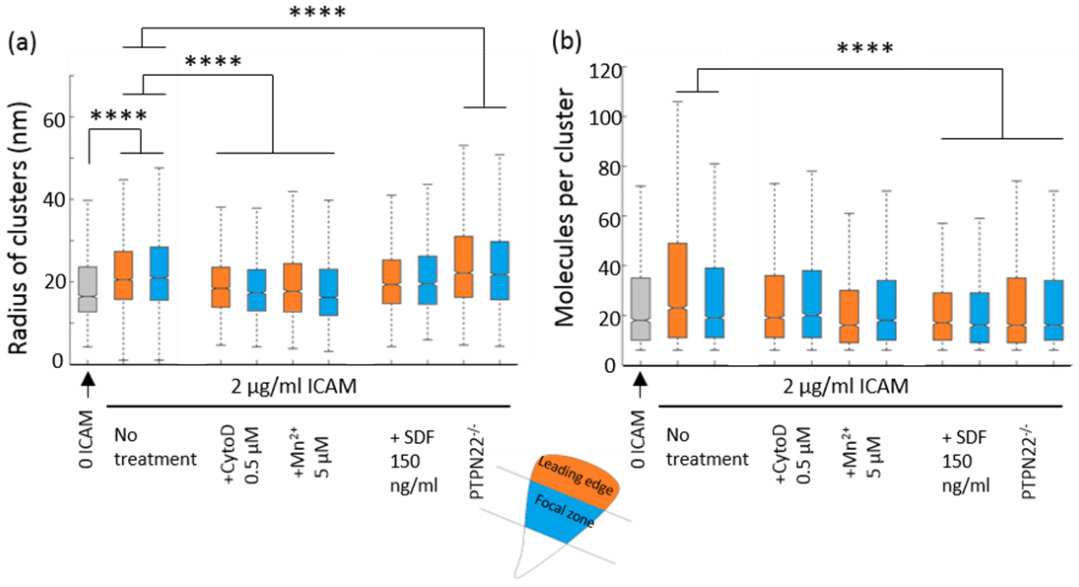

Figure 5-13: **Individual intracellular LFA-1 nanocluster metrics: size and molecules per cluster.** Cluster parameters per cluster were extracted from the 3D imaging volume and plotted irrespective of their z positions. (a) Cluster radius and b) molecules per cluster in the leading edge or focal zone of cells treated with slow down or speed up signals. N = 20 cells from 3 mice 200 + ROIs per condition. ****p< 0.0001

5.4.2 3D LFA-1 clustering per ROI versus z dimension

LFA-1 is known to be under active recycling during cell migration, and the membrane proximal (< 420 nm) population is representative of this population[240,241]. It is not known whether the characteristics of intracellular LFA-1 nanoclusters have a role in determining the speed of cell migration, and might be differentially modulated in comparison to membrane LFA-1 nanoclusters. In order to discern potential changes in particular populations at certain z height, cluster centroids were discerned and cluster metrics plotted within z height bins up to the maximum imaging depth of 420 nm from the height of the coverslip.

Total molecules per region (Figure 5-14a) shows that LFA-1 concentrates at the cell membrane in all migrating cell conditions (red, yellow, purple green and light blue), and in stationary cells (blue). The total amount of LFA-1 is increased in untreated migrating cells (orange bars: glass slides coated with 2 µg/ml ICAM-1) compared to stationary cells (dark blue), across all z heights and in both the leading edge (figure 5-14a) and the focal zone (figure 5-14b). This effect was more pronounced in the leading edge: this is reflected in the average skewness value for clusters in migrating cells (1.34) compared to in stationary cells (1.45) – the graph is shifted to the left hand side, demonstrating that the strongest increase in intracellular LFA-1 occurs close to the membrane.

Compared to untreated cells, upon cell slow down by addition of Cytochalasin D (yellow bars in a and b) or Mn^{2+} (purple bars in 5-14 a and b), the total molecules is significantly reduced in both the leading edge and the focal zone. Upon cell speed increase by addition of CXCL12 (green bars in 5-14 a and b) or PTPN22 knockout (light blue bars in 5-14 a and b), the total number of molecules is restored to levels similar to in untreated migrating cells in the leading edge: skewness 1.41 and 1.44 in CXCL12 treated and $PTPN22^{-/-}$ compared to 1.34 in untreated).

In the focal zone CXCL12 treated cells (green bars) display levels of LFA-1 similar to untreated migrating cells, but $PTPN22^{-/-}$ cells display a reduced level of LFA-1 near the membrane (s = 1.11). This is reflected in a significant difference in skewness: 1.11 for PTPN22 deficient cells (a shift to the left with a longer tail) and 1.47 for CXCL12 treated cells ($p<0.0001$), which is not significantly different to untreated migrating cells at 1.34

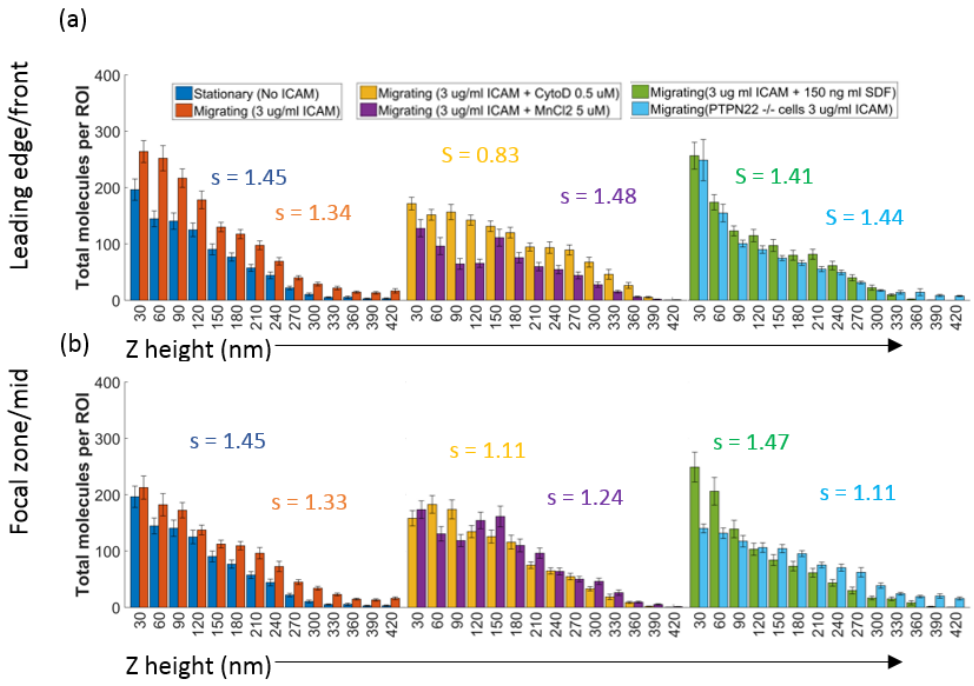

Figure 5-14: **Total LFA-1 molecules per region plotted against z height, in the leading edge and focal zone of T cells treated with either 'slow down' or 'speed up' signals, imaged by iPALM and analysed using 3D Bayesian cluster analysis.** The leftmost plots are conditions: stationary (0 ICAM-1) and migrating untreated (2 ug/ml ICAM). In the middle are Cytochalasin D, and Mn. On the right are CXCL12 and PTPN22$^{-/-}$. A) plots for cluster metric against z height in the leading edge and b) the focal zone. N = 3 mice, 20 cells and 200 ROIs per condition.

In both stationary and migrating cells, the **percentage of molecules in clusters (figure 5-15a)** is clearly increased the closer the clusters are to the cell membrane: there is a peak at 90 nm. Due to the percentage clustering values never falling below 20 %, the skewness values are close to zero. In slow cells, the percentage clustered is the same in cells treated with Cytochalasin D, but is decreased at the membrane proximal zone height in cells treated with Mn^{2+}. In fast cells, the percentage clustered is hugely decreased in both CXCL12 treatment and PTPN22 deficiency at all z heights. The effect is far more pronounced in cells treated with CXCL12 however, suggesting that above the height of the membrane, the percentage of clustered molecules is highly dependent on the presence of CXCL12, and this differs from the effect of PTPN22. Across conditions, there is always more LFA-1 clustered near the cell membrane.

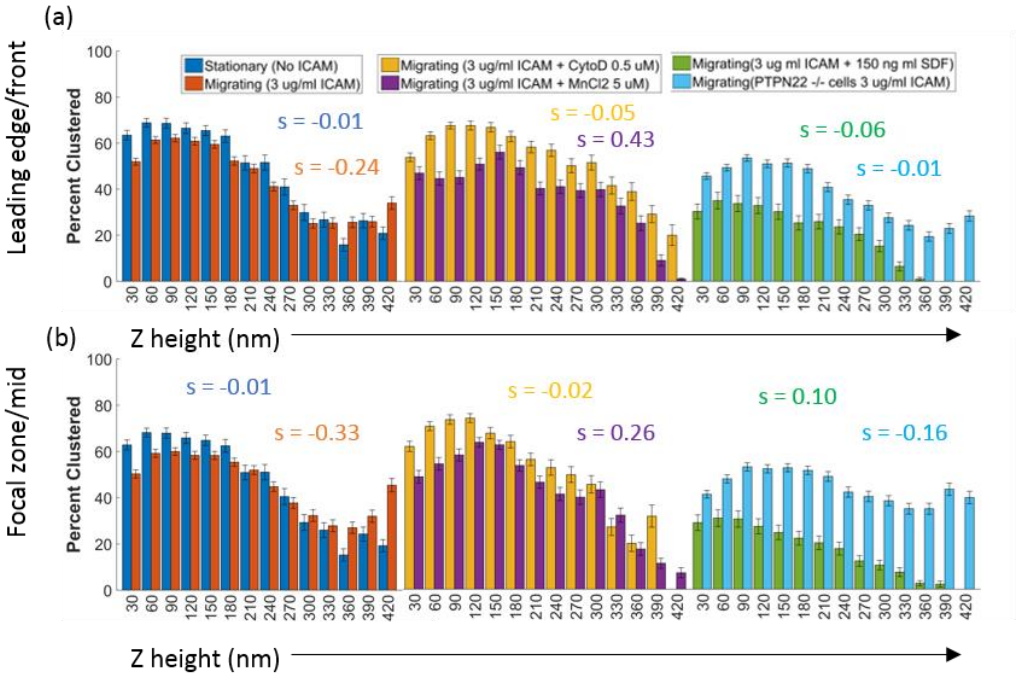

Figure 5-15: **The percentage LFA-1 molecules in clusters plotted against z height, in the leading edge and focal zone of T cells treated with either 'slow down' or 'speed up' signals, imaged by iPALM and analysed using 3D Bayesian cluster analysis.** The leftmost plots are conditions: stationary (0 ICAM-1) and migrating untreated (2 ug/ml ICAM). In the middle are Cytochalasin D, and Mn. On the right are CXCL12 and PTPN22$^{-/-}$. A) and b) Plots for percentage clustered against z height in the a) leading edge and b) the focal zone. N = 3 mice, 20 cells and 200 ROIs per condition.

The **Number of clusters per region (figure 5-16b)** was calculated by calculating cluster centroids, and binning them based on the z height of this coordinate point. Moving from stationary (blue) to migrating with no other treatment (orange) led to absolutely no discernible change in the number of clusters at any z height, in either the leading edge (top line of graphs) or the focal zone (bottom line of graphs). Migrating cells showed a slightly greater skew for the membrane (0.67 for migrating untreated cells (orange) compared to stationary non migrating cells at 1.09 (blue)) in both the leading edge and focal zone. Cells that were slowed down with Mn^{2+} had a deficit of clusters very close to the height of the membrane in both leading edge (s = 1.52) and focal zone (s = 1.10). Cytochalasin D left the number of clusters largely unchanged at all z heights in comparison to untreated migrating cells (s = 0.96 for the leading edge and 1.03 for the focal zone). Cells treated with CXCL12 or deficient for PTPN22 have fewer clusters at the mid z height, and in general. Interestingly, PTPN22 deficient cells display a population of clusters from 300 nm to 420 nm that CXCL12 treated fast cells don't have. This is coupled to a big shift to the right (s = 0.67 for the leading

edge and 0.57 for the focal zone) indicating that the distribution of clusters in PTPN22 cells shifts away from the membrane to above the membrane, higher up in the cell. Overall therefore, fast cells display fewer clusters at all z heights than slower cells, in both the leading edge and the focal zone.

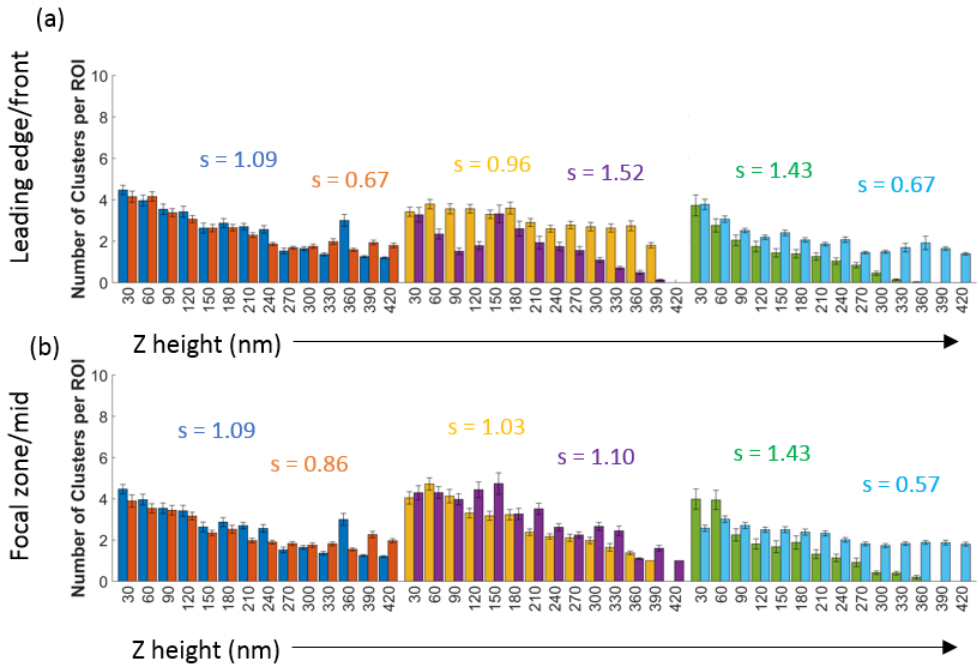

Figure 5-16: **The number of LFA-1 clusters plotted against z height, in the leading edge and focal zone of T cells treated with either 'slow down' or 'speed up' signals, imaged by iPALM and analysed using 3D Bayesian cluster analysis.** The leftmost plots are conditions: stationary (0 ICAM-1) and migrating untreated (2 ug/ml ICAM). In the middle are Cytochalasin D, and Mn. On the right are CXCL12 and PTPN22$^{-/-}$. A) and b) Plots number of clusters against z height in the a) leading edge and b) the focal zone. N = 3 mice, 20 cells and 200 ROIs per condition.

5.4.3 3D LFA-1 clustering versus z dimension: Individual cluster metrics - size and density

In addition to looking at 'per ROI' clustering metrics, information about the size and molecular content of individual clusters were also extracted, and plotted against the z height of the centroid of each cluster. Here, small changes are often significant, due to the sheer amount of data available (1000s of clusters per condition). The radius of clusters and the number of molecules per cluster can be taken holistically as a measure of density: if there is a radius decrease with either no change or an increase in the number of molecules – this translates to an increase in density.

Changes in the **radius of clusters** (figure 5-17) and the height at which they occur are very different in the leading edge (top panels figure 5-17a) as compared to the focal zone (lower panels figure 5-17b). In the leading edge, clusters increase in size very slightly (significantly) as cells start to migrate as compared to when they are stationary, but then remain constant at around 20 nm radius at all z heights. The same 20 nm cluster size is seen across all z heights in the leading edge across conditions, whether cells have decreased speed (treated with Cytochalasin D or Mn^{2+}) or increased speed (treated with CXCL12 or deficient for PTPN22).

In the focal zone however (figure 5-17a, lower panels), there is a clear increase in the size of clusters in migrating cells as compared to stationary cells, focused to a peak around 180 nm above the height of the coverslip. In slower cells treated with Cytochalasin D and Mn^{2+}, compared to untreated migrating cells, there is a great increase in cluster size in the focal zone, especially at a height far above the membrane (300 nm). In fast cells, the opposite is true: cluster size is decreased, especially at the mid to high z height region. CXCL12 induces this effect to a greater extent than PTPN22.

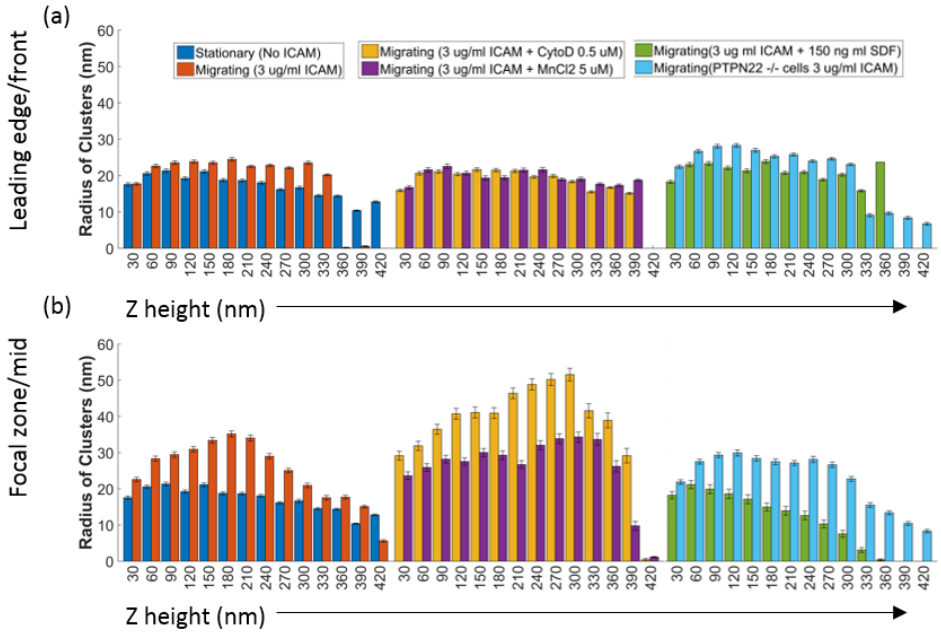

Figure 5-17: **The radius of LFA-1 clusters plotted against cluster z height, in the leading edge and focal zone of T cells treated with either 'slow down' or 'speed up' signals, imaged by iPALM and analysed using 3D Bayesian cluster analysis.** The leftmost plots are conditions: stationary (0 ICAM-1) and migrating untreated (2 ug/ml ICAM). In the middle are Cytochalasin D, and Mn. On the right are CXCL12 and $PTPN22^{-/-}$. A) and b) Plots of the radius of clusters against z height in the a) leading edge and b) the focal zone. N = 3 mice, 20 cells and 200 ROIs per condition.

The **number of molecules per cluster (figure 5-18)** is similarly changeable depending on the location of the cluster in z, but is constant over the leading edge and focal zone. Comparing migrating cells to stationary cells, there is an increase in the size of clusters upon migration, in both the leading edge and focal zone, focused in the membrane proximal region (60 to 120 nm above the coverslip).

In all slow down conditions, the number of molecules per cluster is decreased to a level similar to stationary cells, at all z heights and in both the leading edge and focal zone. A greater decrease is present at high z height in the leading edge of cells treated with Mn^{2+}, which doesn't occur in Cytochalasin D treated cells. In speed up conditions, there is a large drop in the number of molecules per cluster in cells treated with CXCL12 that doesn't occur in cells deficient for PTPN22. This is more prominent in the focal zone than in the leading edge.

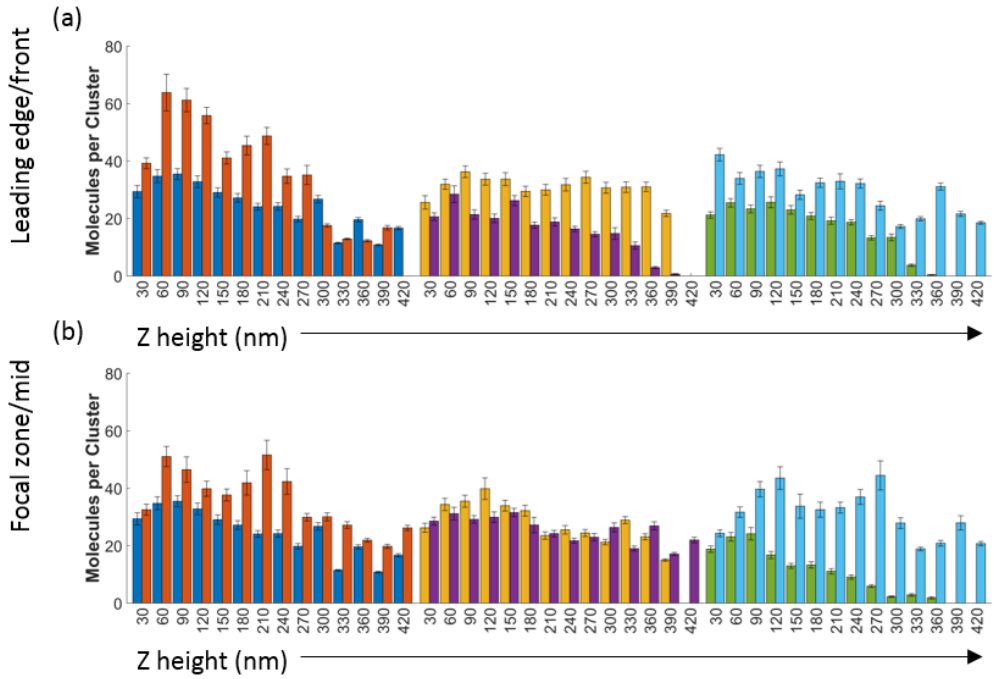

Figure 5-18: **The number of LFA-1 molecules per cluster plotted against cluster z height, in the leading edge and focal zone of T cells treated with either 'slow down' or 'speed up' signals, imaged by iPALM and analysed using 3D Bayesian cluster analysis.** The leftmost plots are conditions: stationary (0 ICAM-1) and migrating untreated (2 ug/ml ICAM). In the middle are Cytochalasin D, and Mn. On the right are CXCL12 and PTPN22$^{-/-}$. A) and b) Plots of number of molecules per cluster against z height in the a) leading edge and b) the focal zone. N = 3 mice, 20 cells and 200 ROIs per condition.

Taking radius and molecules per cluster together, the size increases displayed in the transition from stationary to migrating are coupled to increases in molecular content, therefore the density remains constant. In slow down conditions, more often there is an increase in the size

of clusters, but no increase in the molecular content, therefore this is a density decrease. In speed up conditions, more often there is a decrease in the size of the clusters, with either a concurrent decrease or a maintenance of in the number of molecules per cluster, therefore the density either stays the same or is increased.

5.4.4 Discussion for LFA-1 clustering in 3D

The aim of these experiments was to assess changes in intracellular LFA-1 nanoclustering as a measure of the actively recycled population during cell migration speed modulation. There were two main novel findings:

1. LFA-1 exists in pre-clustered pools above the height of the membrane
2. PTPN22 phosphatase negative cells and CXCL12 treated cells have smaller clusters in the intracellular focal zone
3. Manganese and Cytochalasin D treated cells have larger clusters in the intracellular focal zone

Previously, nano-clusters of LFA-1 in T cells have only been resolved in 2D using TIRF. Here, for the first time, the increased resolving power of iSTORM is used to show that nano-clusters on the size scale of vesicles exist above the height of the membrane. Previously, LFA-1 microclusters have been identified by conventional microscopy during Rab dependent recycling, which fail to form upon inhibition of Rab family proteins, microtubules, or MLCK[71,83]. Such preformed LFA-1 nano-clusters above the height of the membrane therefore most likely represent LFA-1 that is being actively recycled to and from the cell membrane.

Taking LFA-1 clustering per 3D volume, it is clear that unlike in the cell membrane 2D population (section 6.3), there is an increased amount of LFA-1 (total molecules per ROI) when cells are migrating on ICAM-1 as opposed to standing stationary on uncoated glass slides. This would suggest that there is an increased recruitment of LFA-1 from further in the cell to this 420 nm deep membrane proximal zone, which could reflect an increased expression level of integrin LFA-1 upon cell migration – a known phenomenon which backs up this work[242]. This would suggest that LFA-1 exists in pre-clustered pools above the height of the membrane which supply LFA-1 nanoclusters to the membrane, but in turn that there are monomers coming from further in the cell to support the ‘sub membrane’ clusters.

When plotted against their z positions, most of these total molecule changes appear to happen in the membrane proximal region, while the mid z height region is maintained. It is

therefore possible that the total pool of LFA-1 present is largely unaffected during fast or slow migration, pointing to the cell membrane as the place where this happens, and to the two regions being separately regulated.

The second novel finding is that there are changes that occur in the size of such intracellular nano-clusters in two separate cell 'slow down' treatments and two separate cell 'speed up' treatments. Taking the 3D results for intracellular and membrane LFA-1 together with the 2D results (section 6.3) for membrane LFA-1 alone, it can be confidently stated that intracellular LFA-1 clusters change their conformation preferentially in the focal zone, whereas membrane LFA-1 clusters are modulated within both the focal zone and the leading edge regions. An interpretation is that more recycling occurs from the focal zone than the leading edge, and therefore this is where most of the statistically discernable changes occur while comparing median values between conditions. The 2D results show more nanoclusters in the focal zone, which must necessarily be recycled as the cells moves forward to facilitate persistent cell migration. Further evidence for this point is supplied by the existence of separate Rab pathways which are specific for endocytosis of membrane integrin derived from the focal zone, as well as those specific for the leading edge. This would suggest that there are two separate regulated networks of nanoclusters: those in the membrane and those above the height of the membrane, that may be under active recycling or recruitment (shown in generalised model, Figure 5-19).

This separation between the membrane population and the intracellular population is evident in the percentage of molecules in clusters in fast cells (CXCL12 treated, or PTPN22 deficient) compared to slower cells. In 3D, there is an overall decrease in the percentage of clustered molecules, whereas in 2D, in the membrane alone, there is an increase in the percentage of clustered molecules. This points towards the possibility of a separate but complementary clustering program above the membrane distinct from the membrane population of LFA-1. In addition, this effect on the intracellular LFA-1 population is more pronounced in CXCL12 treated cells than PTPN22 deficient cells, suggesting a possible divergence in the two pathways in the regulation of LFA-1 nano-clusters above the membrane, that does not occur in the membrane population on its own.

In terms of individual cluster characteristics – the size and density seem to differ in the intracellular compartment, where the size of clusters in reduced in PTPN22 deficient or CXCL12 treated fast cells. In the membrane, nanoclusters increase in size in faster cells, this would suggest again that there are two separate regulated networks of nanoclusters: those in

the membrane and those above the height of the membrane. Further investigation of the role of such nanoclusters would require multi-colour 3D iSTORM to look at nanoscale colocalization of known signalling intermediates of LFA-1 involved with recycling, such as Rab5, 11 or 13, Mst1 or RAPL. Such a technique is possible but would require new laser lines to be installed on the system, as well as genetically encoded spectrally distinct probes for each molecule of interest, independently validated and imaged sequentially.

Within the 'slowed cell' and 'fast cell' groups of treatments, differences in LFA-1 intracellular clustering become clear between conditions using this technique that are not present in the membrane. This suggests that the signals converge and result in the same outcome for membrane LFA-1 clustering, but not for intracellular clustering. These divergent characteristics are explored below.

CXCL12 but not PTPN22 specific phenomena

Specifically, PTPN22 deficient cells maintained a population of clusters in the leading edge and focal zone at high z heights which were missing in CXCL12 treated cells. Both cell subsets were moving at similar speeds, so it is possible that CXCL12 results in differential recruitment or recycling of LFA-1, manifested in a deficit of clusters in the 270 to 420 nm z height range.

PTPN22 deficient cells also display much less of a pronounced difference in the percentage clustered above the height of the membrane than CXCL12 treated cells. This suggests again that above the height of the membrane, different arms of the pathways are in action which control this intracellular clustering. The CXCL12 treated cells also display much smaller clusters less dense clusters higher up in the cell, whereas PTPN22 deficient cells maintained this population (model in figure 5-19).

Whether small dense membrane clusters in the focal zone emanate from leading edge clusters that persist, changing their characteristics as this occurs, or whether they enter the focal zone region specifically as pre-made packages is unknown. To address this, live cell super resolution localisation microscopy could be carried out to track clusters during their life time – a tool for the analysis of such data has recently been developed[243].

Actin dependent changes in intracellular clustering

Interestingly, the intracellular percentage clustering doesn't change in Cytochalasin D treatment, but changes considerably in cells treated with Mn^{2+}. This provides further indirect evidence for actin corralling being involved in regulating membrane clusters, and for different effects to be playing a role in the submembrane region.

The size of clusters in the focal zone is significantly different between the two slow down signals: Cyto D and Mn^{2+} treatment. The Cytochalasin D treatment induces the appearance of large clusters of around double the size at mid to high z heights to a much greater extent than the Manganese treatment. That the radius trends happen clearly in the focal zone and not the leading edge gives credence to the detection capabilities of the techniques and analysis regimes. It also points to a biological significance of changing the cluster size at mid to high z heights that relates to cell speed, as it is known that this area (the focal zone) is regulated by certain Rab proteins such as Rab-13, whereas leading edge recycling is preferentially regulated by Rab5[85].

To investigate how in-membrane and intracellular nanocluster modulation is carried out, IRIS[242] could be used to investigate actin based corralling of LFA-1 clusters. This segregated membrane model, driven by picket fence rearrangement of membrane proteins is a strong candidate for modulations of this type[106]. New fibre analysis tools are in development (Peters R, in preparation) to address this question. Alternatively, or in conjunction with actin corralling, such in membrane cluster regulation could be controlled by structural proteins based on the signalling of active intermediates, three of which are known to be associated with nascent adhesions (of a similar but slightly larger length scale in slower cell types): phospho397 FAK and phospho416 Src family kinases, including Lck and Fyn. These markers are addressed in section 6.6.

Notes on the system and detection

It is important to note that the detection limit of the system in our hands was a depth of 420 nm. Due to the nature of the technique (a reliance on interferometry), x y and z resolution do not degrade through this imaging depth, therefore fewer molecules higher up in the cell really relate to fewer molecules and not to system limitations. It must also be noted that detection rates are lower in iSTORM in 3D (carried out at Janelia research institute in Ashburn, VA) as compared to dSTORM in 2D (carried out at King's College London) due to the relative powers of the lasers. Therefore the absolute numbers for measures such as total molecules and molecules per cluster should be discounted, and as stated previously, only relative measures be taken. The reduction in total detected emitters does not affect any of the other cluster parameters (see figure 3-13 in section 3).

To summarise, migrating cells adopted a regionally distinct set-up of nanoclustering, where larger clusters dominate in the focal zone submembrane region and smaller ones exist in the leading edge. PTPN22 and CXCL12 conditions increased the size of nano-clusters above the

height of the cell membrane, while Cytochalasin D and Manganese treatments decreased their size – both phenomena occurring in the focal zone. It is known that LFA-1 containing vesicles exist above the height of the membrane, and that some are associated with active FAK, a protein involved in both the early assembly and the recycling/disassembly of adhesions. To investigate whether FAK nano-clusters are regulated above the height of the membrane, and to discern how this relates to nanoscale changes in LFA-1 seen here, types, iSTORM was carried out on the pY397 form of FAK[51,70,72,75,244] in migrating PTPN22 proficient versus deficient cells.

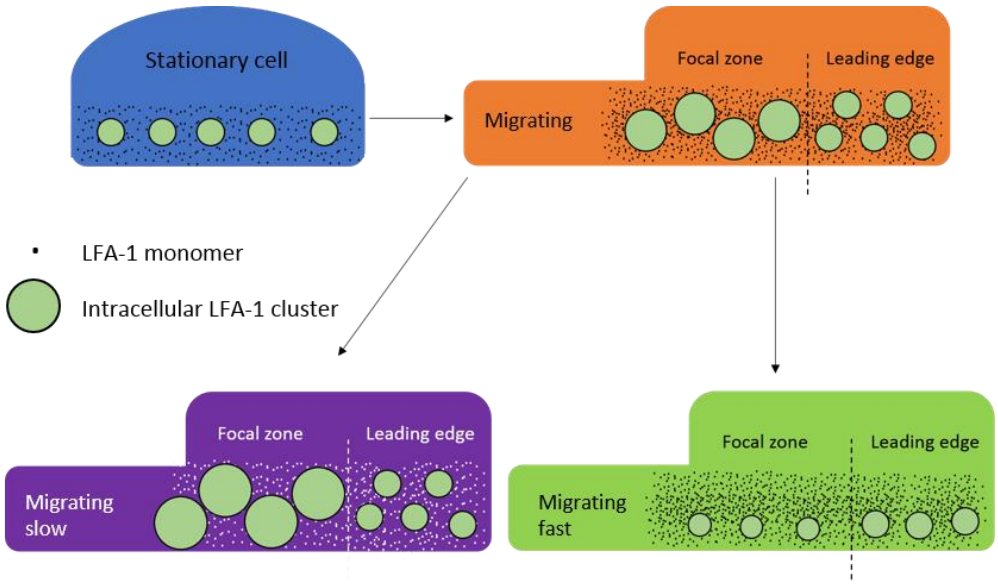

Figure 5-19: Intracellular LFA-1 clusters transition to a regional distribution above the membrane. Most changes related to cell speed occur in the focal zone above the membrane. Transition from stationary to migrating (blue to orange) exhibits a regional discrimination above the membrane into the leading edge, with small clusters , and the focal zone with large clusters. The total amount of LFA-1 is also increased. Cells with decreased speed (purple) exhibit focal zone specific phenomenon of increased size of clusters with fewer molecules per cluster and in total above the membrane. Cells with increased speed (green) exhibit smaller clusters with fewer molecules in the focal zone. The leading edge is unchanged in terms of intracellular LFA-1.

Chapter 6: Nano-adhesion activity

6.1 Intracellular phospho-397 FAK

FAK is known to be one of the first kinases associated to nascent adhesions in other cell types (non-leukocyte)[75]. It is also known to be associated to LFA-1 in vesicles above the height of the membrane[51], and active 397 phosphorylated FAK is known to be associated with the assembly[208] as well as disassembly[68] of focal adhesions. The aim by looking at phosphorylated FAK in wildtype and fast PTPN22 deficient T cells was to find out whether there is a regulated sub membrane population that changes during migration on the nano-scale. This may provide new insight into the clustering of a closely integrin related molecules in its active phosphorylated state, which is associated with integrin contained in vesicles above the membrane[70].

To investigate phospho-FAK in normal migration and fast PTPN22 deficient migration, cells were plated onto ICAM-1 coated glass slides and tracking for 15 minutes. PTPN22$^{-/-}$ cells moved faster (figure 6-1) as shown previously (figure 4-10 and 5-3). The same sample was simultaneously plated onto iSTORM slides and chemically fixed, permeablised and stained with an antibody specific for pY397 FAK.

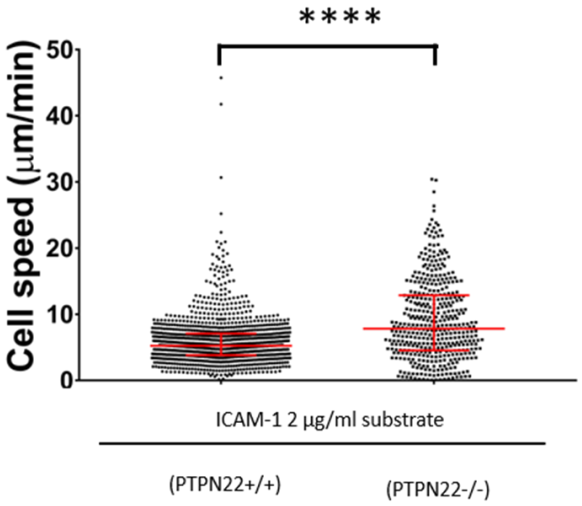

Figure 6-1: **Population level speed measurements of PTPN22$^{-/-}$ cells migrating on ICAM-1 coated coverslips in cells used for iPALM.** These experiments performed on the same sample later imaged in iPALM of pYFAK.

To ensure that this phosphotyrosine targeting antibody was specific to phospho-Y397 FAK, we first used an inhibitor known to block the phosphorylation of FAK at this site (FAK 14). Its chemical structure is shown in figure 6-2c. Cells were treated with the inhibitor and incubated for 10 minutes before plating onto ICAM-1 coated microscope slides, and imaged in the presence of CO_2 and 37 degree temperature for 15 minutes. The final frame taken from representative phase contrast movies where cells have been tracked using automatic tracking software (methods) are shown in figure 6-2a (n = 5 fields of view (FOV) and ~ 300 cells per condition). Quantitation of cell tracking data showed that cells treated with FAK inhibitor at either 5 μg/ml or 10 μg/ml moved much more slowly (figure 6-2b), with many of the cells simply stationary and unpolarised (figure 6-2a). This is the expected effect of dephosphorylating FAK[51] and therefore shows that the inhibitor works as described and does not affect cell viability[245–247]

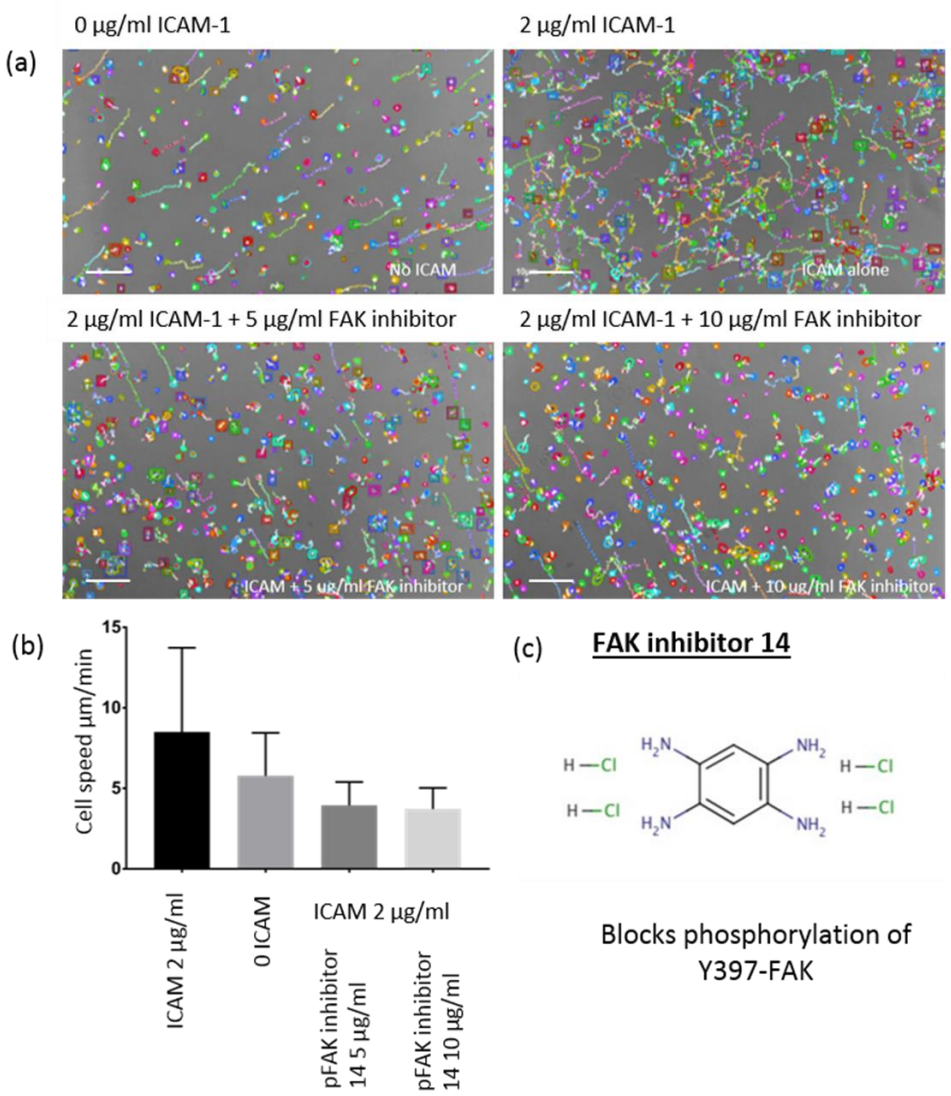

Figure 6-2: **Cells treated with pY397 FAK 14 inhibitor tracked on ICAM-1 coated coverslip.** Non migrating cells (0 µg/ml ICAM) were compared with migrating cells treated with FAK inhibitor at 5 or 10 µg/ml. a) example frames from tracked phase contrast movies. b) plot of cell speeds derived from cell tracking (median and IQR). C) skeletal formula for FAK inhibitor 14. Scale bar 40 µm.

Cells treated with FAK inhibitor at 5 or 10 µg/ml were then fixed, permeablised and stained with the anti-FAK antibody, before being imaged using dSTORM. dSTORM was used instead of confocal microscopy due to its heightened sensitivity. Figure 6-3 shows representative untreated cells, which are polarised and display large amounts of pY397 FAK, as compared to FAK inhibitor treated cells (figure 6-3 middle and right panels) which are rounded and have only a small amount of signal remaining in the periphery. These results were marked and consistent (n = 3 experiments and 34 cells), therefore the anti-p397 FAK antibody was taken forward for use in iSTORM experiments, to investigate the 3D clustering of the molecule, and whether it is similarly modulated above the height of the cell membrane like LFA-1.

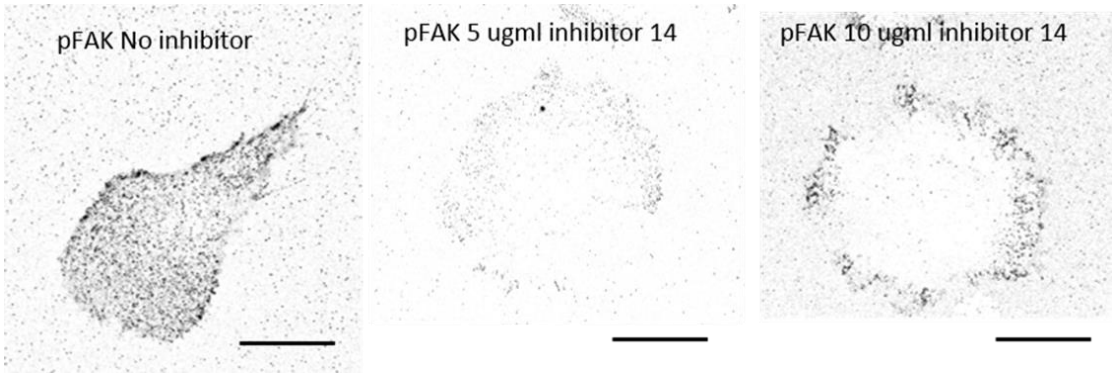

Figure 6-3: **Cells subject to pY397 FAK inhibition display a much reduced level of anti-pY397 FAK detected by dSTORM microscopy.** Cells plated on ICAM-1 were treated with either 5 or 10 µg/ml pY397 FAK inhibitor 14, known to target the 397 tyrosine phosphorylation site. In both cases, cells (representative) were rounded and unmigratory, and pY397 FAK signal was vastly reduced. Scale bar 5 µm.

Stationary and migrating PTPN22$^{+/+}$ and PTPN22$^{-/-}$ cells fixed on ICAM-1 coated coverslips with gold nanorods (methods) were stained with the anti-p397 FAK antibody and located using DIC on the iSTORM (figure 6-4 top panels show representative cells). These were then imaged over 20 000 frames to produce a localised map (figure 6-4 middle panels). 'Empty' regions of the cells relate to the position of fiducials used for alignment of the microscope and maximising the interference contrast[77]. Magnified sections show differences in the heights of populations of pY397 FAK molecules in a representative wildtype stationary cell versus a representative wildtype migratory cell (figure 6-4 lower panels). 2000 x 2000 x 420 nm regions were taken from all regions of stationary cells proficient or deficient for PTPN22, and the segregated leading edge and focal zone of migrating cells proficient or deficient for PTPN22. As in the previous section, 3D clustering was compared between conditions first irrespective of the z heights of the identified clusters, before being compared versus z.

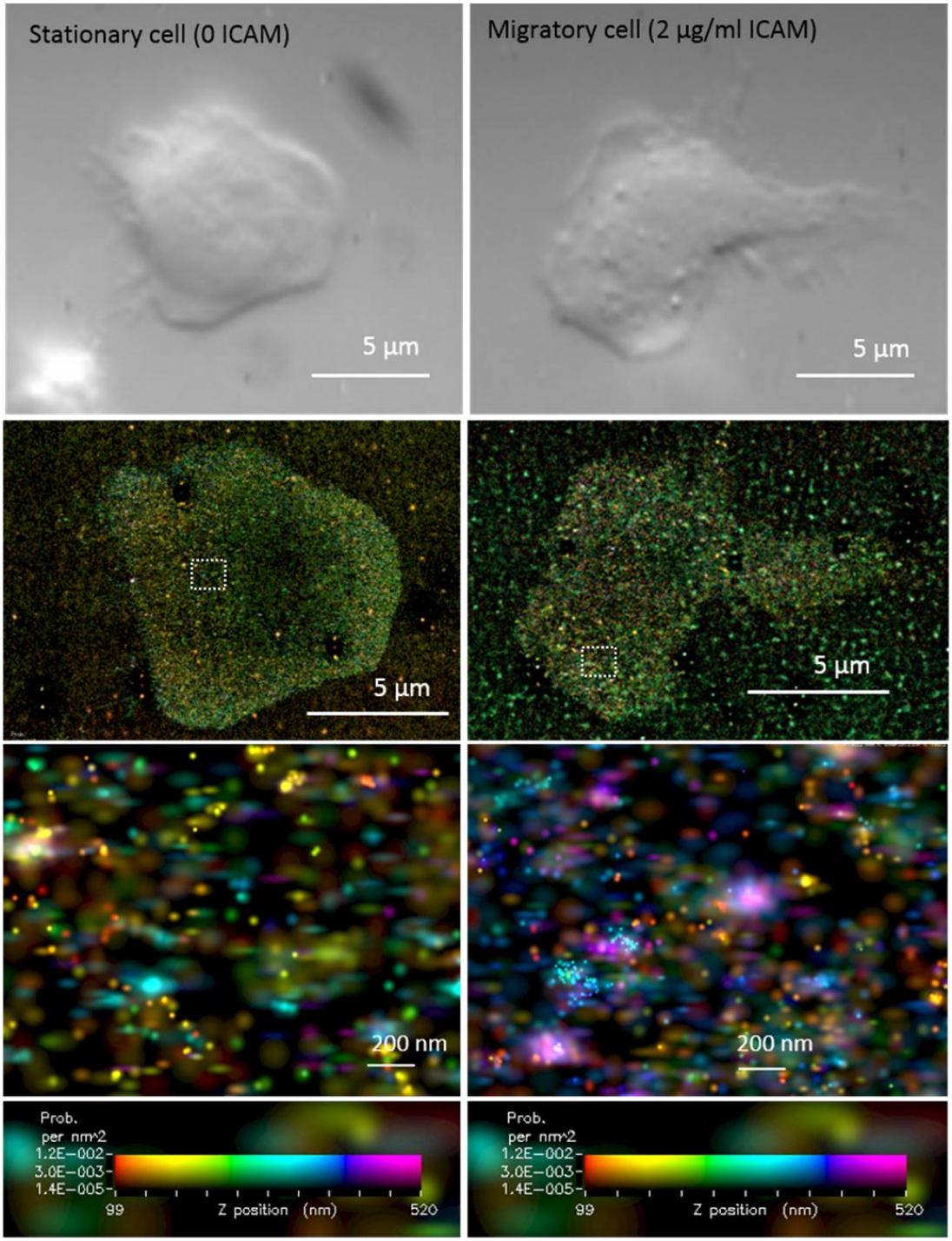

Figure 6-4: **Intracellular nanoscale pY397-FAK imaged to 30 nm isotropic 3D resolution in stationary and migrating PTPN22$^{+/+}$ and PTPN22$^{-/-}$ T cells.** A representative PTPN22$^{+/+}$ stationary cell (left) and migrating cell (right) is shown in DIC (top panels). Middle panels show iPALM images of pY397 FAK in whole cells, and zoomed regions indicated by white boxes are shown below. z position scale bar common to both images is indicated in the lower panels.

6.1.1 3D py397 FAK clustering in PTPN22$^{-/-}$ T cells irrespective of z

In order to interrogate whether nanoclustering changes in phosphorylated Y397 FAK are important for migration speed and/or PTPN22 mediated regulation of integrin clustering, metrics for clusters per 2000 x 2000 x 420 nm region were analysed in cells stationary (0 ICAM-1 on the plate) or migrating (2 µg/ml ICAM-1 surface) at different speeds in cells either proficient of deficient for PTPN22, which migrate faster (figure 6-1). Cluster metrics were plotted irrespective of the z height, such that the following represent overall answers for pY397 FAK clustering across the entire 420 nm depth.

The **total pY397 FAK molecules per region (figure 6-5a)** remained similar throughout the leading edge (orange) 3D volume of PTPN22$^{+/+}$ migrating cells, but dropped significantly in the focal zone (blue) 3D volume of PTPN22$^{+/+}$ migrating cells (n = 3 mice, 20 cells, ****p<0.00001). This trend remains intact in PTPN22$^{-/-}$ migrating cells, but overall there is more pY397FAK in PTPN22$^{-/-}$ migrating cells. PTPN22$^{-/-}$ stationary cells have less pY397 FAK than PTPN22$^{+/+}$ stationary cells.

The **percentage of clustered molecules (figure 6-5b)** increased significantly in PTPN22 proficient migrating cells upon migration (compared to stationary cells), and decreased in PTPN22 deficient cells upon migration (compared to stationary cells). As there was no change in the percentage clustering from *stationary* wildtype cells to *stationary* knockout cells, the decrease seen in knockout cells can be seen to be specific to migration. In terms of percentage clustering in the 3D imaging volume, there is no regional discrimination between the leading edge and focal zone – both display around 60 % clustering in PTPN22$^{+/+}$ and 50 % clustering in PTPN22$^{-/-}$ cells.

The **number of clusters** (figure 6-5c) was unchanged in the transition from stationary to migrating cells in the leading edge, but both PTPN22$^{+/+}$ and PTPN22$^{-/-}$ cells had fewer clusters in the focal zone than the leading edge. There was no significant difference in the number of pY397 FAK clusters between PTPN22$^{+/+}$ and PTPN22$^{-/-}$ cells. pY397 FAK clusters are therefore concentrated in the leading edge of migrating T cells.

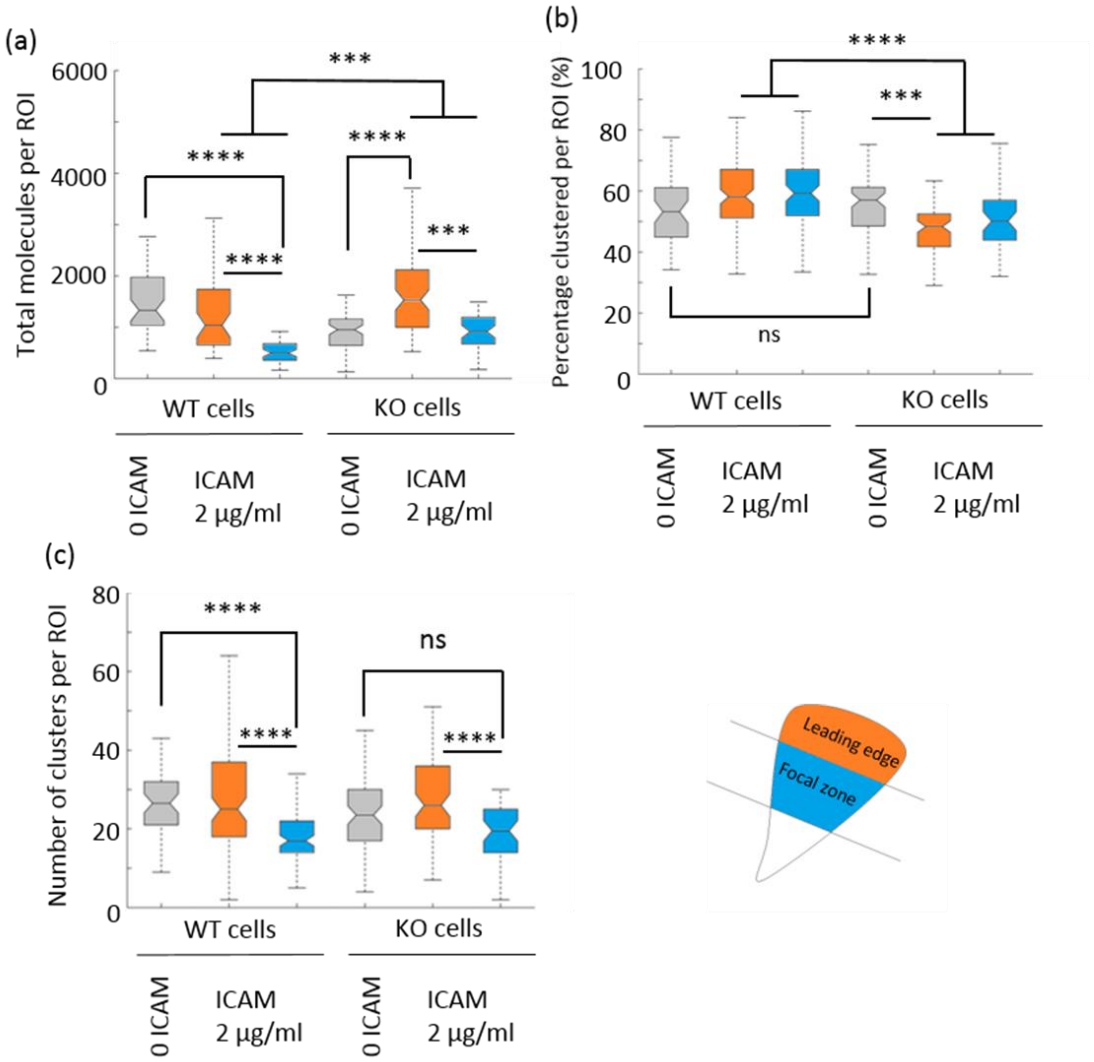

Figure 6-5: **Overall 3D clustering of pY397 FAK in PTPN22 proficient and deficient stationary and migrating T cells.** Cluster parameters per ROI were extracted from the 3D imaging volume and plotted irrespective of their z positions: the total molecules (a), the percentage of those molecules in clusters (b) and the number of clusters (c). N = 20 cells from 3 mice 200 + ROIs per condition. ****p< 0.0001

In addition to per ROI characteristics of clusters (the above), individual pY397 FAK clusters were also interrogated in 3D in terms of their size and molecular density.

Upon migration (comparing stationary cells - grey bars - to migrating cells) overall 3D pY397 FAK clusters get significantly smaller in both the leading edge and focal zone of PTPN22+/+ and PTPN22-/- T cells – a ~ 20 % decrease (median values - figure 6-6a). Clusters are significantly larger in the focal zone (blue) as compared to the leading edge (orange). In PTPN22 deficient cells, this regional trend is maintained, but clusters are larger in both zones (figure 6-6a).

In terms of molecular content, clusters have significantly fewer molecules in PTPN22+/+ migrating cells than they do in stationary cells (figure 6-6b – grey bar compared to orange and blue). This phenomenon is not true in PTPN22-/- cells, where the number of molecules per cluster is significantly decreased in stationary cells, such that migrating PTPN22$^{-/-}$ cells have clusters with the same molecular content as PTPN22$^{+/+}$ cells. Across both PTPN22$^{+/+}$ and PTPN22$^{-/-}$, pY397 FAK clusters in the focal zone of cells contain significantly fewer molecules than clusters in the leading edge (figure 6-6b).

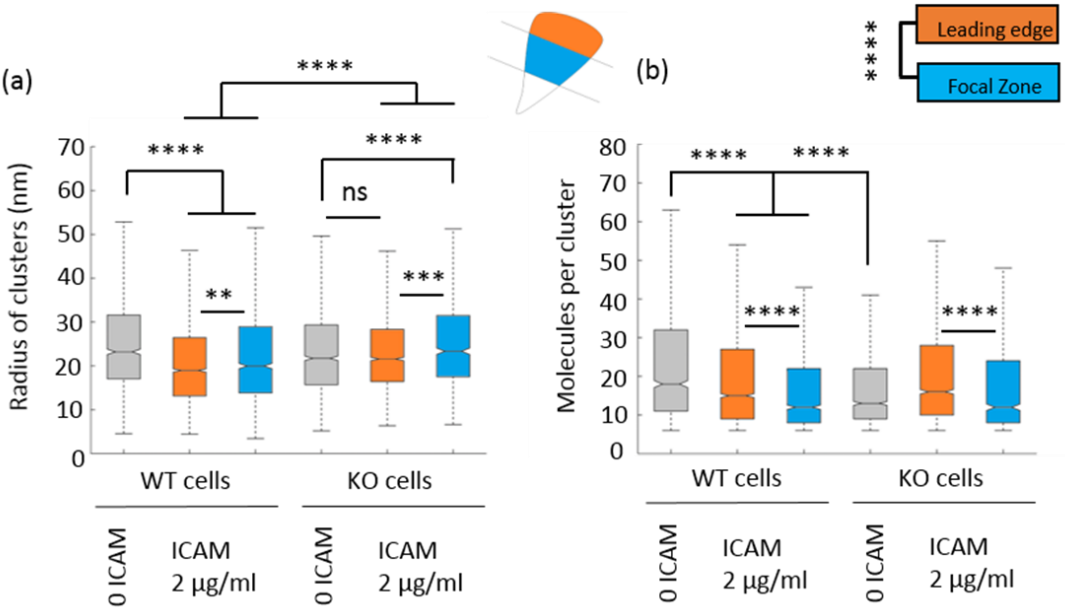

Figure 6-6: **Overall 3D individual cluster metrics size and number of molecules per cluster of pY397 FAK in PTPN22 proficient and deficient stationary and migrating T cells.** Individual cluster parameters per ROI were extracted from the 3D imaging volume and plotted irrespective of their z positions: the radius of clusters (a) and the number of molecules per cluster. N = 20 cells from 3 mice 200 + ROIs per condition. ****p< 0.0001

To summarise, pY397 FAK adopts a regional nanoclustering distribution upon cell migration. In polraised cells, pY397 FAK monomers and clusters are concentrated in the leading edge, with the same percentage in clusters in the LE and FZ. Clusters in the leading edge of PTPN22$^{+/+}$ and PTPN22$^{-/-}$ migrating cells are smaller and with more molecules as compared to clusters in the focal zone. PTPN22$^{-/-}$ cells display less percentage clustering, and their clusters are larger and less dense than those in PTPN22$^{+/+}$.

Clearly, there is a large amount of heterogeneity in the cluster metrics as a function of height, where the clustering across the volume is summarised. In order to further interrogate height biases in characteristics of pY397 FAK clustering, the per ROI and per cluster metrics measured above were plotted against the z dimension.

6.1.2 3D pY397 FAK clustering in PTPN22$^{-/-}$ T cells as a function of z

It is clear that in stationary cells, there are more **total pY397 FAK molecules** close to the height of the membrane in PTPN22+/+ cells (figure 6-7, left). A population close to the membrane in PTPN22-/- stationary cells (orange bars) is no longer present in PTPN22+/+ stationary cells (blue bars). This is reflected in the skewness, which is greater s = 1.20 for PTPN22+/+ cells as opposed to PTPN22-/- cells s = 0.89 describing a skew for total pY397 FAK from the membrane in stationary PTPN22-/- cells.

Upon migration as we have seen in figure 3-5, pYFAK distributes itself in a polarised manner towards the leading edge. In both the leading edge and focal zone, there is more pYFAK near the membrane (all s values positively skewed figure 6-7). PTPN22-/- cells always have more pYFAK molecules than PTPN22+/+ cells, and these plots show that this increase occurs preferentially at z heights closer to the membrane in both the leading edge (middle - yellow and purple) and focal zone (right - light blue and green). In migrating cells, the skewness values for PTPN22+/+ cells (LE = 0.91 FZ = 1.12)) are reduced as compared to PTPN22-/- cells (LE = 1.29 FZ = 1.39), indicating a shift to the right hand side, away from the membrane, deeper into the cell. In other words, there are more molecules deeper in the cell in PTPN22-/- cells as compared to PTPN22+/+ cells. In both PTPN22+/+ and PTPN22-/- cells, there are fewer molecules in the focal zone as compared to the leading edge.

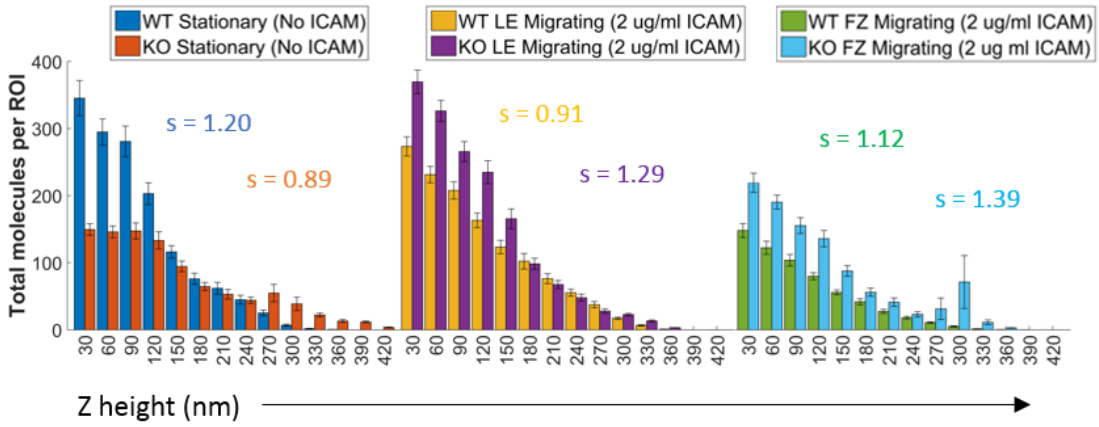

Figure 6-7: **Total pY3197FAK molecules per region plotted against z height, stationary cells and the leading edge/focal zone of migrating cells that were proficient or deficient for PTPN22 imaged by iPALM and analysed using 3D Bayesian cluster analysis.** The leftmost plots are conditions: PTPN22+/+ and KO stationary (0 ICAM-1). In the middle are PTPN22+/+ and KO leading edge migrating cells. On the right are PTPN22+/+ and KO focal zone of migrating cells. Skewness values are colour coded for each plot. N = 3 mice, 20 cells and 200 ROIs per condition.

The **percentage of pY397 FAK molecules participating in clusters** (figure 6-8) also correlates to cell migration characteristics. The skewness values here are closer to 0 but just above, meaning that there is a more gentle preference for the membrane, and that there is a lot of p397FAK clustering higher up in the cell. Comparing PTPN22+/+ and PTPN22-/- stationary cells, PTPN22-/- cells have a greater percentage of clustered molecules all through the cell than PTPN22+/+ cells. Upon migration, the percentage of clustered molecules adopts a distribution where there is more clustering close to the membrane and less clustering deeper into the cell. PTPN22+/+ cells always have more of the population clustered at all z heights and in both regions compared to PTPN22-/- cells.

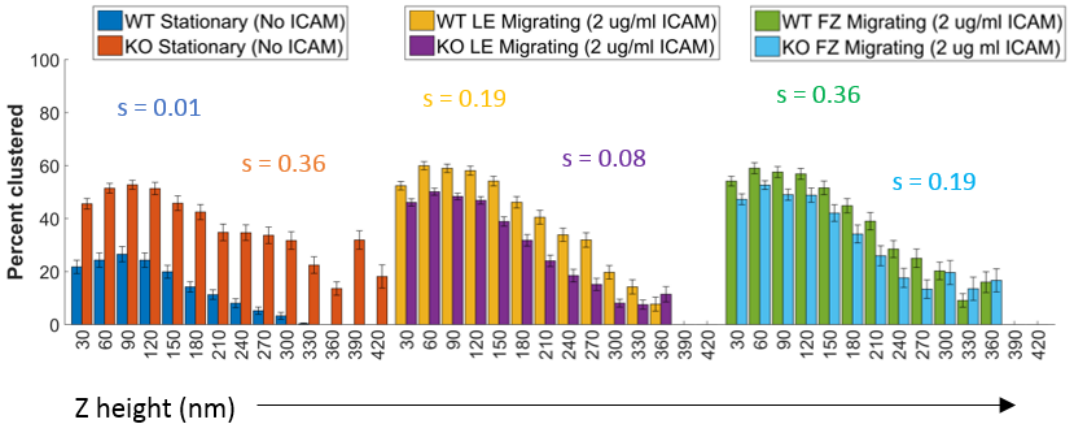

Figure 6-8: **Percent pY3197FAK clustered per region plotted against z height: stationary cells and the leading edge/focal zone of migrating cells that were proficient or deficient for PTPN22 imaged by iPALM and analysed using 3D Bayesian cluster analysis.** The leftmost plots are conditions: PTPN22+/+ and KO stationary (0 ICAM-1). In the middle are PTPN22+/+ and KO leading edge migrating cells. On the right are PTPN22+/+ and KO focal zone of migrating cells. Skewness values are colour coded for each plot. N = 3 mice, 20 cells and 200 ROIs per condition.

In terms of the **number of clusters (figure 6-9)**, upon migration, there is a skew towards the cell membrane coupled to a general increase. This may represent recruitment of pY397 FAK clusters to the membrane upon cell migration from a pool higher up and pre-existing before migration and engagement with ICAM-1. This phenomenon is more severe in the leading edge than the focal zone. There is no significant difference in the z distribution of the number of clusters between migrating PTPN22+/+ and PTPN22-/- cells. While in stationary cells, there are a more clusters higher up in the cell in the PTPN22-/- sample, the skew towards the membrane still remains.

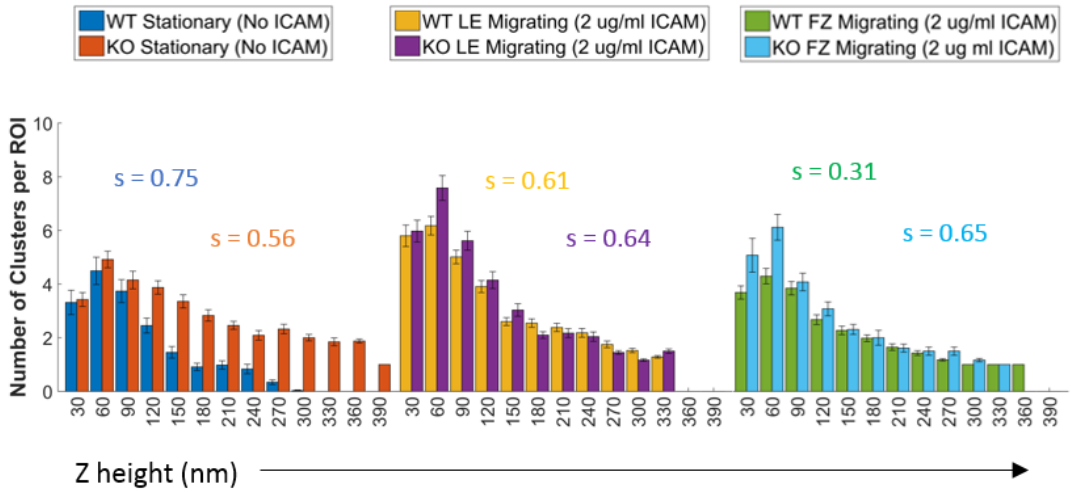

Figure 6-9: **Number of pY3197FAK clusters per region plotted against z height: stationary cells and the leading edge/focal zone of migrating cells that were proficient or deficient for PTPN22 imaged by iPALM and analysed using 3D Bayesian cluster analysis.** The leftmost plots are conditions: PTPN22+/+ and KO stationary (0 ICAM-1). In the middle are PTPN22+/+ and KO leading edge migrating cells. On the right are PTPN22+/+ and KO focal zone of migrating cells. Skewness values are colour coded for each plot. N = 3 mice, 20 cells and 200 ROIs per condition.

As previously, two individual cluster metrics, the size and molecular content, were extracted and plotted against z height within the 420 nm volume from the coverslip for PTPN22+/+ and PTPN22-/- cells. The size of clusters in stationary PTPN22-/- cells is much larger across all z heights in PTPN22-/- cells (figure 6-10a – orange PTPN22-/- bars as compared to blue PTPN22+/+ bars), as is their molecular content(figure 6-10b – orange PTPN22-/- bars as compared to blue PTPN22+/+ bars). Upon migration, this equalises so that PTPN22+/+ cells show the same trends as PTPN22-/- cells in terms of radius and molecules per cluster: in the leading edge larger, higher molecular content clusters are localised in the most part to an area around 90 nm from the coverslip – very close to the cell membrane. Higher up in the cell, clusters are smaller with fewer molecules. In the focal zone, as seen in the whole z volume plots in section 6.1.1, clusters of pY397 FAK are far smaller and consist of fewer molecules also. In the focal zone as in the leading edge, there is a bias towards the membrane that remains, where slightly larger focal zone clusters are in or close to the cell membrane.

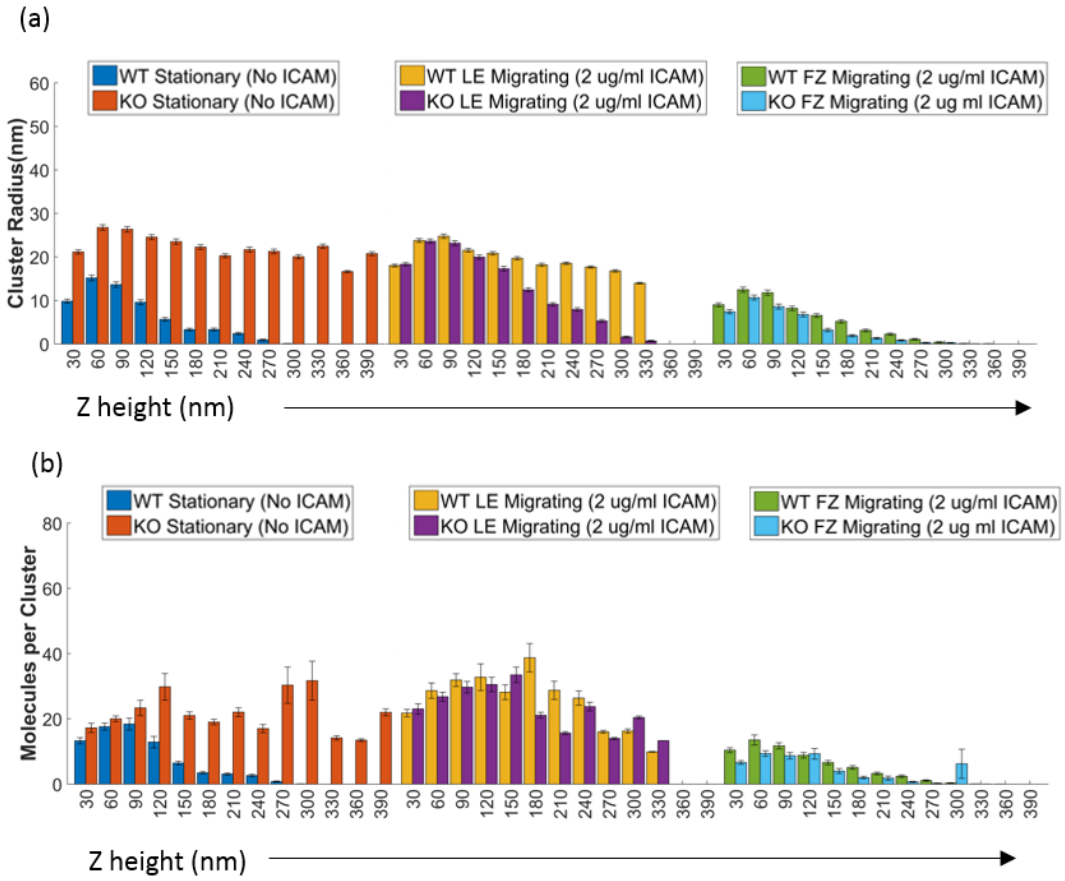

Figure 6-10: **The cluster radius and number of pY3197FAK molecules plotted against z height: stationary cells and the leading edge/focal zone of migrating cells that were proficient or deficient for PTPN22 imaged by iPALM and analysed using 3D Bayesian cluster analysis.** For the radius (a) and the number of molecules (b): The leftmost plots are conditions: PTPN22+/+ and KO stationary (0 ICAM-1). In the middle are PTPN22+/+ and KO leading edge migrating cells. On the right are PTPN22+/+ and KO focal zone of migrating cells. Skewness values are colour coded for each plot. N = 3 mice, 20 cells and 200 ROIs per condition.

6.1.3 Discussion of 3D pY397 FAK clustering

Having established that LFA-1 integrin, the basic unit for ubiquitous ICAM-1 based nano-adhesions, arranges itself in nanoclusters in both the membrane and membrane proximal intracellular region, we next wanted to investigate auto-phosphorylated pY397FAK, one of the first active kinases recruited to nascent adhesions in diverse cell types, and known to be involved in assembly and disassembly of adhesions during recycling, as well as having a presence in integrin containing vesicles[75]. The aim of looking at intracellular FAK in this context was to assess whether its nanoscale 3D distribution is also related to cell speed, and whether that distribution is similar or different to that of LFA-1 integrin.

The first thing that can be concluded is that FAK arranges itself into nanoclusters, as can be seen from the 3D cluster maps (figure 6-4). This is perhaps no surprise, seeing as we know that pY397 FAK associates with integrin LFA-1 based adhesions in T cells, although it is interesting that this nanoclustering not only happens close to the membrane, there are also nanoclusters further up in the cell – only recently was evidence put forward that FAK associates with integrin in preformed vesicles that may be being trafficked to or from the membrane[71]. This therefore backs up the existing literature that pY397FAK is present in all areas of the migrating cell, but is also present in stationary cells, as this form of pY397 FAK is constantly present and almost constitutively phosphorylated[248].

In looking at the results holistically, it is clear that most of the pY397 FAK is localised towards the front edge of the cell (within the leading edge/lamella region). In all cases, the trends seen in the leading edge mirror what goes on in the focal zone, unlike for LFA-1. The 3D distribution of the pY397 FAK molecule is the same in the leading edge and focal zone, its just that there is less of it. There is always more pY397 FAK closer to the membrane, which is more clustered in this region.

The pure amount of FAK in the cell centre was reduced by half in both $PTPN22^{+/+}$ and $PTPN22^{-/-}$ fast moving cells. Interestingly, there is a huge concentration of FAK in both the leading edge and focal zones of the cell when PTPN22 is deficient. This is coupled to a hugely decreased amount of clusters and clustering in stationary cells, perhaps pointing to the lack of this Lck specific control switch, which links to FAK in its recruitment of the Src kinases[73]. Where PTPN22 isn't present, it will allow uncontrolled phosphorylation of Lck at pY394, a potentiator for Lck's ability to activate FAK. There are always slightly more clusters in of pY397 FAK in PTPN22-/- cells than in PTPN22+/+ cells.

Interestingly, when individual cluster parameters are measured, there is a decrease in the cluster size in migrating and stationary PTPN22-/- cells at high z heights. This is aside from the fact also, that in stationary cells there are the biggest changes, with PTPN22-/- cells having large radius FAK clusters similar to during migration, whereas PTPN22+/+ cells lack such clusters. This could be significant biologically (as well as statistically), and indicates that FAK is usually controlled in its cluster size, but when PTPN22 is deficient it can no longer control its activation and clustering (model figure 6-11).

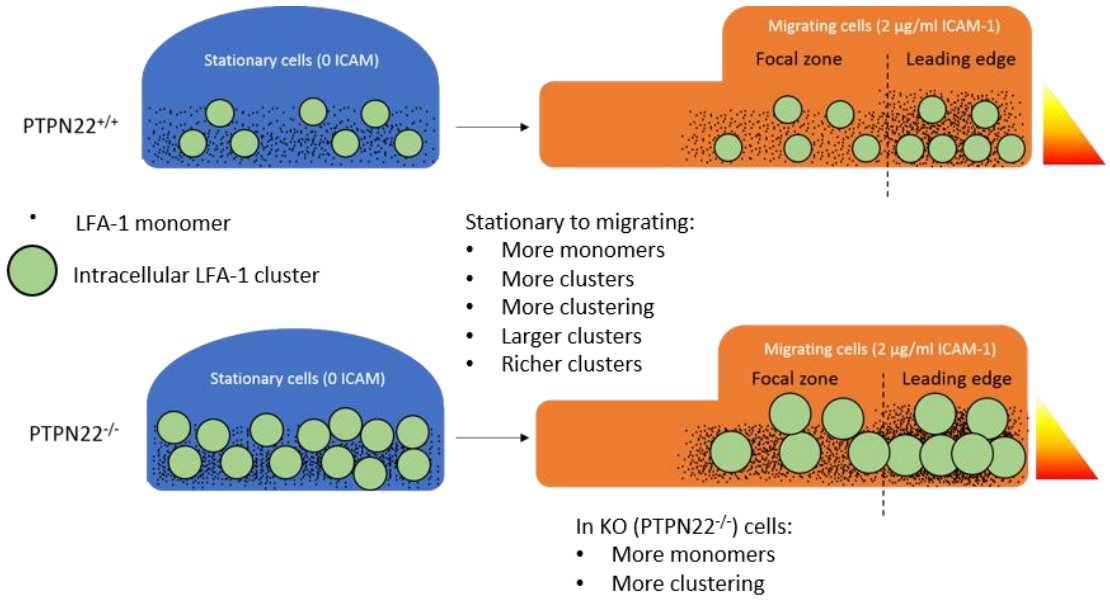

Figure 6-11: **Model for intracellular pY397 FAK nanoclustering in PTPN22$^{+/+}$ (PTPN22+/+) and PTPN22$^{-/-}$ (KO) stationary and migrating cells.** Stationary and migrating cells all exhibit a gradient where the closer to the membrane you are, there are more monomers, more clusters, more clustering, larger clusters and richer clusters (more molecules per cluster) – represented by the colour bars. These trends are also true in switching from a stationary to a migrating state, and between the leading edge and focal zone of migrating cells. In KO cells, pY397 FAK clusters are larger and richer, and there are more monomers and more clustering.

6.2 Cell speed and LFA-1 nano-adhesion activity using two phosphorylated intermediates: pY397 FAK and pY416 Src

T cell nano-adhesions resemble nascent adhesions in non-leukocytes: they are usually < 100 nm in size and their entire lifespan is on the order of minutes to seconds. Adhesion maturation and maintenance into the lamella of nascent adhesions usually involves growth in size. Conversely, T cell nanoadhesions get smaller, denser and closer together in the lamella/focal zone, representing a possible different method of maturation for fast moving cells (section 5).

Nascent adhesions are regulated by certain markers, including pY397 FAK which is associated with the very earliest stages of their formation[73]. As nascent adhesions mature and strengthen, they recruit phosphorylated Src family kinases such as Lck, which SH2 bind to FAK. This results in a known signalling cascade describing an active adhesion, with the recruitment of p130CAS, and a host of proteins involved in actin linkage and regulation of the molecular clutch. The further recruitment of pYFAK induced by this Src binding initiates maturation and disassembly of the adhesion[69].

I wanted to find out whether this distribution is followed from the front to the back of T cells in LFA-1 based nano-adhesions, and whether the selective association of pY397 FAK and or pLck operates regionally on the nanoscale, as reliable markers of, or proxies for integrin activity. Secondly I wanted to discern whether changes in the recruitment of such complexes work to regulate cell migration speed in single cells. Finally, I wanted to compare the recruitment of such kinases in different zones of the cell in a situation where PTPN22, a phosphatase that dephosphorylates Lck and functionally increases the migration speed of T cells, is removed.

By comparing measurements of single cell speeds and clustering with PTPN22-/- cells, I hope to delineate between clustering effects that happen as a necessary result of cell speed changes (ie a correlation between cluster parameters and cell speed within the same condition) or whether the clustering changes (seen on a population level in section 5) are based on PTPN22 deficiency.

To achieve this, cells migrating on an ICAM-1 coated dish were imaged in a heated chamber on the dSTORM microscope, using the 100 x lens to make a 6 x 6 field of view composite image for each frame. This allowed us to image the cells migrating for 10 minutes, then add a

fixative to the sample while the cells were being imaged on the microscope. Cells were then tracked, migrating cells identified and their positions recorded using the software, before being subject to sequential rounds of staining and elution with the inclusion of nanodiamonds as fiducial markers (madSTORM is described in methods). The output of these experiments were 15 to 20 cells per condition with their speed of migration up to the point of chemical fixation recorded, and three channels of clustering data for three molecules of interest in each cell: transmembrane LFA-1, intracellular pY397 FAK and intracellular pY416 Src targeting both pY416 Lck and pY416 Fyn. Several controls were carried out to maintain nanostructure in the transition from live cells to STORM imageable cells on the microscopy stage.

6.2.1 Controls for sequential imaging: cell permeablisation and nano-diamonds

The protocol for this technique was designed to allow imaging of membrane resident LFA-1, and then to image intracellular pY397 FAK and pY416 Src. As this is an antibody staining regimen, the sample must be permeablised in between the LFA-1 staining and the pY397 FAK or pY416 Src staining steps. Permeablisation involves the sequestration of lipids from the membrane, and was therefore care must be taken that proteins of interest are not changing their position because of this lipid rearrangement. Triton x-100 is known to be a relatively harsh detergent, so was tested against saponin, a much gentler permeablisation method, to test its viability for sensitive nanoscale studies of clustered molecules (figure 6-12). Saponin or triton was added to cells which were then stained using anti-pY416 Src, an antibody against an intracellular target. Example localised coordinate maps of pY416Src in cells treated with triton (figure 6-12a) are shown versus saponin (figure 6-12b). Zooms of 2 μm^2 regions taken from these cells are shown in (c) and cluster maps are shown in (d). From the maps, and from the quantitation in figure 6-12e, it is clear that Triton permeablisation resulted in widespread staining which showed an increase in the number of molecules (figure 6-12e) and clusters (figure 6-12f) in the focal zone as compared to the leading edge. Saponin recapitulated this trend, but with far fewer molecules being stained (bars on the right of both plots). Triton resulted in more molecules being detected in a single stain and was therefore taken forward for further testing.

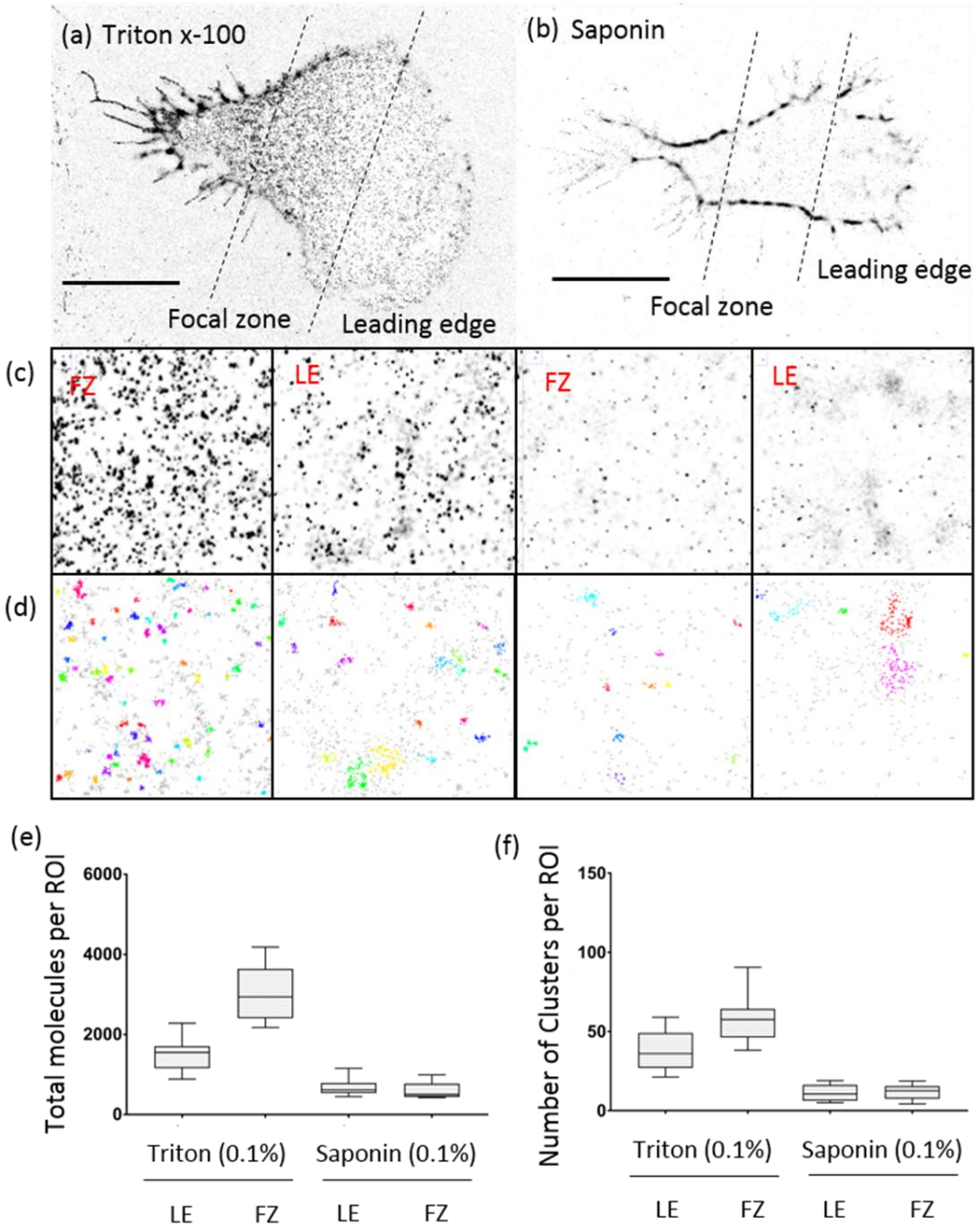

Figure 6-12: **Triton permeablisation allows pY416 Src antibody into cells, whereas saponin staining prevents this.** Migrating T cells were fixed and permeablised with triton (a) or saponin (b) for 10 minutes at 0.1 %. Cells were stained with pY416 Src, an antibody to an intracellular target and imaged by dSTORM (zoomed regions shown in (c) and analysed by Bayesian cluster analysis: example cluster maps are shown in (d). E) plot of total molecules and f) number of clusters in triton treated versus saponin treated cells. Scale bar 4 µm.

madSTORM is a multiplexed technique[146], involving several rounds of antibody staining before cell permeablisation (LFA-1) and after cell permeablisation (pY397 FAK and pY416 Src). While fixation was addressed in section 3, and transient unwanted permeablisation by PFA was minimised with the use of a buffer solution and the addition of glutaraldehyde, the effects of triton x-100 based permeablisation on the nanoscale characteristics of a population of molecules has not been addressed in the context of these experiments. In order to ensure that the addition of Triton caused no displacement to the molecules on the nanoscale, membrane LFA-1 was stained for (as this stain is now well characterised and covered in detail in section 5) and the cells were imaged without (figure 6-13a, cluster maps below) or with triton applied after staining (figure 6-13b, cluster maps below). Triton x-100 at 0.1 % in PBS was found to not affect the nanoscale clustering characteristics of LFA-1 (figure 6-13c to 6-13f) with the one exception of cluster radius (figure 6-13e), which showed only a slight perturbation (~ 2 nm) and was therefore judged to be a reliable method for permeablising cells and the nanoscale imaging of clustered molecules. This test was performed on a limited sample of 10 cells.

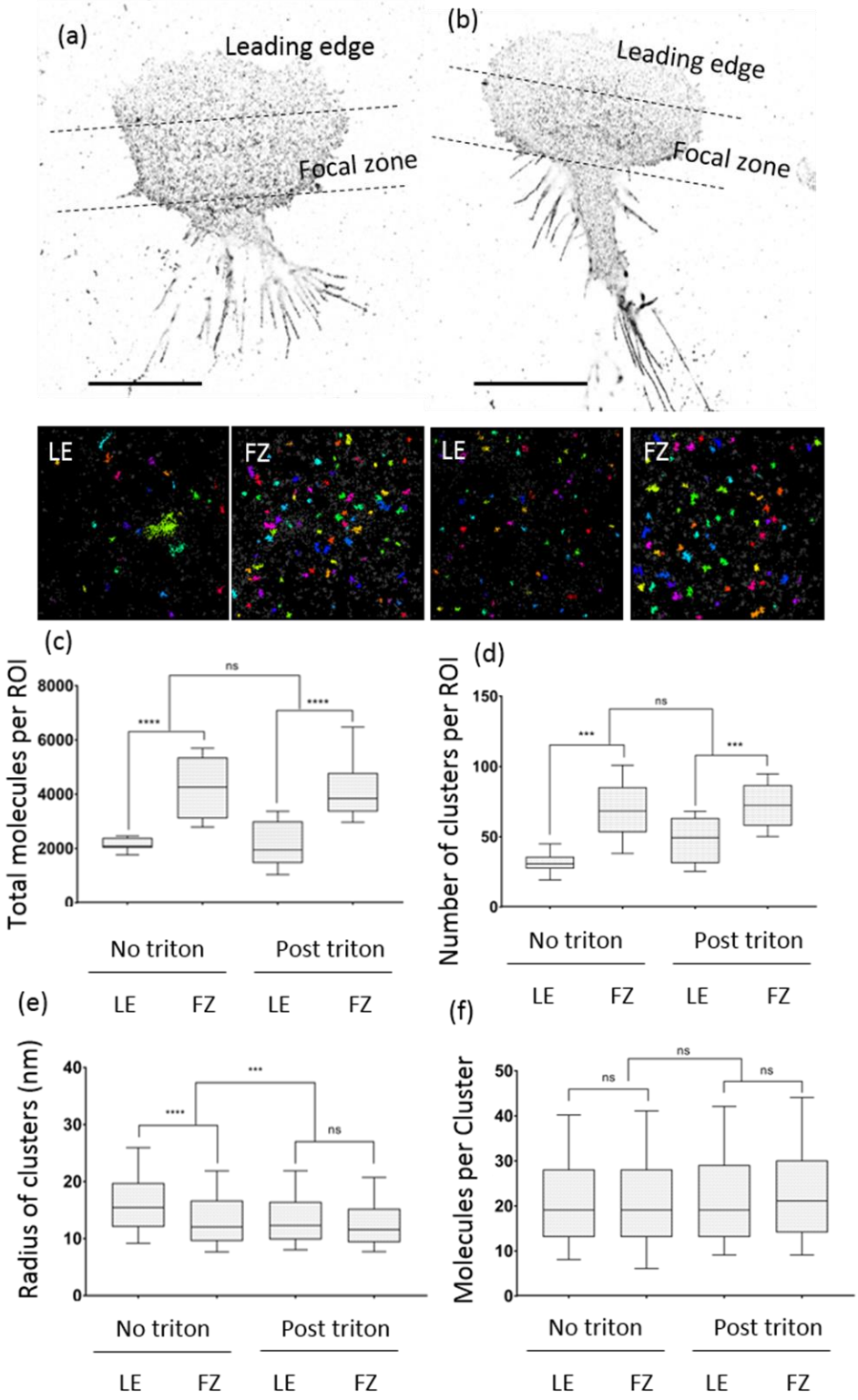

Figure 6-13: **Triton application after staining doesn't change the nanoscale characteristics of LFA-1.** Migrating T cells were fixed and stained for LFA-1 integrin and left untreated (a) or treated (b) with triton x-100 after staining. Cluster analysis of regions was carried out quantitation is shown in plots c to f. Scale bar 4 µm.

In order to register and align the 3 channels after imaging, fiducial nanodiamonds were used. The advantage of such diamonds is that compared to tetraspeck beads, a commonly used fiducial marker, they are reported to be more photostable with an increased quantum yield, allowing precise localisation in every frame and subsequent averaged fiducial correction (AFC) with sub 10 nm alignment error[146]. Nanodiamonds vary in size, within certain limits (dictated by size fractionation done in Keir Neumann's lab at NIH), and their photon output is proportional to this size. To test their stability, and which sized nanodiamonds would be viable for use as fiducial markers, fields of diamonds were imaged by dSTORM and localised over 10 000 frames. Uncertainty values associated to each localisation in each frame are shown in the images of nanodiamond beads (figure 6-14b). Bright diamonds, estimated to be around 80 nm in size were consistently and stably localised with below 10 nm uncertainty. Low emitting (small) diamonds gave a greater spread of uncertainty values at around 20 nm, which were nonetheless stable over the course of acquisition. These tests informed the concentration of diamonds required to achieve at least 5 medium or bright diamonds in the field of view, and was used for all future experiments (protocol described in methods).

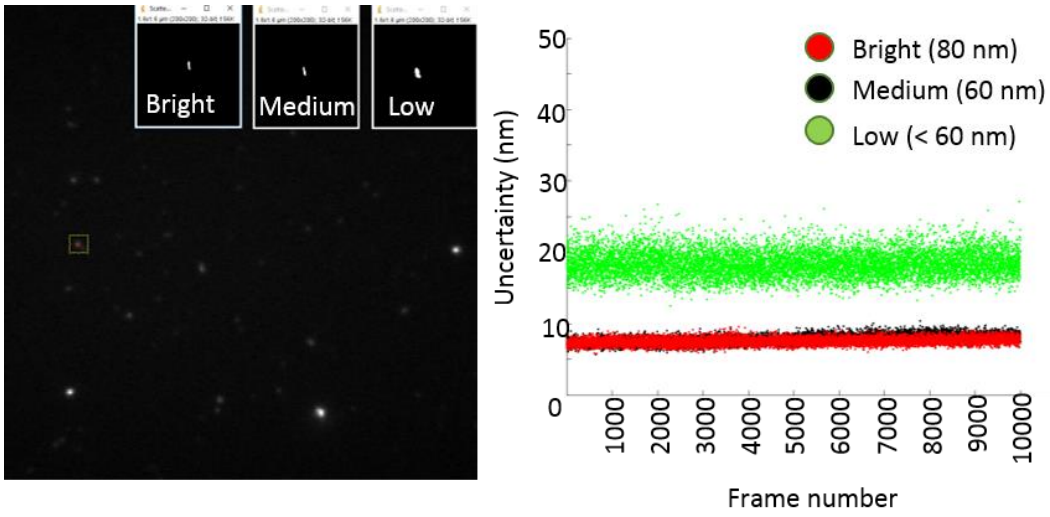

Figure 6-14: **Fluoresencent nanodiamonds that could be localised to < 10 nm precision were chosen for alignment and drift correction.** Diamonds plated onto a glass coverslip were imaged for 10000 frames by dSTORM in the same conditions as for antibody labelled cells. Bright and medium bright non-aggregated diamonds corresponding to larger sizes gave measured uncertainty values of < 10 nm and did not dim. Smaller, lower intensity diamonds (green) were not used.

6.2.2 Population level cell speeds and clustering characteristics of LFA-1, pY397 FAK and pY416 Src in PTPN22$^{-/-}$ and PTPN22$^{+/+}$ migrating T cells

To validate this correlative method of imaging and tracking cells before fixing and staining them, we wanted to replicate the enduring phenotype of increased migration speed in populations of PTPN22 deficient T cells using a different imaging technique, as described above. This was done by imaging the cells migrating on ICAM-1 with an 100 x lens on the dSTORM microscope, creating a large 6 x 6 tiled reconstructed field of view for each frame. Keeping the sample on the stage meant that cell coordinate positions could be recorded, and the same cell brought back into the field of view and aligned for subsequent rounds of dSTORM imaging. Cell tracks were measured manually, in order to match up with the cells imaged later in dSTORM (figure 6-15b). The final 3 frames, totalling ~ 60 seconds, were measured and mean speeds per cell are shown in figure 6-15c, where PTPN22$^{-/-}$ cells moved faster as a population.

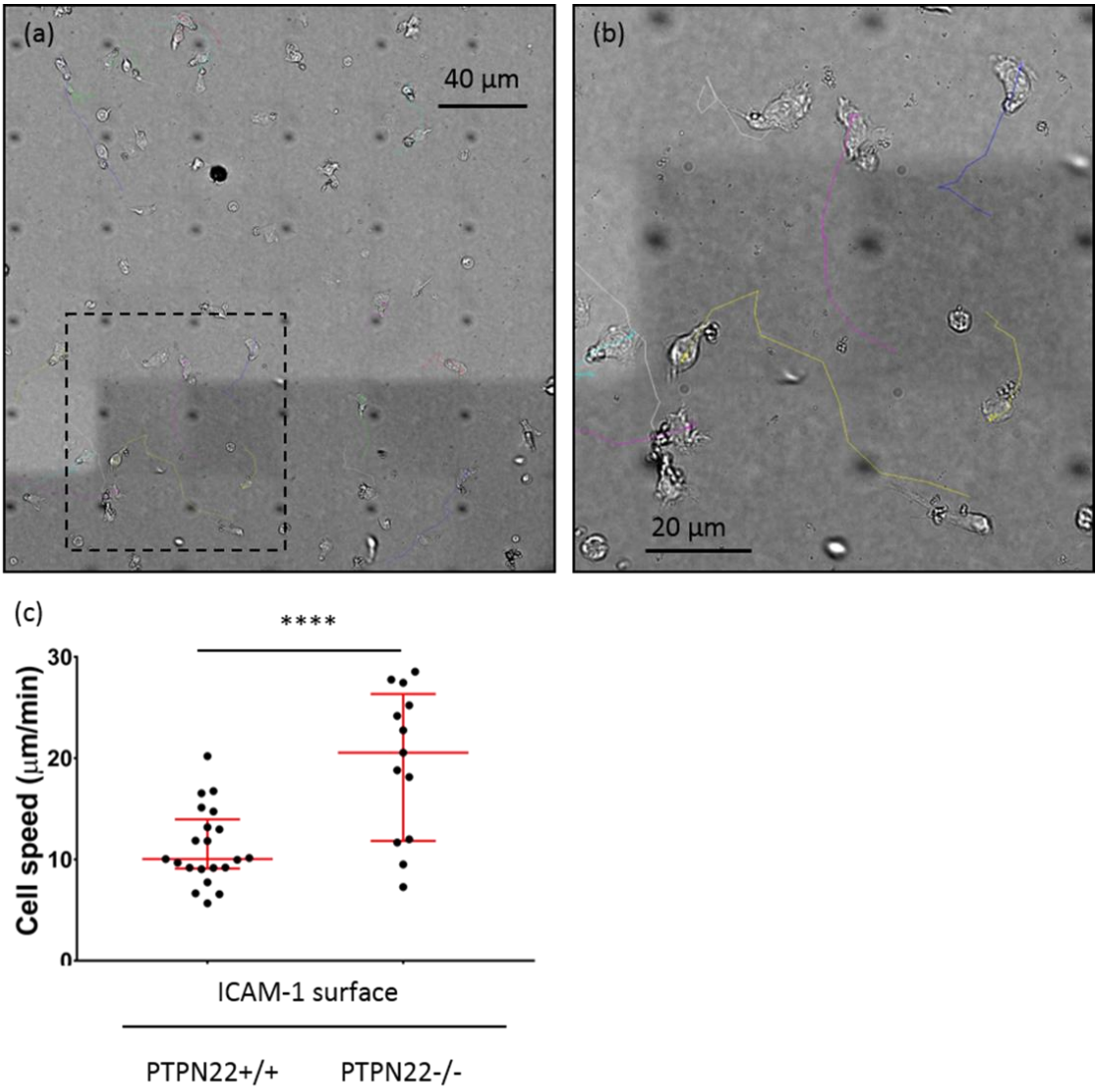

Figure 6-15: 100 x magnification images were stitched into a large field of view and cells were tracked manually prior to fixation, staining and dSTORM imaging. a) A large FOV was attained using 36 small 100 x fields of view stitched together computationally (Nikon elements software) b) zoomed image showing migrating cells were tracked to attain cell speeds, up to the point of fixation on the stage. c) quantitation of cell speeds show that PTPN22-/- cells move faster on average

After 10 minutes of migration, PTPN22$^{+/+}$ or PTPN22$^{-/-}$ cells were fixed on the microscope stage, by adding the fixative to the correct concentration given the volume of solution already present in the microscope dish (methods). This was simply done by reaching into the microscope stage with a pipette. The advantage of continuing imaging during fixation is that any cell scale dysmorphic effects are clearly visible. Migrating cell positions were then recorded using the Nikon elements software package, and the sample was removed from the

microscope for staining. The sample was then removed from the microscope stage, stained and replaced on the stage, before being lined up based on the positions recorded in the software. Each cell was imaged for the first target (LFA-1), then the sample was re-removed from the microscope before being subject to madSTORM antibody elution. To check that all of the antibody had been removed by the madSTORM buffer, the sample was then replaced on the microscope and each cell imaged again (see methods). Then for the next target, the sample was once again removed from the microscope, restained and imaged again. This was repeated for LFA-1, pY397 FAK and pY416 Src in ~20 cells per condition, derived from a mixed culture containing cells from 3 mice.

A representative cell is shown in figure 6-16 to illustrate the process. Figure 6-16a shows a cell tracked from a large FOV up to the moment of fixation (t = 60). Figure 6-16b shows example frames from raw STORM imaging for each channel in the cell tracked in 6-16a. Figure 6-16c shows example gaussian uncertainty representations of localised images for each channel, and all three channels merged together after alignment using nanodiamonds. Zoomed regions at three different length scales show the preferential association of pY416 Src (yellow) and pY397 FAK (blue) clusters with particular LFA-1 clusters (orange). Bayesian cluster analysis was performed on regions of interest chosen from the leading edge and focal zone of the cells, and cluster metrics were extracted – full protocol is described in methods and discussed in section 5.

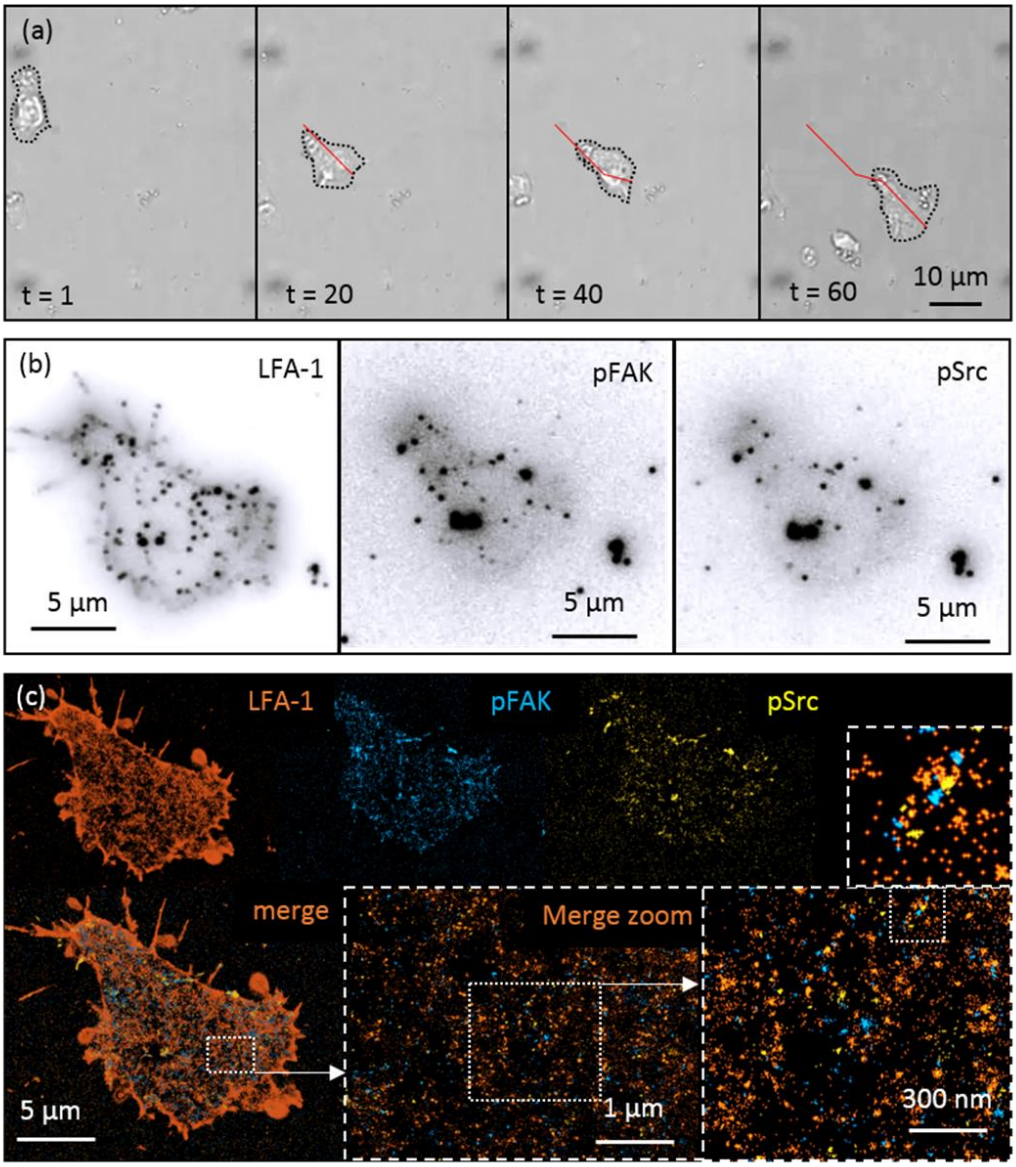

Figure 6-16: **Manually tracked cells were fixed, stained and LFA-1, pY397 FAK and pY416 Src imaged using madSTORM imaging.** a) Migrating cells were tracked to attain cell speeds, up to the point of fixation on the stage. b) example STORM acquisition raw frames for each target. C) localised coordinate maps for each target with zooms to show features.

In order to get a broad overview of the clustering of LFA-1, pY397 FAK and pY416 Src, cluster metrics per ROI were plotted for the leading edge and focal zone of migrating PTPN22$^{+/+}$ and PTPN22$^{-/-}$ T cells.

LFA-1 cluster metrics followed the same trends as previously (section 5): in PTPN22$^{+/+}$ (left side of plots in figure 6-17) and PTPN22$^{-/-}$ cells (right side of plots in figure 6-17) there were more molecules (figure 6-17a) and clusters (figure 6-17c) in the focal zone than the leading edge, and a smaller percentage clustered (figure 6-17b). PTPN22$^{-/-}$ cells also recapitulated the

main phenotype from the section 5: they had far fewer clusters than the PTPN22$^{+/+}$ PTPN22+/+ cells (figure 6-17c). It should be noted that the total molecules in PTPN22$^{-/-}$ cells were increased compared to PTPN22+/+ cells (figure 6-17a) – the opposite trend to section 5 figure 5-7, which had much higher sample size. The effects of total molecule changes on other cluster parameters are however negligible within reasonable limits, as shown in section 3, figure 3-13.

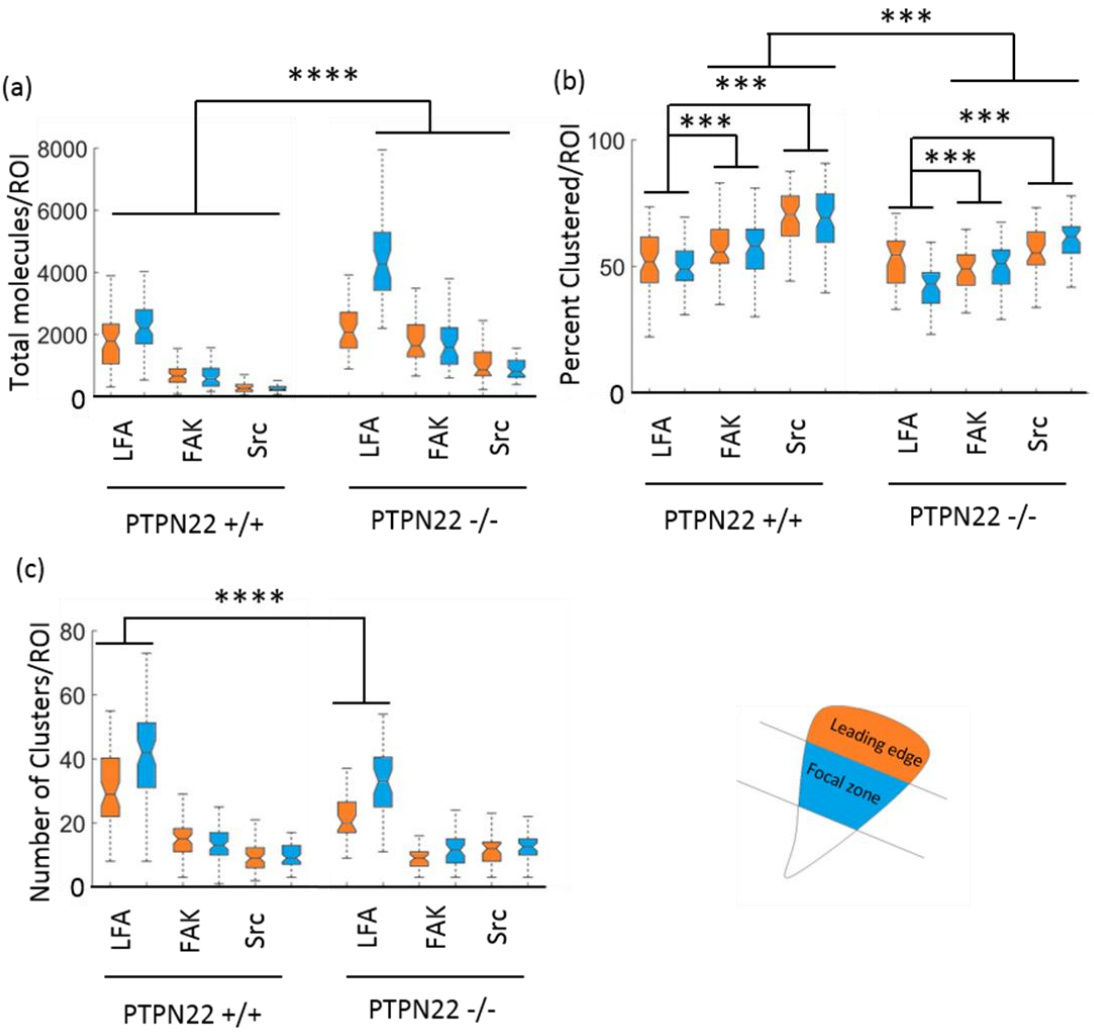

Figure 6-17: **Cluster metrics per ROI for LFA-1, pY397FAK and pY416 Src family kinases extracted from WT PTPN22$^{+/+}$ and KO PTPN22$^{-/-}$ T cells migrating on ICAM-1.** The total molecules per ROI (a), percent clustered per ROI (b) and the number of clusters per ROI (c) for the leading edge (orange) and focal zone (blue) of LFA-1, pY397 FAK or pY416 Src in migrating T cells.

pY397 FAK and pY416 Src both became more abundant in PTPN22-/- cells (figure 6-18a), with a lower percentage participating in clusters (figure 6-18b). There was no change in the number of FAK or Src clusters between slower PTPN22+/+ cells and faster PTPN22-/- cells (figure 6-18c).

Individual cluster metrics on the size and molecular density of clusters were altered in the same way as in section 5 for LFA-1 but to a greater extent: namely clusters got larger with more molecules in PTPN22$^{-/-}$ cells (figure 6-18a and b). Between the leading edge and focal zone in PTPN22+/+ and PTPN22-/- cells, LFA-1 recapitulated its tendency to form smaller denser clusters in the focal zone (comparing blue FZ bars to orange LE bars for LFA-1 in figure 6-18a and 6-18b). pY397 FAK clusters and pY416 Src clusters were measured as significantly larger and were composed of more molecules in PTPN22-/- cells as compared to PTPN22+/+ cells, and this was even more pronounced in the leading edge than the focal zone (figure 6-18a and b).

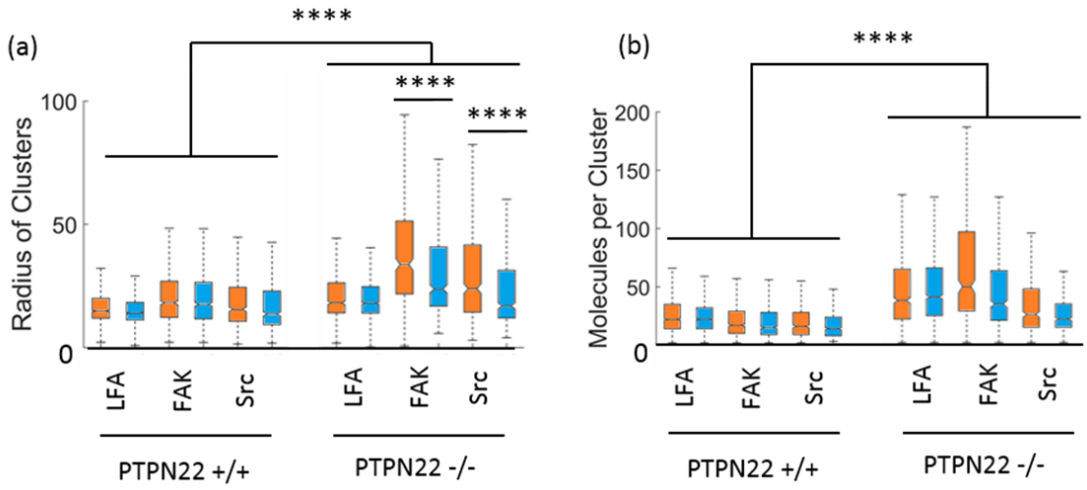

Figure 6-18: **Cluster size and number of molecules per cluster all increase in faster moving PTPN22 cells in the case of LFA-1, pY397FAK and pY416Src.** LFA-1 clusters are larger (a) and denser (b) in faster moving PTPN22-/- cells. pY397 FAK and pY416 Src clusters are also larger and denser in faster moving PTPN22-/- cells. pY397 FAK and pY416 Src cluster become more strongly regionally discriminated in terms of their size in PTPN22-/- cells (a): clusters in the leading edge are larger than those in the focal zone, though the molecular content stays roughly the same.

6.2.3 Discussion for population level clustering of LFA-1, pY397 FAK and pY416 Src in this system

The most interesting phenomenon described here is the increase in the size and molecular content of FAK and Src cluster in PTPN22$^{-/-}$ cells, which is greater than the increase (still present) in LFA-1 clusters. This could point to a building of the adhesion framework. Src clusters are always smaller and contain less molecules than FAK clusters, which also fits with the literature that Lck and Fyn are recruited as a result of FAK recruitment and activation, and all of this is followed by more FAK recruitment in mature adhesions.

That there is a bias towards the leading edge having larger and denser FAK and SFK clusters in fast moving PTPN22$^{-/-}$ cells is indicative of a regulatory mechanism that really relies on clusters solidifying their adhesive ability in the leading edge. It is possible that by this point, they have recruited p130CAS and can recycle the kinases: this would be the subject of future investigations, but fits with the 3D pY397 FAK data shown in section 6.1.

The opposite trend is seen in the total molecules between PTPN22+/+ and PTPN22-/- cells in the new correlative data shown in this section compared to the data shown in the previous section. This can confidently be attributed to a smaller sample size (20 cells for this section, as opposed to the 70 to 80 in section 5). In addition, we have already shown that alterations in the total molecules, which are known to be quite variable due to detection rates, antibody binding constants and the stochasticity of the technique, do not affect the other clustering metrics in a given sample (figure 3.13, section 3).

Clustering differences in LFA-1 for radius and molecules per cluster were less drastic in the previous dataset. This may be because we knew that all of the cells chosen here were migrating, whereas in the population data shown in section 5, we had no guarantee that the cells imaged by dSTORM were moving. Therefore these migrating cell phenomena are amplified in the this data, and dulled in the data shown in section 5, even with greater n numbers. This points to the suggestion that this data is inherently more powerful due to making single cell measurements of known migrators.

6.3 Nanoclustering versus cell speed in single cells

In order to discern whether LFA-1 clustering, pY397 FAK clustering or pY416 Src clustering was correlated to cell speed in single cells, cell speeds prior to fixation were compared to cluster analysis metrics for these three targets in single cells.

Means of the cluster metrics quantified above were taken for each cell, and were plotted versus the mean cell speed for each individual cell prior to fixation. Linear regression was used to fit the data, and Pearson's tests were used to assess any correlation between cell speed and clustering characteristics. Curved dotted lines describe confidence intervals for each linear fit.

6.3.1 Nanocluster characteristics of LFA-1 trends towards correlation with cell speed

Figure 6-19a shows the total molecules versus speed for LFA-1, where each dot on the graph describes a single cell: its mean cell speed taken from the last 3 frames before its fixation (this method was used due to the 'lunging' type migration utilised by migrating T cells: the goal was to measure cell speed at the point of fixation), and its **mean total molecules** (figure 6-19) from ~ 6 regions of interest per cell. Data from the leading edge and focal zone are plotted on each graph, for PTPN22+/+ cells on the left (orange and blue) and PTPN22-/- cells on the right (green and light blue). There is a significant negative inverse correlation between total molecules and cell speed for in the leading edge of PTPN22+/+ cells, which is not present in PTPN22-/- cells. The number of total LFA-1 molecules appears higher in PTPN22-/- cells, but this is not a significant change.

There is no statistically significant correlation between **cell speed and the percentage of clustering** in either PTPN22+/+ or PTPN22-/- cells (figure 6-19b), but there is a positive trend towards more clustering being associated with higher cell speed. This trend is more prevalent in the focal zone of both PTPN22+/+ (figure 6-19b – dark blue points and line) and PTPN22-/- cells (figure 6-19b – light blue points and line). There is also no statistically significant correlation between **cell speed and the number of clusters**, in either zone of PTPN22+/+ or PTPN22-/- cells (figure 6-19c). In PTPN22+/+ cells in the leading edge and focal zone, there is a trend towards an inverse correlation where faster cells have fewer clusters, but this is not significant and has a weak r value of -0.28 for the leading edge and -0.21 for the focal zone (figure 6-19c). R values are above zero for PTPN22-/- cells, describing the opposite (non significant) trend.

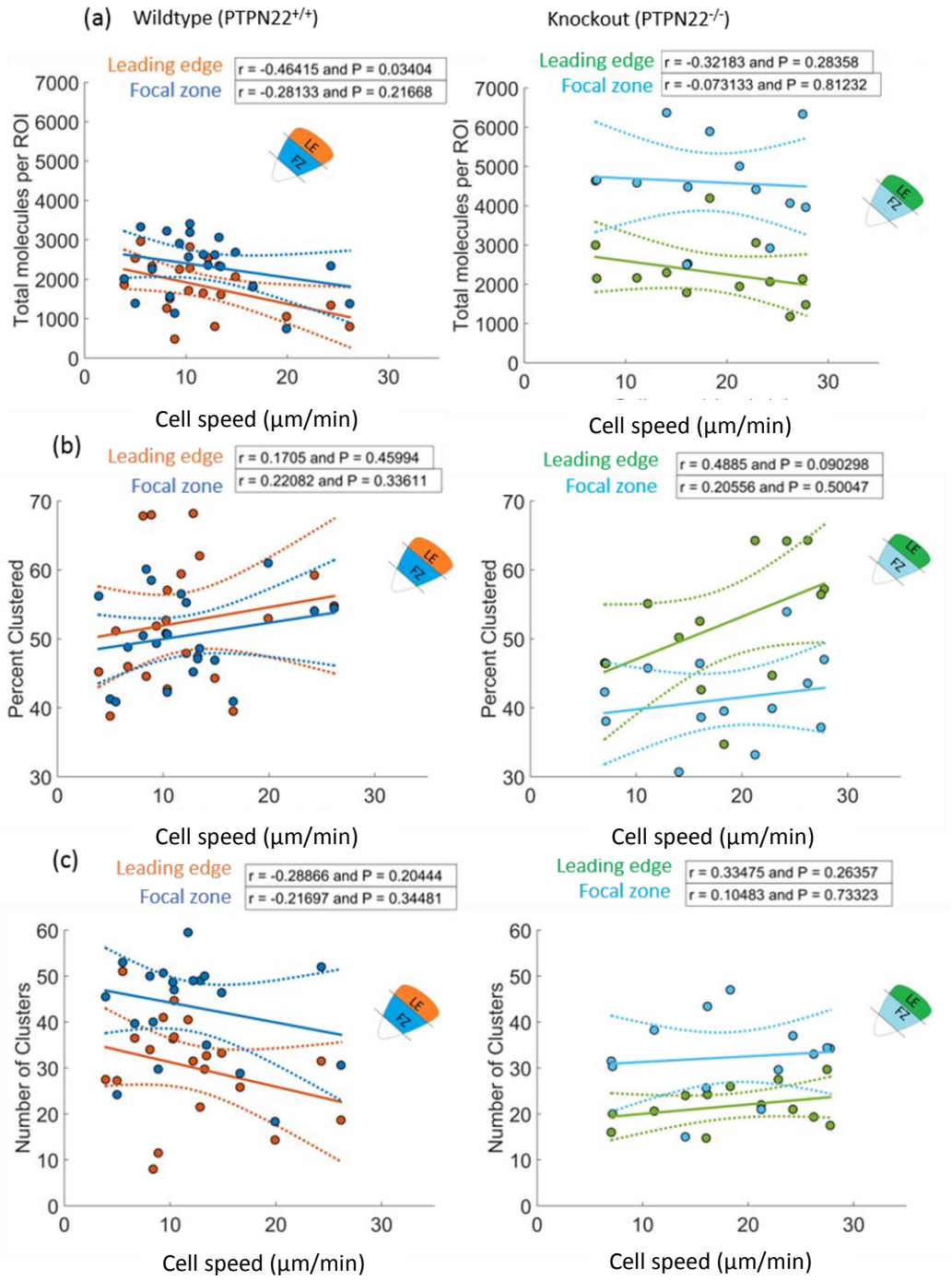

Figure 6-19: **LFA-1 clustering metrics per region versus cell speed in single PTPN22+/+ (orange and dark blue) and KO (green and light blue) T cells.** Mean cluster metrics per cell were plotted against mean cell speed (dots). Linear regression (solid line with dotted confidence intervals) and pearson's analysis provide an r value for each metric vs cell speed plot. This is done in PTPN22$^{+/+}$ PTPN22+/+ cells (entire left column, orange and blue) and PTPN22$^{-/-}$ KO cells (entire right column, green and light blue) for total number of molecules (a), the percentage clustered (b) or the number of clusters (c). n = 21 PTPN22+/+ and 14 KO cells from a mixed culture derived from 3 mice each condition.

In terms of individual clustering characteristics, the radius and number of molecules per cluster also does not correlate to cell speed in either PTPN22$^{+/+}$ or PTPN22$^{-/-}$ cells (figure 6-20), and no striking trends are visible.

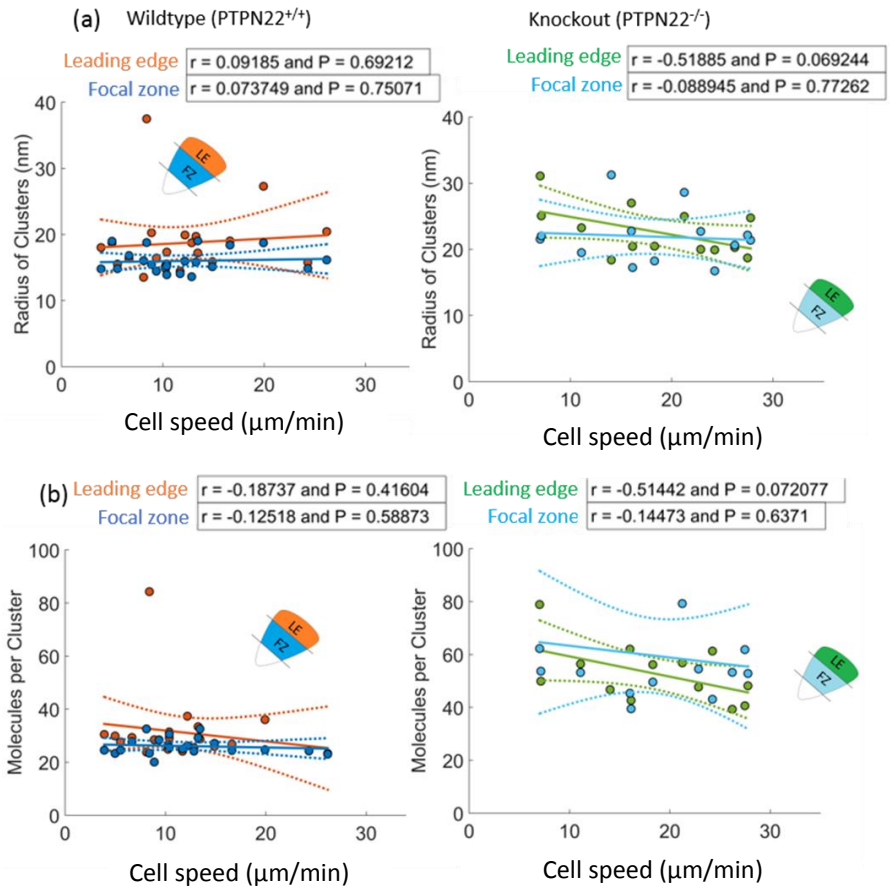

Figure 6-20: **Individual LFA-1 clustering metrics (size and molecules per cluster) versus cell speed in single PTPN22+/+ and PTPN22-/- migrating T cells.** Mean cluster metrics per cell were plotted against mean cell speed (dots). Linear regression (solid line with dotted confidence intervals) and Pearson's analysis provide an r value for each metric vs cell speed plot. This is done in PTPN22$^{+/+}$ WT cells (entire left column, orange and blue) and PTPN22$^{-/-}$ KO cells (entire right column, green and light blue) for the radius of clusters (a) or the number of molecules per cluster (b). n = 21 PTPN22+/+ and 14 PTPN22-/- cells from a mixed culture derived from 3 mice per condition.

6.3.2 Nanocluster characteristics of pY397 FAK inversely correlates with cell speed

In the same cells, pY397 FAK clustering metrics were plotted against cell speed. The total molecules (figure 6-21a), percent clustered (figure 6-21b) and number of clusters (figure 6-21c) in PTPN22+/+ and PTPN22-/- cells were not directly correlated to cell speed in single cells. A trend towards fewer clusters being associated with higher cell speeds was observed in PTPN22+/+ cells (figure 6-21c left), which was no longer present in PTPN22-/- cells (figure 6-21c right). This mirrors what happens for LFA-1 (figure 6-19).

In terms of individual cluster characteristics, the radius of pY397 FAK clusters in the focal zone of PTPN22+/+ cells displayed a non-significant trend towards larger clusters being associated with higher cell speeds (figure 6-22a left), which was not present in PTPN22-/- cells (figure 22a right). The number of molecules per cluster exhibit no correlation to cell speed for pY397 FAK in PTPN22+/+ or PTPN22-/- cells (figure 6-22b).

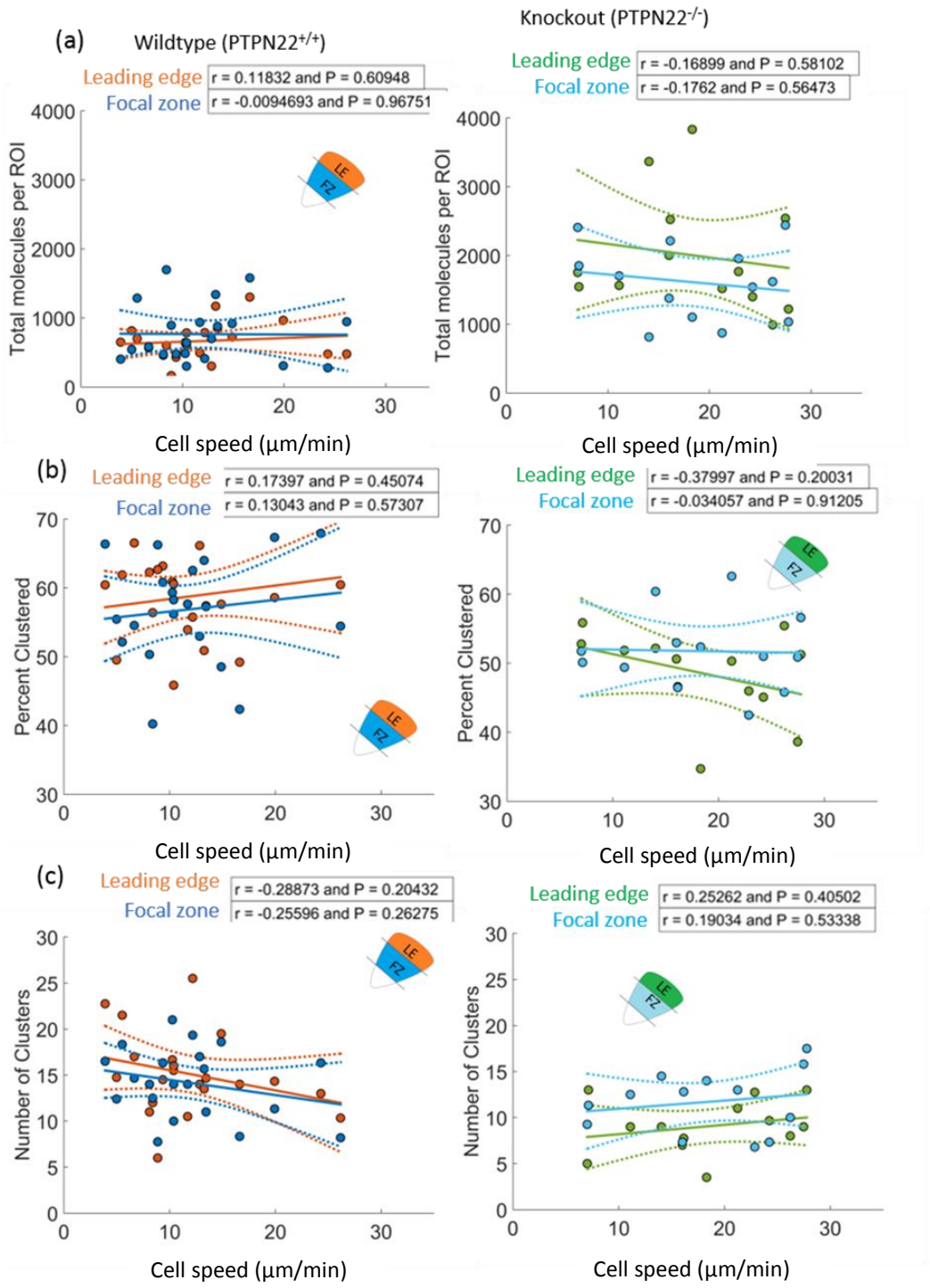

Figure 6-21: **p397FAK clustering metrics per region are uncorrelated with cell speed in single PTPN22+/+ and PTPN22-/- T cells.** Mean cluster metrics per cell were plotted against mean cell speed (dots). Linear regression (solid line with dotted confidence intervals) and pearson's analysis provide an r value for each metric vs cell speed plot. This is done in PTPN22$^{+/+}$ cells (entire left column, orange and blue) and PTPN22$^{-/-}$ KO cells (entire right column, green and light blue) for total number of molecules (a), the percentage clustered (b) or the number of clusters (c). n = 21 PTPN22+/+ and 14 PTPN22-/- cells from a mixed culture derived from 3 mice each condition.

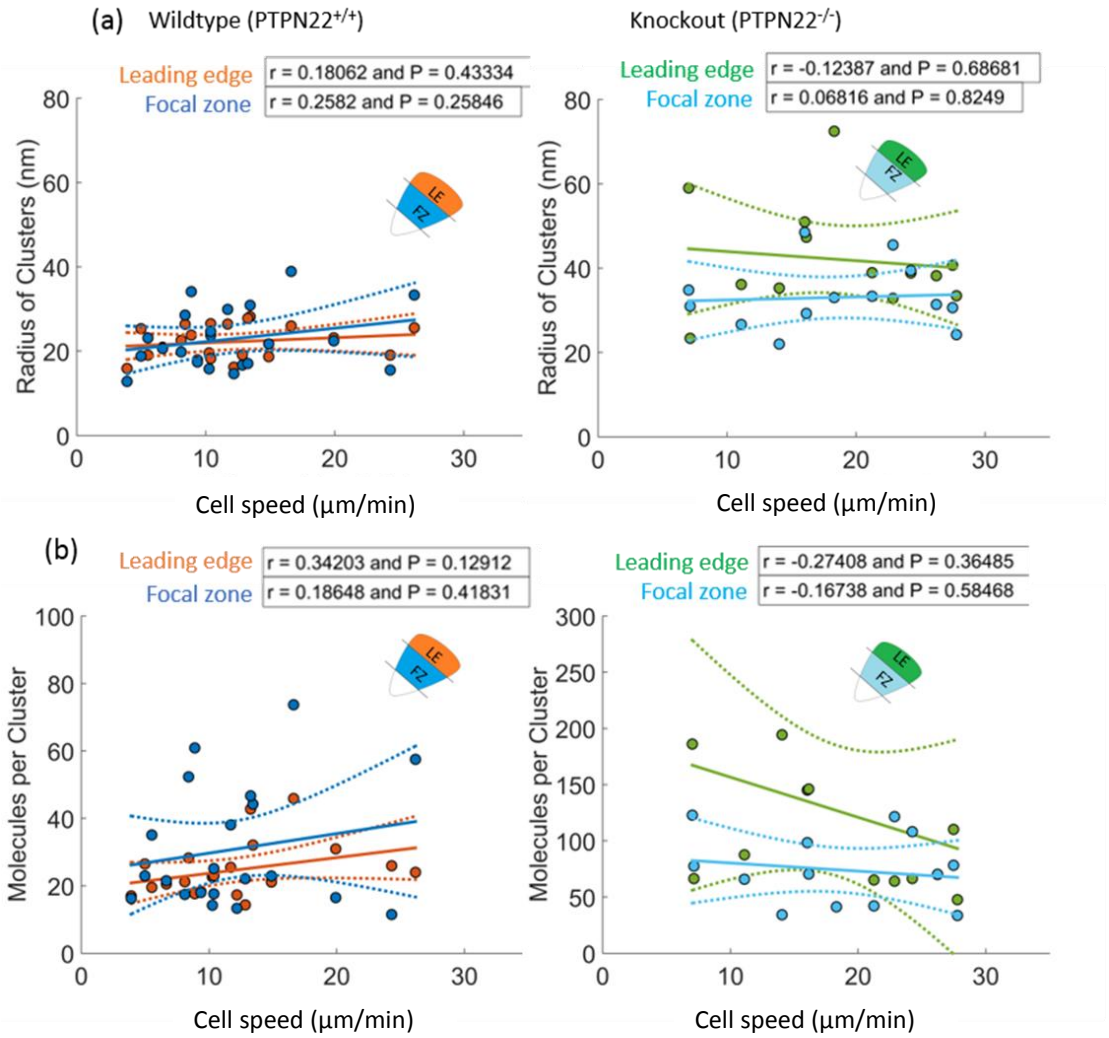

Figure 6-22: **p397FAK cluster density is correlated with cell speed in PTPN22+/+ cells, and not in PTPN22-/- cells.** Mean cluster metrics per cell were plotted against mean cell speed (dots). Linear regression (solid line with dotted confidence intervals) and Pearson's analysis provide an r value for each metric vs cell speed plot. This is done in PTPN22$^{+/+}$ cells (entire left column, orange and blue) and PTPN22$^{-/-}$ KO cells (entire right column, green and light blue) for the radius of clusters (a) or the number of molecules per cluster (b). n = 21 PTPN22+/+ and 14 KO cells from a mixed culture derived from 3 mice per condition.

6.3.3 Nanocluster characteristics of pY416 Src do not correlate with cell speed

The **total number of pY416 Src molecules** in was uncorrelated with cell speed in either PTPN22+/+ or PTPN22-/- cells (figure 6-23a). The total molecules were increased in PTPN22-/- cells overall but again (as seen in figure 6-23), there is no correlation to cell speed. There was also no correlation between **the percentage of clustering and cell speed**, in either region of PTPN22+/+ or PTPN22-/- cells (Figure 6-23b). There was a smaller percentage clustered in PTPN22-/- cells (figure 6-23). The **number of clusters** was very low in PTPN22+/+ cells, and there was no correlation to cell speed (figure 6-23c left). In PTPN22-/- cells there was also no correlation, but the number of clusters was much higher (figure 6-23c right).

In terms of individual cluster characteristics, the pY416 Src in PTPN22+/+ and PTPN22-/- cells displayed no correlations for **radius or molecules per cluster** versus cell speed (figure 6-24a and b).

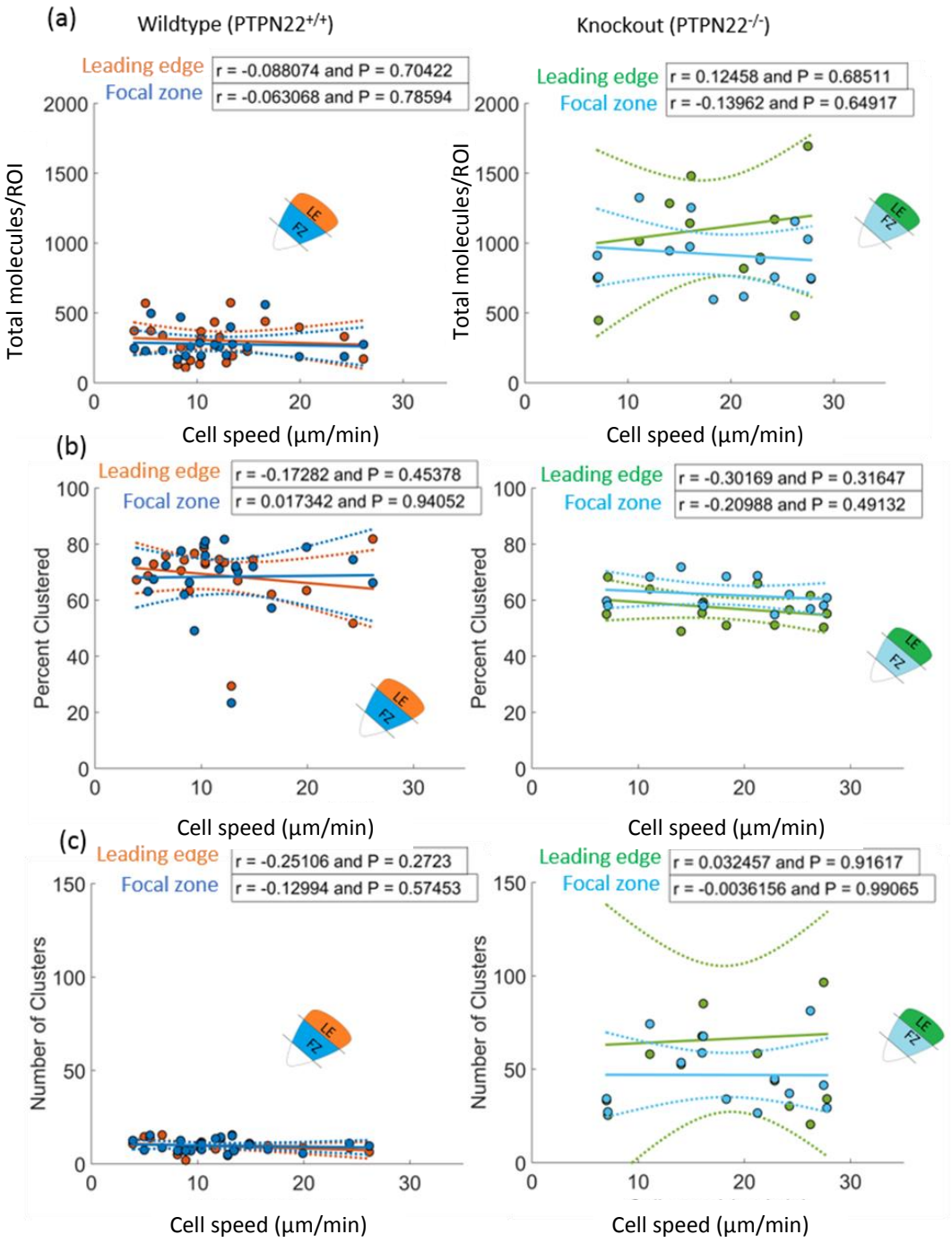

Figure 6-23: **p416Src clustering metrics per region are uncorrelated with cell speed in single PTPN22+/+ and PTPN22-/- T cells** Mean cluster metrics per cell were plotted against mean cell speed (dots). Linear regression (solid line with dotted confidence intervals) and pearson's analysis provide an r value for each metric vs cell speed plot. This is done in PTPN22$^{+/+}$ cells (entire left column, orange and blue) and PTPN22$^{-/-}$ KO cells (entire right column, green and light blue) for total number of molecules (a), the percentage clustered (b) or the number of clusters (c). n = 21 PTPN22+/+ and 14 PTPN22-/- cells from a mixed culture derived from 3 mice each condition

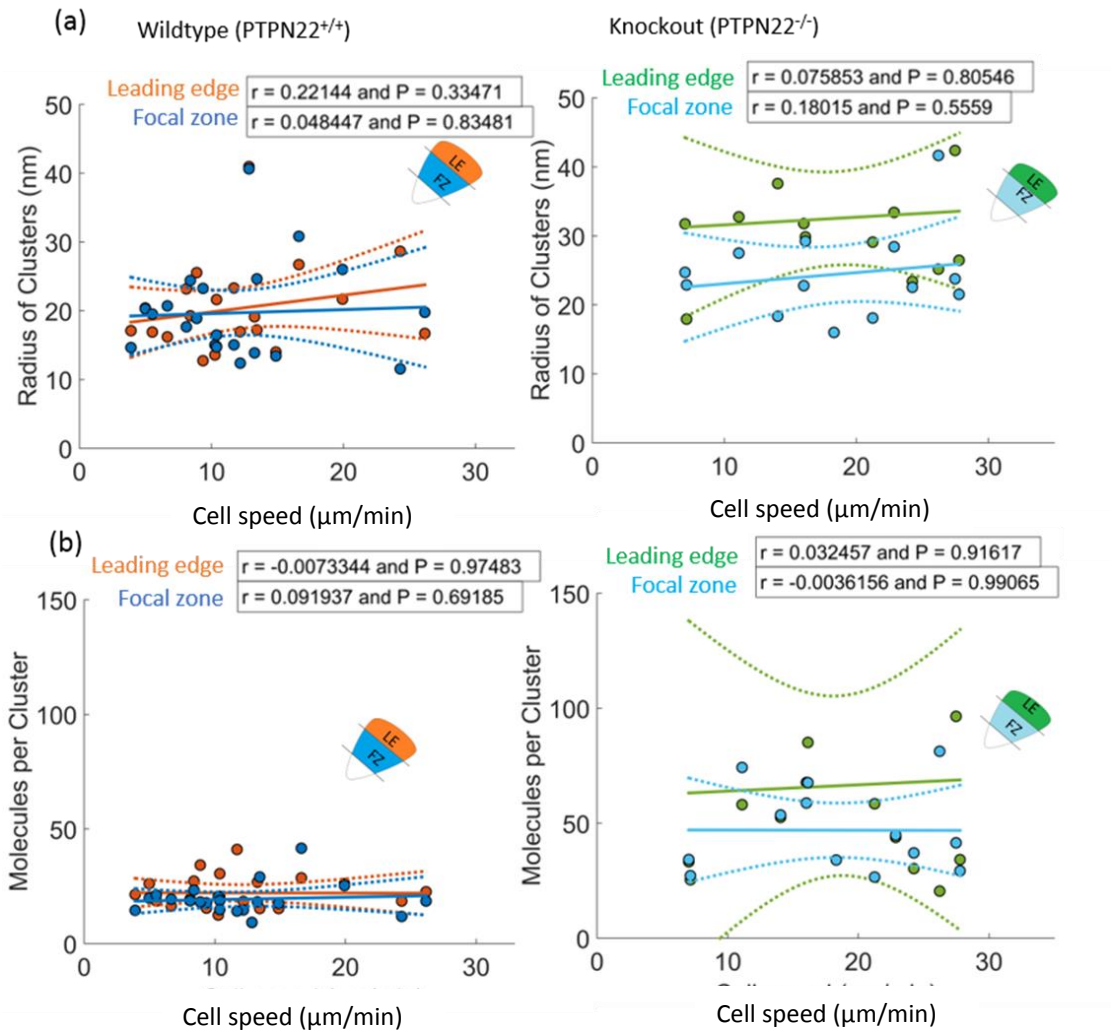

Figure 6-24: **p416Src cluster density is not correlated with cell speed in PTPN22+/+ or PTPN22-/- cells.** Mean cluster metrics per cell were plotted against mean cell speed (dots). Linear regression (solid line with dotted confidence intervals) and Pearson's analysis provide an r value for each metric vs cell speed plot. This is done in PTPN22$^{+/+}$ cells (entire left column, orange and blue) and PTPN22$^{-/-}$ KO cells (entire right column, green and light blue) for the radius of clusters (a) or the number of molecules per cluster (b). n = 21 PTPN22+/+ and 14 PTPN22-/- cells from a mixed culture derived from 3 mice per condition.

6.3.4 Discussion for nanocluster characteristics versus cell speed

Interesting correlations occurred in both FAK and Src with cell speed, but not with LFA-1. This would suggest that LFA-1 clustering is a fairly stable clustering characteristic. We have already seen (section 5) that there are modulations of the clustering characteristics on a population

level, which relate to a functional phenotype of increased or decreased cell speed under a host of conditions, one of these is PTPN22 deletion.

The conclusion from that data is that LFA-1 cluster characteristics are functionally important for cell speed. However, this doesn't seem to be true based on data acquired here, from single cells. Cluster characteristics still change based on removing PTPN22, in the same way as in section 5. This would suggest that the clustering changes seen are directly related to the pathways in question, and that nanoscale clustering changes in LFA-1 may not be as important as the clusters associations with other molecules, and how they are signalling.

In terms of pY397 FAK clusters on their own, their frequency in PTPN22+/+ cells is inversely correlated with cell speed. This is joined by an increase in the radius (though not significant) and an increase in molecular density, which positively correlates to cell speed increases. This would back up the literature describing nascent adhesions in other cell types, which grow in size and density as they mature[73,78]. This is the first link to the being associated with cell speed increases, pointing to perhaps more mature, or more molecularly diverse clusters being associated with cell speed increases.

This theory has added credence when pY416 Src is imaged, and describes a special role for PTPN22. The size of clusters and molecules per cluster are both positively correlated with cell speed: faster cells have larger clusters with more pY416 Src in PTPN22-/- cells. This would fit with the literature, as PTPN22 is a Src kinase control switch and its mutation is a loss of function event. Without it, it is possible that clusters of pY416 Src can just grow in size and become uncontrolled.

The weak correlations that are seen more clearly on a less correlative population basis might also be explained by low sample size. Looking at single cell functional outcomes like migration speed, correlated to nanoclustering characteristics is powerful, but as with most fluorescence microscopy based imaging experiments, n numbers are low. For this type of quantitative data in general, experiments would benefit from automation, for example using machine learning techniques to identify cells and automatically image 1000s in one day.

6.4 Co-localisation of LFA-1, pY416 Src and pY397 FAK in migrating T cells

The next section focuses on defining LFA-1 clusters in terms of their activity, based on two phosphorylated intermediates known to delineate between very early adhesions, later

adhesions and very late adhesions. To do this I used pY397 FAK and pY416 Src, which collaborate in nascent adhesions in non-leukocytes and are present in lymphocytes.

Recently "nascent" adhesions, which resemble T cell nanoadhesions in terms of size, were characterised in non-leukocytes during migration. In these cells, these adhesions recruit pY397 FAK immediately after ligand binding. Maturation is induced by the recruitment of pY416 Src, followed by reinforcement of the adhesion with more pY397 FAK, which is coupled to an increase in adhesion size. Unlike these nascent adhesions, T cell nano-adhesions do not grow in size as they move backwards from the lamellipodia to the lamella (leading edge to focal zone): in fact they become smaller and denser (data in section 5). In the absence of PTPN22 phosphatase T cells move faster, and PTPN22 controls the phosphorylation of Lck downstream of integrin engagement.

In order to discern at what stage of maturation the smaller, denser LFA-1 adhesions are at, and whether PTPN22 induced migration speed alterations change the relationship of these two phosphorylated intermediates with nanoscale LFA-1 clusters, migrating PTPN22 proficient and deficient T cells were tracked, fixed on the stage and stained with LFA-1, pY397 FAK and pY416 Src using the madSTORM sequential labelling technique. Super resolution microscopy was carried out on the cells and each channel was aligned using nanodiamonds. Colocalization analysis was then carried out as per[152].

6.4.1 Pearson's correlation coefficient co-cluster analysis

2 μm^2 regions of interest were cropped out from localised and aligned (methods) STORM images of each channel. To do colocalization analysis a matlab script was used to carry out Ripley's K analysis of clusters in 2 μm^2 regions of interest cropped out from localised and aligned (methods) STORM images of each channel. Here, an arbitrary 50 nm search radius is used for Ripley's K analysis of each point J. Ripley's K is carried out for each channel individually (figure 6-25a and b) to measure clustering of molecules of channel 1 with other molecules of channel 1 to derive L(r). Then, Cross Ripley's K analysis is carried out where around each point j from channel 1 a radius is drawn and the number of molecules from channel 2 within the radius are counted to derive L(r) cross. The same is done for channel 1 molecules around channel 2 central molecules, as this is asymmetric analysis and the clustering of molecule a to b is not likely to be the same as the amount of clustering of b to a due to, for example, there being more clusters of one of the populations than the other (figure 6-26).

L(r) cross can then be plotted against L(r) for each region of interest. The graph in figure 6-25 shows a correlation close to 1, and is divided up so that the top right corner shows clusters colocalised with clusters. Dots are coloured according to the amount of molecules at each position. The Pearson's correlation coefficient of this graph can be taken as a measure of co-clustering between any two given channels (in this case it is close to 1).

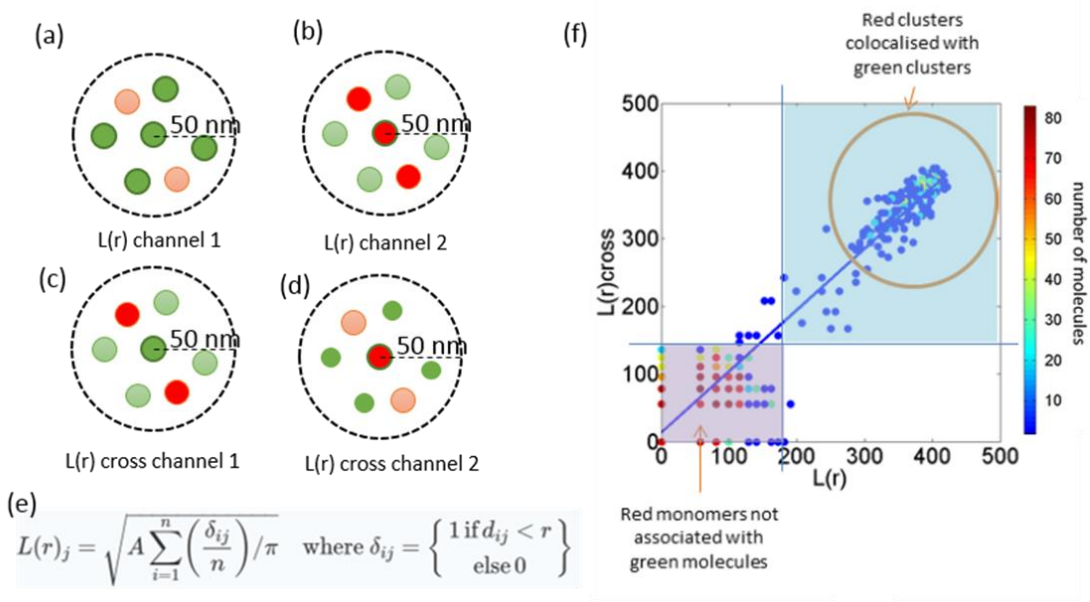

Figure 6-25: **Rossy colocalization method.** a and b) a search radius of 50 nm is drawn around each point j, for each channel. Ripley's K analysis (e) is carried out for each point, and L(r) derived. c) shows cross analysis, where red points are counted centred around each green point j, and vice versa (d). f) Example figure adapted from Rossy et al. L(r) cross vs L(r). Plot shows a very strong correlation, indicating a high degree of co-clustering. The pseudo-colour represents the number of individual molecules at each position.

This analysis was carried out on the same regions of interest from the same dataset as in the above sections. Figure 6-27 shows representative L(r) cross versus L(r) plots derived from a single region for the colocalization of p397 FAK with pY416 Src in the leading edge of wildtype migrating T cells. The main advantage of this kind of analysis is that it analyses cluster colocalization as opposed to simply molecular colocalization. This is important in order to look at changes in the behaviour of nanoclusters.

Each channel in this analysis is compared asymettrically. First, channel 1 is compared with channel 2 and then channel 2 is compared with channel 1. This is because hypothetically, all clusters of species A might be colocalised with species B, giving a high PCC for colocalization; at the same time, there might be many clusters of species B which are free of species A, because species B is far more abundant, or forms more clusters. This is explained in figure 6-26.

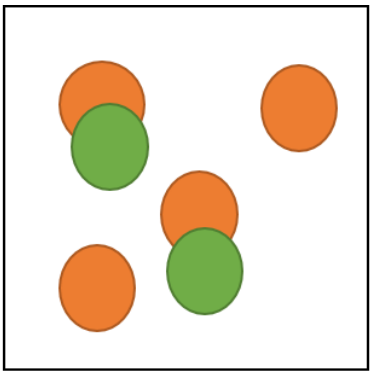

Figure 6-26: Explanation of asymettric colocalization analysis.

Plots of L(r) versus L(r) cross provide a visualisation of co-clustering: the better the correlation, the more clusters of species a colocalise with clusters of species b. Example plots from a single representative ROI are shown in figure 6-27 for pY397 FAK > pY416 SRC (left) and pY416 Src > pY397 FAK (right). Pearson's correlation coefficients were calculated from these plots for each region as a measure of cluster colocalization.

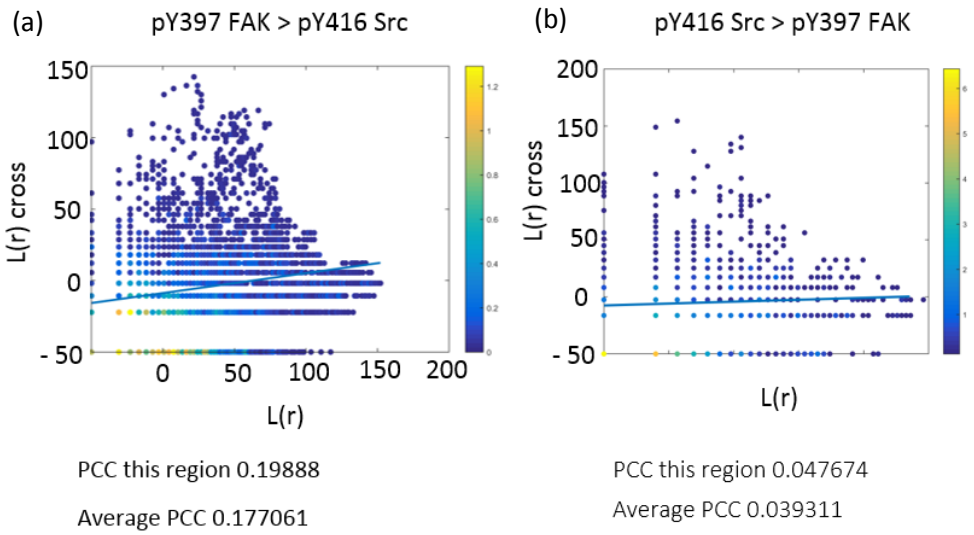

Figure 6-27: Example L(r) cross versus L(r) colocalization plots for pY397 FAK clusters with pY416 Src clusters. (a) and (b) pY416 Src clusters with pY397 FAK clusters. Pearson's correlation coefficients are given below. Average PCC refers to data from n = 21 mice.

Pearson's correlation coefficients for all regions per condition were compared in the leading edge and focal zone of migrating PTPN22$^{+/+}$ and PTPN22$^{-/-}$ cells. Figure 6-28 shows PCC values for colocalization of clusters of LFA-1 with clusters of pY397 FAK. PCC mean values are all below 0.1, meaning the majority of clusters of LFA-1 are not colocalised with clusters of pY397FAK (figure 6-28a). There is a significant increase in the amount of colocalization in PTPN22$^{-/-}$ cells as compared to PTPN22$^{+/+}$ cells, which occurs both in the leading edge and the focal zone ($p<0.0001$). When the amount of colocalization of pY397 FAK clusters with LFA-1 clusters is measured (figure 6-28b), there is more colocalization (a trend, not significant) in the leading edge of both PTPN22+/+ and PTPN22-/- cells. There is almost no colocalization of pY397 FAK with LFA-1 clusters in the focal zone of PTPN22+/+ cells, but in PTPN22-/- cells colocalization increases in both zones.

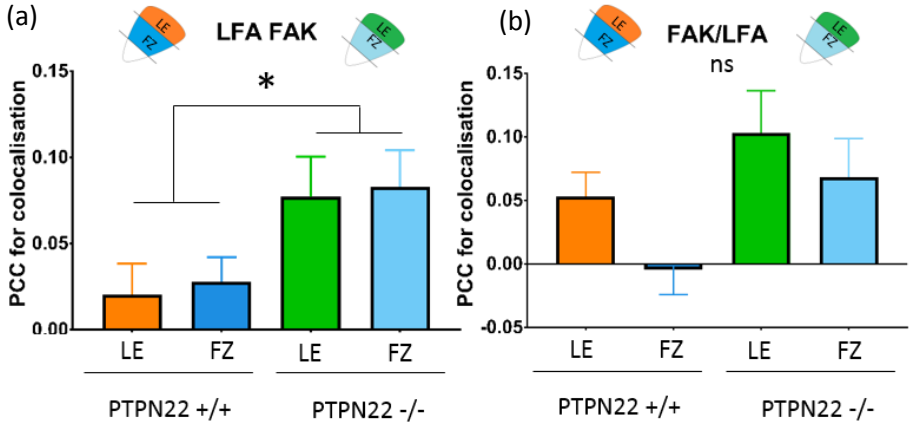

Figure 6-28: **Pearson's correlation coefficient for clusters of LFA-1 colocalised with pY397 FAK, and clusters of pY397 FAK colocalised with clusters of LFA-1.** Clustering and colocalisation was quantified using a 50 nm fixed search radius: a) LFA-1 cluster colocalisation with pY397 FAK clusters, b) pY397FAK cluster colocalization with LFA-1 clusters. N = 21 PTPN22+/+ cells and 13 PTPN22 -/- cells.

LFA-1 cluster colocalization with pY416 Src occurs to a low level (PCC ranging from 0.021 to 0.042), but almost doubles in the focal zone of PTPN22-/- cells as compared to PTPN22+/+ cells (not significant) (figure 6-29a). When pY416 Src cluster colocalisastion with LFA-1 is quantified, clusters are actively un-colocalised in the leading edge of PTPN22+/+ cells. In the focal zone of PTPN22-/- cells, there is positive colocalization (mean value 0.06).

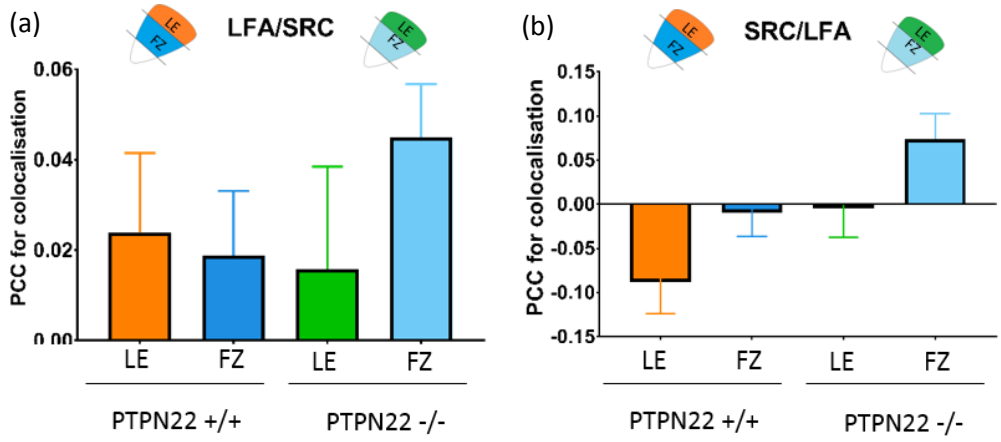

Figure 6-29: **Pearson's correlation coefficient for clusters of LFA-1 colocalised with pY416 SRC, and clusters of pY416 SRC colocalised with clusters of LFA-1.** Clustering and colocalisation was quantified using a 50 nm fixed search radius: a) LFA-1 cluster colocalisation with pY416 SFKclusters, b) pY416 SFK cluster colocalization with LFA-1 clusters. N = 21 PTPN22+/+ cells and 13 PTPN22 -/- cells.

pY397 FAK cluster colocalization with pY416 Src is uncorrelated in PTPN22+/+ cells, wheras PTPN22-/- cells display the biggest increase seen in this analysis. Still most of the pY397 FAK clusters are uncolocalised with pY416 Src clusters, but there is a strongly significant increase from PTPN22+/+ to PTPN22-/- involving more cluster colocalization in the PTPN22-/-s. When Src clustering with FAK is analysed (figure 6-30b), Src is anti-correlated with FAK in PTPN22+/+ cells, and correlated with in PTPN22-/- cells. In the focal zone of PTPN22-/- cells, there is a significant increase in the PCC value for Src colocalization with FAK clusters.

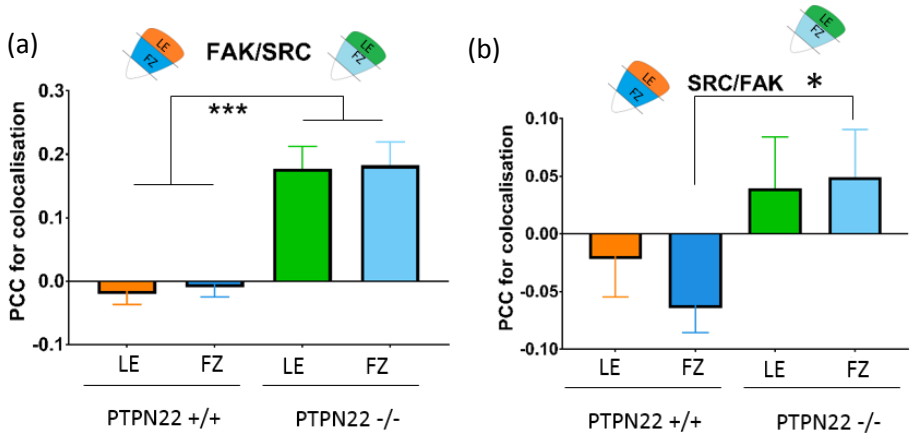

Figure 6-30: **Pearson's correlation coefficient for clusters of pY397 FAK colocalised with pY416 SRC, and clusters of pY416 SRC colocalised with clusters of pY397 FAK.** Clustering and colocalisation was quantified using a 50 nm fixed search radius. N = 21 PTPN22+/+ cells and 13 KO cells.

Overall, PTPN22-/- cells display more nanoscale colocalization of LFA-1 with pY397 FAK everywhere in the membrane proximal zone, and display an increase specifically in the focal zone of LFA-1 colocalization with pY416 Src. pY397 FAK and pY416 Src nanoclusters colocalise together more often in PTPN22-/- cells than in PTPN22+/+ cells.

6.4.2 PCC colocalization versus cell speed

To compare the contribution of LFA-1/pY397 FAK/pY416 Src nanocluster colocalization to cell speed directly, the PCC values calculated in the last section were average for each cell, and plotted against a per cell value for cell speed prior to fixation.

PCC values versus cell speed were compared first for LFA-1 > pY397 FAK in the leading edge and focal zone of PTPN22+/+ (figure 6-31a) and PTPN22-/- (figure 6-31b) cells. There was no

significant correlation between increased cluster colocalization and cell speed, but trends were towards a positive correlation between cell speed and LFA-1>pY397FAK colocalization. These trends were stronger in the leading edge than the focal zone in both PTPN22+/+ and PTPN22-/- cells, and they were weaker in PTPN22-/- cells than PTPN22+/+ cells. PCC values for pY397 FAK > LFA-1 cluster colocalization also showed non significant positive correlation with increased cell speed. This trend was stronger in the PTPN22+/+ (figure 6-31c) cells than PTPN22-/- cells (figure 6-31d).

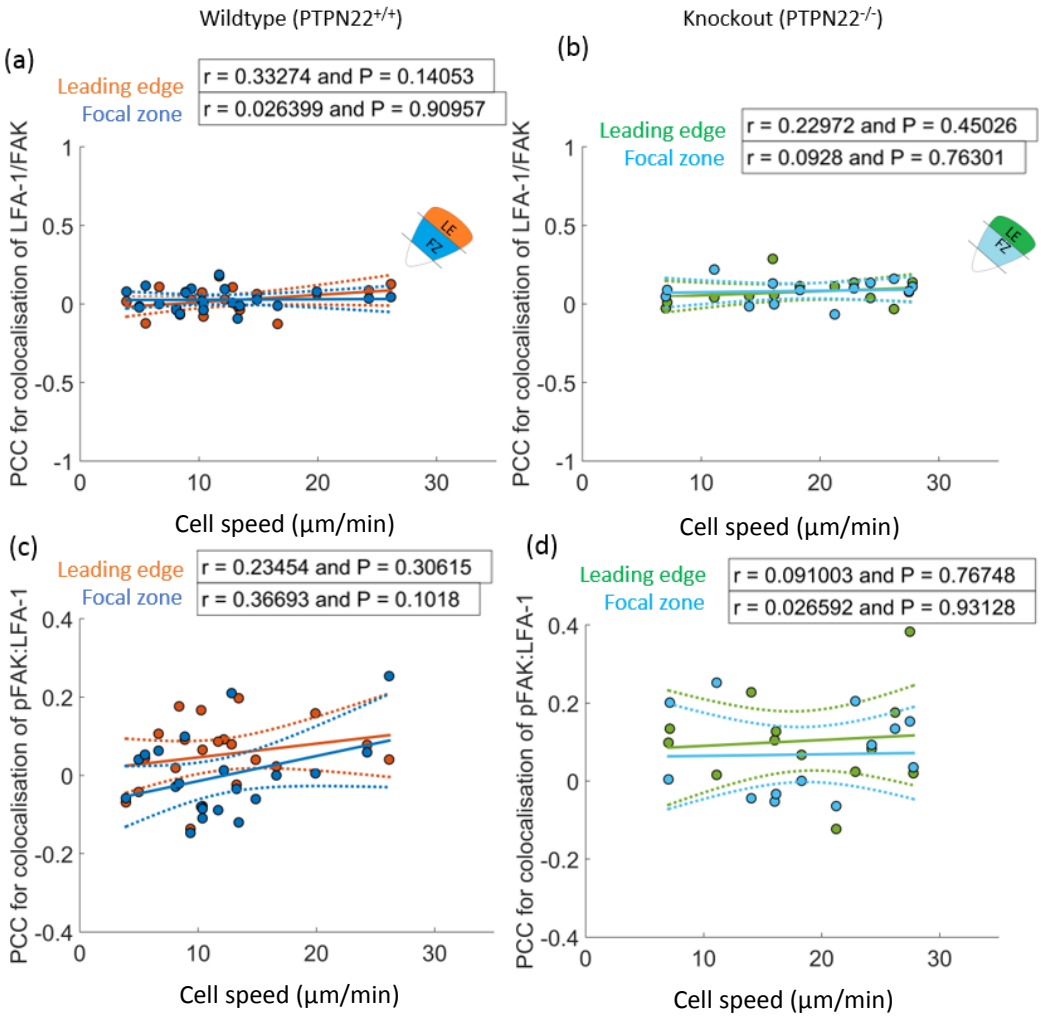

Figure 6-31: **Pearson's correlation coefficient for clusters of LFA-1 colocalised with pY397 FAK, and clusters of pY397 FAK colocalised with clusters of LFA-1 versus cell speed.** Clustering and colocalisation was quantified using a 50 nm fixed search radius. PCC colocalization values for LFA-1 clustering with pY397 FAK in a) PTPN22+/+ cells and b) PTPN22-/- cells. PCC colocalization values for pY397 FAK clustering with LFA-1 in c) PTPN22+/+ and b) KO cells. N = 21 PTPN22+/+ cells and 13 PTPN22-/- cells.

Next, PCC values for colocalization of LFA-1 with pY416 Src were compared to cell speed in the same way. There were no correlations here, and P values were high, indicating that any trends

were due to chance. Therefore, in this dataset, LFA-1/pY416 Src (or vice versa) cluster colocalization does not relate to cell speed in single cells.

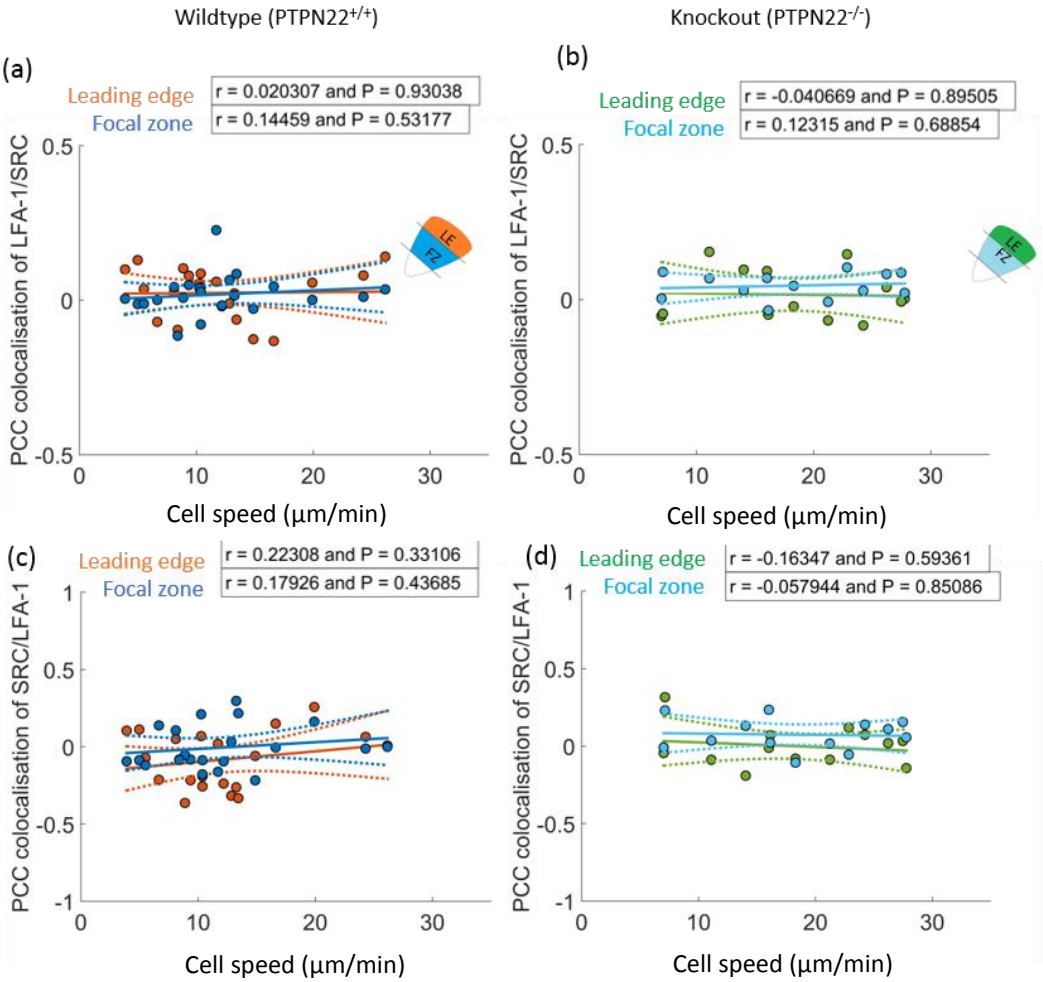

Figure 6-32: **Pearson's correlation coefficient for clusters of LFA-1 colocalised with pY416 Src, and clusters of pY416 Src colocalised with clusters of LFA-1 versus cell speed.** Clustering and colocalisation was quantified using a 50 nm fixed search radius, cell speed from live tracking prior to fixation. PCC colocalization values for LFA-1 clustering with pY416 Src in a) PTPN22+/+ cells and b) KO cells. PCC colocalization values for pY416 Src clustering with LFA-1 in c) PTPN22+/+ and b) KO cells. N = 21 PTPN22+/+ cells and 13 KO cells.

Finally, PCC values for colocalization of pY397 FAK with pY416 Src were compared to cell speed. PTPN22+/+ cells displayed a trend towards positive correlation in the focal zone (r = 0.33) which was non-significant. This was abrogated in PTPN22-/- cells, which displayed no trend towards a correlation between increased FAK/Src colocalization and cell speed. When comparing pY416 Src > pY397 FAK colocalization (figure 6-32c and d) there are trends towards positive correlation between more colocalization and cell speed. In PTPN22-/- cells these trends are abrogated.

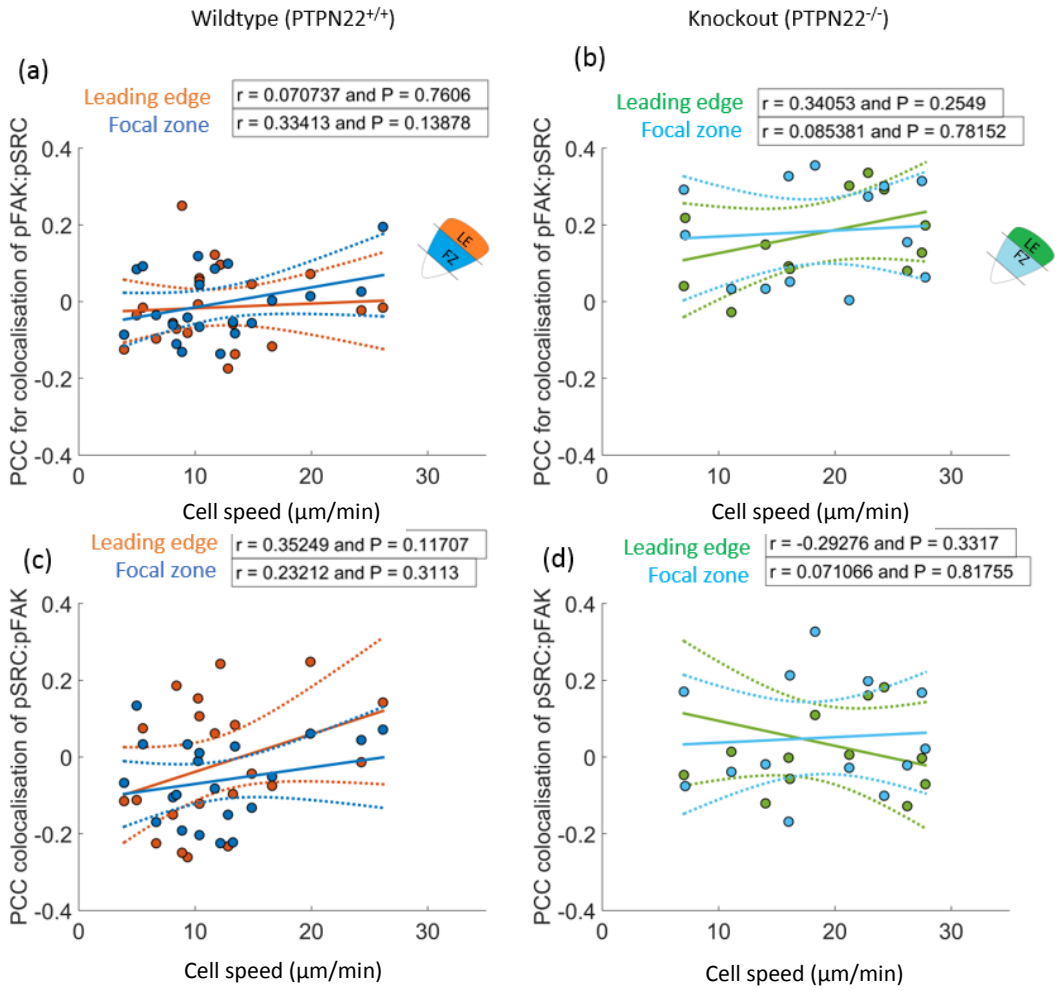

Figure 6-33: **Pearson's correlation coefficient for clusters of pY397 FAK colocalised with pY416 Src, and clusters of pY416 Src colocalised with clusters of pY397 FAK versus cell speed.** Clustering and colocalisation was quantified using a 50 nm fixed search radius, cell speed from live tracking prior to fixation. PCC colocalization values pY397 FAK clustering with pY416 Src in a) PTPN22+/+ cells and b) KO cells. PCC colocalization values for pY397 FAK clustering with pY416 Src in c) PTPN22+/+ and b) KO cells. N = 21 PTPN22+/+ cells and 13 KO cells.

6.4.3 Discussion of colocalization studies of 3 nanoclustering molecules versus cell speed

Here, the colocalization of two phosphorylated markers with integrin was measured in T cells proficient and deficient for a gene which affects cell migration and is downstream of integrin engagement. To summarise the results 1) the colocalization of phosphorylated intermediates with integrin LFA-1 and with each other is altered in PTPN22 $^{-/-}$ cells, 2) there are trends

towards more co-clustering of these intermediates that correlate with higher cell speeds 3) that these trends are altered or abrogated in PTPN22$^{-/-}$ cells.

LFA-1 FAK:

LFA-1/pY397 FAK co-clusters existed at low numbers. Colocalization was increased in both directions in PTPN22 deficient cells which migrate faster (figure 6-28). While there was no significant correlation between cell speed and coclustering of LFA-1 with pY397 FAK (figure 6-31), there was a positive trend in PTPN22+/+ cells that was decreased in PTPN22-/- cells. This was especially apparent when comparing pY397 FAK clustering with LFA-1, suggesting that the pY397 FAK population is less coupled to cell speed in PTPN22-/- cells as compared to wildtypes. While repeats of this experiment have to be done before firm conclusions can be drawn, one might surmise that pY397 FAK clustering more with LFA-1 in PTPN22-/- cells but no longer being associated with cell speed points to a role independent to migration speed in the case of this molecule in this pathway. With further experiments, this trend might hold.

LFA-1 Src:

In PTPN22 deficient cells, there was a focal zone specific increase in co-clustering of LFA-1 with Src. That there was no correlation between cell speed and colocalization of LFA-1 with pY416 Src (figure 6-32), indicates that this characteristic isn't as important for T cell migration capacity. This would indicate a separate role for this interaction aside from migration speed, though these trends would have to be checked by repeating this experiment.

FAK Src:

Co-localisation of pY397 FAK and pY416 Src increased in PTPN22-/- cells (figure 6-30). In PTPN22+/+ cells moving at higher speed there are trends towards more colocalization of FAK and Src, but these trends are abrogated in PTPN22 deficient cells which move faster. Again, repeats are required, but where pY416 Src and pY397 FAK are together should consititute a mature adhesion. That these changes occur cell wide suggests a novel mechanism for T cell migration.

In general, functions of increased pY397 FAK/pY416 Src/LFA-1 clustering in PTPN22-/- cells seen here could be explored, such as this pathways link's to T cell receptor signalling. Both FAK and Src kinases are activated downstream of growth factor receptors, including epidermal growth factor receptor (EGFR) mediating cell survival, as well as being linked to the cyclin D pathway which has a role in the proliferation of cancer cells[249].

6.4.4 Future improvements:

Together, the method of colocalization analysis presented here gives a general answer and has advantages over existing methods including that this method quantifies 'cluster colocalization' and not 'molecular colocalization'. However unlike the Bayesian method, a search radius must be arbitrarily chosen, which limits the amount of heterogeneity between regions that the method can correctly identify. It also doesn't take into account uncertainty of localisations or uneven background. In the future, I will develop a 'purity' based technique by analysing merged channels using Bayesian cluster analysis, before assigning molecules to each channel and measuring the amount of crossover between individual clusters. By using this technique, a range of radii and thresholds are scanned through and the best one is picked. Individual cluster characteristics will be available, such as the size and density of colocalising clusters, allowing for much more detailed 'per cluster' colocalization analysis. In addition, there is the possibility to extract metrics of colocalization of several species with each other, giving a simple method of analysis that can be extended to multiple biological questions.

On the whole, PCCs are low because there are much fewer molecules and clusters in the pY397 FAK and the pY416 Src channels. This is partly due to the high amount of LFA-1 in the cell membrane – there is no published comparison of absolute numbers of pY397 FAK and pY416 Src molecules as compared to LFA-1 in this membrane proximal region of cells, but it is likely that the pY397 FAK and pY416 Src population is dwarfed by the LFA-1 population this close to the cell membrane. To maximise the signal, it is likely that the madSTORM protocol could be improved: the authors notes in a follow up paper, the use of TBS instead of PBS prevents interaction of the PBS with phosphorylatable tyrosines which can interfere with epitopes, preventing antibodies from reaching them. Therefore, the signal from both pY397 FAK and pY416 Src channels is likely lower than it could be, and will be improved using this method in the future. In addition, these experiments will be repeated to increase the n number, in order to investigate the trends described above.

Chapter 7: Discussion

7.1 Summary of presented results

T cells necessarily are amongst the most migratory cells of the human body. In order to migrate through diverse environments, each single cell must co-opt a constantly treadmilling actin engine with integrin based adhesions, which convert mechanical signals to and from the actin in order to generate forward movement. Integrin based adhesions in leukocytes are much smaller than those conventionally studied in other cell types[67,110,250], necessitating the use of super resolution microscopy to investigate them. In this thesis, functional effects were explored of a variety of inside-out and outside-in integrin signalling pathways on cell migration speed, actin flow and engagement to adhesions and integrin LFA-1 nano-clustering. In particular, a focus is placed on the effects of an autoimmune disease predisposing mutation in PTPN22 phosphatase, a potent negative regulator of Src and Syk family kinases important for integrin signalling[88]. Finally, the regulation of such LFA-1 nano-adhesions were explored, by using phosphorylated intermediates as measures of their activity.

Super resolution localisation microscopy is a young field that has developed quickly. Before addressing the biological problem, possible imaging artefacts were addressed and the entire process ratified. Labelling, fixation and acquisition were addressed prior to analysis of the data using new quantitative tools, to ensure that reproducible data could be gleaned for relative comparison of molecular nano-architecture between experimental conditions.

To investigate their effects on cell migration, primary murine effector T cells were exposed to inside-out/outside in signalling modulations. 10 x magnification phase contrast microscopy and automated tracking software was then used to track the speed of the cells. This showed that cells treated with Manganese ions, which increase integrin affinity or Cytochalasin D, an

actin polymerisation inhibitor exhibited reduced migration speed. Conversely, CXCL12 addition or PTPN22 deficiency increased migration speed.

To assess the effects of these conditions on actin flow and engagement to adhesions, lifeact GFP positive transgenic T cells were imaged by TIRF microscopy. Flow speed and engagement were measured using modified STICS software compatible for fast moving lymphocytes. Here, actin flow speed was found to be positively correlated to cell speed. Conversely, aactin engagement to adhesions was inversely correlated to cell speed: faster cells displayed less engagement cell wide.

To investigate the whether nanoscale changes to the adhesions occur under these conditions of fast and slow cell migration, integrin LFA-1 nanoclustering was quantified in the migrating T cell membrane. 2D STORM was used to produce pointillist maps and Bayesian cluster analysis was used to characterise membrane LFA-1 organisation. This showed that all polarised migrating cells adopt adhesion contraction in the focal zone – clusters are smaller, denser, and packed closer together, as compared to the leading edge lamellipodia. Coupled to this finding, increased speed of migration under PTPN22 deficiency or CXCL12 treatment was coupled to an increase in the size of LFA-1 nano-clusters, suggesting a functionally important role for the regulation of cell migration speed.

Due to its being constantly recycled, experiments in the next section asked whether integrin nanoclusters existed above the height of the membrane, and whether this population is also nano-spatially regulated upon cell speed modulation. 3D integrin nanoclustering within the cell was explored through use of 3D iSTORM and 3D Bayesian cluster analysis, revealing a similarly regulated system of submembrane nanoscale LFA-1 clustering, representing a membrane proximal subset of the cycling population. Here, nanoclustering changes related to cell speed were confined to the focal zone, 100 to 420 nm above the cell membrane. In this zone, PTPN22 deficient and CXCL12 treated cells displayed a decrease in intracellular cluster size, and Manganese/CytoD cells displayed an increase.

The penultimate section addressed the contribution of constitutively phosphorylated focal adhesion kinase (pY397 FAK) to the 3D picture of nanoscale integrin regulation. This was inspired by work in the field which refers to newly discovered FAK/Integrin/Talin containing vesicles in non-leukocytes[71]. Here, FAK assumed cell wide changes in PTPN22 deficient cells where clusters became larger. FAK nanoclusters were also much more closely spaced in the submembrane leading edge, an area known to be the highly dependent on the formation of new ‘nascent’ adhesions dependent on the early inclusion of pY397 FAK.

Previously, integrin LFA-1 'activity' has been measured based largely on the affinity of the molecule, irrespective of the nano-scale make up of the adhesions themselves. To address this, constitutively phosphorylated pY397 FAK and pY416 Src family kinases (such as Lck) were used as proxy markers of LFA-1 nanocluster activation, in cells that had been tracked live up to the moment of fixation. Such a 'single cell correlative' approach allowed matching of the cell speed to cluster characteristics. The number of clusters per region displayed a negative correlative trend in PTPN22 proficient cells which was ablated in PTPN22 deficient cells. In addition the colocalization of nanoclusters of all three molecules was compared and in particular, pY397 FAK association with LFA-1 was increased in PTPN22 deficient cells.

Together, these experiments suggested a highly local regulation of nanoclustering which functionally changes cell speed. Below, a model is proposed describing the basic set up for 'nano-adhesion' regulation in migrating T cells.

Basic model for nano-adhesion organisation in effector T cell migration

In the cell membrane (figure 7-1 2D):

1. LFA-1 clusters are smaller, denser and more closely spaced in the focal zone than the leading edge membrane in all conditions
2. pYFAK clusters are smaller and closer together in the focal zone as compared to the leading edge, and colocalise with a small percentage of LFA-1 clusters cell wide
3. pYSrc nanoclusters are smaller than pYFAK clusters, and smaller still in the focal zone. They colocalise with a small percentage of LFA-1 clusters cell wide.

In the submembrane space (figure 7-1 3D):

1. Intracellular LFA-1 clusters are larger above the focal zone than above the leading edge
2. Intracellular pYFAK clusters are sparser above the focal zone as compared to the leading edge
3. Actin flows anterograde and retrograde in the leading edge, and only retrograde in the focal zone
4. At any one time >70 % of the cortical actin network is engaged to adhesions

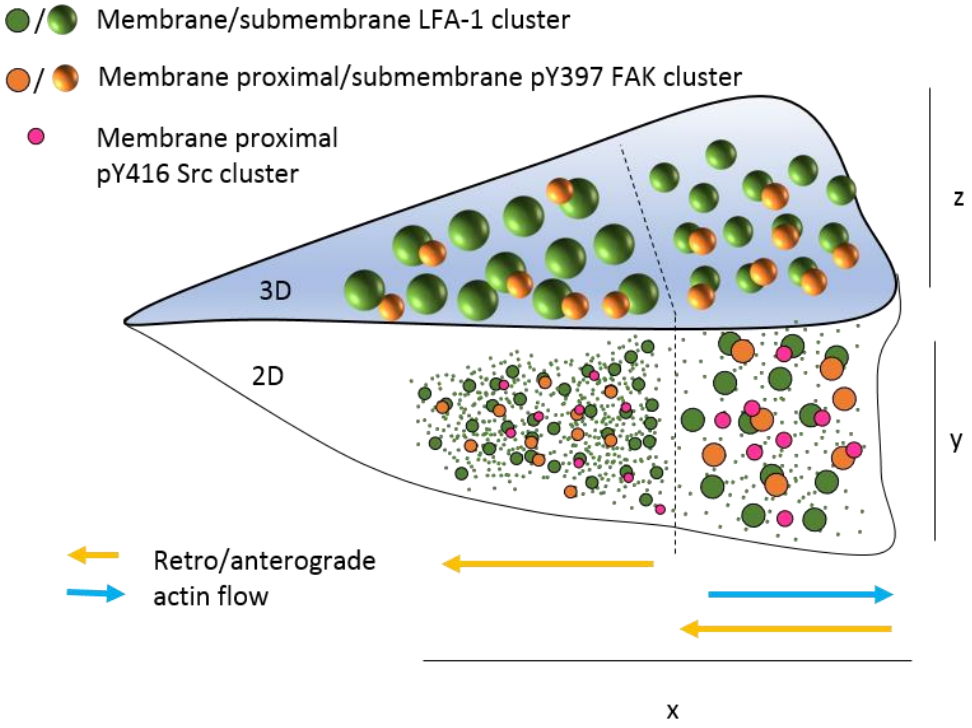

Figure 7-1: **Model for segmented nanoclustering in migrating T cell.** Schematic shows a summary of nanoclustering and actin phenomena in a migrating T cell. Spheres are intracellular clusters, circles are membrane or membrane proximal clusters. Diagram includes LFA-1, pY397 FAK, pY416 Src family kinase and actin flow.

Main nanoscale changes during speed alterations in effector T cell migration

Changes in this base nanoclustering model occur as described above, in fast moving PTPN22 deficient or CXCL12 treated cells, and slow moving Manganese or Cytochalasin treated cells.

In the cell membrane (figure 7-2):

1. LFA-1 membrane clusters were larger and less dense in fast cells compared to slow cells
2. A significant amount more cell wide colocalization of LFA-1 occurs with pY397 FAK and pY416 Src nanoclusters in PTPN22 deficient as compared to proficient cells.

In the submembrane space (figure 7-2):

1. LFA-1 clusters are smaller above the membrane in fast cells
2. pY397 FAK clusters are larger above the membrane in fast cells.

Overall in the membrane, LFA-1, pY397 FAK and pY416 Src clusters become larger in faster PTPN22 deficient cells. Intracellular LFA-1 clusters get smaller in the submembrane zone above the focal zone, and pY397 FAK clusters larger above the membrane cell wide.

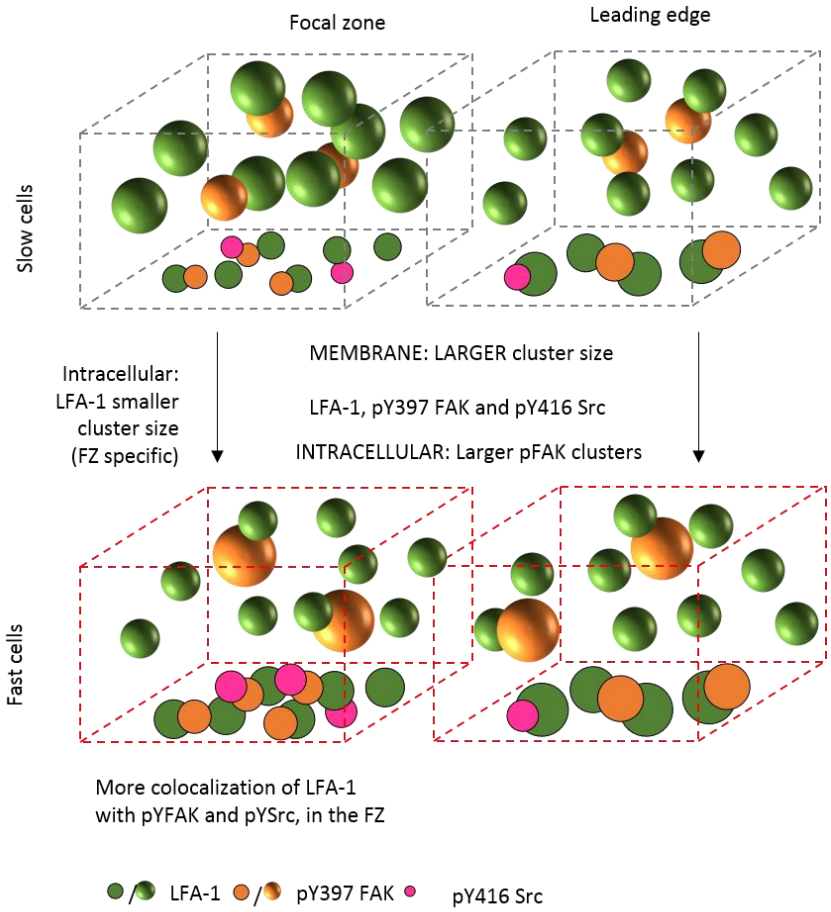

Figure 7-2: **Model for nanoclustering changes upon migration speed modulation. Boxes show cutaways of clusters in the membrane/submembrane in slow cells (Manganese, CytoD treated) and fast cells (CXCL12 treated, PTPN22 deficient).** Spheres are intracellular clusters, circles are membrane or membrane proximal clusters.

7.2 The biological importance of nanoclustering

The migratory capacity of a T cell is a great predictor of its potency during immunity[5,6]. The chemokine/cytokine signals that effector T cells of different subsets receive determine their ability to move quickly and to fight disease, shuttling signals from sites of infection to lymph nodes and to other cells. Naïve cells experience a jump in their migratory capacity upon antigen recognition and re-activated memory effector cells are extremely efficient at quickly reaching regions of new infection[20]. Their migration seems to be augmented, and while our chemical and mechanical understanding of how this happens has advanced in recent years,

nano-spatial regulation has heretofore been out of the reach of conventional microscopes. Here, I have shown that nanoscale regulation of LFA-1 based 'nano-adhesions' in T cells mediate cell migration, working synergistically with chemical and mechanical signals to transfer energy from actin retrograde flow to cell forward movement. Changes in these non-binary characteristics are likely to be very important for understanding disease processes, such as in the transition to autoimmunity.

PTPN22 phosphatase represents a potential candidate for a gene that plays a part in this transition[88–90]. As discussed, mutation at R620W in PTPN22/Lyp/PEP it is the best predictor of autoimmune disease aside from MHC itself, and predisposes for quite distinct and different autoimmune conditions[88,93]. These factors, coupled with biochemical links to control of integrin signalling, would indicate that PTPN22 mutation represents a basic, single cell level malfunction which results in this predisposition. This thesis proposes that the regulation of migration on the nanoscale is a good candidate for where this malfunction may occur.

Results presented in this thesis replicated a consistent functional phenotype in all cases: PTPN22 deficient cells migrate faster on an ICAM-1 coated glass coverslip. This was coupled to an increase in actin flow speed, together with less engagement of the actin at any one point in time with the molecular clutch. In fast moving cells, there was less immobile actin, suggesting a more transient link to the molecular clutch as cells move forwards at high speed. Actin flow speed more closely matched the cell speed in fast cells than in slowed cells, suggesting that in the end more of the force of the actin engine is being translated into forward cell movement. This suggests that more transient engagement of actin with the clutch results in better translation of actin flow speed to forward cell movement. How this works is highly likely to be down to the regulation of the adhesions themselves in their relation to actin.

The clutch itself is made up of integrin nanoclusters, and this is the first time that extra small clusters like these have been investigated in terms of T cell migration and autoimmune predisposition. Modulations that occur in integrin cluster size, density and spacing are here linked to cell speed and the linkage to the actin cytoskeleton, and suggest that T cells have a system of adhesion regulation quite different from non-leukocytes.

The existence of focal adhesions in T cells has been up for debate for a long period of time. As time has passed, and many different groups have worked on large adhesions and their association with actin, T cells have been left in the dark. This can be put down to the fact that adhesions in T cells are markedly different to adhesions studied in other cells. They are very small, necessitating super resolution microscopy to even discern them. Here, it is

demonstrated that unlike other adhesions, individual integrin nano-clusters don't grow in size as they mature and instead group together on the nano-scale, while individual clusters get smaller and denser. Indeed, it is important to note that in most conventional diffraction limited microscopy data, T cell adhesions sometimes appear larger in the focal zone. Comparing super resolved data with diffraction limited TIRF data shows that this effect is a consequence of multiple nanoclusters grouping together, which are clearly separated on the nanoscale, but appear as a mass of signal in lower resolution techniques[219]. This grouping may represent a different method of maturation, which is more along the lines of early nascent adhesion regulation[81,192], and puts an emphasis on a new definition for T cell nano-adhesion maturation during T cell migration. Individual nanoclusters of ~ 60 nm in diameter (the average size within the focal zone) may function as more dynamic signalling platforms than large adhesions, to facilitate faster turnover and regulation as T cells move quickly through diverse environments.

In its most basic form, experiments in section 5 show for the first time that for cell migration, integrin nano-clustering must be different in the focal zone to what it is in the leading edge: in some sense this can be thought of as a 'polarised' arrangement. T cells adopt a polarised morphology during most forms of migration *in vivo*[251], and as covered in section 6, the T cell leading edge harbours very different proteins and regulatory processes to the focal zone and uropod. The base behaviour of LFA-1 nano-clusters shown here in the transition from stationary to migrating T cells fit well into current models of LFA-1 affinity polarisation, and it may be highly significant that this front/middle discrimination is maintained even as the overall cluster characteristics change upon cell speed up under CXCL12 chemokine treatment or PTPN22 deficiency.

To look deeper into the regulation of such nanoclusters, the 3D submembrane region was investigated, because we know that LFA-1 is constantly recycled to and from the membrane[210,238]. Secondly, LFA-1 colocalization with phospho-FAK and phsopho-Src (encompassing Lck and Fyn) was investigated, because we know that they label different stages of nascent adhesion formation[73]; we theorised here that on the nanoscale we might be able to quantify these stages in their relation to cell migration.

3D work shown here revealed for the first time a changeable network of intracellular LFA-1 and pY397 FAK nano-clusters. Both populations are highly changeable in the lamella region, above the focal zone of the cell, and can be taken as a snapshot of the actively recycled portion. It is likely that these clusters reside within lipid vesicles, based on work previously

showing integrins (although not LFA-1, and not in T cells) being present in conjunction with FAK, Talin and vinculin in an active state of recycling[71], though this would have to be confirmed in T cells on the nanoscale. That LFA-1 clusters above the membrane get smaller, whereas pY397 FAK clusters get bigger in faster moving cells presents an interesting case, where the inclusion of pY397 FAK could be a signal for the vesicles to merge with the membrane at an increased rate. To investigate this possibility, live cell tracking followed by fixed cell 3D iPALM labelled for both targets, combined with colocalization analysis would be a realistic future experiment. Labelling the RabGTPases, which might preferentially target nanoclusters rich in pY397 FAK to the focal zone (Rab11 and Rab5) or the leading edge (Rab13) would be instructive[83], especially in the context of PTPN22 deficiency which here appears to affect the submembrane clustered population of LFA-1/pY397 FAK. Here we provide preliminary evidence that PTPN22 affects a population of LFA-1 likely to be undergoing active recycling, which may be separate from in-membrane regulation of LFA-1 cluster size, affected by both PTPN22 and CXCL12 in fast cells, and conversely affected by cell slow down induced by Manganese and Cytochalasin D.

LFA-1 colocalization on the nanoscale with phosphorylated kinases as a proxy measure for activation is an unstudied area. A lot is known about FAK and Src family kinases as markers of LFA-1 activation which can be borrowed from the nascent adhesion field and tested in T cells[34,68,71,83]. Crucially, it is known that phosphorylated intermediates such as pY397 FAK and pY416 Src (Lck and Fyn) are highly associated to integrin regulation and are highly constitutively phosphorylated[69,70]These are therefore very good candidates for nano-spatio temporal regulation. Data in this thesis show that there are changes induced by PTPN22 deficiency in the increased amount of LFA-1 membrane clusters that are associated with active FAK and Src family kinases. Due to the action of PTPN22 in deactivating Lck[67], and the way Lck regulates FAK[70], it is possible that this is a mechanism that changes the nano-spatial arrangement of these proteins, usually controlling their concentration within adhesions. PTPN22 deficiency therefore represents a situation where LFA-1 adhesions are more associated with pYFAK and pYLck, and that this relates to their linkage to the actin cytoskeleton and the ability of nanoadhesions to translate forward mobility. Short term future work in this area would look at expanding the repertoire of proteins that could be used as proxy measures for LFA-1 nanocluster signalling pathways.

7.3 Future work in the short term

To extend this analysis, pretested antibodies to targets within very early adhesions would be used in multicolour super resolution studies. Firstly, talin and vinculin would be used, and coupled to pY397 FAK and pY416 Src. Talin marks adhesions that are under tension, and due to the sequential revealment of cryptic sites, vinculin content in nano-adhesions could be used as a proxy measure for the quantitative amount of tension[81,82]. It would be interesting to see whether the amount of vinculin within individual adhesions scales with force across T cell nano-adhesions, which could be measured with new tension sensor tools based on FRET[252,253] that could potentially be super resolved. Extending this to 3D using iSTORM would be a clear step, to confirm or deny the existence of regulated talin/vinculin/FAK/integrin containing vesicles[85,86] in the submembrane space. Unpicking how individual nanoclusters are signalling using these proxy measures, would be linked to cell function by comparing PTPN22 deficient cells with cells treated under the same battery of conditions applied in this thesis. In addition, specific inhibitors of different parts of the actin cytoskeleton for example CK666 for the dendritic arp2/3 direction network and SMIFH2 for formin driven actin could be used to discern possible nanoscale regulation methods for nanoclusters under tension or at different stages of activation. These experiments could be done immediately, but would ideally be carried out with improvements which now exist for the acquisition and analysis techniques that are described below.

Acquisition improvements to the madSTORM technique, such as the use of TBS buffer instead of PBS, are reported to increase the amount of bound antibody to fragile phospho-epitopes[254]. These improvements will increase the potential for these techniques to be able to quantify relative amounts (molecules per cluster) of pY397 FAK and/or pY416 Src within adhesions. Because of what we known about the sequential nature of the localisation of these proteins to focal adhesions, we will be able to compare the relative activity of LFA-1 nanoadhesions segregated into different regions of the migrating T cell.

How the clusters are regulated, whether this is down to the actin cytoskeleton in a picket fence mechanism on the one hand, or whether each cluster is regulated by its association with scaffold proteins, is a problem that has a high degree of solvability at the current time. In fixed cells, this is only limited by the amount of targets that can be specifically labelled and imaged sequentially. 3 target imaging in this thesis was achieved by madSTORM, relying on sequential imaging, elution and relabelling of 647 tagged antibodies to different targets[146,254]. A readily

available improvement to this is DNA PAINT[145], which like madSTORM can be extended to multiple proteins of interest, but also does not require elution buffer, only a simple but thorough wash step. Actin imaging can be achieved in tandem through use of a IRIS[242] – a 'PAINT-like' technique that relies on transient binding of the lifeact peptide to achieve super resolved images.

Of course, multiple super resolved targets would increase the complexity of the analysis and interpretation. These tools must be developed in tandem. Fibre tracing software being developed in the lab will provide a quantitative measure of mesh size, and could feasibly be combined with cluster analysed regions to investigate the relationship between mesh size and, for example, nano-cluster size.

In order to extend cluster colocalization to an individual cluster basis, a Bayesian 'purity' measurement is in development in the lab. The cluster colocalization tool used in this thesis gives an overview, per region of interest, of the co-clustering by producing a Pearson's correlation coefficient between self-clustering of molecule A and co-clustering with molecule B. It was successfully used to discern that PTPN22 deficient migrating cells display more pYFAK, pYSrc, LFA-1 nano-cluster colocalization cell wide. To extract further, more detailed information a tool that measures the overlap between individual clusters identified using the Bayesian cluster analysis approach will be used. This 'purity' measurement would allow us to interrogate fringe characteristics such as, for example a subset of very larger nanoclusters of species A that are associated with only very small subsets of clusters of species B. A further extension to this would be to group together species A and B as one population and look at their individual colocalization with nanoclusters of species C. In the context of pY397 FAK, pY416 Src, talin and vinculin this may well allow us to find subsets of clusters in heterogeneous data that are marked for very specific tasks.

Within a given sample, there are many thousands of clusters, and a lot of heterogeneity. This thesis, and indeed most of biology, was mostly focused on looking at the median/mean values of these wide distributions to discern (successfully) reproducible differences between conditions. However, it is highly likely that clusters on the tail ends of this distribution are also functionally important. The high resolution, and statistical power intrinsic to super resolution techniques gives us information about this population, but it is not exploited. This thesis almost gets to the point of addressing this problem: it is not unreasonable to think that nanoclusters of certain characteristics densities, sizes and spacings might be associated to particular nano-clusters of different signalling intermediates, and that this might be

functionally important – for example here where we see that there is more cluster colocalization between LFA-1/pY397 FAK/pY416 Lck in PTPN22$^{-/-}$ cells.

7.4 Future work in the medium to long term

While it is true that T cells adopt polarised modes of migration in wide contexts, and use LFA-1 based adhesions and actin flow to navigate them[15,220,251], other leukocytes such as DCs have been reported to adopt modes of migration through tissues that are integrin independent[24]. Different systems for *in vitro* cell migration will therefore be explored to investigate the flow of the cytoskeleton, and the use of integrin based nano-adhesions in T cells in environments that recapitulate a confined interstitial environment. A useful, controllable and super resolution compatible version of this comes in the form of microchannels[255–257]in which ICAM-1 + and ICAM-1 – migration could be compared correlatively in TIRF, first by tracking the actin in the transgenic live T cells as in chapter x, then by fixing the cells and using madSTORM or DNA PAINT to discern actin ultrastructure and co-clustering of LFA-1, pYFAK, pYSrc, vinculin and talin. It is an open question as to whether PTPN22 deficiency affects confined migration of T cells in the same way as it affects 2D migration.

Interstitial migration also consists of migration between collagen fibres[220], which are formed in collaboration with chemokine networks. Amazing images of T cells making contact with an antigen presenting cell in collagen using the lattice lightsheet system have provided proof of concept that this can be done[211], which to some extent recapitulates the most difficult stage of T cell migration: through a dense, interstitial tissue in a collagen rich environment.

This aside, the gold standard for studying T cell migration is direct *in vivo* imaging, and great strides have been made in studying leukocytes in lymph nodes using two-photon microscopy. There has so far only been a single example of *in vivo* super resolution localisation microscopy, which used lightsheet STORM to image TCR nanoclusters upon activation by pMHC[254]. This kind of set up could be achieved with the right microscope set up. Advances in the formation of thinner lightsheets made up of non-diffracting beams[211], and the use of adaptive optics[258] to account for scattering and refractive index differences when imaging through tissue have the potential to broaden the application of such single molecule techniques.

Work presented in this thesis has made steps towards creating a system that is correlative – where migration behaviour of cells is tracked up until the moment of fixation, and cluster behaviour is then related back to the cell speed of single cells at that moment in time. Of

course, the way to improve this technique would simply be to image single molecules and cells live, simultaneously, and this is in my opinion the future of the field.

What is lacking here is temporal resolution, to capture the interactions of nanoscale clusters regulated on a very quick timescale. A different way to look at the problem of temporal resolution in super resolution microscopy images is to think of the minimum amount of data required for it to be reliably and reproducibly analysable: if one only requires a limited amount of localisations in clusters to identify a cluster, then the time required to acquire a single frame of data will be vastly reduced. To address this, the Bayesian analysis tool was stress tested to discern the minimum number of localisations per reconstructed point map required to identify individual clusters. Based on this, a new quantitation tool is under development in the Owen lab which groups subsets of frames together to reliably track clusters live over short time periods (Juliette Griffié, in preparation).

While this tool has the potential to be extremely helpful, what is required in the field is better fluorophores, that are compatible for such live SLM microscopy work. Some groups, particularly at Janelia farm, VA[259] and at Osaka university in Japan[260], have started to develop multi-blinkers, with a high fluorescence yield that work at low laser power. You can imagine that if the goal is to track clusters in which there are blinking fluorophores, it might be advantageous to have a fluorescent emitter that blinks more than once in the same cluster. In this way, clusters can be tracked for longer before they use up their budget of fluorophores within them. On the other hand, multi-blinking itself is problematic, as it can lead to false clusters. Investigations into the statistical weight of multi-blinking in a new, hypothetical fluorophore could be undertaken to find out whether, as an example 1) cluster size stays the same in a situation where the ground truth is that cluster size stays the same and 2) cluster size differs where the ground truth is that it differs.

A great problem with super resolution microscopy is the low number of cells that are imaged typically per dataset. Here, significant effort was made to capture reasonable numbers of cells from each mouse, and to only take experiments forward if phenomena were recapitulated across cells derived from several animals. A second problem, related to the low n numbers is user bias: in the experiments presented in section 5, there was a certain amount of necessary bias in picking fixed polarised cells which were assumed to be undergoing migration at the time of migration. This was mitigated/controlled for in two ways 1) a wealth of investigator experience in discerning the distinct morphological features of a cell that was migrating at the time of migration and 2) that phase contrast movies of the same sample (though not the same

subset of cells) were captured to discern that at any one time, almost 100 % of the cells in the polarised field of view were undergoing migration. It was very reassuring that the nanoclustering phenotypes we saw in section 5 were recapitulated in section 6, where an even more correlative approach was used to measure clustering in cells that had been tracked up to the moment of fixation, and could therefore confidently be assumed to have clustering programs used for migration.

High throughput automation of super resolution microscopy would solve the n number problem, the multiblinking problem, all of this correlative fixed cell work and in the future, live cell SLM and the investigation of fringe phenomena. Indeed, the full quantitative power of SLM in particular has not been exploited. As a possible solution, Masahiro Ueda at Osaka university recently demonstrated a machine which automates single particle tracking across thousands of live cells per day (Masahiro Ueda, 2017: talk given at thematic biophysical society meeting, Taipei) (my record is 80 cells), which could be co-opted for super resolution STORM imaging. A 96 well plate containing the transfected cells is added to the microscope, and the positions of the cells in x and y and the focal position in z is identified using a machine learning algorithm which teaches itself, based on provided priors how to recognise a cell in a field of view. Single particle tracking was carried out automatically on each cell, before addition of a drug treatment using a robot arm, then the process was repeated. Analysed tracks allowed Masahiro to converge on a reliable answer that was not clear amongst heterogeneous data of lower n number.

The advent of CRISPR/Cas9 gene editing will prove invaluable to many fields, and one is fluorescence microscopy. The advantage of fixed cell work is that antibodies, and even small probes like nanobodies, as well as other techniques like DNA-PAINT can be used to image proteins of interest. For live cell work, fluorescent proteins are often genetically encoded to continue from the N-terminus of target proteins, and provided to the cell within a plasmid which is constantly transcribed and translated by host machinery. There are many problems with this approach, as overexpression of a given protein intrinsically affects associated signalling pathways, which may change the localisation/regulation of the protein under investigation. CRISPR/Cas solves the first problem, where chosen fluorescent probes tagged to proteins can be coded directly into the correct locus in the genome and transcribed/regulated as normal. With the correct genes, expertise and controls, this can be achieved today. The second problems is the probe itself: the behaviour of such tagged proteins may not always be physiological due to the effect of having a large FP attached to the N-terminus. First of all its transcription and translation, or transport from the ER into/out of the golgi may be altered[261].

This includes the possibility of refolding errors due to the large FP, or even after an unknown ablation of a previously important interaction which cannot be controlled for. These aspects would have to be tested for each new fusion, but could feasibly be achieved given time. To allay these problems, in the medium to long term, new live compatible probes are under development that are very small, and are therefore less likely to affect the function of a given endogenous protein (Nils Gustafsson, UCL, 2017 in preparation). The brightness and detectiblity of these probes will be key and may in the future allow for live cell imaging of endogenous protein, which exists at generally a much lower copy number than overexpressed proteins provided by the experimenter in transfected plasmids.

A subset of this thesis was dedicated to chemical fixation techniques, which can be optimised to produce reproducible relative answers, but all suffer from epitope masking and changes to ultrastructure. The gold standard fixation technique available is cryogenic freezing in vitreous ice[127,262], where the high heat capacity of liquid ethane allows for such fast freezing that water molecules can't form a crystal lattice, and all membrane and protein features in cells are preserved. Efforts are now being made to combine this with fluorescent labelling in super resolution, to allow for the identification of structures using fluorescent probes that can be correlated to EM images of the same structures in the same sample (Harald Hess, 2017 in preparation).

With all of these improvements in mind, in the next 5 to 10 years, super resolution microscopy will be in a position to address many new biological problems, where multiple species of individual protein nano-clusters can be measured *in vivo* with very high n numbers. For T cell biologists, this will fuel a new way of thinking about the biological relevance of nano-spatio temporal regulation, and in the field of migration may help us to elucidate how nano-clustering signal islands in the T cell membrane can change to spread a signal through a cell, which can lead to functional changes in first the cell itself, then a population of cells which might lead to the diverse range of autoimmune diseases seen here to be predisposed for by a SNP in a single phosphatase gene.

Publications

Journal Publications

1. **M. Shannon,** J. Pineau, J. Griffie, G. Cornish* and A. Cope* and D.M. Owen*. *Clutch engagement, actin dynamics and nanoscale LFA-1 integrin clustering are tuned for high speed in PTPN22 -/- autoimmune predisposing T cells during migration.* (In preparation) **Equal senior authors*
2. **M. Shannon**, G.L. Burn, A.P. Cope, G. Cornish* and D.M. Owen*. *Application of Super-resolution microscopy to the analysis of protein clustering in T cells*. Biochemical Society Transactions 43(3), 315-321 (2015) **Equal senior author*.
3. J. Griffié, L. Shlomovich, D.J. Williamson, **M. Shannon**, J. Aarons, S. Khuon, G. Burn, L. Boelen, R. Peters, A.P. Cope, E.A.K. Cohen, P. Rubin-Delanchy and D.M. Owen. *3D Bayesian cluster analysis of super-resolution iPALM data reveals the recruitment of LAT vesicles to the T cell immunological synapse.* Scientific Reports (submitted).
4. J. Griffié, **M. Shannon**, C.L. Bromley, L. Boelen, G.L. Burn, D.J. Williamson, N. Heard, A.P. Cope, D.M. Owen* and P. Rubin-Delanchy*. *Bayesian cluster analysis of single molecule localisation microscopy data*. Nature Protocols 11, 2499-2514 (2016). **Equal senior author*.

Book chapters

1. G.W. Ashdown*, J. Griffié*, **M. Shannon,** and D.M. Owen. *Correlations and colocalization* in Working with imaging data in the biosciences: A primer, Edited by Anne Wheeler and Ricardo Henriques, Wiley, Chichester, UK (2017, in press). *These authors contributed equally.

Other publications

1. **M. Shannon.** *Leukosomes engage stealth mode by altering their protein shell.* Online at nanotechweb.org from the IoP. Edited by Dr. Anna Demming. (2017)
2. **M. Shannon.** *Fast live nanoscopy reveals protein confinement in neurons.* News piece.Online at nanotechweb.org from the IoP. Edited by Dr. Anna Demming. (2017)
3. **M. Shannon.** *Multiple posts as editor of the Randall Science Blog.* Online at science.kcl.fyi.
4. G.W. Ashdown, G.L. Burn, J. Griffié, **M. Shannon,** and D.M. Owen. *Quantification of super-resolution images.* In *Microscopy&Analysis*, Edited by Chris Parmenter. John Wiley & Sons Ltd., Hoboken, NJ, US (2015).

Conference presentations

1. D.S. Ushakov, G.W. Ashdown, O. Nussbaumer, **M. Shannon**, R. Beatson, L. Abeler-Dömer, D.M. Owen and A.C. Hayday. *Super-resolution microscopy of tissue resident $\gamma\delta$ T cells*. Microscopy and Microscience Congress, Manchester, UK (2017) (poster).
2. **M. Shannon**, G. Cornish, A.P. Cope and D.M. Owen. *Super-resolution microscopy of T cell migration*. Janelia Farm Advanced Imaging Center Conference, Ashburn, VA, US (2017) (poster).

3. **M. Shannon**, G. Cornish, A. Cope, D.M. Owen. *Linking nanoscale integrin clustering with the molecular clutch in migrating T cells.* London Super Resolution group conference, London, UK. (2017) (conference talk).
4. **M. Shannon**, G. Cornish, A. Cope, D.M. Owen. *Linking actin engagement with integrin nanoclustering using super resolution in PTPN22 -/- T cells.* King's Bioscience Institute symposium, London, UK. (2016) (conference talk).
5. **M. Shannon**, G.L. Burn, A.P. Cope, G. Cornish and D.M. Owen. *Application of Super-resolution microscopy to the analysis of protein clustering in T cells*. Super-resolution Imaging in Infection and Immunity Symposium, Oeiras, Portugal (2015) (conference talk).
6. **M. Shannon**, G. Cornish and D.M. Owen. *Molecular quantification of actin dynamics in effector T cells*. UCL super-resolution symposium, London, UK (2015) (poster).
7. **M. Shannon**, G. Cornish and D.M. Owen. *Actin flow and integrin nanoclustering in migrating T cells.* Randall division retreat, London, UK (conference talk). (2015). (Conference talk)

References

1. Dutton, R. W., Bradley, L. M. & Swain, S. L. T CELL MEMORY. *Annu. Rev. Immunol.* **16,** 201–223 (1998).

2. Buchholz, V. R., Schumacher, T. N. M. & Busch, D. H. T Cell Fate at the Single-Cell Level. *Annu. Rev. Immunol.* **34,** 65–92 (2016).

3. Liston, A., Lesage, S., Wilson, J., Peltonen, L. & Goodnow, C. C. Aire regulates negative selection of organ-specific T cells. *Nat. Immunol.* **4,** 350–354 (2003).

4. Anderson, M. S. *et al.* Projection of an Immunological Self Shadow Within the Thymus by the Aire Protein. *Science* **298,** 1395–1401 (2002).

5. Beltman, J. B., Marée, A. F. M., Lynch, J. N., Miller, M. J. & de Boer, R. J. Lymph node topology dictates T cell migration behavior. *J. Exp. Med.* **204,** 771–80 (2007).

6. Bousso, P. & Robey, E. Dynamics of CD8+ T cell priming by dendritic cells in intact lymph nodes. *Nat. Immunol.* **4,** 579–585 (2003).

7. Kremer, K. N., Kumar, A. & Hedin, K. E. G alpha i2 and ZAP-70 mediate RasGRP1 membrane localization and activation of SDF-1-induced T cell functions. *J. Immunol.* **187,** 3177–85 (2011).

8. Charbonnier, L.-M., Wang, S., Georgiev, P., Sefik, E. & Chatila, T. A. Control of peripheral tolerance by regulatory T cell-intrinsic Notch signaling. *Nat. Immunol.* **16,** 1162–73 (2015).

9. Iberg, C. A., Jones, A. & Hawiger, D. Dendritic Cells As Inducers of Peripheral Tolerance. *Trends in Immunology* **38,** 793–804 (2017).

10. Murphy, K., Travers, P., Walport, M., & Janeway, C. *Janeway's immunobiology (8th ed.).* (Garland Science, 2012).

11. Wolint, P., Betts, M. R., Koup, R. A. & Oxenius, A. Immediate Cytotoxicity But Not Degranulation Distinguishes Effector and Memory Subsets of CD8 + T Cells. *J. Exp. Med.* **199,** 925–936 (2004).

12. Kaech, S. M., Hemby, S., Kersh, E. & Ahmed, R. Molecular and Functional Profiling of Memory CD8 T Cell Differentiation. *Cell* **111,** 837–851 (2002).

13. Masopust, D. Preferential Localization of Effector Memory Cells in Nonlymphoid Tissue. *Science* **291,** 2413–2417 (2001).

14. Gebhardt, T. *et al.* Memory T cells in nonlymphoid tissue that provide enhanced local immunity during infection with herpes simplex virus. *Nat. Immunol.* **10,** 524–530 (2009).

15. Teijeira, A. *et al.* T Cell Migration from Inflamed Skin to Draining Lymph Nodes Requires Intralymphatic Crawling Supported by ICAM-1/LFA-1 Interactions. *Cell Rep.* **18,** 857–865 (2017).

16. Sallusto, F., Lenig, D., Förster, R., Lipp, M. & Lanzavecchia, A. Two subsets of memory T lymphocytes with distinct homing potentials and effector functions. *Nature* **401,** 708–712 (1999).

17. Wohler, J., Bullard, D., Schoeb, T. & Barnum, S. LFA-1 is critical for regulatory T cell homeostasis and function. *Mol. Immunol.* **46,** 2424–8 (2009).

18. Cox, M. A., Barnum, S. R., Bullard, D. C. & Zajac, A. J. ICAM-1–dependent tuning of memory CD8 T-cell responses following acute infection. *Proc. Natl. Acad. Sci.* **110,** 1416–1421 (2013).

19. Neve-Oz, Y., Razvag, Y., Sajman, J. & Sherman, E. Mechanisms of localized activation of the T cell antigen receptor inside clusters. *Biochim. Biophys. Acta - Mol. Cell Res.* **1853,** 810–821 (2015).

20. van Heijst, J. W. J. *et al.* Recruitment of Antigen-Specific CD8+ T Cells in Response to Infection Is Markedly Efficient. *Science* **325,** 1265–1269 (2009).

21. Butcher, E. C. & Picker, L. J. Lymphocyte homing and homeostasis. *Science* **272,** 60–6 (1996).

22. Salmi, M. *et al.* Selective endothelial binding of interleukin-2-dependent human T-cell lines derived from different tissues. *Proc. Natl. Acad. Sci. U. S. A.* **89,** 11436–40 (1992).

23. von Andrian, U. H. & Mackay, C. R. T-Cell Function and Migration — Two Sides of the Same Coin. *N. Engl. J. Med.* **343,** 1020–1034 (2000).

24. Lämmermann, T. *et al.* Rapid leukocyte migration by integrin-independent flowing and squeezing. *Nature* **453,** 51–5 (2008).

25. Friedl, P., Borgmann, S. & Bröcker, E. B. Amoeboid leukocyte crawling through extracellular matrix: lessons from the Dictyostelium paradigm of cell movement. *J. Leukoc. Biol.* **70,** 491–509 (2001).

26. Friedl, P. & Weigelin, B. Interstitial leukocyte migration and immune function. *Nat. Immunol.* **9,** 960–969 (2008).

27. Katakai, T., Habiro, K. & Kinashi, T. Dendritic Cells Regulate High-Speed Interstitial T Cell Migration in the Lymph Node via LFA-1/ICAM-1. *J. Immunol.* **191,** 1188–1199 (2013).

28. Boscacci, R. T. *et al.* Comprehensive analysis of lymph node stroma-expressed Ig superfamily members reveals redundant and nonredundant roles for ICAM-1, ICAM-2, and VCAM-1 in lymphocyte homing. *Blood* **116,** 915–925 (2010).

29. Woolf, E. *et al.* Lymph node chemokines promote sustained T lymphocyte motility without triggering stable integrin adhesiveness in the absence of shear forces. *Nat. Immunol.* **8,** 1076–1085 (2007).

30. Raab, M. *et al.* T Cell Receptor 'Inside-Out' Pathway via Signaling Module SKAP1-RapL Regulates T Cell Motility and Interactions in Lymph Nodes. *Immunity* **32,** 541–556 (2010).

31. Harris, T. H. *et al.* Generalized Lévy walks and the role of chemokines in migration of effector CD8+ T cells. *Nature* **486,** 545–8 (2012).

32. Dustin, M. L. Stop and go traffic to tune T cell responses. *Immunity* **21,** 305–14 (2004).

33. Constantin, G. *et al.* Chemokines Trigger Immediate β2 Integrin Affinity and Mobility Changes: Differential Regulation and Roles in Lymphocyte Arrest under Flow. *Immunity* **13,** 759–769 (2000).

34. Smith, A. *et al.* A talin-dependent LFA-1 focal zone is formed by rapidly migrating T lymphocytes. *J. Cell Biol.* **170,** 141–51 (2005).

35. Alexandrova, A. Y. *et al.* Comparative dynamics of retrograde actin flow and focal adhesions: formation of nascent adhesions triggers transition from fast to slow flow. *PLoS One* **3,** e3234 (2008).

36. Shannon, M. J., Burn, G., Cope, A., Cornish, G. & Owen, D. M. Protein clustering and spatial organization in T-cells. *Biochem. Soc. Trans.* **43,** 315–21 (2015).

37. Evans, R., Lellouch, A. C., Svensson, L., McDowall, A. & Hogg, N. The integrin LFA-1 signals through ZAP-70 to regulate expression of high-affinity LFA-1 on T lymphocytes. *Blood* **117,** 3331–42 (2011).

38. Ponti, A., Machacek, M., Gupton, S. L., Waterman-Storer, C. M. & Danuser, G. Two distinct actin networks drive the protrusion of migrating cells. *Science* **305,** 1782–6 (2004).

39. Gupton, S. L., Eisenmann, K., Alberts, A. S. & Waterman-Storer, C. M. mDia2 regulates actin and focal adhesion dynamics and organization in the lamella for efficient epithelial cell migration. *J. Cell Sci.* **120,** 3475–87 (2007).

40. Ridley, A. J. *et al.* Cell migration: integrating signals from front to back. *Science* **302,** 1704–9 (2003).

41. Tybulewicz, V. L. J. Vav-family proteins in T-cell signalling. *Curr. Opin. Immunol.* **17,** 267–74 (2005).

42. Filbert, E. L., Le Borgne, M., Lin, J., Heuser, J. E. & Shaw, A. S. Stathmin regulates microtubule dynamics and microtubule organizing center polarization in activated T cells. *J. Immunol.* **188,** 5421–7 (2012).

43. Yi, J., Wu, X. S., Crites, T. & Hammer, J. A. Actin retrograde flow and actomyosin II arc contraction drive receptor cluster dynamics at the immunological synapse in Jurkat T cells. *Mol. Biol. Cell* **23,** 834–52 (2012).

44. Jurado, C., Haserick, J. R. & Lee, J. Slipping or gripping? Fluorescent speckle microscopy in fish keratocytes reveals two different mechanisms for generating a retrograde flow of actin. *Mol. Biol. Cell* **16,** 507–18 (2005).

45. Thievessen, I. *et al.* Vinculin–actin interaction couples actin retrograde flow to focal adhesions, but is dispensable for focal adhesion growth. *J. Cell Biol.* **202,** 163–177 (2013).

46. Springer, T. A. & Dustin, M. L. Integrin inside-out signaling and the immunological synapse. *Curr. Opin. Cell Biol.* **24,** 107–115 (2012).

47. Hynes, R. O. Integrins: bidirectional, allosteric signaling machines. *Cell* **110,** 673–87 (2002).

48. Green, C. E. *et al.* Dynamic shifts in LFA-1 affinity regulate neutrophil rolling, arrest, and transmigration on inflamed endothelium. *Blood* **107,** 2101–11 (2006).

49. Zhang, X., Wojcikiewicz, E. & Moy, V. T. Force Spectroscopy of the Leukocyte Function-Associated Antigen-1/Intercellular Adhesion Molecule-1 Interaction. *Biophys. J.* **83,** 2270–2279 (2002).

50. Chang, A. C. *et al.* Single Molecule Force Measurements in Living Cells Reveal a

Minimally Tensioned Integrin State. *ACS Nano* **10,** 10745–10752 (2016).

51. Sun, Z., Guo, S. S. & Fässler, R. Integrin-mediated mechanotransduction. *J. Cell Biol.* **215,** 445–456 (2016).

52. Nordenfelt, P. *et al. Direction of actin flow dictates integrin LFA-1 orientation during leukocyte migration*. *bioRxiv* (2016). doi:10.1101/071936

53. Nordenfelt, P., Elliott, H. L. & Springer, T. A. Coordinated integrin activation by actin-dependent force during T-cell migration. *Nat. Commun.* **7,** 13119 (2016).

54. Hogg, N. *et al.* How T cells use LFA-1 to attach and migrate. *Immunol. Lett.* **92,** 51–54 (2004).

55. Ardouin, L. *et al.* Vav1 transduces TCR signals required for LFA-1 function and cell polarization at the immunological synapse. *Eur. J. Immunol.* **33,** 790–7 (2003).

56. Grönholm, M. *et al.* TCR-induced activation of LFA-1 involves signaling through Tiam1. *J. Immunol.* **187,** 3613–9 (2011).

57. Luo, B.-H., Carman, C. V. & Springer, T. A. Structural Basis of Integrin Regulation and Signaling. *Annu. Rev. Immunol.* **25,** 619–647 (2007).

58. Qu, A. & Leahy, D. J. Crystal structure of the I-domain from the CD11a/CD18 (LFA-1, alpha L beta 2) integrin. *Proc. Natl. Acad. Sci.* **92,** 10277–10281 (1995).

59. Thomas, W. For catch bonds, it all hinges on the interdomain region. *J. Cell Biol.* **174,** 911–3 (2006).

60. Zhu, C., Yago, T., Lou, J., Zarnitsyna, V. I. & McEver, R. P. Mechanisms for flow-enhanced cell adhesion. *Ann. Biomed. Eng.* **36,** 604–21 (2008).

61. Kong, F., García, A. J., Mould, A. P., Humphries, M. J. & Zhu, C. Demonstration of catch bonds between an integrin and its ligand. *J. Cell Biol.* **185,** 1275–84 (2009).

62. Shimaoka, M., Takagi, J. & Springer, T. A. Conformational Regulation of Integrin Structure and Function. *Annu. Rev. Biophys. Biomol. Struct.* **31,** 485–516 (2002).

63. Kim, M., Carman, C. V & Springer, T. A. Bidirectional Transmembrane Signaling by Cytoplasmic Domain Separation in Integrins. *Science* **301,** 1720–1725 (2003).

64. Kim, M., Carman, C. V, Yang, W., Salas, A. & Springer, T. A. The primacy of affinity over clustering in regulation of adhesiveness of the integrin {alpha}L{beta}2. *J. Cell Biol.* **167,** 1241–53 (2004).

65. Stanley, P. *et al.* Intermediate-affinity LFA-1 binds alpha-actinin-1 to control migration at the leading edge of the T cell. *EMBO J.* **27,** 62–75 (2008).

66. Constantin, G. *et al.* Chemokines trigger immediate beta2 integrin affinity and mobility changes: differential regulation and roles in lymphocyte arrest under flow. *Immunity* **13,** 759–69 (2000).

67. Burn, G. L. *et al.* Superresolution imaging of the cytoplasmic phosphatase PTPN22 links integrin-mediated T cell adhesion with autoimmunity. *Sci. Signal.* **9,** ra99 (2016).

68. Webb, D. J. *et al.* FAK–Src signalling through paxillin, ERK and MLCK regulates adhesion disassembly. *Nat. Cell Biol.* **6,** 154–161 (2004).

69. Chapman, N. M. & Houtman, J. C. D. Functions of the FAK family kinases in T cells:

beyond actin cytoskeletal rearrangement. *Immunol. Res.* **59,** 23–34 (2014).

70. Kleinschmidt, E. G. & Schlaepfer, D. D. Focal adhesion kinase signaling in unexpected places. *Curr. Opin. Cell Biol.* **45,** 24–30 (2017).

71. Nader, G. P. F., Ezratty, E. J. & Gundersen, G. G. FAK, talin and PIPKIγ regulate endocytosed integrin activation to polarize focal adhesion assembly. *Nat. Cell Biol.* **18,** 491–503 (2016).

72. Sieg, D. J., Hauck, C. R. & Schlaepfer, D. D. Required role of focal adhesion kinase (FAK) for integrin-stimulated cell migration. *J. Cell Sci.* **112 (Pt 1,** 2677–91 (1999).

73. Swaminathan, V., Fischer, R. S. & Waterman, C. M. The FAK-Arp2/3 interaction promotes leading edge advance and haptosensing by coupling nascent adhesions to lamellipodia actin. *Mol. Biol. Cell* **27,** 1085–100 (2016).

74. Davidson, D. & Veillette, A. PTP-PEST, a scaffold protein tyrosine phosphatase, negatively regulates lymphocyte activation by targeting a unique set of substrates. *EMBO J.* **20,** 3414–3426 (2001).

75. Lawson, C. *et al.* FAK promotes recruitment of talin to nascent adhesions to control cell motility. *J. Cell Biol.* **196,** 223–232 (2012).

76. Case, L. B. *et al.* Molecular mechanism of vinculin activation and nanoscale spatial organization in focal adhesions. *Nat. Cell Biol.* **17,** 880–92 (2015).

77. Kanchanawong, P. *et al.* Nanoscale architecture of integrin-based cell adhesions. *Nature* **468,** 580–584 (2010).

78. Choi, C. K. *et al.* Actin and α-actinin orchestrate the assembly and maturation of nascent adhesions in a myosin II motor-independent manner. *Nat. Cell Biol.* **10,** 1039–1050 (2008).

79. Hu, K., Ji, L., Applegate, K. T., Danuser, G. & Waterman-Storer, C. M. Differential transmission of actin motion within focal adhesions. *Science* **315,** 111–5 (2007).

80. Yan, J., Yao, M., Goult, B. T. & Sheetz, M. P. Talin Dependent Mechanosensitivity of Cell Focal Adhesions. *Cell. Mol. Bioeng.* **8,** 151–159 (2015).

81. Goult, B. T. *et al.* RIAM and vinculin binding to talin are mutually exclusive and regulate adhesion assembly and turnover. *J. Biol. Chem.* **288,** 8238–49 (2013).

82. Yao, M. *et al.* Mechanical activation of vinculin binding to talin locks talin in an unfolded conformation. *Sci. Rep.* **4,** 4610 (2015).

83. Alanko, J. *et al.* Integrin endosomal signalling suppresses anoikis. *Nat. Cell Biol.* **17,** 1412–1421 (2015).

84. Ling, K. *et al.* Tyrosine phosphorylation of type Igamma phosphatidylinositol phosphate kinase by Src regulates an integrin-talin switch. *J. Cell Biol.* **163,** 1339–1349 (2003).

85. Nishikimi, A. *et al.* Rab13 acts downstream of the kinase Mst1 to deliver the integrin LFA-1 to the cell surface for lymphocyte trafficking. *Sci. Signal.* **7,** ra72-ra72 (2014).

86. Katagiri, K., Imamura, M. & Kinashi, T. Spatiotemporal regulation of the kinase Mst1 by binding protein RAPL is critical for lymphocyte polarity and adhesion. *Nat. Immunol.* **7,** 919–28 (2006).

87. Svensson, L. *et al.* Calpain 2 controls turnover of LFA-1 adhesions on migrating T

lymphocytes. *PLoS One* **5,** e15090 (2010).

88. Burn, G. L., Svensson, L., Sanchez-Blanco, C., Saini, M. & Cope, A. P. Why is PTPN22 a good candidate susceptibility gene for autoimmune disease? *FEBS Lett.* **585,** 3689–98 (2011).

89. Begovich, A. B. *et al.* A missense single-nucleotide polymorphism in a gene encoding a protein tyrosine phosphatase (PTPN22) is associated with rheumatoid arthritis. *Am. J. Hum. Genet.* **75,** 330–7 (2004).

90. Bottini, N., Vang, T., Cucca, F. & Mustelin, T. Role of PTPN22 in type 1 diabetes and other autoimmune diseases. *Semin. Immunol.* **18,** 207–13 (2006).

91. Brand, O., Gough, S. & Heward, J. HLA, CTLA-4 and PTPN22: the shared genetic master-key to autoimmunity? *Expert Rev. Mol. Med.* **7,** 1–15 (2005).

92. Cloutier, J. F. & Veillette, A. Cooperative inhibition of T-cell antigen receptor signaling by a complex between a kinase and a phosphatase. *J. Exp. Med.* **189,** 111–21 (1999).

93. Svensson, L., Burn, G., Sanchez-Blanco, C., Zamoyska, R. & Cope, A. Lyp/PTPN22 is a negative regulator of integrin mediated T cell adhesion and migration; the disease associated PTPN22 allelic variant is a loss of function mutant that perturbs T cell migration. *Ann. Rheum. Dis.* **70,** A7–A7 (2011).

94. Cloutier, J. F. & Veillette, A. Association of inhibitory tyrosine protein kinase p50csk with protein tyrosine phosphatase PEP in T cells and other hemopoietic cells. *EMBO J.* **15,** 4909–18 (1996).

95. Gregorieff, A., Cloutier, J. F. & Veillette, A. Sequence requirements for association of protein-tyrosine phosphatase PEP with the Src homology 3 domain of inhibitory tyrosine protein kinase p50(csk). *J. Biol. Chem.* **273,** 13217–22 (1998).

96. Fiorillo, E. *et al.* Autoimmune-associated PTPN22 R620W Variation Reduces Phosphorylation of Lymphoid Phosphatase on an Inhibitory Tyrosine Residue. *J. Biol. Chem.* **285,** 26506–26518 (2010).

97. Swaminathan, V. *et al.* Actin retrograde flow actively aligns and orients ligand-engaged integrins in focal adhesions. *Proc. Natl. Acad. Sci. U. S. A.* **114,** 10648–10653 (2017).

98. Zhang, X. *et al.* Talin depletion reveals independence of initial cell spreading from integrin activation and traction. *Nat. Cell Biol.* **10,** 1062–1068 (2008).

99. Sherman, E., Barr, V. & Samelson, L. E. Super-resolution characterization of TCR-dependent signaling clusters. *Immunol. Rev.* **251,** 21–35 (2013).

100. Dupré, L., Houmadi, R., Tang, C. & Rey-Barroso, J. T Lymphocyte Migration: An Action Movie Starring the Actin and Associated Actors. *Front. Immunol.* **6,** 586 (2015).

101. Smith-Garvin, J. E., Koretzky, G. A. & Jordan, M. S. T cell activation. *Annu. Rev. Immunol.* **27,** 591–619 (2009).

102. Beemiller, P., Jacobelli, J. & Krummel, M. F. Integration of the movement of signaling microclusters with cellular motility in immunological synapses. *Nat. Immunol.* **13,** 787–95 (2012).

103. Owen, D. M. *et al.* High plasma membrane lipid order imaged at the immunological synapse periphery in live T cells. *Mol. Membr. Biol.* **27,** 178–89 (2010).

104. Varma, R., Campi, G., Yokosuka, T., Saito, T. & Dustin, M. L. T cell receptor-proximal signals are sustained in peripheral microclusters and terminated in the central supramolecular activation cluster. *Immunity* **25,** 117–27 (2006).

105. Williamson, D. J. *et al.* Pre-existing clusters of the adaptor Lat do not participate in early T cell signaling events. *Nat. Immunol.* **12,** 655–62 (2011).

106. Ritchie, K., Iino, R., Fujiwara, T., Murase, K. & Kusumi, A. The fence and picket structure of the plasma membrane of live cells as revealed by single molecule techniques (Review). *Mol. Membr. Biol.* **20,** 13–8

107. Krogsgaard, M. *et al.* Agonist/endogenous peptide-MHC heterodimers drive T cell activation and sensitivity. *Nature* **434,** 238–43 (2005).

108. Gaus, K., Le Lay, S., Balasubramanian, N. & Schwartz, M. A. Integrin-mediated adhesion regulates membrane order. *J. Cell Biol.* **174,** 725–34 (2006).

109. Gaus, K., Chklovskaia, E., Fazekas de St Groth, B., Jessup, W. & Harder, T. Condensation of the plasma membrane at the site of T lymphocyte activation. *J. Cell Biol.* **171,** 121–31 (2005).

110. van Zanten, T. S., Cambi, A., Joosten, B., Figdor, C. G. & Garcia-Parajo, M. F. Hotspots of GPI-Anchored Proteins and Integrin Nanoclusters Function as Nucleation Sites for Cell Adhesion. *Biophys. J.* **98,** 577a (2010).

111. van Zanten, T. S. *et al.* Direct mapping of nanoscale compositional connectivity on intact cell membranes. *Proc. Natl. Acad. Sci. U. S. A.* **107,** 15437–42 (2010).

112. Carman, C. V & Springer, T. A. Integrin avidity regulation: are changes in affinity and conformation underemphasized? *Curr. Opin. Cell Biol.* **15,** 547–556 (2003).

113. Chang, B.-J., Chou, L.-J., Chang, Y.-C. & Chiang, S.-Y. Isotropic image in structured illumination microscopy patterned with a spatial light modulator. *Opt. Express* **17,** 14710 (2009).

114. Ashdown, G. W., Cope, A., Wiseman, P. W. & Owen, D. M. Molecular Flow Quantified beyond the Diffraction Limit by Spatiotemporal Image Correlation of Structured Illumination Microscopy Data. *Biophys. J.* **107,** L21-3 (2014).

115. Rust, M. J., Bates, M. & Zhuang, X. Sub-diffraction-limit imaging by stochastic optical reconstruction microscopy (STORM). *Nat. Methods* **3,** 793–796 (2006).

116. Heilemann, M. *et al.* Subdiffraction-resolution fluorescence imaging with conventional fluorescent probes. *Angew. Chem. Int. Ed. Engl.* **47,** 6172–6 (2008).

117. Betzig, E. *et al.* Imaging intracellular fluorescent proteins at nanometer resolution. *Science* **313,** 1642–5 (2006).

118. Huang, B., Babcock, H. & Zhuang, X. Breaking the diffraction barrier: super-resolution imaging of cells. *Cell* **143,** 1047–58 (2010).

119. Eggeling, C. *et al.* Direct observation of the nanoscale dynamics of membrane lipids in a living cell. *Nature* **457,** 1159–62 (2009).

120. Klar, T. A., Wollhofen, R. & Jacak, J. Sub-Abbe resolution: from STED microscopy to STED lithography. *Phys. Scr.* **T162,** 14049 (2014).

121. Gustafsson, M. G. L. Nonlinear structured-illumination microscopy: wide-field

fluorescence imaging with theoretically unlimited resolution. *Proc. Natl. Acad. Sci. U. S. A.* **102,** 13081–6 (2005).

122. Gustafsson, M. G. L. Surpassing the lateral resolution limit by a factor of two using structured illumination microscopy. SHORT COMMUNICATION. *J. Microsc.* **198,** 82–87 (2000).

123. Moerner, W. E. & Kador, L. Optical detection and spectroscopy of single molecules in a solid. *Phys. Rev. Lett.* **62,** 2535–2538 (1989).

124. Hess, S. T., Girirajan, T. P. K. & Mason, M. D. Ultra-High Resolution Imaging by Fluorescence Photoactivation Localization Microscopy. *Biophys. J.* **91,** 4258–4272 (2006).

125. Thompson, R. E., Larson, D. R. & Webb, W. W. Precise nanometer localization analysis for individual fluorescent probes. *Biophys. J.* **82,** 2775–83 (2002).

126. Ayache, J., Beaunier, L., Boumendil, J., Ehret, G. & Laub, D. in *Sample Preparation Handbook for Transmission Electron Microscopy* 125–170 (Springer New York, 2010). doi:10.1007/978-0-387-98182-6_6

127. Dubochet, J. Cryo-EM--the first thirty years. *J. Microsc.* **245,** 221–4 (2012).

128. Al-Amoudi, A. *et al.* Cryo-electron microscopy of vitreous sections. *EMBO J.* **23,** 3583–8 (2004).

129. Dempsey, G. T., Vaughan, J. C., Chen, K. H., Bates, M. & Zhuang, X. Evaluation of fluorophores for optimal performance in localization-based super-resolution imaging. *Nat. Methods* **8,** 1027–36 (2011).

130. Huang, B., Wang, W., Bates, M. & Zhuang, X. Three-dimensional super-resolution imaging by stochastic optical reconstruction microscopy. *Science* **319,** 810–3 (2008).

131. Olivier, N., Keller, D., Gönczy, P., Manley, S. & Warren, J. Resolution Doubling in 3D-STORM Imaging through Improved Buffers. *PLoS One* **8,** e69004 (2013).

132. Ovesný, M., Křížek, P., Borkovec, J., Svindrych, Z. & Hagen, G. M. ThunderSTORM: a comprehensive ImageJ plug-in for PALM and STORM data analysis and super-resolution imaging. *Bioinformatics* **30,** 2389–90 (2014).

133. Tokunaga, M., Imamoto, N. & Sakata-Sogawa, K. Highly inclined thin illumination enables clear single-molecule imaging in cells. *Nat. Methods* **5,** 159–161 (2008).

134. Shtengel, G. *et al.* Interferometric fluorescent super-resolution microscopy resolves 3D cellular ultrastructure. *Proc. Natl. Acad. Sci. U. S. A.* **106,** 3125–30 (2009).

135. Ripley, B. D. Tests of `Randomness' for Spatial Point Patterns. *Journal of the Royal Statistical Society. Series B (Methodological)* **41,** 368–374 (1979).

136. Ripley, B. D. Modelling Spatial Patterns. *Journal of the Royal Statistical Society. Series B (Methodological)* **39,** 172–212 (1977).

137. Owen, D. M. *et al.* PALM imaging and cluster analysis of protein heterogeneity at the cell surface. *J. Biophotonics* **3,** 446–54 (2010).

138. Doguwa, S. I. On Second Order Neighbourhood Analysis of Mapped Point Patterns. *Biometrical J.* **31,** 451–459 (1989).

139. Rossy, J., Owen, D. M., Williamson, D. J., Yang, Z. & Gaus, K. Conformational states of

the kinase Lck regulate clustering in early T cell signaling. *Nat. Immunol.* **14,** 82–9 (2013).

140. Griffié, J. *et al.* A Bayesian cluster analysis method for single-molecule localization microscopy data. *Nat. Protoc.* **11,** 2499–2514 (2016).

141. Rubin-Delanchy, P. *et al.* Bayesian cluster identification in single-molecule localization microscopy data. *Nat. Methods* **12,** 1072–1076 (2015).

142. Peters, R., Owen, D. & Griffie, J. Analysis of Fibrous Spatial Point Patterns from Single-Molecule Super-Resolution Microscopy Data. *Biophys. J.* **112,** 142a (2017).

143. Griffié, J., Boelen, L., Burn, G., Cope, A. P. & Owen, D. M. Topographic prominence as a method for cluster identification in single-molecule localisation data. *J. Biophotonics* **8,** 925–934 (2015).

144. Griffié, J. *et al.* 3D Bayesian cluster analysis of super-resolution data reveals LAT recruitment to the T cell synapse. *Sci. Rep.* **7,** 4077 (2017).

145. Jungmann, R. *et al.* Multiplexed 3D cellular super-resolution imaging with DNA-PAINT and Exchange-PAINT. *Nat. Methods* **11,** 313–8 (2014).

146. Yi, J. *et al.* madSTORM: a superresolution technique for large-scale multiplexing at single-molecule accuracy. *Mol. Biol. Cell* **27,** 3591–3600 (2016).

147. Perry, G. L. W. SpPack: spatial point pattern analysis in Excel using Visual Basic for Applications (VBA). *Environ. Model. Softw.* **19,** 559–569 (2004).

148. Clark, P. J. & Evans, F. C. Distance to Nearest Neighbor as a Measure of Spatial Relationships in Populations. *Ecology* **35,** 445–453 (1954).

149. Koyama-Honda, I. *et al.* Fluorescence imaging for monitoring the colocalization of two single molecules in living cells. *Biophys. J.* **88,** 2126–36 (2005).

150. Sengupta, P. *et al.* Probing protein heterogeneity in the plasma membrane using PALM and pair correlation analysis. *Nat. Methods* **8,** 969–75 (2011).

151. Malkusch, S. *et al.* Coordinate-based colocalization analysis of single-molecule localization microscopy data. *Histochem. Cell Biol.* **137,** 1–10 (2012).

152. Rossy, J., Cohen, E., Gaus, K. & Owen, D. M. Method for co-cluster analysis in multichannel single-molecule localisation data. *Histochem. Cell Biol.* **141,** 605–12 (2014).

153. Brownlie, R. J. *et al.* Lack of the phosphatase PTPN22 increases adhesion of murine regulatory T cells to improve their immunosuppressive function. *Sci. Signal.* **5,** ra87 (2012).

154. Dai, X. *et al.* A disease-associated PTPN22 variant promotes systemic autoimmunity in murine models. *J. Clin. Invest.* **123,** 2024–2036 (2013).

155. Schachtner, H. *et al.* Tissue inducible Lifeact expression allows visualization of actin dynamics in vivo and ex vivo. *Eur. J. Cell Biol.* **91,** 923–929 (2012).

156. Lewandoski, M., Meyers, E. N. & Martin, G. R. Analysis of Fgf8 gene function in vertebrate development. *Cold Spring Harb. Symp. Quant. Biol.* **62,** 159–68 (1997).

157. Huang, F., Schwartz, S. L., Byars, J. M. & Lidke, K. A. Simultaneous multiple-emitter fitting for single molecule super-resolution imaging. *Biomed. Opt. Express* **2,** 1377–93

(2011).

158. Meijering, E., Dzyubachyk, O. & Smal, I. Methods for cell and particle tracking. *Methods Enzymol.* **504,** 183–200 (2012).

159. Wilson, C. A. & Theriot, J. A. A correlation-based approach to calculate rotation and translation of moving cells. *IEEE Trans. Image Process.* **15,** 1939–1951 (2006).

160. Hebert, B., Costantino, S. & Wiseman, P. W. Spatiotemporal image correlation spectroscopy (STICS) theory, verification, and application to protein velocity mapping in living CHO cells. *Biophys. J.* **88,** 3601–14 (2005).

161. Fujiwara, K. Techniques for localizing contractile proteins with fluorescent antibodies. *Curr. Top. Dev. Biol.* **14,** 271–96 (1980).

162. Robinson, R. W. & Snyder, J. A. An innovative fixative for cytoskeletal components allows high resolution in colocalization studies using immunofluorescence techniques. *Histochem. Cell Biol.* **1,** 1–1 (2003).

163. Smith, J. E. & Reese, T. S. Use of aldehyde fixatives to determine the rate of synaptic transmitter release. *J. Exp. Biol.* **89,** 19–29 (1980).

164. Rizzoli, S. O. & Betz, W. J. The Structural Organization of the Readily Releasable Pool of Synaptic Vesicles. *Science* **303,** 2037–2039 (2004).

165. Kamin, D., Revelo, N. H., Rizzoli, S. O., Levitan, E. & Schwander, M. FM Dye Photo-Oxidation as a Tool for Monitoring Membrane Recycling in Inner Hair Cells. *PLoS One* **9,** e88353 (2014).

166. Parsons, J. T., Horwitz, A. R. & Schwartz, M. A. Cell adhesion: integrating cytoskeletal dynamics and cellular tension. *Nat. Rev. Mol. Cell Biol.* **11,** 633–43 (2010).

167. Auinger, S. & Small, J. V. Chapter 14 Correlated Light and Electron Microscopy of the Cytoskeleton. *Methods in Cell Biology* **88,** 257–272 (2008).

168. Small, J. V., Rottner, K., Hahne, P. & Anderson, K. I. Visualising the actin cytoskeleton. *Microsc. Res. Tech.* **47,** 3–17 (1999).

169. Koestler, S. A., Auinger, S., Vinzenz, M., Rottner, K. & Small, J. V. Differentially oriented populations of actin filaments generated in lamellipodia collaborate in pushing and pausing at the cell front. *Nat. Cell Biol.* **10,** 306–13 (2008).

170. Zhuang, X. Nano-imaging with Storm. *Nat. Photonics* **3,** 365–367 (2009).

171. Xu, K., Zhong, G. & Zhuang, X. Actin, Spectrin, and Associated Proteins Form a Periodic Cytoskeletal Structure in Axons. *Science* **339,** 452–456 (2013).

172. Whelan, D. R. & Bell, T. D. M. Image artifacts in Single Molecule Localization Microscopy: why optimization of sample preparation protocols matters. *Sci. Rep.* **5,** 7924 (2015).

173. Tanaka, K. A. K. *et al.* Membrane molecules mobile even after chemical fixation. *Nat. Methods* **7,** 865–6 (2010).

174. Georgiades, P., Allan, V. J., Dickinson, M. & Waigh, T. A. Reduction of coherent artefacts in super-resolution fluorescence localisation microscopy. *J. Microsc.* **264,** 375–383 (2016).

175. Burgert, A., Letschert, S., Doose, S. & Sauer, M. Artifacts in single-molecule localization

microscopy. *Histochem. Cell Biol.* **144,** 123–31 (2015).

176. Ries, J., Kaplan, C., Platonova, E., Eghlidi, H. & Ewers, H. A simple, versatile method for GFP-based super-resolution microscopy via nanobodies. *Nat. Methods* **9,** 582–4 (2012).

177. De Castro, M. A. G., Hobartner, C. & Opazo, F. Aptamers provide superior stainings of cellular receptors studied under superresolution microscopy. *PLoS One* **12,** e0173050 (2017).

178. Bates, M., Huang, B., Dempsey, G. T. & Zhuang, X. Multicolor super-resolution imaging with photo-switchable fluorescent probes. *Science* **317,** 1749–53 (2007).

179. Jones, S. A., Shim, S.-H., He, J. & Zhuang, X. Fast, three-dimensional super-resolution imaging of live cells. *Nat. Methods* **8,** 499–508 (2011).

180. Platonova, E., Winterflood, C. M. & Ewers, H. A simple method for GFP- and RFP-based dual color single molecule localization microscopy. *ACS Chem. Biol.* **10,** 1411–1416 (2015).

181. Lampe, A., Haucke, V., Sigrist, S. J., Heilemann, M. & Schmoranzer, J. Multi-colour direct STORM with red emitting carbocyanines. *Biol. Cell* **104,** 229–237 (2012).

182. Chan, C. E. & Odde, D. J. Traction dynamics of filopodia on compliant substrates. *Science* **322,** 1687–91 (2008).

183. Chen, L., Vicente-Manzanares, M., Potvin-Trottier, L., Wiseman, P. W. & Horwitz, A. R. The integrin-ligand interaction regulates adhesion and migration through a molecular clutch. *PLoS One* **7,** e40202 (2012).

184. Gardel, M. L. *et al.* Traction stress in focal adhesions correlates biphasically with actin retrograde flow speed. *J. Cell Biol.* **183,** 999–1005 (2008).

185. Case, L. B. & Waterman, C. M. Integration of actin dynamics and cell adhesion by a three-dimensional, mechanosensitive molecular clutch. *Nat. Cell Biol.* **17,** 955–963 (2015).

186. Ridley, A. J. Rho GTPases and cell migration. *J. Cell Sci.* **114,** 2713–2722 (2001).

187. Burridge, K. & Guilluy, C. Focal adhesions, stress fibers and mechanical tension. *Exp. Cell Res.* **343,** 14–20 (2016).

188. van Hoorn, H. *et al.* The Nanoscale Architecture of Force-Bearing Focal Adhesions. *Nano Lett.* **14,** 4257–4262 (2014).

189. Brown, C. M. *et al.* Probing the integrin-actin linkage using high-resolution protein velocity mapping. *J. Cell Sci.* **119,** 5204–14 (2006).

190. Ishibashi, M. *et al.* Integrin LFA-1 regulates cell adhesion via transient clutch formation. *Biochem. Biophys. Res. Commun.* **464,** 459–466 (2015).

191. Havrylenko, S., Mezanges, X., Batchelder, E. & Plastino, J. Extending the molecular clutch beyond actin-based cell motility. *New J. Phys.* **16,** 105012 (2014).

192. Wiseman, P. W. *et al.* Spatial mapping of integrin interactions and dynamics during cell migration by image correlation microscopy. *J. Cell Sci.* **117,** 5521–34 (2004).

193. Changede, R., Xu, X., Margadant, F. & Sheetz, M. P. Nascent Integrin Adhesions Form on All Matrix Rigidities after Integrin Activation. *Dev. Cell* **35,** 614–621 (2015).

194. Sun, Z., Lambacher, A. & Fässler, R. Nascent Adhesions: From Fluctuations to a Hierarchical Organization. *Curr. Biol.* **24,** R801–R803 (2014).

195. Zimmermann, J. *et al.* Actin filament elasticity and retrograde flow shape the force-velocity relation of motile cells. *Biophys. J.* **102,** 287–95 (2012).

196. Goddette, D. W. & Frieden, C. Actin polymerization. The mechanism of action of cytochalasin D. *J. Biol. Chem.* **261,** 15974–80 (1986).

197. Dransfield, I., Cabañas, C., Craig, A. & Hogg, N. Divalent cation regulation of the function of the leukocyte integrin LFA-1. *J. Cell Biol.* **116,** 219–26 (1992).

198. Freeman, S. A. *et al.* Integrins Form an Expanding Diffusional Barrier that Coordinates Phagocytosis. *Cell* **164,** 128–140 (2016).

199. Tabdanov, E. *et al.* Micropatterning of TCR and LFA-1 ligands reveals complementary effects on cytoskeleton mechanics in T cells. *Integr. Biol. (Camb).* **7,** 1272–84 (2015).

200. Abram, C. L. & Lowell, C. A. The Ins and Outs of Leukocyte Integrin Signaling. *Annu. Rev. Immunol.* **27,** 339–362 (2009).

201. Bleul, C. C., Fuhlbrigge, R. C., Casasnovas, J. M., Aiuti, A. & Springer, T. A. A highly efficacious lymphocyte chemoattractant, stromal cell-derived factor 1 (SDF-1). *J. Exp. Med.* **184,** 1101–9 (1996).

202. Isabelle Petit, D. J. S. R. The SDF-1–CXCR4 signaling pathway: a molecular hub modulating neo-angiogenesis. *Trends Immunol.* **28,** 299 (2007).

203. Peled, A. *et al.* The chemokine SDF-1 activates the integrins LFA-1, VLA-4, and VLA-5 on immature human CD34(+) cells: role in transendothelial/stromal migration and engraftment of NOD/SCID mice. *Blood* **95,** 3289–96 (2000).

204. Kremer, K. N. *et al.* Stromal cell-derived factor-1 signaling via the CXCR4-TCR heterodimer requires phospholipase C-β3 and phospholipase C-γ1 for distinct cellular responses. *J. Immunol.* **187,** 1440–7 (2011).

205. Valignat, M.-P., Theodoly, O., Gucciardi, A., Hogg, N. & Lellouch, A. C. T lymphocytes orient against the direction of fluid flow during LFA-1-mediated migration. *Biophys. J.* **104,** 322–31 (2013).

206. Kumar, A. *et al.* CXCR4 Physically Associates with the T Cell Receptor to Signal in T Cells. *Immunity* **25,** 213–224 (2006).

207. Gómez-Móuton, C. *et al.* Segregation of leading-edge and uropod components into specific lipid rafts during T cell polarization. *Proc. Natl. Acad. Sci. U. S. A.* **98,** 9642–7 (2001).

208. Raab, M. *et al.* LFA-1 activates focal adhesion kinases FAK1/PYK2 to generate LAT-GRB2-SKAP1 complexes that terminate T-cell conjugate formation. *Nat. Commun.* **8,** 16001 (2017).

209. Fujiwara, T. K. *et al.* Confined diffusion of transmembrane proteins and lipids induced by the same actin meshwork lining the plasma membrane. *Mol. Biol. Cell* **27,** 1101–19 (2016).

210. Svensson, L., Stanley, P., Willenbrock, F. & Hogg, N. The Gαq/11 Proteins Contribute to T Lymphocyte Migration by Promoting Turnover of Integrin LFA-1 through Recycling. *PLoS One* **7,** e38517 (2012).

211. Chen, B.-C. *et al.* Lattice light-sheet microscopy: Imaging molecules to embryos at high spatiotemporal resolution. *Science* **346,** 1257998–1257998 (2014).

212. Monks, C. R. F., Freiberg, B. A., Kupfer, H., Sciaky, N. & Kupfer, A. Three-dimensional segregationofsupramolecular activation clustersinTcells. *Nature* **395,** 82–86 (1998).

213. Kliche, S. *et al.* CCR7-mediated LFA-1 functions in T cells are regulated by 2 independent ADAP/SKAP55 modules. *Blood* **119,** 777–785 (2011).

214. Brdika, T., Pavlistova, D., Albrecht, L., Bruyns, E. & Schraven, B. Phosphoprotein Associated with Glycosphingolipid-enriched Microdomains (PAG), a Novel Ubiquitously Expressed Transmembrane Adaptor Protein, Binds the Protein Tyrosine Kinase Csk and Is Involved in Regulation of T Cell Activation. *J. Exp. Med.* **191,** 1591–1604 (2000).

215. Zhu, X. *et al.* Integrin-dependent activation of MAP kinase: a link to shape-dependent cell proliferation. *Mol. Biol. Cell* **6,** 273–82 (1995).

216. Mendoza, M. C., Vilela, M., Juarez, J. E., Blenis, J. & Danuser, G. ERK reinforces actin polymerization to power persistent edge protrusion during motility. *Sci. Signal.* **8,** ra47-ra47 (2015).

217. Mendoza, M. C. *et al.* ERK-MAPK Drives Lamellipodia Protrusion by Activating the WAVE2 Regulatory Complex. *Mol. Cell* **41,** 661–671 (2011).

218. Okabe, S., Fukuda, S. & Broxmeyer, H. E. Activation of Wiskott-Aldrich syndrome protein and its association with other proteins by stromal cell–derived factor-1α is associated with cell migration in a T-lymphocyte line. *Exp. Hematol.* **30,** 761–766 (2002).

219. Bakker, G. J. *et al.* Lateral mobility of individual integrin nanoclusters orchestrates the onset for leukocyte adhesion. *Proc. Natl. Acad. Sci.* **109,** 4869–4874 (2012).

220. Reichardt, P. *et al.* A role for LFA-1 in delaying T-lymphocyte egress from lymph nodes. *EMBO J.* **32,** 829–43 (2013).

221. Hogg, N., Laschinger, M., Giles, K. & McDowall, A. T-cell integrins: more than just sticking points. *J. Cell Sci.* **116,** 4695–705 (2003).

222. Stewart, M. P., Cabanas, C. & Hogg, N. T cell adhesion to intercellular adhesion molecule-1 (ICAM-1) is controlled by cell spreading and the activation of integrin LFA-1. *J. Immunol.* **156,** 1810–7 (1996).

223. Cairo, C. W., Mirchev, R. & Golan, D. E. Cytoskeletal Regulation Couples LFA-1 Conformational Changes to Receptor Lateral Mobility and Clustering. *Immunity* **25,** 297–308 (2006).

224. Smith, A. *et al.* The role of the integrin LFA-1 in T-lymphocyte migration. *Immunol. Rev.* **218,** 135–46 (2007).

225. de Chaumont, F. *et al.* Icy: an open bioimage informatics platform for extended reproducible research. *Nat. Methods* **9,** 690–6 (2012).

226. Kent, S. P., Ryan, K. H. & Siegel, A. L. Steric hindrance as a factor in the reaction of labeled antibody with cell surface antigenic determinants. *J. Histochem. Cytochem.* **26,** 618–621 (1978).

227. Pleiner, T. *et al.* Nanobodies: site-specific labeling for super-resolution imaging, rapid epitope-mapping and native protein complex isolation. *Elife* **4,** e11349 (2015).

228. Tomosugi, W. *et al.* An ultramarine fluorescent protein with increased photostability and pH insensitivity. *Nat. Methods* **6,** 351–3 (2009).

229. Stiel, A. C. *et al.* 1.8 A bright-state structure of the reversibly switchable fluorescent protein Dronpa guides the generation of fast switching variants. *Biochem. J.* **402,** 35–42 (2007).

230. Matsuda, T., Miyawaki, A. & Nagai, T. Direct measurement of protein dynamics inside cells using a rationally designed photoconvertible protein. *Nat. Methods* **5,** 339–45 (2008).

231. Grotjohann, T. *et al.* rsEGFP2 enables fast RESOLFT nanoscopy of living cells. *Elife* **1,** e00248 (2012).

232. Hofmann, M., Eggeling, C., Jakobs, S. & Hell, S. W. Breaking the diffraction barrier in fluorescence microscopy at low light intensities by using reversibly photoswitchable proteins. *Proc. Natl. Acad. Sci. U. S. A.* **102,** 17565–9 (2005).

233. Tiwari, D. K. & Nagai, T. Smart fluorescent proteins: innovation for barrier-free superresolution imaging in living cells. *Dev. Growth Differ.* **55,** 491–507 (2013).

234. Pageon, S. V., Nicovich, P. R., Mollazade, M., Tabarin, T. & Gaus, K. Clus-DoC: a combined cluster detection and colocalization analysis for single-molecule localization microscopy data. *Mol. Biol. Cell* **27,** 3627–3636 (2016).

235. Andronov, L., Orlov, I., Lutz, Y., Vonesch, J.-L. & Klaholz, B. P. ClusterViSu, a method for clustering of protein complexes by Voronoi tessellation in super-resolution microscopy. *Sci. Rep.* **6,** 24084 (2016).

236. Roca-Cusachs, P. *et al.* Integrin-dependent force transmission to the extracellular matrix by α-actinin triggers adhesion maturation. *Proc. Natl. Acad. Sci. U. S. A.* **110,** E1361-70 (2013).

237. Bachir, A. I. *et al.* Integrin-Associated Complexes Form Hierarchically with Variable Stoichiometry in Nascent Adhesions. *Curr. Biol.* **24,** 1845–1853 (2014).

238. Stanley, P., Tooze, S. & Hogg, N. A role for Rap2 in recycling the extended conformation of LFA-1 during T cell migration. *Biol. Open* **1,** 1161–8 (2012).

239. Bridgewater, R. E., Norman, J. C. & Caswell, P. T. Integrin trafficking at a glance. *J. Cell Sci.* **125,** 3695–3701 (2012).

240. Osborne, D. G., Piotrowski, J. T., Dick, C. J., Zhang, J.-S. & Billadeau, D. D. SNX17 Affects T Cell Activation by Regulating TCR and Integrin Recycling. *J. Immunol.* **194,** 4555–4566 (2015).

241. Kondo, N. *et al.* NDR1-Dependent Regulation of Kindlin-3 Controls High-Affinity LFA-1 Binding and Immune Synapse Organization. *Mol. Cell. Biol.* **37,** e00424-16 (2017).

242. Kiuchi, T., Higuchi, M., Takamura, A., Maruoka, M. & Watanabe, N. Multitarget super-resolution microscopy with high-density labeling by exchangeable probes. *Nat. Methods* **12,** 743–746 (2015).

243. Griffie, J., Owen, D., Rubin-Delanchy, P. & Burn, G. Quantitative Analysis of Membrane Protein Clustering from Live-Cell, Single-Molecule Super-Resolution Microscopy Data. *Biophys. J.* **112,** 144a–145a (2017).

244. Iskratsch, T., Wolfenson, H. & Sheetz, M. P. Appreciating force and shape — the rise of

mechanotransduction in cell biology. *Nat. Rev. Mol. Cell Biol.* **15,** 825–833 (2014).

245. Saphirstein, R. J. *et al.* The Focal Adhesion: A Regulated Component of Aortic Stiffness. *PLoS One* **8,** e62461 (2013).

246. Hochwald, S. N. *et al.* A novel small molecule inhibitor of FAK decreases growth of human pancreatic cancer. *Cell Cycle* **8,** 2435–2443 (2009).

247. Golubovskaya, V. M. *et al.* A Small Molecule Inhibitor, 1,2,4,5-Benzenetetraamine Tetrahydrochloride, Targeting the Y397 Site of Focal Adhesion Kinase Decreases Tumor Growth. *J. Med. Chem.* **51,** 7405–7416 (2008).

248. Parsons, J. T. Focal adhesion kinase: the first ten years. *J. Cell Sci.* **116,** 1409–1416 (2003).

249. Weber, K. S. C. *et al.* Cytohesin-1 is a dynamic regulator of distinct LFA-1 functions in leukocyte arrest and transmigration triggered by chemokines. *Curr. Biol.* **11,** 1969–1974 (2001).

250. Cambi, A. *et al.* Organization of the integrin LFA-1 in nanoclusters regulates its activity. *Mol. Biol. Cell* **17,** 4270–81 (2006).

251. Hor, J. L. *et al.* Spatiotemporally Distinct Interactions with Dendritic Cell Subsets Facilitates CD4+ and CD8+ T Cell Activation to Localized Viral Infection. *Immunity* **43,** 554–565 (2015).

252. Morimatsu, M., Mekhdjian, A. H., Chang, A. C.-C., Tan, S. J. & Dunn, A. R. Visualizing the interior architecture of focal adhesions with high-resolution traction maps. *Nano Lett.* 150302160837001 (2015). doi:10.1021/nl5047335

253. Morimatsu, M., Mekhdjian, A. H., Adhikari, A. S. & Dunn, A. R. Molecular tension sensors report forces generated by single integrin molecules in living cells. *Nano Lett.* **13,** (2013).

254. Yi, J. *et al.* Highly Multiplexed, Super-resolution Imaging of T Cells Using madSTORM. *J. Vis. Exp.* e55997–e55997 (2017). doi:10.3791/55997

255. Charras, G. & Paluch, E. Blebs lead the way: how to migrate without lamellipodia. *Nat. Rev. Mol. Cell Biol.* **9,** 730–6 (2008).

256. Wilson, K. *et al.* Mechanisms of leading edge protrusion in interstitial migration. *Nat. Commun.* **4,** 2896 (2013).

257. Irimia, D., Charras, G., Agrawal, N., Mitchison, T. & Toner, M. Polar stimulation and constrained cell migration in microfluidic channels. *Lab Chip* **7,** 1783–90 (2007).

258. Wang, C. *et al.* Multiplexed aberration measurement for deep tissue imaging in vivo. *Nat. Methods* **11,** 1037–40 (2014).

259. Grimm, J. B. *et al.* Bright photoactivatable fluorophores for single-molecule imaging. *Nat. Methods* **13,** 985–988 (2016).

260. Tiwari, D. K. *et al.* A fast- and positively photoswitchable fluorescent protein for ultralow-laser-power RESOLFT nanoscopy. *Nat. Methods* **12,** 515–518 (2015).

261. Snapp, E. Design and use of fluorescent fusion proteins in cell biology. *Curr. Protoc. cell Biol.* **Chapter 21,** Unit 21.4 (2005).

262. Dubochet, J. *et al.* Cryo-electron microscopy of vitrified specimens. *Q. Rev. Biophys.* **21,**

129 (2009).